CERN-THESIS-2006-138

Instituut voor
Kern- en Stralingsfysica
Departement natuurkunde en sterrenkunde
Faculteit Wetenschappen

KATHOLIEKE UNIVERSITEIT
LEUVEN

Coulomb excitation of neutron rich Zn isotopes

Promotoren:
Prof. Dr. P. Van Duppen
Prof. Dr. M. Huyse

Proefschrift ingediend tot
het behalen van de graad van
doctor in de wetenschappen
door

Jarno Van de Walle

Leuven - 2006

Dank U / Thank You ...

Prof. Piet Van Duppen en Prof. Mark Huyse voor de kans die ze me hebben geboden om aan het Instituut voor Kern- en Stralingsfysica een doctoraat te starten. De voorbije vier jaar heb ik de vriendelijke werkatmosfeer, de gedetailleerde besprekingen van het experimentele werk en de continue steun ontzettend weten te appreciëren.

De groep Kernspectroscopie : Dieter, Dmitri, Farouk, Hilde, Irina, Ivan, Jan (Ponsaers en Van Roosbroeck), Jean-Charles, Jeroen, Johnny, Karen, Maria, Nick, Oleg, Pascale, Paul, Riccardo, Sarah, Shelley, Thomas and Yuri. Speciale vermelding voor Hilde, Dieter, Jan en Jeroen voor de vele plezante momenten !

Het gehele IKS, voor de vriendelijke atmosfeer en de leuke babbels tussendoor.
Josee, Katia en Sally voor begrip en geduld op te brengen voor een administratieve kneus als mezelf ...
Luc, Joris en Bert van het IT-team voor de geappreciëerde support.
De mensen van de dienst electronica en mechanica, speciaal aan Lucien, Maurice en collega's voor het "in no time" realiseren van de meest dringende verzoeken ...

All people at (REX-)ISOLDE for the continued support of the IS412 experiments over the years.
The MINIBALL collaboration and those who contributed during the IS412 experiments. Your help was largely appreciated !
Oliver Niedermaier, Martin Lauer, Vinzenz Bildstein for all support concerning analysis and hardware ...
Heiko Scheit, Nigel Warr, Dirk Weisshaar, Heinz-Georg Thomas, Rudi Lutter and Roman Gernhauser for the training and patient explanations of all MINIBALL related issues.

Het thuisfront : mijn ouders, broer(s) Han en Björn, Britt en Lennert. Speciale vermeldingen voor Annelies, Caro, Joost, Stijn en Thomas ... voor de ontelbare fijne momenten.

... Ilse. Voor alles.

Jarno
Gent-Leuven, september 2006

Contents

Introduction

Models to describe the nuclear medium have been developed ever since the discovery of the nucleus by E. Rutherford in 1907. One of the first major successes in the forties was the so-called "shell model". The "magic" nucleon numbers, which were found to have a "stabilizing" effect on the nucleus, were predicted by this model. These magic numbers are indicated in Fig. 1. Another model, developed in the sixties by Bohr and Mottelson, describes the nucleus from a geometrical point of view, where the excitation spectrum is explained by the dynamics of a rotating or vibrating small sphere (much like a "liquid drop").
Although these models provide a partial description of the nuclear medium, the microscopic understanding of the strong (residual) interaction between nucleons remains problematic. In order to probe subtle effects of the microscopic strong interaction on the nuclear structure, new experiments are needed on isotopes where no data is available. This leads to regions of the nuclear chart with extreme N/Z ratio's. Most of these isotopes are radioactive and short lived, which poses stringent experimental difficulties. In Fig. 1 the stable isotopes are indicated with black squares, the radioactive isotopes in grayscales.
Next to the microscopic understanding of the strong (residual) interaction between nucleons in nuclei far off the line of beta stability, the nuclear structure of these isotopes is relevant in nucleosynthesis calculations during the explosive ending of an ancient star. "Bottle-neck" or "waiting point" nuclei are key points in the description of this process and determine the final abundances of isotopes in the universe. One such "waiting point" is ^{78}Ni. In recent years many experiments have been performed in the region around this nucleus : minus one proton = Co, plus one proton = Cu, plus two protons = Zn, etc... In Fig. 1 this "region of interest" is indicated with a white dashed square.
This work can be seen as a continuation of the spectroscopic decay studies of Cu isotopes, where the level structure of Zn isotopes was probed. In the present work the quadrupole transition probability to the first 2_1^+ state is measured via Coulomb excitation, at the Radioactive Ion Beam facility ISOLDE with the MINIBALL gamma spectrometer. These experiments will give insight into the development of collectivity in heavy Zn isotopes.
This work is divided in six parts : 1- a general introduction is given on the shell model and collective models, 2- a number of experimental observables and measuring techniques are presented, with the emphasize on the B(E2,$2_1^+ \rightarrow 0_1^+$) quantity, 3- the experimental setup (MINIBALL + REX-ISOLDE) is described in detail, 4- the Coulomb excitation experiment together with the radioactive beam quality (contamination) are discussed at length, 5- results are presented of the Coulomb excitation experiment on $^{A=74,76,78}$Zn (2004), and 6- the results are compared to recent shell model calculations, collective model approaches and the new data are discussed within the existing B(E2,$2_1^+ \rightarrow 0_1^+$) systematics in the Ni region.

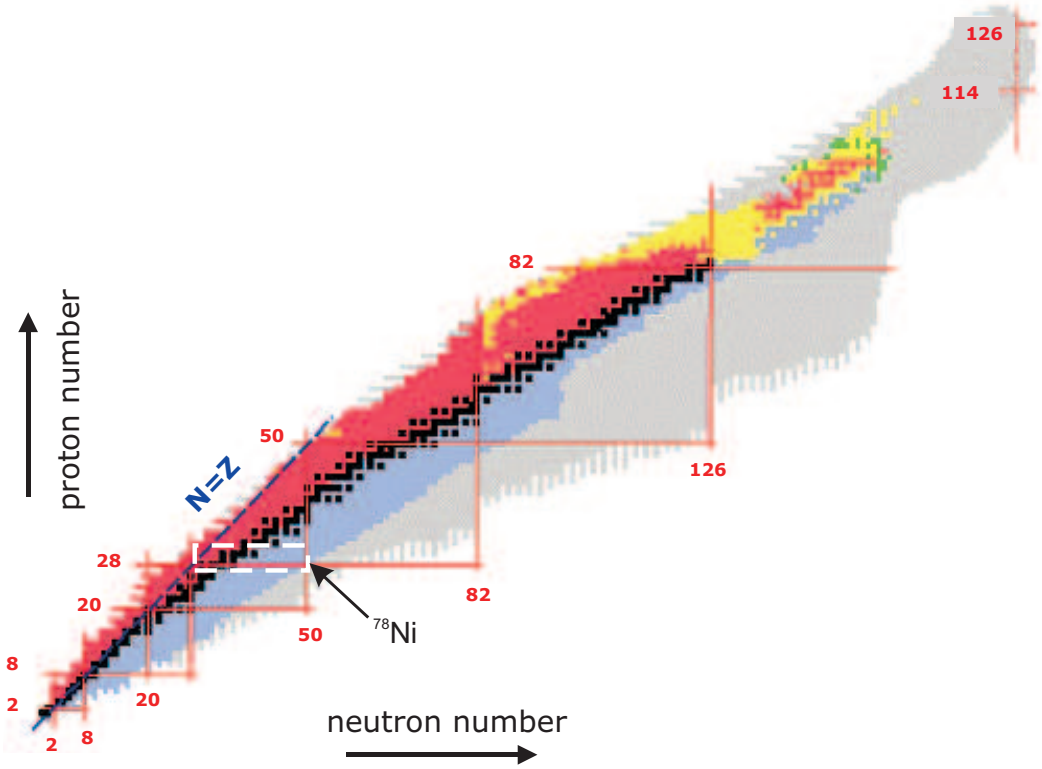

Figure 1: The chart of nuclides. The different grayscales refer to the decay mode of the isotopes: α-decay, β^+, β^--decay and spontaneous fission. The stable isotopes are colored in black. The light grey area corresponds to the unknown, but predicted isotopes.

Chapter 1

Nuclear Structure

Since the early scattering experiment by Rutherford it is recognized that the atom consists of a small massive nucleus and a diffuse electron cloud around it. The nucleus consists of positively charged protons and neutral neutrons, both referred to as nucleons. The small difference in rest mass between them points to a subnuclear structure. Indeed, the nucleons consist of elementary particles called quarks. Three families of each three quarks are known today, where nucleons consist of "family I" up and down quarks. Nucleons are strongly bound together in a volume of radius $\sim 10^{-15}$m, which is 10^5 times smaller then a typical atomic radius (10^{-10}m). The fact of strong binding over a small volume indicates the existence of a strong, attractive and short range force acting between the nucleons, overcoming the repulsive Coulomb force between protons. This force is called the *strong interaction* and acts on hadrons, particles with an underlying quark structure. The saturation property of the binding energy per nucleon indicates that the nucleons interact only with nearest neighbors, which can be shown by simple arguments (see [Cas00]).
Heisenberg introduced the concept of isotopic spin (=isospin,T) to indicate the difference between protons and neutrons. Protons have projected isospin T_z=-$\frac{1}{2}$ and neutrons have projected isospin T_z=+$\frac{1}{2}$. Accordingly, a pp(nn) system has total projected isospin T_z=-1(+1). The p-n has projected isospin 0. The isospin triplet T_z=-1(pp),0(pn),1(nn) has total isospin 1, and consequently there exists an isospin T=0 with T_z=0, so the p-n system has a T=0 as well as a T=1 component. The isospin introduces an additional component in the nuclear wave functions. Accordingly, the interaction between the nuclear wave functions exhibits an isospin dependence. From properties of the deuteron (1p-1n system) [1] and nucleon-nucleon scattering data it is seen that *the T=0 component of the nucleon-nucleon interaction is the most attractive and leads to more configuration mixing, collectivity and deformation* [Cas00].

1.1 The Nuclear shell model

1.1.1 The nuclear mean field

The nuclear medium is a strongly interacting system of a finite number of fermions, described by the Hamiltonian :

$$H = \sum_{i=1,A} T_i + \frac{1}{2} \sum_{i,j=1...A} V(i,j) \tag{1.1}$$

[1] The ground state is found to have nuclear spin $J^{\pi}=1^{+}$ and total isospin T=0.

where V(i,j) is the strong two body nucleon-nucleon interaction, A the number of fermions and T_i the kinetic energy of the i^{th} nucleon. This Hamiltonian can be re-written as

$$H = \left[\sum_{i=1,A}(T_i + U(r_i))\right] + \left[\frac{1}{2}\sum_{i,j=1...A} V(i,j) - \sum_{i=1,A} U(r_i)\right] = H_0 + H_1 \qquad (1.2)$$

where $U(r_i)$ is a central "mean field" potential generated by the nucleons themselves. The first term, H_0, describes the motion of A nucleons, independent of each other in the central potential U(r). The second term, H_1, is referred to as the residual interaction and describes the interaction between valence nucleons. By an appropriate choice of $U(r_i)$, H_1 can be treated as a perturbation.
Historically, the first mean field potential (U(r)) started from the harmonic oscillator potential (shown in Fig. 1.1 A), with additional interaction terms $\alpha\vec{l}\cdot\vec{s}$ and $\beta\vec{l}\cdot\vec{l}$. The first is referred to as the "spin-orbit" interaction and $\alpha(r)=U_{ls}\frac{1}{r}\frac{dU(r)}{dr}$, where $U(r)=\frac{U_0}{1+e^{(r-R_0)/a}}$ with $R_0=r_0A^{1/3}$ (r_0=1.27 fm) and a=0.67 fm [May50, Hey94]. The resulting quantized energy levels are shown in Fig. 1.2. In this approach, the known "magic nucleon numbers", characterized by larger binding energies and additional stability, were predicted by theory. This model became known as "the shell model", because of the grouping of energy levels into "shells", which are separated by larger energy gaps.

1.1.2 Microscopic mean field

The original shell model utilized a phenomenological shape for the mean field potential U(r), i.e. the modified harmonic oscillator potential (see above). A more microscopical base for the mean field U(r) is governed by the Hartree-Fock (HF) method. Starting from a given nucleon-nucleon interaction potential $V(\vec{r},\vec{r'})$, an initial 'guess' of the mean field and a ground state wave function of the nucleus, an optimized $U_{HF}(\vec{r})$ is iteratively calculated based on a minimization of the total nuclear energy. This HF potential is given by : $U_{HF}(\vec{r})=\int \rho(\vec{r'})V(\vec{r},\vec{r'})dr'$ with $\rho(\vec{r'})=\sum_{j(occ)}|\Psi_j(\vec{r'})|^2$ where the sum runs over all occupied orbitals j. A two body interaction which is often used in "self-consistent" HF calculations is the "Skyrme force" [Hey94]. An example of such calculated HF mean field potentials for protons and neutrons separately is given in Fig. 1.1 B for ^{100}Zn and ^{100}Sn. The neutron density is higher and the nuclear radius of the neutron volume is more diffuse in the neutron rich ^{100}Zn, compared to the N=Z nucleus ^{100}Sn.

1.2 Residual interactions in the shell model

In the shell model, nucleons are grouped in shells, separated by large energy gaps. *Valence nucleons* move on orbits belonging to a shell which is not completely filled. Because of the availability of free orbits in the valence space, valence nucleons can scatter through the two body interaction from one orbit to another, yielding the excitation spectrum of the nucleus. While in the mean field approach, an optimized central potential was calculated in order to minimize the residual interactions (H_1), the shell model approach focusses on the properties of the *residual interaction between valence nucleons* and incorporates the effect of the underlying core in the so-called *effective* residual interaction.

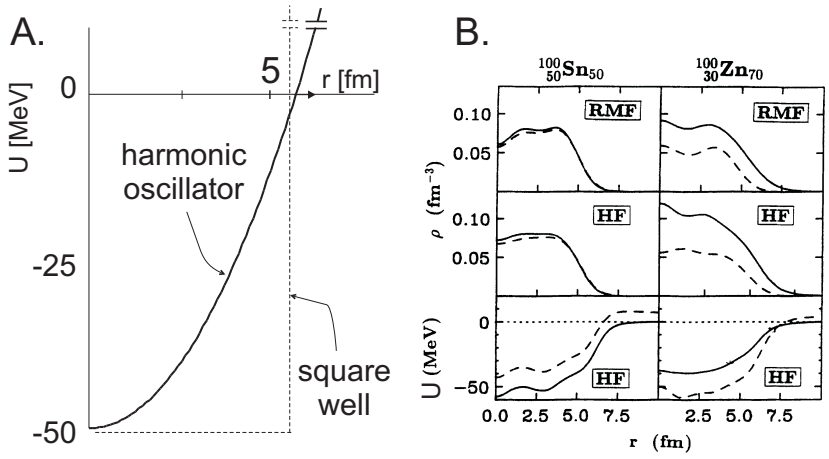

Figure 1.1: *A. Schematic mean field potential : the harmonic oscillator and the square well potential (A=100, R=1.25A$^{1/3}$). B. Mean field potentials and nuclear matter densities calculated with the Hartree-Fock method and in the Relativistic Mean Field approach (taken from [Dob94]). The dashed/full line corresponds to the proton/neutron density and mean field.*

Whereas mean field theories calculate global properties of the nucleus, such as binding energies, root mean square radii ($<r^2>$), masses and half lives, the shell model calculates detailed spectroscopic information, which can be directly compared to experimental information.
In shell model calculations, different approaches exist for the description of the effective residual interaction. A brief summary is given in the following, for a more detailed overview, see [Mae06].

1. Microscopic effective interactions : These interactions are based on Brueckner's G-matrix theory. It treats two nucleons in the nuclear medium in a way analogue to scattering of two nucleons in vacuum [Mae06]. The G-matrix theory deals with the hard repulsive core of the free nucleon-nucleon interaction and makes the resulting effective interaction well-behaved at short distances. An example is the interaction derived by Hjorth-Jensen *et al.* for the $2p_{3/2}$,$1f_{5/2}$,$2p_{1/2}$,$1g_{9/2}$ valence space [Hjo95] and the GXPF1 interaction for the full pf-shell ($1f_{7/2}$,$2p_{3/2}$,$1f_{5/2}$,$2p_{1/2}$) by Honma *et al.* [Hon04]. Adjusted versions of these and other interactions exist, where parameters are fitted to experimental data in the considered mass region where the interaction applies. An example is given by the monopole corrections in the Hjorth-Jensen interaction [Pov81, Now96] where the resulting interaction gives a good description of many spectroscopic properties of Ni- and Cu-isotopes. Recently, the Hjorth-Jensen interaction was fitted to experimental data in the $pf_{5/2}$-g shell, resulting in an isospin dependent set of interaction matrix elements [Lis04].

2. Phenomenological effective interactions : The two-body interaction matrix elements and the single particle energies are fitted to experimental data in the considered mass region. Parameter values are adjusted by means of a least-squares fitting procedure [Bru77]. An example of such an interaction in the sd-shell is the Brown and Wildenthal interaction ([Bro88]).

3. Schematic effective interactions : Departing from basic properties of the nuclear

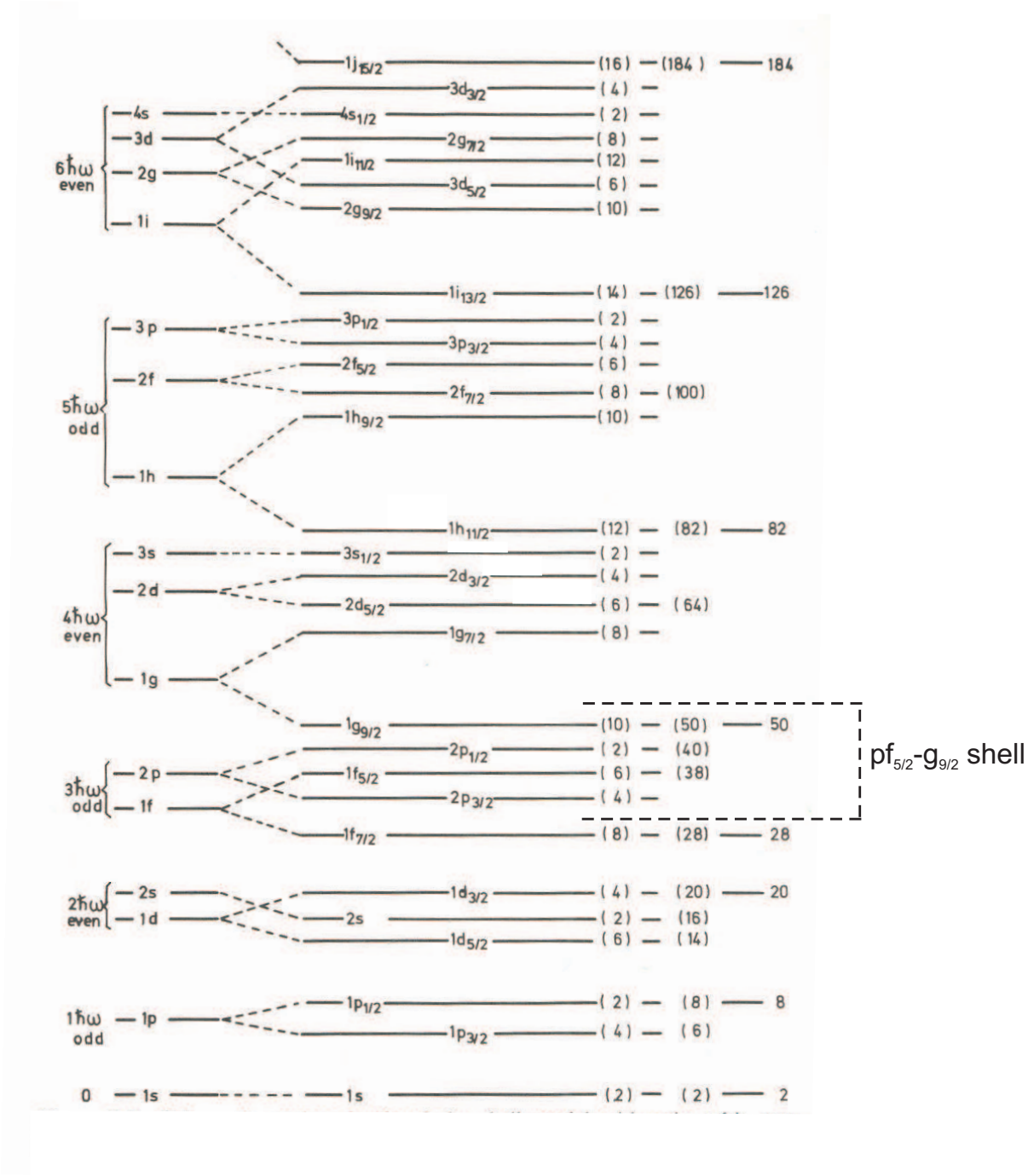

Figure 1.2: *Quantized energy levels originating from the modified harmonic oscillator potential. The pf-shell and the $g_{9/2}$ level (between nucleon numbers 28 and 50) is the region which will be discussed in this work. Picture taken from [Rin80].*

force, such as its short range character, a simple form for the effective interaction can be utilized. An illustrative example is the delta-interaction [Bru77] and its extension with a spin exchange component. The particular characteristic of these interactions provide insight in the description of nuclear structure properties.

A full diagonalization of the Hamiltonian H (eq. 1.2), yielding eigenvalues of the nuclear energy levels, is practically not possible for many valence nucleon systems, since the matrix dimension ($H_{i,j}$) becomes too large. Therefore, an inert core of nucleons is assumed which do not play a role in the excitation spectrum of the nucleus. The assumption of an inert core with valence nucleons outside this core is called "truncation" and is a *key element* in shell model calculations. A natural truncation in the shell model is governed by the major shells, separated by large energy gaps. A clear distinction is made between the *inert closed shell* (the core nucleus) and the *valence nucleons* which are allowed to move in a selected set of shell model orbits and interact with each other through the *residual interaction*, e.g. ^{56}Ni(^{40}Ca) closed core + the $pf_{5/2}g_{9/2}$(pf) valence shell.
The Hamiltonian describing the residual interaction between valence nucleons outside a closed shell can be written as :

$$H = H_{monopole} + H_{multipole} \tag{1.3}$$

where the monopole Hamiltonian is given by :

$$H_{monopole} = \sum_{j_\pi} \tilde{\epsilon_{j_\pi}} \mathbf{n}_{j_\pi} + \sum_{j_\nu} \tilde{\epsilon_{j_\nu}} \mathbf{n}_{j_\nu} \tag{1.4}$$

with $\tilde{\epsilon_{j_{\pi,\nu}}}$ the monopole-corrected single particle proton,neutron energies (referred to as the "effective single particle energies") and $\mathbf{n}_{j_{\pi,\nu}}$ the number operator in the $j_{\pi,\nu}$ shell. The eigenvalues of the monopole Hamiltonian should reproduce the energies of single proton(neutron) states in odd-A nuclei with Z(N) equal to a magic number plus or minus one proton(neutron) [Smi04]. $H_{monopole}$ is related to the evolution of the spherical mean field and determines the position of single particle energy levels. The higher-order multipoles determine correlations which are not present in the spherical mean field and are responsible for configuration mixing between levels and the relative energy splitting between different angular momentum states. The importance of the quadrupole term in the multipole decomposition (λ=2) is motivated by the fact that *in most even-even nuclei, the first excited state has $J^\pi = 2^+$*. Pairs of nucleons are broken by the quadrupole residual interaction and they create $J^\pi = 2^+$ excited states. It has been recognized that many features of low-lying excited states, for example in even-even nuclei, can be attributed to the quadrupole interaction [Cas00]. Mixing between several 2^+ states will lower the state which is the most symmetric in interchange of nucleon coordinates. The lowering of this coherent 2_1^+ state is an indication for the amount of p-n quadrupole interaction. In general, the higher order terms in the multipole expansion of the residual interaction are responsible for the distortion of the spherical shape, e.g. quadrupole distortion for the 2^+ state. With increasing p-n interaction, the higher order terms will dominate the overall structure and the nucleons will display "collective behavior" (see par.1.4).

1.2.1 The pairing interaction

The coupling of pairs of nucleons in the same orbit to a $J=0^+$ state is energetically favored by a strong, short range and attractive *pairing interaction*, where the matrix

elements are given by :

$$\langle j_1 j_2 J|V_{pair}|j_3 j_4 J'\rangle = -(-1)^{l_1+l_3} G\sqrt{j_1+\frac{1}{2}}\sqrt{j_3+\frac{1}{2}}\delta_{j_1 j_2}\delta_{j_3 j_4}\delta_{J0}\delta_{J'0}. \tag{1.5}$$

Pairs of like nucleons in the same orbit j, which are coupled to J=0 can scatter to an unoccupied orbit j', above the Fermi level, where they are coupled again to J'=0. Particles around the Fermi level take part in this scattering process, since nucleons deep below the Fermi level are blocked by the Pauli principle. Due to this "pair scattering", the Fermi level is smeared out and the orbits around the Fermi level are *partially filled*, as shown in Fig. 1.3. The probability that an orbital i around the Fermi level is occupied by a particle or a hole is given by : V_i (particle) and U_i (hole), where

$$U_i = \frac{1}{\sqrt{2}}(1+\frac{(\epsilon_i-\lambda)}{\sqrt{(\epsilon_i-\lambda)^2+\Delta^2}})^{\frac{1}{2}} \tag{1.6}$$

$$V_i = \frac{1}{\sqrt{2}}(1-\frac{(\epsilon_i-\lambda)}{\sqrt{(\epsilon_i-\lambda)^2+\Delta^2}})^{\frac{1}{2}} \tag{1.7}$$

and λ is the Fermi energy in the nucleus, Δ is the pairing gap parameter and ϵ_i are the single particle energies (=SPE). The number of valence particles in orbit i is given by n=$\sum_i V_i^2$. The pairing gap parameter Δ is related to the particle and hole occupation probabilities :

$$\Delta = G\sum_{i,j} U_i V_j. \tag{1.8}$$

Single particles in the partially filled orbits are called quasi-particles and are described by a linear combination of particle and hole wave functions. The energy of these quasi-particles is different from the "normal" single particle energies in the same orbit ϵ_i. The quasi particle energy is given by :

$$E_i = \sqrt{(\epsilon_i-\lambda)^2+\Delta^2}. \tag{1.9}$$

Without pairing (Δ=0) this reduces again to the energy difference between the single particle energy of a particle in orbit i and the Fermi level. The simplest excitation in this quasi-particle picture is to *create* from the vacuum state (J=0) two quasi-particles. The energy of the excitation is then the sum of the 2 created quasi particles :

$$E_{ex} = \sqrt{(\epsilon_i-\lambda)^2+\Delta^2}+\sqrt{(\epsilon_j-\lambda)^2+\Delta^2}. \tag{1.10}$$

A two quasi particle excitation has a minimal excitation energy of 2Δ, which is called the *pairing gap*. In the case of even-even nuclei, there are no "unpaired nucleons" within one orbit i (with SPE ϵ_i). The pairing interaction explains why in all even-even nuclei, the ground state is a 0^+ state.

1.2.2 Two particle energy spectrum

Considering the case of two identical nucleons (T=1,$\pi-\pi$ or $\nu-\nu$) in the same orbit which interact through a δ-interaction, a simple result is obtained for the energy

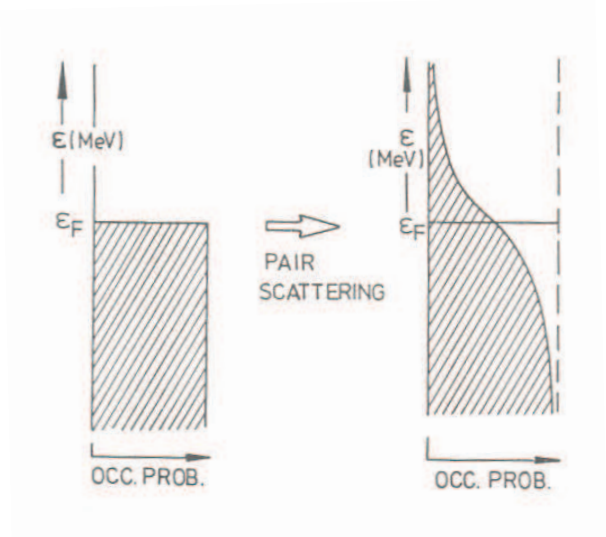

Figure 1.3: *Left : occupation of the levels up to the Fermi level (ϵ_F), on the right the occupation of the levels with pair scattering. Levels below and above the Fermi level are partially filled.*

splitting between states with different J=|j_1-j_2|...j_1+j_2=0,2,4,...,2j :

$$\begin{aligned} \Delta E(j^2, J) &= -V_0 F_R(nl) A(j^2 J) \qquad \text{where} \\ A(j^2 J) &= \frac{(2j+1)^2}{2} \begin{pmatrix} j & j & J \\ \frac{1}{2} & -\frac{1}{2} & 0 \end{pmatrix}^2 \\ &\approx \frac{sin^2\frac{\theta}{2}}{\pi j^2 sin\theta} \qquad \text{for large j,J and J even} \end{aligned} \tag{1.11}$$

where F_R(nl) is an integral over radial coordinates which depends on the radial overlap of the nucleon wave functions and V_0 is the strength of the interaction. The angle θ between the two angular momenta ($\vec{j}$) is approximately given by cosθ=$\frac{J^2}{2j^2}$-1 (see Fig. 1.4, [Cas00]). This result is illustrative for most of the low lying excited states in single magic even-even nuclei with two nucleons outside a closed core. As an example, the 0^+,2^+,4^+,6^+ and 8^+ states in ^{70}Ni (Z=28 and N=40 + $\nu 1g^2_{9/2}$) are shown in Fig. 1.4. The dashed line indicates the energy splitting given by eq. 1.11. This result illustrates that from a basic schematic force as the δ-interaction, it can be understood why the first excited state in many (but not all) even-even nuclei is a 2^+ state.

1.3 Deformed mean field

As more and more valence nucleons are added the proton-neutron interaction energy gradually builds up and the nucleus will deviate from its spherical shape and end up in an energetically more favorable deformed shape. In these cases, the nucleus can be described from a more macroscopically point of view. The radius describing the nuclear surface can be expanded as :

$$R(t) = R_{av}\left(1 + \sum_{\lambda \geq 1} \sum_{\mu=-\lambda}^{+\lambda} \alpha_{\lambda\mu}(t) Y_{\lambda\mu}(\theta, \phi)\right) \tag{1.12}$$

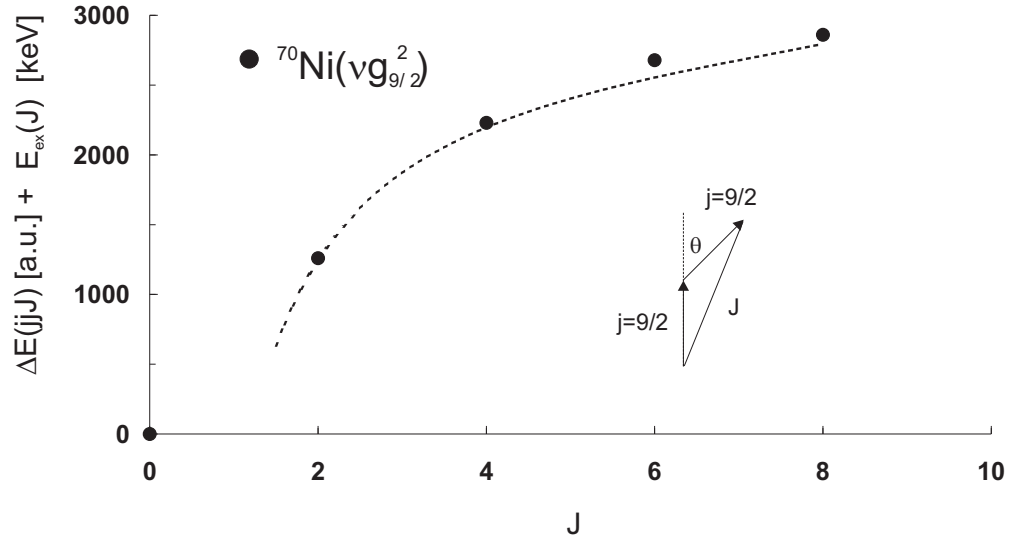

Figure 1.4: *Illustration of the energy splitting induced by the multipole parts of a δ-interaction for identical nucleons (T=1) in the same orbit (j), coupled to total spin J. The experimental 2^+,4^+,6^+ and 8^+ states in ^{70}Ni (Z=28 and N=40 + $\nu g^2_{9/2}$) are shown for comparison. Data is taken from [nndc] (all spins are uncertain, except for the ground state 0^+).*

where R_{av} is the average radius in the equilibrium state and $\alpha_{\lambda\mu}(t)$ are time dependent amplitudes of the vibration [Cas00, Kra88]. The nucleus can be excited with angular momenta λ. In the case of λ=1 the nucleus exhibits a net displacement of its center of mass relative to its center of charge. This mode of E1 type, is referred to as the "scissors mode" or the "Giant Dipole Resonance" and is generally at high excitation energy (8-20 MeV). The low lying excitation spectrum of deformed nuclei are dominated by λ=2 excitations (quadrupole,E2). Using the transformation from the laboratory frame to the intrinsic frame, the five $\alpha_{\lambda=2,\mu}$ parameters are reduced to three real parameters $a_{2,0}$, $a_{2,2}=a_{2,-2}$ and $a_{2,1}=a_{2,-1}=0$. These variables can be parameterized as :

$$a_{20} = \beta_2 cos\gamma \qquad \text{and} \qquad a_{22} = a_{2-2} = \frac{1}{\sqrt{2}}\beta_2 \sin\gamma. \tag{1.13}$$

The nuclear quadrupole deformation can then be described in terms of β_2 and γ. For γ=0°(60°) prolate(oblate) shapes result, respectively. For γ not a multiple of 60°, a triaxial shape results ([Hey94]). The λ=2 excitation will be discussed more extensively in par. 1.4.

A microscopical basis for the deformed structure of the nucleus is governed by the Nilsson model. A single nucleon with total angular momentum j orbiting a spherical symmetric closed core nucleus can be interpreted in the light of the independent particle model. But what happens if this single nucleon orbits a deformed nucleus ? The interaction of the single nucleon with the underlying core depends then on the relative orientation of the nucleons orbit with respect to the time averaged shape of the deformed core. The degeneracy of the substates in the spherical case will be lifted according to the projection of the spin j on the symmetry axis of the deformed nucleus (referred to as the quantum number Ω=j,j-1,j-2,...). The amount of energy splitting between the substates depends now on the relative interaction of the Ω-orbits with the

deformed nucleus. The Nilsson model describes the evolution of these splittings between the K-states, as a function of deformation. In Fig. 1.5 the splitting of the single particle orbits is plotted as a function of deformation parameter ϵ_2[2]. The labelling of the orbits is : Ω[N,n_z,Λ] with N the principal quantum number of the major oscillator shell (see Fig. 1.2), n_z the number of quanta associated with the wave function moving along the z-direction and Λ the projection of the orbital angular momentum on the z-axis. The $1g_{9/2}$ orbit splits in five two-fold degenerate components, where the first two orbits are strongly downsloping for prolate (ϵ_2>0) and oblate (ϵ_2<0) deformation. The upper two orbits at the prolate side strongly favor sphericity since the energy increases strongly. At the oblate side, the upper two orbits are rather insensitive to deformation. In a deformed nucleus, the single particle wave function will be a mixture of these pure "Nilsson single particle" orbits.

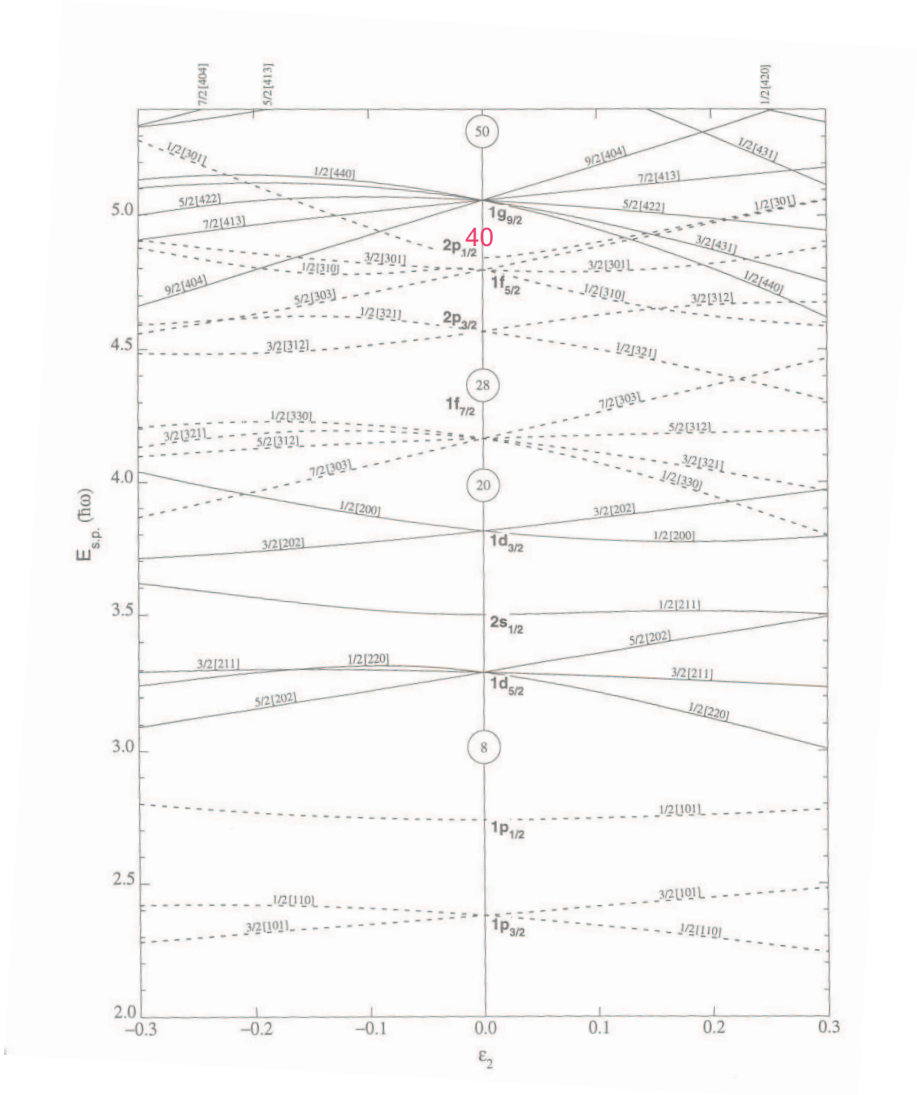

Figure 1.5: *Evolution of the single particle energies as a function of deformation parameter in the Nilsson model (taken from [Fir96]).*

[2] ϵ_2 is related to the more 'common' deformation parameter β_2=$\sqrt{\frac{\pi}{5}}[\frac{4}{3}\epsilon_2+\frac{4}{9}\epsilon_2^2+\frac{4}{27}\epsilon_2^3+\frac{4}{81}\epsilon_2^4]$ [Fir96]

1.4 Collectivity in the Nuclear Medium

In the situation of many valence neutrons and protons, the large residual proton-neutron interaction energy becomes dominant and the residual interaction cannot be treated any longer as a perturbation on the spherical mean field. The nucleons will show "collective behavior", resulting in energy spectra that are indicative for vibrational or rotational collective modes of motion. A crucial role in this is played by the T=0 part of the residual proton-neutron interaction as has been highlighted by several authors ([Cas00, Fed79]). One of the issues addressed in this work is how the collectivity in nuclei with large neutron excess evolves when going towards a neutron shell closure. The number of valence neutrons interacting with the valence protons through the collectivity inducing T=0 interaction will then gradually decrease. A sign for collectivity in the nuclear medium is found in the low-energy excitation spectrum and the associated electromagnetic decay properties (E/Mλ) of the nucleus, since these exhibit similarities to the quantized vibrator or rotor.

1.4.1 The Vibrational Model

An elegant collective model is the vibrational model, related to the λ=2 excitation in eq. 1.12. In the vibrational model the λ=2 excitation is seen as a one phonon excitation carrying two units of angular momentum (units $\hbar$). A two phonon excitation results in three states with angular momenta : 0^+,2^+,4^+ while a three phonon excitation results in 0^+,2^+,3^+,4^+ and 6^+ states. The pure harmonic vibrational model predicts in a natural way that the ground state of an even-even nucleus is a 0^+ state, while the first excited state is 2^+, followed by 0_2^+,2_2^+,4_1^+ states at twice the energy of the first 2^+ state. The three phonon states occur at three times this energy, where as well octupole excitation (λ=3) might occur (3^- state). The degeneracy of the 2-phonon states is lifted due to residual interactions between the two phonons. It results in a splitting of the 0_2^+,2_2^+ and 4_1^+ levels, which can be calculated with the help of "Coefficients of Fractional Percentage" ([Cas00, Tal63]). One of the fingerprints for the applicability of the vibrational model is the energy ratio $E(4_1^+)/E(2_1^+)$ which is 2 for pure harmonic vibration and typically 2-2.5 in realistic situations. An illustrative example of vibrational behavior is seen in the Cd isotopic chain (Z=48), where the valence protons in the open proton shell interact strongly with the valence neutrons in the open neutron shell, leading to collective behavior (Fig. 1.6). The drop of the energy ratio towards N=50 can be interpreted as the loss in quadrupole collectivity as one of the major shell closures is reached (decrease in π-ν interaction energy).

1.4.2 The Rotational Model

Another collective approach is to view the nucleus as an axially symmetric rigid rotating system along an axis perpendicular to the symmetry axis. The Hamiltonian describing the rotating system is given by :

$$H = \frac{\hbar^2}{2\mathcal{J}}\vec{I}^2 \tag{1.14}$$

where $\mathcal{J}$ is the moment of inertia of the system and $\vec{I}$ is the total angular momentum. $\vec{I}$ is the sum of angular momentum generated by the core rotation ($\vec{R}$) and the intrinsic angular momentum of unpaired valence nucleons ($\vec{J}$). The projection of $\vec{I}$ on the symmetry axis is denoted K. Since $\vec{R}$ is perpendicular to the symmetry axis, the projection of $\vec{J}$ is identical to the projection of $\vec{I}$. The total rotational energy can be considered

as the superposition of rotational motion on intrinsic excitation, characterized by the projected angular momentum K :

$$E_{rot} = \frac{\hbar^2}{2\mathcal{J}}[J(J+1) - K^2]. \tag{1.15}$$

Considering the low lying excitation spectrum in even-even nuclei, the low lying rotational energy levels are labelled by K=0, J^π=0^+,2^+,4^+,... and are given by : $E(2_1^+)$ =$6\frac{\hbar^2}{2\mathcal{J}}$, $E(4_1^+)$ =$20\frac{\hbar^2}{2\mathcal{J}}$,... An important result here is the signature for rotational behavior, following from the energy ratio $\frac{E_{4_1^+}}{E_{2_1^+}}$=3.33. In Fig. 1.6A, the evolution of this ratio is plotted for the N=40 line. A gradual evolution towards collective, rotational behavior is observed.

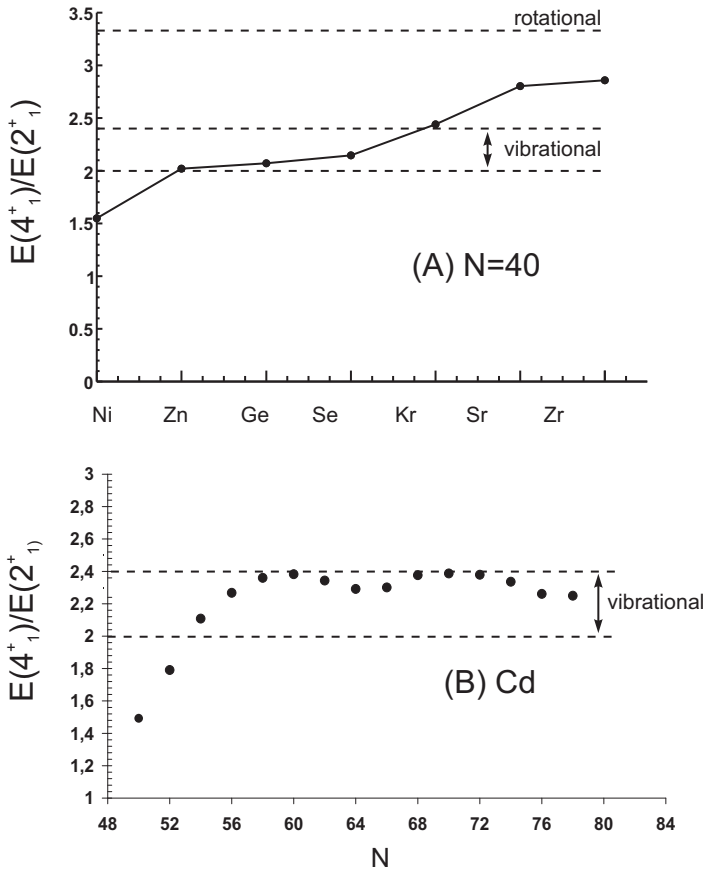

Figure 1.6: *(A) The onset of deformation along the N=40 line, indicated by the $E(4_1^+)/E(2_1^+)$ ratio (2.4=vibrational, 3.33=rotational).(B) The Cd isotopic chain displays vibrational behavior in the mid-shell between N=50 and N=82, based on the $E(4_1^+)/E(2_1^+)$ ratio.*

Chapter 2

Experimental Techniques and Observables

2.1 Experimental observables

The energy of the first excited 2^+ state in even-even nuclei and the B(E2,$0_1^+ \rightarrow 2_1^+$) strength are correlated. This correlation will be discussed in the following, together with the evolution of both quantities as a function of the neutron(proton) number. Both quantities (2_1^+ and B(E2,$2_1^+ \rightarrow 0_1^+$)) reflect the underlying shell structure of the nuclear medium and their evolution illustrates the evolution of the shell structure in extreme N/Z regions. This will be illustrated for the region between Z=28-N=40 ($^{68}_{28}$Ni) and Z=28-N=50 ($^{78}_{28}$Ni). The proton shell closures above and below Z=28 : Z=20 (Ca) and Z=50 (Sn) will be touched upon for comparison. A series of other experimental observables reflecting the shell structure and its evolution with neutron/proton number are given in addition.

2.1.1 The E(2_1^+) state and B(E2,$0_1^+ \rightarrow 2_1^+$) strength

In general, the electromagnetic transition strength of multipolarity λ is defined as :

$$B(L\lambda, J_i \rightarrow J_f) = \sum_{M_i,M_f} |\langle \alpha_f, J_f M_f | O(L,\lambda M) | \alpha_i, J_i M_i \rangle|^2 \quad (2.1)$$

$$= \frac{1}{2J_i+1} | < \alpha_f, J_f || O(L,\lambda) || \alpha_i, J_i > |^2 \quad (2.2)$$

where the electromagnetic operator O(L,λ, M) has either an electric (L=E) or magnetic (L=M) character and $\alpha_{i,j}$ are any set of additional quantum numbers characterizing the states |i,f> and L,M are the orbital angular momentum and the magnetic quantum number. The electromagnetic operator O(L=E,λM) might be replaced by :

$$\mathcal{M}(E\lambda M) = \int \rho(\vec{r}) r^L Y_{LM}(\vec{r}) d\vec{r} \qquad \text{and}$$

$$\rho(\vec{r}) = \sum_{k=1}^{A} e(k) \delta(\vec{r} - \vec{r}_k)$$

where e(k)=0 for neutrons and 1e for protons. The quadrupole transition strength is thus defined as :

$$B(E2, 0_1^+ \rightarrow 2_1^+) = |\langle \Psi_{2_1^+} || \mathcal{M}(E2) || \Psi_{0_1^+} \rangle|^2 \quad (2.3)$$

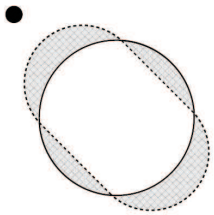

Figure 2.1: *Schematic illustration of how a single nucleon may polarize the underlying core.*

The B(E2) value is expressed in units $e^2b^2=10^4e^2fm^4$ ([1]). The number of nucleons participating in the transition is related to the composition of the nuclear wave functions involved. In an extreme single particle picture, where only one nucleon contributes to the transition, the so-called "Weisskopf" unit is defined as :

$$\begin{aligned} B^W(EL) &= \frac{1}{4\pi}(\frac{3}{L+3})^2(1.2A^{1/3})^{2L} \qquad [e^2fm^{2L}] \\ B^W(ML) &= \frac{10}{\pi}(\frac{3}{L+2})^2(1.2A^{1/3})^{2L-2} \qquad [\mu_N^2 fm^{2L-2}] \end{aligned}$$

for the electric and magnetic multipoles of order L (μ_N=the nuclear magneton=0.105 e·fm). The transformation from $B(E2,2_1^+ \rightarrow 0_1^+)$ in units of e^2fm^4 to W.u. is given by :

$$B(E2,2^+ \rightarrow 0^+)_{W.u.} = \frac{16.8}{A^{4/3}} B(E2,2^+ \rightarrow 0^+)_{[e^2fm^4]}.$$

Expressed in these "Weisskopf Units" (W.u.), the B(E2) value is a measure for the amount of collectivity in the nucleus. Values close to 1 indicate pure single particle transitions, while typical collective E2 transitions in spherical vibrational nuclei have B(E2) values ∼10-50 W.u. The B(E2) values within the vibrational model exhibit the following relationship [Boh75]:

$$B(E2,4_1^+ \rightarrow 2_1^+) = 2 \cdot B(E2,2_1^+ \rightarrow 0_1^+), \tag{2.4}$$

which results from the selection rule for E2 transitions between states within one vibrational band (ΔN_{ph}=1). The $B(E2,0_1^+ \rightarrow 2_1^+)$ value is related to the lifetime of the 2_1^+ state :

$$\tau_{\gamma,2_1^+}[ps] = 40.81 \times 10^{13} E_{keV}^{-5} / B(E2) \uparrow_{e^2b^2} . \tag{2.5}$$

This relationship is widely used in experiments where the lifetime of the excited state is measured. Other techniques will be touched upon in the following.
In shell model calculations, the reduced transition probability $B(E2,0_1^+ \rightarrow 2_1^+)$, can be calculated within the limited model space. As was pointed out in par. 1.2, calculations are performed for only a limited number of valence nucleons, which are restricted to move in selected valence orbits and are totally decoupled from the underlying inert closed shell. The latter may not always be the case, since single nucleons can *polarize* the underlying core, as indicated in Fig. 2.1. To account for this polarization effect, *effective* proton(neutron) charges $e_\pi^{eff}(e_\nu^{eff})$ are introduced into the calculations. The

[1] b=barn=$10^{-28}m^2$. In the following, $(2)0_1^+ \rightarrow (0)2_1^+$ will be omitted in the expression $B(E2,(2)0_1^+ \rightarrow (0)2_1^+)$ when it is clear from the context that $(2)0_1^+ \rightarrow (0)2_1^+$ is meant.

B(E2) value can be expressed as a sum of π and ν amplitudes :

$$\begin{aligned} B(E2, 0_1^+ \rightarrow 2_1^+) &= (M_p)^2 \\ &= (e_\pi^{eff} A_\pi + e_\nu^{eff} A_\nu)^2 \qquad \text{where} \\ A_\pi &= \langle 2_1^+ || \mathcal{M}(E2) || 0_1^+ \rangle_\pi \\ A_\nu &= \langle 2_1^+ || \mathcal{M}(E2) || 0_1^+ \rangle_\nu . \end{aligned} \tag{2.6}$$

In the case of a proton(neutron) closed shell, the proton(neutron) amplitude will be zero.
In order to understand the evolution of the 2_1^+ energy as a function of number of valence nucleons and its relationship with the B(E2,$0_1^+ \rightarrow 2_1^+$) value, two considerations can be made [Cas00] :

1. Microscopically : due to configuration mixing between N ($\phi_1, \phi_2, ...\phi_N$) levels, the mixed wave function with the most coherence ($=\frac{1}{\sqrt{N}}(\phi_1 + \phi_2 + ... + \phi_N)$) will be lowered in energy. Thus, lowering of the 2_1^+ energy is an indication for increasing coherence in the wave function and collectivity in the structure, which in turn increases the B(E2) strength.

2. In the shell model : in singly magic nuclei, the structure will stabilize due to the large energy needed to create excitations in the closed shell. The reduced $\pi - \nu$ interaction in the valence space will reduce the collectivity of the system.

Within the shell model, coherence in the 2_1^+ state can very well be described using the concept of seniority [Tal63]. The quantity seniority is defined as the smallest number (ν) out of n particles in a configuration j^n that can produce a given spin J. The remaining n-ν particles are coupled to spin J=0. The introduction of seniority has important consequences for a range of tensor operators. Considering a 2 body odd-tensor operator $V_{i,j}$ it can be proven (see [Cas00]) that the following relationship holds:

$$\langle j^n \alpha J | \sum_{i<k}^{n} V_{ik} | j^n \alpha' J \rangle = \langle j^\nu \alpha J | \sum_{i<k}^{\nu} V_{ik} | j^\nu \alpha' J \rangle + \frac{n-\nu}{2} V_0 \delta_{\alpha,\alpha'} \tag{2.7}$$

where α(') is any set of additional quantum numbers and $V_0 = \langle j^2 0 | V_{12} | j^2 0 \rangle$. Applying this seniority result to the energy separation between $J^\pi = 0^+$ (ν=0) and $J^\pi = 2^+$ (ν=2) states in even-even nuclei with n valence nucleons gives :

$$E(j^n, \nu = 2, J = 2) - E(j^n, \nu = 0, J = 0) = \langle j^2, J = 2 | V | j^2 J = 2 \rangle - V_0. \tag{2.8}$$

This result is independent from the number of valence nucleons and only depends on the (2-body) interaction V and the pairing properties (V_0). In this seniority picture, the energy of the 2_1^+ state in an isotopic chain is constant when filling a j-orbit up to n=2j+1 nucleons. This picture neglects strong shell effects as they occur near closed shells.
A similar result can be obtained for the B(E2) strength. The quadrupole operator $\mathcal{M}$(E2) is a 1-body even tensor operator, connecting ν with ν-2 and ν states. It can be shown (see [Cas00]) that in this case of a $\Delta\nu$=2 E2 transitions, the B(E2) value is given by :

$$B(E2, J_i \rightarrow J_f) = \frac{1}{2J_i + 1} |\langle J_f || \mathbf{E2} || J_i \rangle|^2 \approx f(1 - f) \tag{2.9}$$

where f=n/(2j+1) is the fractional filling of a shell j. In the seniority picture, the B(E2) value exhibits a parabolic behavior when filling a single j shell, peaking at mid-shell.

The Sn and Ca isotopic chains are good examples of seniority nuclei : the energy of the 2_1^+ state is constant between N=50-82 (Fig. 2.7-top), while in the Ca isotopes, the energy of the 2_1^+ energy level is rather constant between N=22 and N=26 (N=20 and N=28 are the shell closures and the $1f_{7/2}$ is gradually filled, see bottom part of Fig. 2.2) and the B(E2) value exhibits a parabolic behavior, which peaks at mid-shell (N=24, see top part of Fig. 2.2). If seniority is a good quantum number, the energy should be constant.

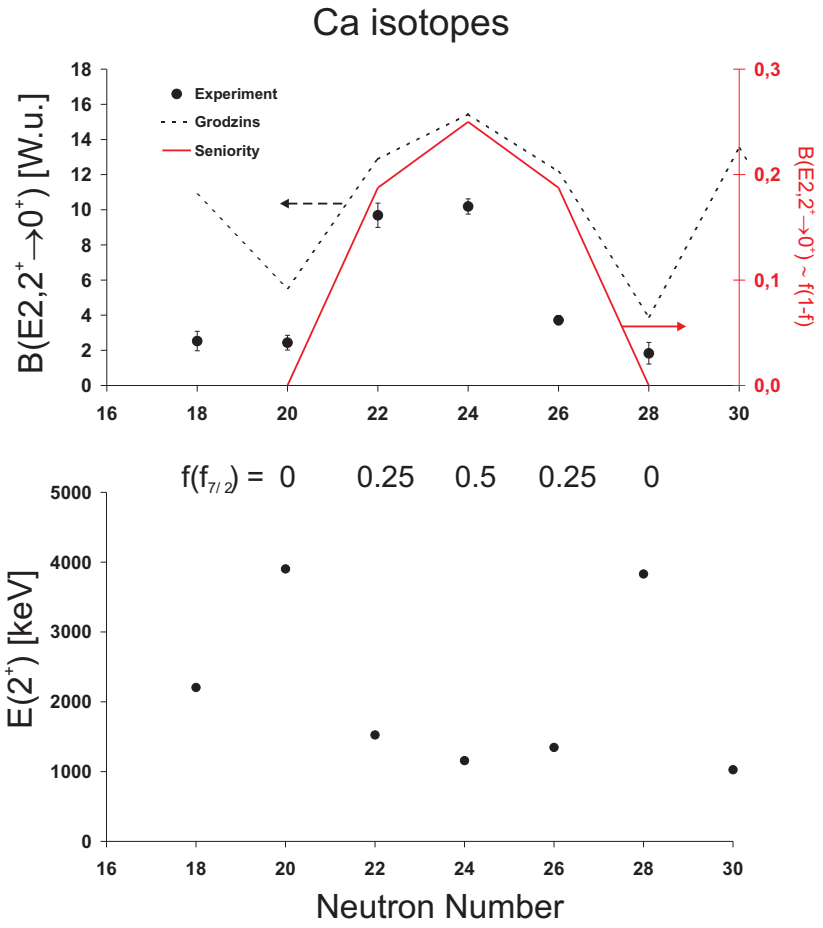

Figure 2.2: *The seniority scheme applied to Ca isotopes. Top : the B(E2) values exhibit a parabola like behavior, as expected from the seniority scheme (in red). Bottom : the $E(2_1^+)$ states are rather constant for N=22-26. At the neutron shell closures N=20,28, the energy increases.*

Grodzins Rule

Grodzins adopted a result from "the hydrodynamical model with irrotational flow" by Bohr and Mottelson : an expression for the mean lifetime of the 2_1^+ state (τ=$T_{1/2}$/ln(2)) $\tau[ps] \approx E_{keV}^{-4} Z^{-2} A^{1/3}$ [Boh75]. The dependence on $A^{1/3}$ was replaced by A and an empirical fit was performed to all known $E(2_1^+)$ and B(E2) values [Gro62]. Raman *et al.* allowed the exponents of E and A to vary and performed a "global best fit" to all known data points [Ram01]. The most recent expression for τ [Ram01] (translated to

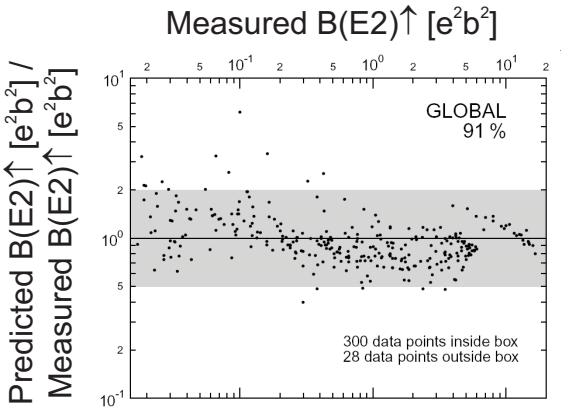

Figure 2.3: *The predictions by the empirical Grodzins rule compared to experimental B(E2) values. Picture taken from [Ram01].*

B(E2) via eq.2.5) is given by :

$$B(E2, 0_1^+ \rightarrow 2_1^+) = (2.57 \pm 0.45) E^{-1} Z^2 A^{-2/3}. \tag{2.10}$$

The absolute values predicted by this "global best fit" formula differ somewhat from the measured B(E2,$0_1^+ \rightarrow 2_1^+$) values, but a simple "renormalization" predicts the trend more accurately [Ram01]. 91% of all data points in 2001 agreed within 50% to the predicted value of the Grodzins rule, as seen in Fig. 2.3.

The arguments given above concerning the evolution of E(2_1^+) and B(E2,$0_1^+ \rightarrow 2_1^+$) give some insight in the nature of this E(2_1^+) ·B(E2,$0_1^+ \rightarrow 2_1^+$) =constant relation. The coherent and mixed 2_1^+ wave function is strongly lowered in energy and the collective character boosts the B(E2,$0_1^+ \rightarrow 2_1^+$) value up, which explains the inverse relationship between E(2_1^+) and B(E2,$0_1^+ \rightarrow 2_1^+$) . The Grodzins rule works remarkably well for nuclei with moderate N/Z ratios, whereas for extreme N/Z ratio's the rule should be checked in its simplicity.

Experimental techniques

B(E2) values are measured with a range of experimental techniques :

1. Coulomb excitation : this technique will be discussed in detail in section 2.2. Due to the electromagnetic Coulomb interaction between the stationary target and the incoming beam particles, part of the target and beam particles are internally excited. This inelastic scattering process is, below the Coulomb barrier, exactly described by semi-classical perturbation theory. In Coulomb excitation experiments, the nuclear information is extracted from either the inelastic scattered target or beam particles, eventually in coincidence with the de-excitation γ-rays. The measured excitation probability is a direct measure for the B(E2) value. [Ald56] Coulomb excitation at higher beam energies (25-300 MeV/u) is referred to as intermediate energy Coulomb excitation. In this case, relativistic corrections are needed in the description of the excitation process. The detection of inelastically scattered particles is limited to forward scattering angles, corresponding to higher impact parameters (bigger distance between the two colliding nuclei). [Gla01]

2. Delayed Coincidence (Lifetime measurement) : the isotope is produced in an excited state (e.g. in fusion evaporation reactions) [Gor97, Maz05] or the nuclear

states are selectively populated by β-decay [Mac05]. The investigated levels are characterized by their γ-decay and the delay between the transitions in a cascade is measured. Fast timing methods on β-particles are used (in beta decay) to deduce the lifetimes.

3. Doppler Shift Attenuation Method (DSAM) : the registration of γ-rays emitted during the slowing down of an excited recoiling nucleus yields the life time of the excited state. The line shape of the detected transition peak is crucial in the analysis and depends on the history of slowing down and on the properties (lifetime) of the excited state [Pet06, Ken02].

4. Electron Scattering : a high energy electron beam impinges with the investigated nucleus. The longitudinal part of the "form factor" of the inelastically scattered electron beam is measured. The form factor is calculated using the "Distorted Wave Born Approximation" (DWBA) and fitted to the experimental profile. The electric transition probability is one of the parameters in the fitting procedure. [Ube71]

5. Recoil Distance Method (RDM) : An RDM setup consists of two target foils. In the first thin foil (target) excited states are populated and the excited nucleus leaves the foil with a large velocity. In a second foil (stopper), the nucleus is stopped. The distance between the two foils is chosen such that the flight time is of the order of the lifetime of the excited state. The lifetime is extracted from the changing intensities of fully doppler shifted and stopped γ-rays, as a function of target-to-stopper distance. [Kru00]

Experimental results

To illustrate the structural evolution indicated by the 2_1^+ state and the B(E2) in even-even nuclei, the available information on isotopes near Z=28 (Ni(Z=28),Zn(Z=30) and Ge(Z=32)) is discussed in the following (closed shell $\pm$ two protons/neutrons nuclei). In closing this part, recent results on Cd(Z=48),Sn(Z=50) and Te(Z=52) are discussed for comparison and to illustrate the importance of experiments with Radioactive Ion Beams (RIBs).

Ni-isotopes (Z=28) In Fig. 2.4 (top) the known experimental B(E2,$2_1^+ \rightarrow 0_1^+$) systematics for Ni isotopes is plotted and in Fig. 2.5 (top) the experimental E(2_1^+) ,E(4_1^+) ,E(2_2^+) and E(0_1^+) states are drawn.
The high E(2_1^+) at N=28 and 40 hints to the possible magicity of these two neutron numbers, where the E(2_1^+) in ^{56}Ni(N=28) is considerably higher then in ^{68}Ni(N=40). In [Kra94] the E(2_1^+) in ^{56}Ni was interpreted in a shell model picture as an isoscalar 1p-1h configuration with a relatively large B(E2,$2_1^+ \rightarrow 0_1^+$) value because of the large coherent $1f_{7/2} \rightarrow 2p_{3/2}$ and $1f_{7/2} \rightarrow 1f_{5/2}$ contributions (with equal neutron and proton components). The B(E2,$2_1^+ \rightarrow 0_1^+$) value in ^{68}Ni is much lower compared to ^{56}Ni. This low B(E2,$2_1^+ \rightarrow 0_1^+$) value in ^{68}Ni was interpreted in [Sor02] as originating from the enhanced neutron pair scattering at N=40, which is referred to as the superfluid behavior of the neutrons. It has been pointed out theoretically in [Lan03] that most of

the E2 strength in ^{68}Ni resides at excitation energies around 5-6 MeV. These states are predicted, within the shell model approach, to have a large 1p-1h proton component ([Lan03]). The 2_1^+ state was calculated in the same work to be mainly a 2p-2h neutron excitation, with 25% 1p-1h proton excitations. "Quasi Random Particle Approximation" (see [Rin80]) calculations from the same reference calculated the 1-phonon 2_1^+ state to have 90% neutron component. The same QRPA calculations predict that the E2 strength in ^{56}Ni is exhausted by the excitation to the first 2_1^+ state. The main conclusion from [Lan03] is that the small observed B(E2,$2_1^+ \rightarrow 0_1^+$) value is not necessarily an argument for a shell closure at N=40, but simply reflects the fact that the 2_1^+ state is primarily a neutron excitation.
The B(E2) values in the Ni chain show a parabolic evolution between 2 magic nuclei (see Fig. 2.4, top), hinting a seniority-like behavior. Recent measurements and shell model calculations on Ni isotopes between N=28 and N=40 ([Ken01]) have outlined the necessity of including proton excitations across the Z=28 "closed shell" in order to reproduce the "bell-shape" behavior of the B(E2,$2_1^+ \rightarrow 0_1^+$) values. In Fig. 2.4 (top) the shell model calculation, taken from [Ken01] is plotted for up to five proton excitations from the $f_{7/2}$ orbit to the upper (pf)-shell. With less protons excited from the Z=28 core, the shape of the B(E2,$2_1^+ \rightarrow 0_1^+$) curve flattens out (see ref. [Ken01]).
The recently measured B(E2) value in ^{70}Ni (intermediate energy coulex at GANIL, [Per06] is remarkably high. In [Per06] this is interpreted as a rapid polarization of the proton core when neutrons are added to the $1g_{9/2}$.
As seen in Fig. 2.5 (top), the first excited state in ^{68}Ni is in fact the 0_2^+ state (at 1.7 MeV) instead of the 2_1^+ state. Although this 0_2^+ state was observed only once in a ^{70}Zn(^{14}C,^{16}O)^{68}Ni reaction [Ber82], it has been calculated (in the same work) within the framework of the Hartree-Fock-Bogoliubov mean field theory as a second, deformed minimum (β=0.4) in the potential energy surface, and in the shell model it has been calculated as two strongly coupled neutron quasi-particles, excited across N=40 [Ber82].
Above N=40, the trend in the 2_1^+ energy is remarkable, since there is a gradual decrease of E(2_1^+) up to A=76 (the 2 neutron hole state in ^{78}Ni) [Maz05], even though a shell stabilizing effect might be expected from the N=50 neutron shell closure. It has been suggested that this might be an indication of a decreased neutron pairing interaction at extreme N/Z(=1.71 for ^{76}Ni) ratio's [Wal06].
The dashed black line in Fig. 2.4 (top) is the "classic" Grodzins prediction, based on the known E(2_1^+) . The curve is normalized to the point with the smallest error bar (^{60}Ni). The overall trend is fairly well predicted by the Grodzins rule, although the fine details in ^{58,68}Ni need a more microscopic description.

Zn-isotopes (Z=30) The experimental B(E2,$2_1^+ \rightarrow 0_1^+$) values in the Zn isotopic chain show a similar trend towards N=40 as the Ni isotopes up to ^{68}Zn : a parabolic behavior towards a shell closure (Fig. 2.4 (middle)). Though at N=40 (^{70}Zn), the B(E2,$2_1^+ \rightarrow 0_1^+$) value suddenly increases. This observation was qualitatively interpreted in [Lee02] as the *onset of deformation*, with three arguments supporting this increased collectivity : 1- the addition of 2 protons outside the Z=28 closed shell; 2- the maximum of neutron pairing at N=40 (see Ni discussion and [Sor02]) and 3- the presence of the strongly downsloping l=4 Nilsson neutron orbital close to the Fermi surface (see Fig. 1.5). For a β-value of 0.23 (extracted from the B(E2,$2_1^+ \rightarrow 0_1^+$) value), positive parity single particle levels in the Nilsson diagram penetrate into the region of negative parity states. Since there is no clear distinction between positive and negative

parity states, a large B(E2) value can be generated (E2 transitions are parity conserving). Shell model calculations taken from [Ken02] indicate that the inclusion of the $1g_{9/2}$ in the valence space is crucial in order to reproduce the increased B(E2,$0_1^+ \rightarrow 2_1^+$) value in ^{70}Zn. These calculations are included in Fig. 2.4 (middle) : the solid black line represents results in the $1f_{7/2}$+pf valence space, *without the $g_{9/2}$ included*, the long dashed line represents results in the pf+$\mathbf{g}_{9/2}$ valence space (no $1f_{7/2}$). The increase in B(E2,$2_1^+ \rightarrow 0_1^+$) strength continuous for ^{72}Zn ([Lee02]). In the latter reference, the increased B(E2) strengths were reproduced in shell model calculations, using a ^{48}Ca core and the $f_{7/2}$+pf+$g_{9/2}$ valence space, where 8 neutrons are "frozen" in the $1f_{7/2}$ orbital. Both [Lee02] as [Ken02] indicate the crucial role played by the $\nu g_{9/2}$ orbital in the structure of these nuclei.

A first observation in Fig. 2.5 (top,middle) is that the E(2_1^+) states in Zn are overall lower compared to Ni. A second observation in Fig. 2.5 (middle) shows an additional overall decrease of the 2_1^+ energy in Zn isotopes between N=40-50 compared to N=28-40. Both might be understood from the increased π-ν-interaction between the two protons outside the Z=28 shell and the N=40-50 neutron shell, which brings in an amount of collectivity. Another argument for the decrease between N=40-50 might be a reduced pairing energy for neutrons, the energy needed to break up a pair [Van05]. The near constancy of the E(2_1^+) between N=28-40 and N=40-50 hints the applicability of the seniority scheme in the two regions.

The energy ratio E(4_1^+) /E(2_1^+) is ≈2.1-2.4 over the full range N=28 up to 48. This would indicate a vibrational character of these nuclei. The same vibrational-like trend, is observed for the E(2_2^+) /E(2_1^+) ratio. Though, the E(0_2^+) /E(2_1^+) ratio strongly decreases towards N=40. A similar behavior at N=40 was observed in ^{68}Ni, where 0_2^+ becomes the first excited state. This was interpreted as a two-quasi-particles neutron excitation across the N=40 sub-shell gap.

As observed from the E(4_1^+) /E(2_1^+) ratio's, the stable Zn isotopes and ^{62}Zn exhibit vibrational like behavior. Though, B(E2,$4_1^+ \rightarrow 2_1^+$) transition strengths have been measured ([Les05a,Les05b,Koi03]) and the measured B(E2,$4_1^+ \rightarrow 2_1^+$) /B(E2,$2_1^+ \rightarrow 0_1^+$) ratio's range from 0.6-1, which is far from the vibrational value of 2. Several publications have reported results obtained with more "advanced" collective models such as the "Deformed Configuration Mixing shell model" (^{66}Zn, [Aha81]), the cranked Nilsson-Strutinsky model (^{66}Zn, [Koi03],^{68}Zn, [Koi04]) and the "Quasiparticle-Phonon Model" ($^{62-72}$Zn, [Vri77]). These calculations reproduce the B(E2,$4_1^+ \rightarrow 2_1^+$) /B(E2,$2_1^+ \rightarrow 0_1^+$) <2 behavior, indicating that the lighter Zn isotopes are more complex deformed nuclei, compared to the vibrational approximation.

The predictions by the Grodzins rule are plotted in Fig. 2.4 (middle,normalized to ^{68}Zn). There is a fair agreement for the stable Zn isotopes and ^{72,74}Zn. The standard global systematics, given by the Grodzins rule predicts a parabolic behavior towards the N=50 neutron shell closure. The E(2_1^+) used for N=50 in the Grodzins formula is the SMI predictions (1.7 MeV). The data points for N=46 and 48 will be added in this work and N=44 was remeasured.

The study of the onset of deformation in the Zn isotopic chain above N=40 is the main physics case in this work. The measurement of B(E2) values in this chain up to N=50 is crucial to understand the influence of the supposed N=50 neutron shell closure on the collectivity in the nuclear system. An important question to put is whether large scale shell model calculations are able to reproduce the moderate collectivity in the nuclear medium.

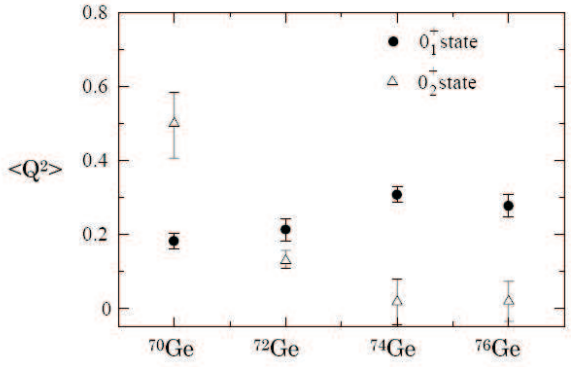

Figure 2.6: *Measured $<Q^2>$ values in Ge around N=40 (^{72}Ge), indicating the nature of the second 0^+ state in this region. Figure taken from [Sug03].*

Ge-isotopes (Z=32) In Ge, a similar trend towards collective behavior is observed when neutrons are added to the $g_{9/2}$ orbit : the decrease of $E(2_1^+)$ compared to the Ni isotopes is identical to the decrease observed in Zn isotopes. The constancy of $E(2_1^+)$ between N=28-40 and N=40-50 is similar to the Zn systematics. The first $E(2_1^+)$ known in the lighter N=50 isotopes (above ^{78}Ni) is at 1348 keV in ^{82}Ge. This high energy is an indication for the persistence of the N=50 shell gap.
The higher B(E2) values (∼10-35 W.u.) indicate more collectivity in the system due to the increased π-ν interaction. At N=40, again a low lying 0_2^+ state is observed. This can be understood in the light of the neutron pair scattering across the N=40 sub-shell.
The experimental $<Q^2>$ of the 0_1^+ and 0_2^+ states are plotted in Fig. 2.6, illustrating the structural evolution of the ground state between ^{70}Ge and ^{76}Ge. Up to ^{70}Ge, the 0_2^+ state is interpreted as a deformed intruder state [Sug03], whereas from ^{74}Ge on the 0_1^+ state takes over this deformed character and 0_2^+ favors sphericity [Toh00, Toh01].
Recent measurements of the $B(E2,2_1^+ \rightarrow 0_1^+)$ values at the Radioactive Ion Beam Facility Oak Ridge National Laboratory (ORNL) on ^{78,80,82}Ge have provided new data on radioactive Ge isotopes ([Pad05]). Shell model calculations from the same reference are shown in Fig. 2.4 (bottom). The steep trend downward to N=50 is predicted by the shell model calculations, indicating that the shell model effective residual interaction accurately incorporates the stabilizing shell closure at N=50 and generates the right amount of collectivity in the nuclear system for N<50.
Predictions by the Grodzins rule for Ge are plotted in Fig. 2.4 (bottom,dashed line). A fair agreement is observed for stable Ge isotopes (^{70,72,74,76}Ge). Though, at N=44 the deviation from the "standard global systematics" given by the Grodzins rule is already apparent and increases towards N=48. At N=50 the correspondence is again nearly perfect. The deviation from the Grodzins rule sets in when two neutrons are added to the nucleus where the $B(E2,2_1^+ \rightarrow 0_1^+)$ value reached its maximum (for neutrons filling the $1g_{9/2}$).

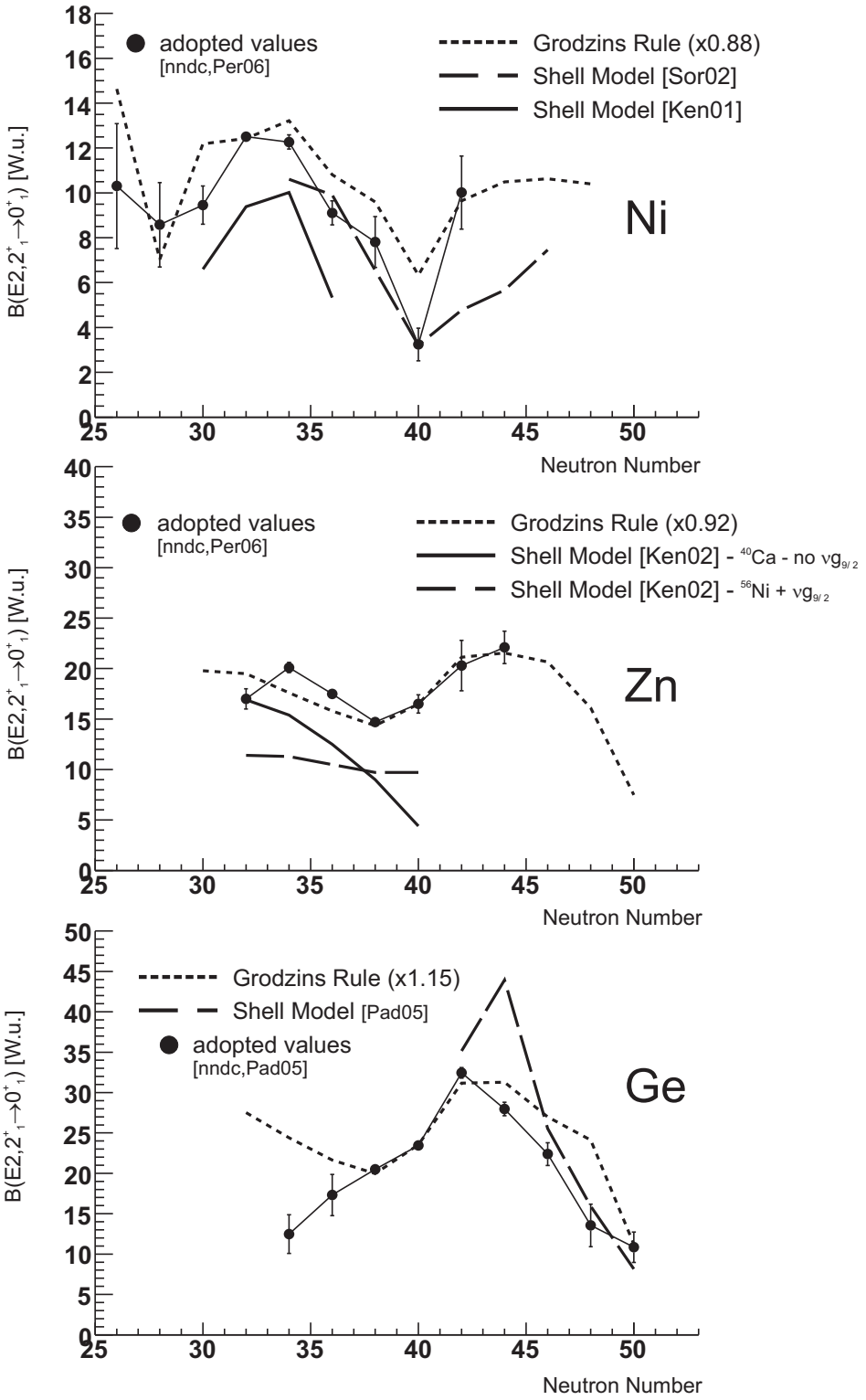

Figure 2.4: *Experimental $B(E2,2_1^+ \rightarrow 0_1^+)$ values in W.u. for Ni(top), Zn(middle) and Ge(bottom) isotopes with several theoretical predictions (see text for details). Experimental values are taken from [nndc], except for : ^{74}Zn,^{70}Ni [Per06] and $^{78,80,82}Ga$ [Pad05].*

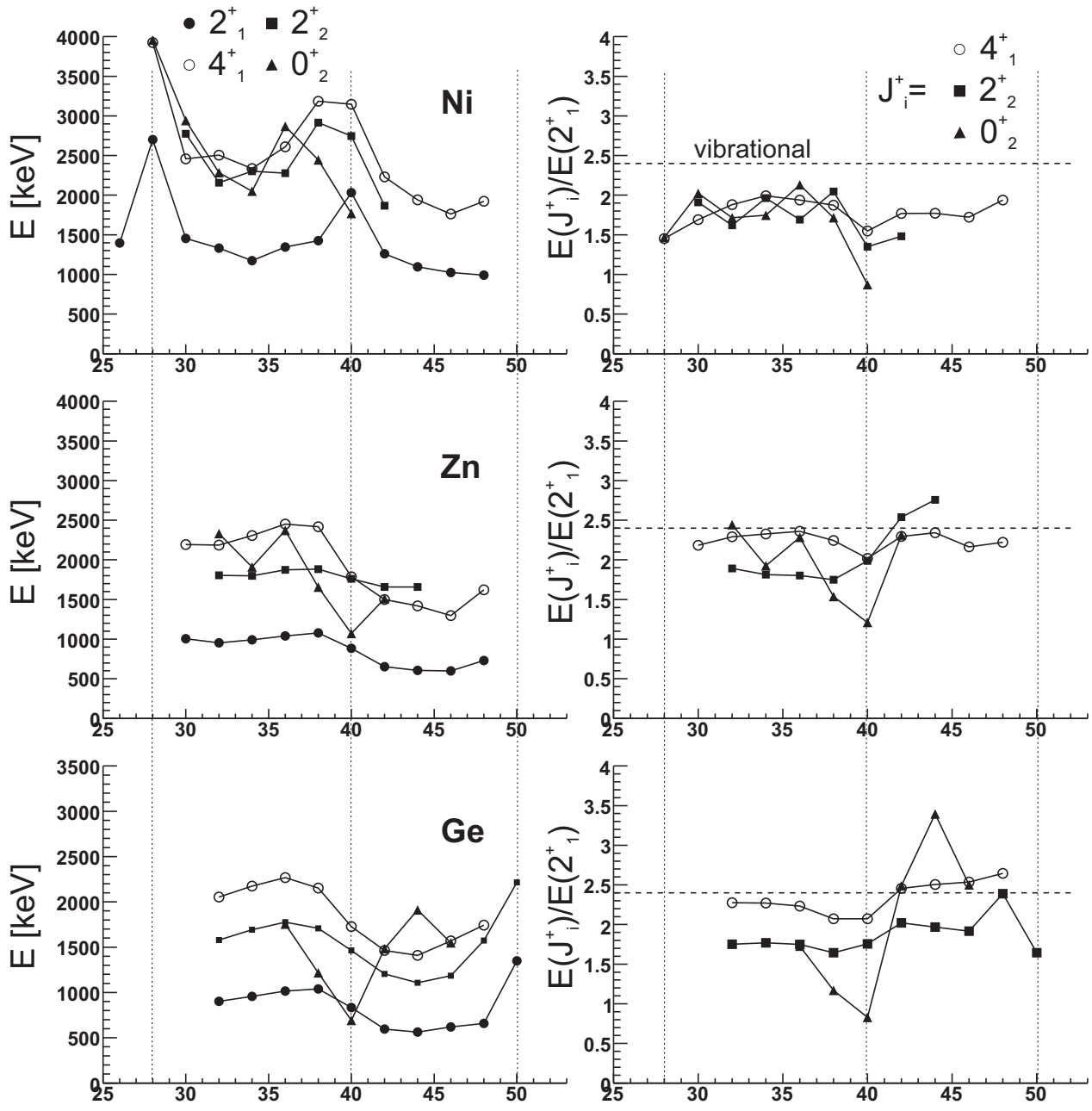

Figure 2.5: *Left : $E(2_1^+)$,$E(4_1^+)$,$E(2_2^+)$ and $E(0_2^+)$ in Ni, Zn and Ge isotopes. Right : $E(4_1^+)/E(2_1^+)$, $E(2_2^+)/E(2_1^+)$ and $E(0_2^+)/E(2_1^+)$ for Ni, Zn and Ge isotopes.*

Sn (Z=50), Cd (Z=48) and Te (Z=52) In Fig. 2.7 (top) the E(2_1^+) states are shown for Cd(Z=48), Sn(Z=50) and Te(Z=52). The overall lower E(2_1^+) energy for Cd and Te, compared to Sn (proton shell closure Z=50) is due to the π-ν residual interaction in the open shell nuclei Cd and Te. The near constancy of the 2_1^+ state reflects seniority-like behavior. At N=82, a strong neutron shell closure is observed (the E(2_1^+) for ^{132}Sn is 4.04MeV). An exceptional behavior for the E(2_1^+) was observed across this shell closure at N=84 in $^{136}_{52}$Te (N/Z=1.62) and $^{134}_{50}$Sn (N/Z=1.68) ([Rad02,Bee04]) : the E(2_1^+) is much lower in these isotopes compared to $^{132}_{52}$Te (N/Z=1.54) and $^{130}_{50}$Sn (N/Z=1.60), see Fig. 2.7 (top). Shell Model calculations do not reproduce the observed E(2_1^+) states ([Rad02, Sar01]) and a symmetric E(2_1^+) was expected for Sn and Te from $^{136-140}_{56}$Ba (N/Z=1.43-1.50) and $^{138-142}_{58}$Ce (N/Z=1.38-1.45) systematics [Rad05a]. In [Rad02] a "simplistic seniority two" assumption for the 2_1^+ state and mixing of π^2 $^{134}_{52}$Te$_{82}$, ν^2 $^{134}_{50}$Sn$_{84}$ and ν^{-2} $^{130}_{50}$Sn$_{80}$ basis states indicated a predominantly ν^2 character for the observed 2_1^+ state in $^{136}_{52}$Te.
Recently, the E(2_1^+) and B(E2,$0_1^+ \rightarrow 2_1^+$) values for ^{136}Te have been interpreted in the framework of the QRPA model [Ter02]. It was observed that the B(E2,$0_1^+ \rightarrow 2_1^+$) value is sensitive to the neutron pairing gap Δ_n at the neutron shell closure N=82 (see Fig. 2.8). A decreased neutron pairing gap reproduces the asymmetric experimental results for both E(2_1^+) as B(E2,$2_1^+ \rightarrow 0_1^+$) . The reduction decreases the energy required to break a neutron pair to form a 2_1^+ state, relative to that required to break a proton pair. The low lying 2_1^+ state in ^{136}Te has thus predominantly a 2ν character [Rad05b]. It is suggested that the reduced neutron pairing energy is a general feature that occurs for N/Z>1.60 systems, such as ^{76}Ni, ^{80}Zn, ^{130}Sn and ^{136}Te [Wal06].
For neutron rich Sn and Te isotopes a considerable deviation from the Grodzins rule was observed [Hab02] (dashed lines in Fig. 2.7, bottom) : for N=84 Sn and Te it is observed that both E(2_1^+) and B(E2,$2_1^+ \rightarrow 0_1^+$) decrease.
A "modified" Grodzins rule was recently proposed by Habs *et al.* [Hab02], where an explicit dependence on the neutron number is introduced :

$$E(2_1^+)[keV] \cdot B(E2) \uparrow [e^2b^2] = 2.57Z^2A^{-2/3}(a + b(N - \bar{N})) \tag{2.11}$$

where (a,b)=(1.288,-0.088) are parameters which were fit to all the available data in Z=46-58 isotopes and $\bar{N}$ is the neutron number for which the nuclear mass within an isobaric chain reaches its minimum[2]. The new rule describes the available data within 20%, while with the "normal" Grodzins rule typical deviations of 50% are common. Still, for extreme neutron rich systems, the deviation remains (see [Hab02]).

2.1.2 Single particle energy levels

In par. 1.2 it was highlighted that the monopole part of the residual interaction determines the evolution of single-particle energies. Considering the reference single-particle proton energy at the closed shell (such as derived from HF theory), indicated by ϵ_{j_π}. The evolution of this single-particle energy due to the interaction between the valence proton and the filled neutron orbital is given by [Smi04, Fed79]:

$$\tilde{\epsilon_{j_\pi}} = \epsilon_{j_\pi} + n_\nu E_{j_\pi j_\nu} \tag{2.12}$$

where n_ν is the number of valence neutrons occupying the j_ν orbital and

$$E_{j_\pi j_\nu} = \frac{\sum_J \langle j_\pi j_\nu; J|V|j_\pi j_\nu; J\rangle (2J+1)}{\sum_J (2J+1)}. \tag{2.13}$$

[2] $\bar{N}$ is obtained by differentiating Weizsacker's mass formula, see [Hab02].

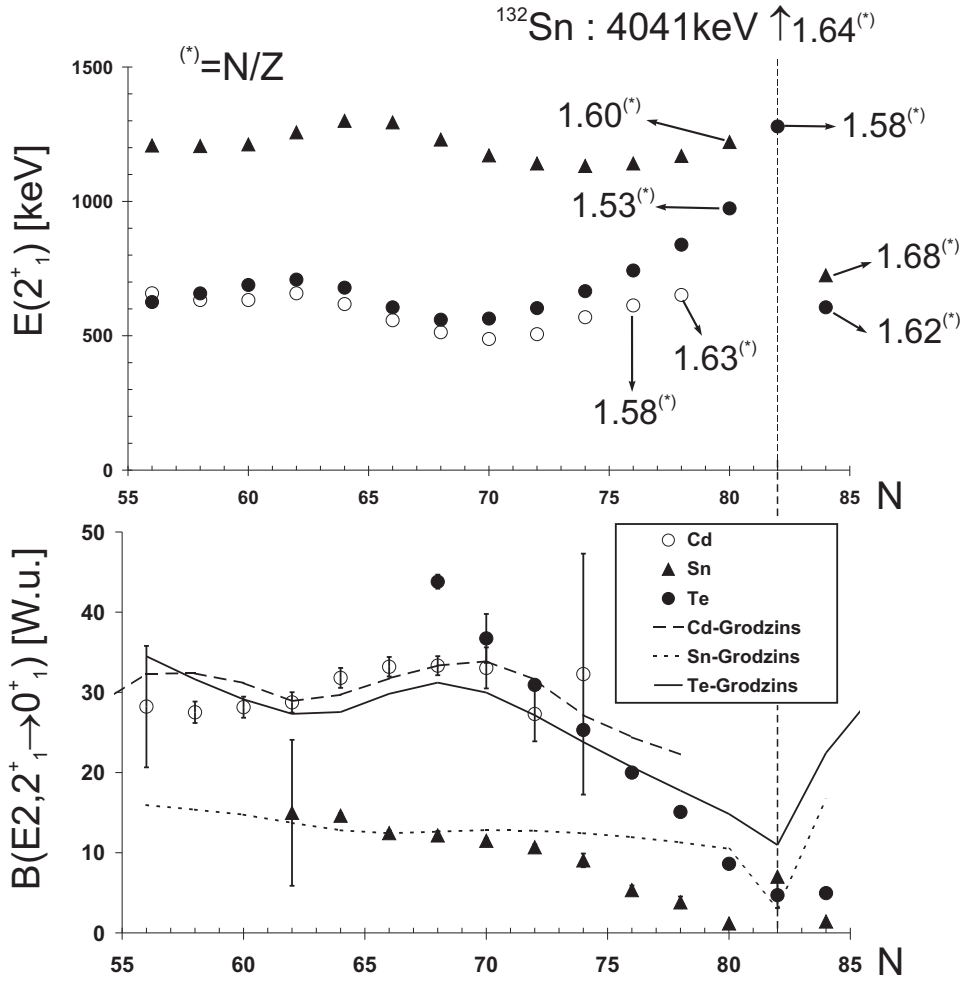

Figure 2.7: *Top : experimental $E(2_1^+)$ energies for Cd, Sn and Te isotopes. The constancy of the energy indicates the validity of the seniority scheme in the valence space. The N/Z ratio is indicated with a $^{(*)}$. Bottom : experimental B(E2) values in W.u. for Cd, Sn and Te isotopes. The values for Te and Cd are significantly higher ∼30W.u. in the mid-shell region, indicating higher collectivity. Towards the N=82 shell closure, the collectivity drops dramatically. The dashed line is the Grodzins prediction for the $B(E2,2_1^+ \rightarrow 0_1^+)$. Strong deviations are observed for neutron rich systems. Data are adopted from [nndc, Rad02, Rad05a, Rad05b, Bee04].*

where only the monopole part of V contributes. $\tilde{\epsilon_{j_\pi}}$ is referred to as the monopole corrected single-particle energy. The effect of the monopole part on the single-particle energies is exemplified in Fig. 2.9 B for odd Cu isotopes, where large scale shell model calculations are compared to experimental energy levels. From Fig. 1.2 it is seen that adding one proton to a Z=28 core brings this proton in a $2p_{3/2}$ orbit. The experimentally observed level sequence in the Z=29 (Cu) isotopic chain is shown in Fig. 2.9 B. The single particle energies in these Cu isotopes are proton excitation from the ground state ($2p_{3/2}$) to the above shell model orbitals. The last three measured single particle levels (N=40,42,44) are measured in a β^--decay study of ^{69,71,73}Ni [Fra01, Fra98]. In these studies the levels are inferred from the selective feeding from the $9/2(^+)$ ground

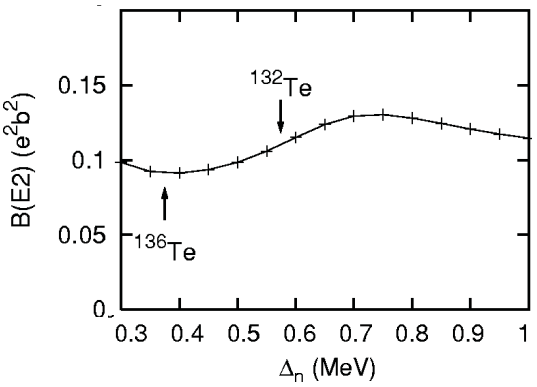

Figure 2.8: *The $B(E2,0_1^+ \rightarrow 2_1^+)$ value for ^{136}Te as a function of the neutron pairing gap. Picture taken from [Ter02].*

state of ^{69,71,73}Ni to excited states in ^{69,71,73}Cu. The strong lowering of the $1f_{5/2}$ single particle energy is due to the monopole interaction between this level and the (paired) neutrons gradually filling the $1g_{9/2}$ orbit. The nature of the monopole interaction has recently been reviewed by Otsuka *et al.* [Ots05]. The monopole interaction is a long range term, coupling protons and neutrons and strongly attractive between $j_<$ and $j'_>$ orbits (but repulsive between $j_<$ and $j'_<$ orbits). The index $>$ ($<$) represents $j^{(')}=l^{(')}+(-)\frac{1}{2}$. The monopole interaction has an important $\sigma \cdot \sigma\tau \cdot \tau$ component, where σ is a Pauli spinor, operating on the spin part of the nuclear wave function and τ is the charge exchange operator. In Fig. 2.9 C the interaction is schematically shown between $\nu g_{9/2}=j_>$ and $\pi f_{5/2}=j'_<$ (attractive p-n interaction lowers the excitation energy of the $\pi 1f_{5/2}$). The solid and dashed black lines in Fig. 2.9 B are shell model calculations performed with the computer codes OXBASH and ANTOINE (resp.). The crucial difference between the two calculations is the residual interaction used. The solid line represents a calculation using a realistic nucleon-nucleon interaction (see par. 1.2), based on the G-matrix interaction by Hjorth-Jensen [Hjo95] for the $pf_{5/2}$g-shell, where T=1 neutron and proton interactions are separately fitted to new experimental data in Ni and N=50 isotopes [Lis05] (labelled SMII). The dashed line represents an effective residual interaction based on the same G-matrix realistic interaction but where the monopole interaction strength was modified to reproduce spectroscopic properties in Ni and Cu ([Smi04] and references therein, labelled SMI). The $\pi 1f_{5/2}$-$\pi 2p_{3/2}$ level crossing is predicted to occur between A=43,44 by SMII, while SMII predicts the crossing between A=48-49.

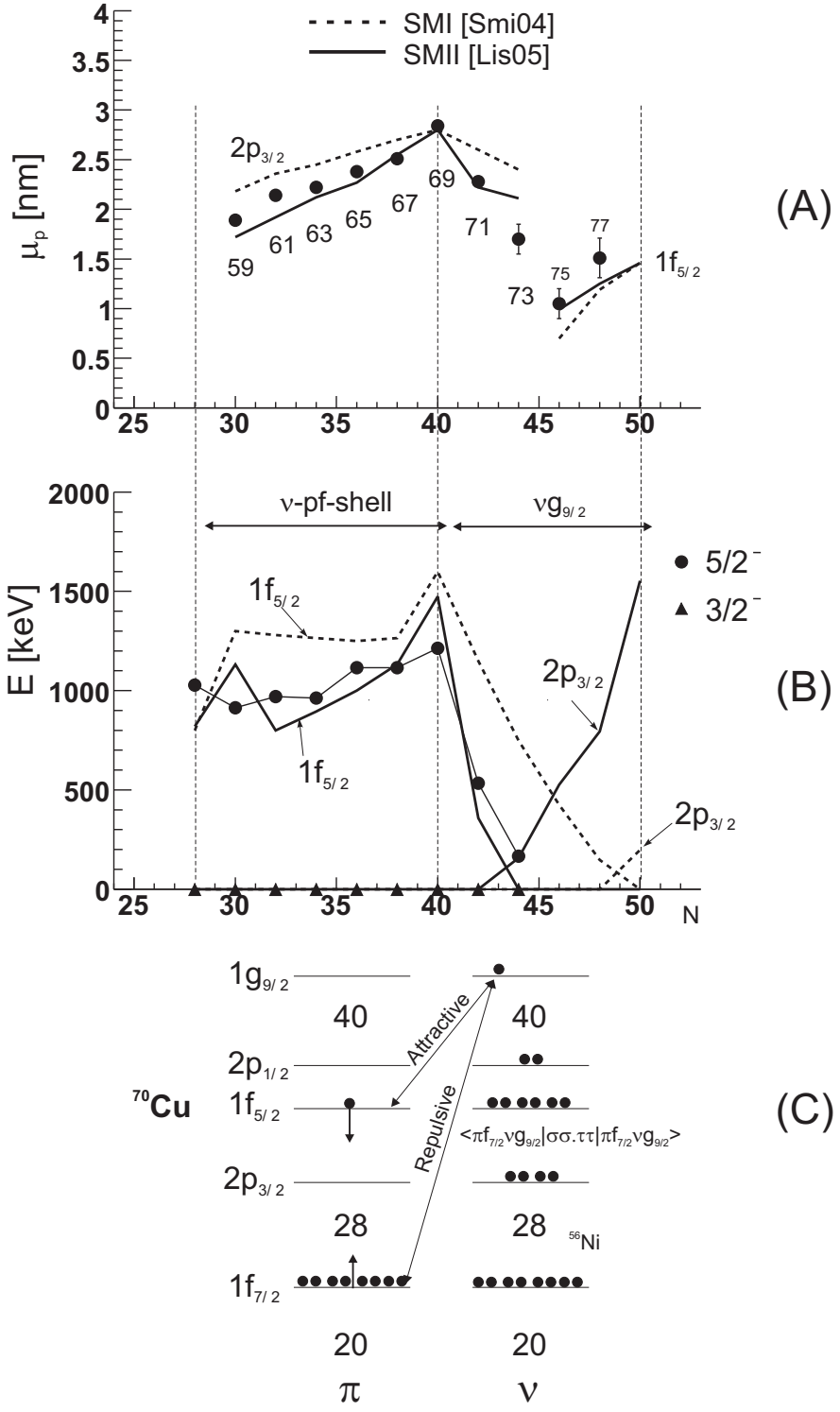

Figure 2.9: *(A) Experimental magnetic moments of the ground state in odd Cu isotopes compared to large scale shell model calculations (full line is the prediction for $2p_{3/2}$, while the dashed line is the prediction for $1f_{5/2}$). The difference between SMI and SMII calculations is explained in the text. (B) Experimental and calculated proton single particle energies in $_{29}Cu$ isotopes. (C) Shell model orbitals involved in the single particle energy level structure of Cu isotopes. The $1f_{5/2}$ energy level interacts strongly with the $1g_{9/2}$ level through the attractive monopole interaction. Dashed(full) lines correspond to SMI(SMII) calculations. The experimental points on $^{57,69,71}Cu$ are taken from [Gol04,Rik00,Van00], whereas the points on $^{73,75,77}Cu$ are preliminary unpublished results from in-source laser spectroscopy at ISOLDE [Fla06].*

2.1.3 Magnetic moments

The magnetic moment of a nuclear state with spin I is given by μ=gIμ_N, where g is called the *gyromagnetic ratio* and μ_N the nuclear magneton. The g factor of a state identifies the nuclear spin and vice versa. By using the "free" proton and neutron magnetic moments (μ_π=+2.793μ_N,μ_ν=-1.913μ_N) the single particle moment of a nucleus can be calculated. These values are referred to as "Schmidt values". In-medium effects (the presence of other nucleons,meson exchange currents,...) modify the "free" nucleon magnetic moments. Single particle magnetic moments will therefore be calculated using "effective" π and ν moments. Shell model calculations of the nuclear g-factor are indicative for the underlying shell structure. The measurement of the nuclear g-factor is in general based on the detection of the angular distribution of radiation (β-particles and gamma's). An overview of the several techniques can be found in [Ney03]. In Fig. 2.9 A, measured g factors in odd Cu isotopes are compared to shell model calculations (SMI and SMII, see par. 2.1.2). The calculations are performed for a ground state $2p_{3/2}$ up to ^{73}Cu, from thereon a ground state $1f_{5/2}$ is assumed. The latter three points are recent ISOLDE measurements ([Fla05]). In comparison with the shell model calculation it is seen that the $1f_{5/2}$ orbit becomes the ground state between A=42 and 46.

2.1.4 Mass measurements

From mass measurements shell effects appear due to the enhanced binding of the nuclear system (and consequently the lower mass) near closed shells. In Fig. 2.10 the difference between measured mass and predicted mass from the liquid drop model (LDM, Weizsacker formula) is shown. Despite additional terms to the Weizsacker mass formula, accounting for shell effects, it is seen that near closed shells (magic numbers) the measured mass is substantially lower then the mass predicted by LDM. In the inset of Fig. 2.10, recent mass measurements on Ni,Cu and Ga are given, obtained at the ISOLTRAP setup in ISOLDE [Gue05]. The aim of the latter experiment was to map the fine structure of the neutron pairing energy and to find signatures for closed or open (neutron) shells in the considered mass region [Gue05].

2.1.5 Two neutron separation energies (S_{2n})

The energy needed to remove two neutrons from the nucleus S_{2n}[MeV]=-M(A,Z)+M(A-2,Z)+2n with M(A,Z) the atomic masses and n the neutron mass) is plotted in Fig. 2.11 for Ca,Ni and Zn isotopes (values taken from [Wap03b]). If more energy is needed, the 2 neutrons are stronger bound in the nuclear medium. When crossing a closed shell this energy decreases, indicative for a shell effect (as exemplified for the closed neutron shells N=20 and N=28 in the Ca isotopes). The situation in the Ni isotopes, especially around N=40, is somehow cumbersome. From recent Ni mass measurement at the ISOLTRAP setup in ISOLDE no clear N=40 (sub-)shell closure was observed [Gue05], as observed from the S_{2n} energies plotted in Fig. 2.11. This peculiar feature has been interpreted as a manifestation of the superfluid character of the valence neutrons [Sor02]. In that picture, pairs of neutrons are scattered across the N=40 (sub-)shell gap and thus contributing to the 0^+_1 state. In Fig. 2.11 the S(2n) values for the Zn isotopes are given as well. In black, the values from [Wap03b] are plotted, while in green, recent mass measurements up to $^{81}_{30}Zn_{51}$ by the ISOLTRAP collaboration (ISOLDE) are shown [Her06]. Near N=50 a slight drop is observed, though the shell closure would be observed in the S_{2n} at N=52 (^{82}Zn).

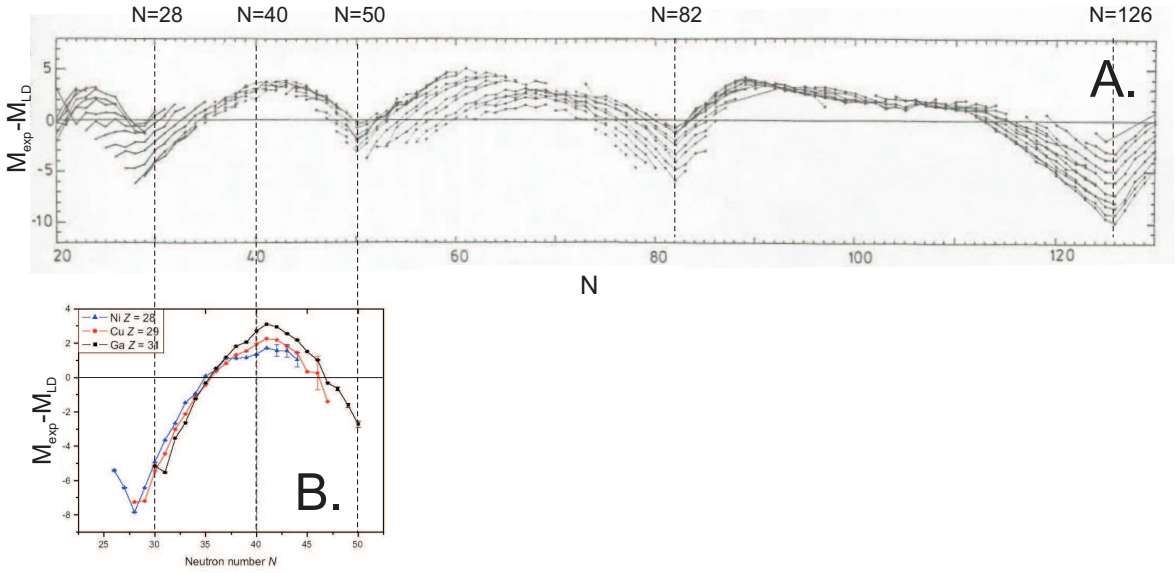

Figure 2.10: *A. The difference between the experimental mass and the value from the liquid drop model. Big discrepancies are observed near magic numbers N=28,50,82 and 126 (taken from [Hey95]). B. Recent mass measurements on Ni,Cu and Ga isotopes performed at the ISOLTRAP setup in ISOLDE. The small kinks near N=40 indicate a (small) subshell closure near N=40 (taken from [Gue05]).*

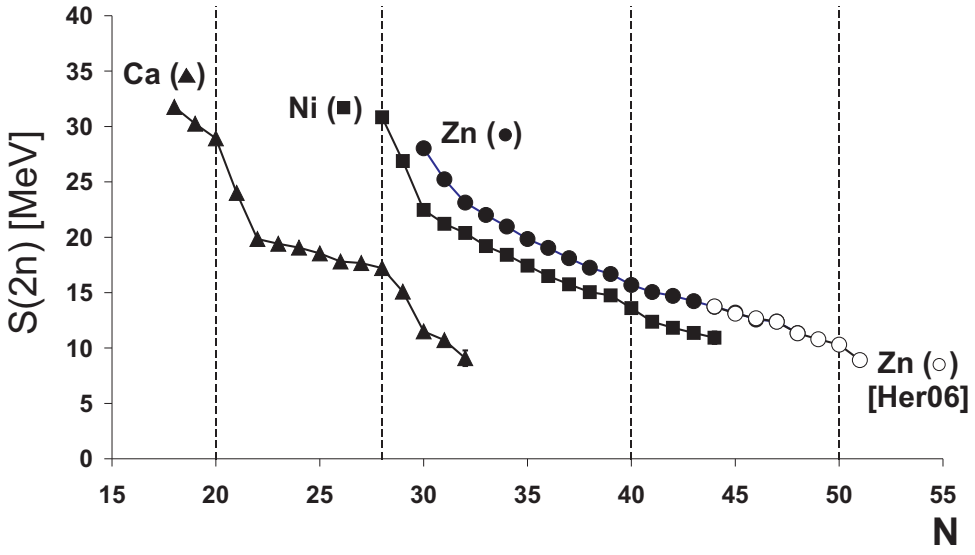

Figure 2.11: *Two neutron separation energies for Ca, Ni and Zn. Data for Ca, Ni and Zn are taken from [Wap03b], while the open circles are recent experimental values from the ISOLTRAP setup [Her06]. Error bars are included, if not visible these are smaller then the marker size.*

2.2 Coulomb excitation

2.2.1 Elastic and Inelastic scattering

The scattering process of a projectile nucleus ${}^{A_P}_{Z_P}\mathrm{X}_{N_P}$ on a target nucleus ${}^{A_T}_{Z_T}\mathrm{Y}_{N_T}$ is shown in Fig. 2.12. The process is described by the time dependent Schrödinger equation

$$i\hbar\frac{\partial}{\partial t}|\Psi(t)\rangle = (H_0 + V(\vec{r}(t)))|\Psi(t)\rangle \tag{2.14}$$

where V($\vec{r}$(t)) is in this case the electromagnetic interaction. The electromagnetic interaction between target and projectile can be decomposed in its multipole components. The monopole-monopole part of the electrostatic interaction causes the nuclei to scatter elastically, yielding the known Rutherford scattering process. The monopole-multipole components induce inelastic scattering, where one (or both) of the nuclei is (are) excited. The differential cross section for excitation of the nucleus to a state n is given by :

$$\frac{d\sigma_n}{d\Omega} = \frac{d\sigma_R}{d\Omega}\cdot P_n \tag{2.15}$$

where $\frac{d\sigma_R}{d\Omega} = \frac{1}{4}a^2\sin^{-4}(\vartheta/2)$ is the Rutherford elastic scattering cross section with

$$a \;=\; 0.71999(1 + A_P/A_T)Z_P Z_T/E_P[fm] \tag{2.16}$$

[Ald75] (half the distance of closest approach in a head-on collision) where A_P=mass of the nuclei in the beam, A_T=mass of the target nucleus, Z_P=Z of the nuclei in the beam, Z_T=Z of the target nucleus, E_P=the beam energy in MeV. P_n is the probability for excitation to state n. The wave function of the scattered nucleus after the collision is written as

$$\Psi(x,t) = \sum_{n=0} a_n(t)\Psi_n(x) = \sum_{n=0} a_n(t)|n> \tag{2.17}$$

where n is a sum over final states, n=0 being the elastic scattering process. The probability for an excitation from the ground state to state n is then

$$P_n = |a_n|^2. \tag{2.18}$$

In Fig. 2.13 the cross sections are plotted for a nucleus with a 0^+ ground state and a first excited 2^+ state[3]. The elastic scattering cross section is given by $\sigma_R \cdot P_{n=0}$, while the inelastic scattering cross section is given by $\sigma_R \cdot P_{n=2}$, where $|\mathrm{P}_{n=0}|^2+|\mathrm{P}_{n=2}|^2=1$.

2.2.2 Nuclear interaction

The theory on Coulomb excitation is valid as long as the excitation process is governed solely by the electromagnetic interaction. The distance of closest approach as a function of the "center of mass" (CM) scattering angle ϑ is given by [Ald75] :

$$b(\vartheta) \;=\; a(1 + 1/sin(\vartheta_{CM}/2)) \tag{2.19}$$

In order to ensure that nuclear contributions to the excitation process are negligible, the nuclear surfaces of the two colliding nuclei should be separated by a certain "safe" distance Δ, which takes into account the range of the nuclear force (some fm) and the surface diffuseness of the nuclear density distribution. A value for Δ can be determined by comparing measured and calculated scattering cross sections for combinations of

[3]For simplicity higher energy levels are omitted at this stage.

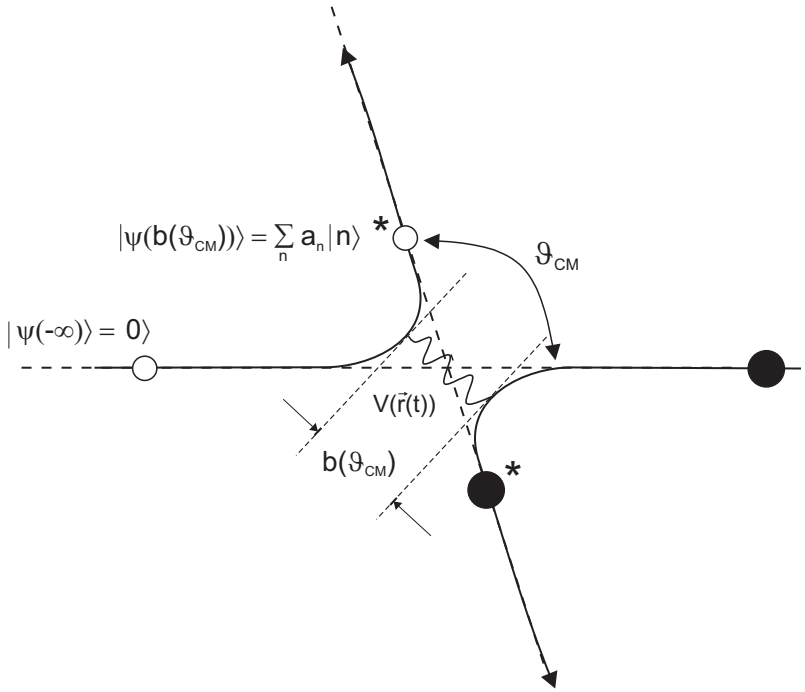

Figure 2.12: *The scattering of a nucleus* ${}^{A_P}_{Z_P}X_{N_P}$ *on a target nucleus* ${}^{A_T}_{Z_T}Y_{N_T}$.

heavy projectiles(targets) and different beam energies. Here, a typical value of $\Delta \approx 5$ fm is assumed [Nie05, Wil80]. The condition is formulated as

$$b(\vartheta) \quad \geq \quad R_1 + R_2 + \Delta \tag{2.20}$$

with R_i=1.25$A_i^{1/3}$ fm (i=1,2) and Δ=5 fm. In Fig. 2.14 it is seen that for all mass combinations in the three experiments, this condition is fulfilled over the full detected CM range.

2.2.3 First order perturbation theory

If the interaction between projectile and target is weak, the expansion coefficients a_n can be calculated in a first order perturbation approach :

$$a_{if} = \frac{1}{i\hbar}\int_{-\infty}^{+\infty}\langle f|V(\vec{r}(t))|i\rangle exp(i\omega t)dt \tag{2.21}$$

with ω=(E_f-E_i)/$\hbar$=ΔE/$\hbar$. In general, the probability to excite from a level i to a level f is then : P_{if}=$|a_{if}|^2$, analogue to eq. 2.18. The differential cross section for an electric transition of multipolarity λ can be calculated with first order perturbation theory (see [Ald75]) :

$$d\sigma_{E\lambda} = (\frac{Z_1 e}{\hbar v})^2 a^{-2\lambda+2} B(E\lambda, I_0 \rightarrow I_f) df_{E\lambda}(\vartheta, \xi) \tag{2.22}$$

where Z_1 is the charge number of the projectile(target) for target(projectile) excitation, v=$\sqrt{\frac{2}{m_P}(E_P - \Delta E_n(1 + m_P/m_T))}$ (ΔE_n=the excitation energy) and ξ=$\frac{\Delta E_n}{\hbar}\frac{a}{v}$ (= the

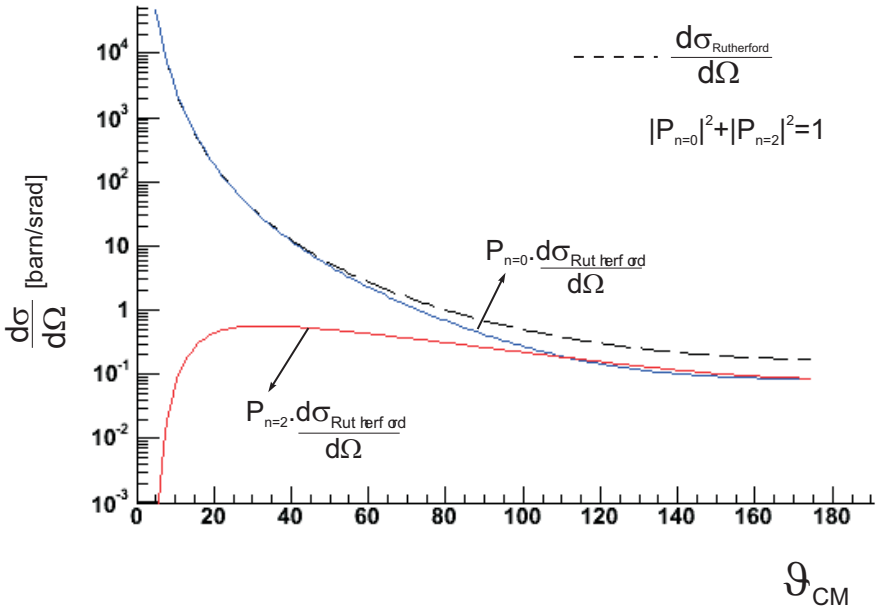

Figure 2.13: *The elastic and inelastic cross section for a nucleus with 0^+ ground state and 2^+ first excited state. The cross sections were calculated for ^{74}Zn ($B(E2,2_1^+ \rightarrow 0_1^+)=0.22\ e^2b^2$ and $E(2_1^+)=606\ keV$) on ^{120}Sn, where Zn is excited. Only the 2_1^+ level was included in the calculation.*

adiabaticity parameter). The function

$$\frac{df_{E\lambda}(\vartheta,\xi)}{d\Omega} \sim R_\lambda^2(\vartheta,\xi) sin^{-4}(\vartheta/2) \tag{2.23}$$

contains the familiar factor $\sin^{-4}$ -known from the elastic Rutherford scattering cross section- occurs together with a dimensionless "orbital integral" R_λ [Ald75] which de-

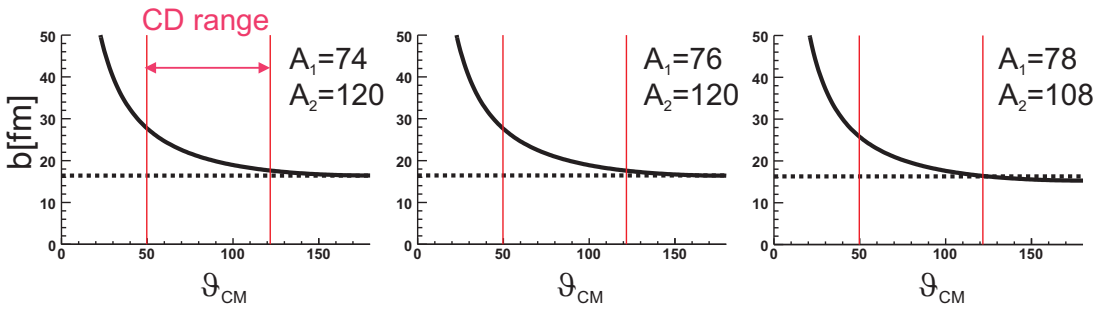

Figure 2.14: *The distance of closest approach as a function of scattering angle in the CM. The dashed line indicates the 'safe distance' and the solid lines mark the limits of the particle detector. These calculations were performed for the parameters given in table 5.19 in Chapter 6.*

pends solely on ϑ and ξ :

$$R^2_\lambda(\vartheta,\xi) = |\frac{(2\lambda-1)!!}{(\lambda-1)!}|^2 \frac{\pi}{2\lambda+1} \sum_\mu |Y_{\lambda\mu}(\frac{\pi}{2},0) I_{\lambda\mu}(\vartheta,\xi)|^2 \tag{2.24}$$

where the parameter ξ is defined as :

$$\xi = 7.29735^{-3} Z_1 Z_2 \left(\frac{1}{v_f/c} - \frac{1}{v_i/c}\right) \tag{2.25}$$

[Ald75] with $v_{i/f}$ the initial/final velocity of the scattered particle. The function $df_{E\lambda}(\vartheta,\xi)/d\Omega$ is shown in Fig. 2.15A the function is plotted for different values of ξ. It is seen that for higher values of ξ (higher excitation energies, or lower beam energy) the maximum is shifted to higher CM angles. The factor B(E2,$I_0 \rightarrow I_f$) is the reduced transition probability, related to the nuclear matrix elements of the electric multipole operator :

$$B(E\lambda, I_0 \rightarrow I_f) = \frac{1}{2I_0+1} |\langle I_f || \mathcal{M}(E\lambda) || I_0 \rangle|^2 \tag{2.26}$$

The total electric excitation cross section after integration over ϑ is given by

$$\sigma_{E\lambda} = (\frac{Z_1 e}{\hbar v})^2 a^{-2\lambda+2} B(E\lambda, I_0 \rightarrow I_f) f_{E\lambda}(\xi). \tag{2.27}$$

Likewise, the total magnetic excitation cross section is given by :

$$\sigma_{M\lambda} = (\frac{Z_1 e}{\hbar c})^2 a^{-2\lambda+2} B(M\lambda, I_0 \rightarrow I_f) f_{M\lambda}(\xi). \tag{2.28}$$

The functions $f_{E/M\lambda}(\xi)$ are plotted in Fig. 2.15 B/C. The magnetic excitation cross section is reduced by a factor of $(v/c)^2$, compared to the electric excitation cross section. In the energy range considered in this work (v/c$\sim$7%), this factor is $\simeq$0.005. The semi-classical description of the Coulomb excitation process is valid as long as the Coulomb field (monopole-monopole term) prevents the projectile from penetrating into the target nucleus. This is 'translated' to the condition that the wave length λ, associated with the projectile is much smaller than the distance of closest approach in a head-on collision (b), or:

$$\eta = b/2\lambda = Z_1 Z_2 e^2/\hbar v \gg 1 \tag{2.29}$$

with $Z_1(Z_2)$ the charge of the beam(target) nucleus and v the relative velocity at large distances. The parameter η is called the *Sommerfeld parameter*.
A sufficient condition for the validity of the first order perturbation theory approach is that all possible excitation probabilities are small. In order to excite a state $|f\rangle$ from $|i\rangle$ by the time dependent electromagnetic interaction $V(\vec{r}(t))$, the collision time τ_{col}=a/v (see 2.19) needs to be shorter or of the same magnitude as the excitation time for a given excitation energy ΔE_{if} in the nucleus : $\tau_{nucl}=\hbar/\Delta E_{if}$. This is reflected in the *adiabaticity parameter* ξ :

$$\xi = \frac{\tau_{col}}{\tau_{nucl}} = \frac{a\Delta E_{if}}{\hbar v} \leq 1 \tag{2.30}$$

which was already defined in a more general context above (see eq. 2.25). For small velocities, the projectile is able to follow the perturbation caused by $V(\vec{r}(t))$ adiabatically, so the excitation probability decreases. From Fig. 2.15B it is seen that with decreasing velocity (increasing ξ), the excitation probability decreases exponentially.

A classical treatment of the orbital motion is valid as long as the excitation energy does not significantly modify the trajectory, i.e. : $\frac{\Delta E_n}{E}=\frac{2\xi}{\eta}<<1$ ([Ald75]). This is automatically fulfilled when 2.30 and 2.29 are met.
The excitation probability depends on the strength of the interaction, given by the matrix element of the *action integral* (expressed in units $\hbar$ [Ald75])

$$\begin{aligned}\chi_{n,m}(\vartheta) &= \langle m|\int_{-\infty}^{+\infty} V(\vec{r}(t))dt|n\rangle \\ &\approx \langle m|V(b(\vartheta))|n\rangle\tau_{coll} \\ &= \langle m|V(b(\vartheta))|n\rangle b(\vartheta)/v \end{aligned} \tag{2.31}$$

where V(b(ϑ)) is the magnitude of the interaction at the distance of closest approach, τ_{coll} is the interaction time and n,m are the initial and final state. This expression is directly comparable to eq. 2.21, for ΔE=0. The χ matrices, which are dimensionless if measured in units $\hbar$, can therefore be interpreted as $\pm\sqrt{P_n(\vartheta,\xi=0)}$. It is convenient to define the χ-matrices for ϑ=180°. Substituting the electrostatic potential V(b(ϑ)) by its monopole part $Z_1Z_2e^2/b(\vartheta)$, eq. 2.31 becomes $Z_1Z_2e^2/\hbar v$, which is exactly the *Sommerfeld parameter* η. Recalling the condition for the applicability of the first order theory : the monopole part of the interaction should prevent the nuclei from penetrating into each other and the excitation probability should be small, compared to unity. This can now be formulated in terms of the action integrals : $\chi_{0,0}=\eta\gg1$ and $\chi_{n,m}<1$. Measured in units $\hbar$, $\chi_{n,m}$ denotes the number of quanta of angular momentum $\lambda\hbar$ which are exchanged during the collision. In table 2.1 the three parameters discussed above are given for the three experiments described in this work.
The nuclei investigated in this work all have a 0_1^+ ground state, while the first excited state is a 2_1^+ state. The excitation is thus limited to E2 transitions. By measuring the total excitation cross section for the $0_1^+\rightarrow2_1^+$ transition, the nuclear matrix element $\langle I_0||M(E\lambda)||I_f\rangle|$ can be measured. From this matrix element several nuclear parameters are extracted : the B(E2) value, the deformation parameter β_2 and the lifetime $\tau_{2_1^+}$ of the 22_1^+ state.

2.2.4 Higher-order perturbation theory

To second order the excitation amplitudes a_{if} are given by :

$$a_{if} = a_{if}^{(1)} + \sum_z a_{izf}^{(2)} \tag{2.32}$$

where the first term is the first order amplitude (eq. 2.21)and

$$a_{izf}^{(2)} = \frac{1}{i\hbar}^2 \int_{-\infty}^{+\infty} \langle f|V(\vec{r}(t))|z\rangle exp(i\omega t)dt \tag{2.33}$$

$$\times \int_{-\infty}^{+\infty} \langle z|V(\vec{r}(t))|f\rangle exp(i\omega' t)dt \tag{2.34}$$

where ω=(E_f-E_z)/$\hbar$, ω'=(E_z-E_i)/$\hbar$. The excitation from state i (E_i) to state f (E_f) goes through the intermediate states z (E_z). A full derivation of the second order theory can be found in [Ald75].

Effect of the quadrupole moment

An interesting case where the second order perturbation theory becomes significant is when the intermediate state z is one of the magnetic substates of the final level

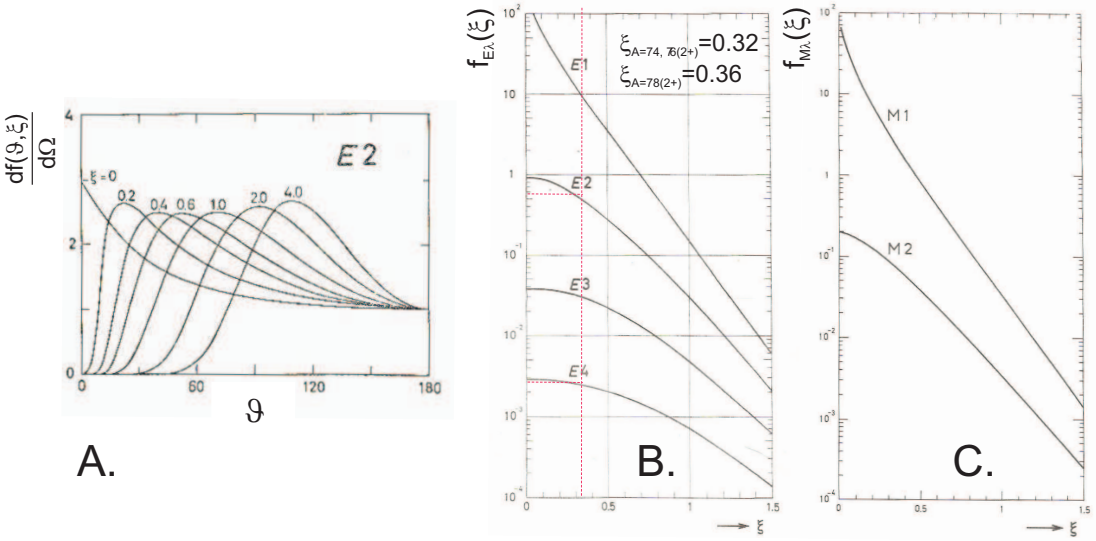

Figure 2.15: *(A) The differential function $df_{E2}/d\Omega/d\Omega$, related to the differential cross section according to eq. 2.22. (B,C) The integrated function $f_{E(M)\lambda}$. Pictures are taken from [Ald56]. The dashed line indicates the ξ value for the A=74 experiment in this work.*

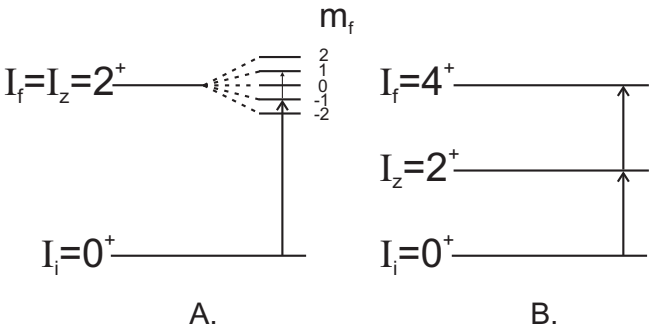

Figure 2.16: *A. Interference with the quadrupole moment of the final level. B. 2-step excitation to the final level.*

(Fig. 2.16A). The transition z→f occurs through the interaction with the quadrupole moment of the final state. The strength of this term depends on the magnitude of the matrix element M_{zf}, in the case of I_i=0,I_z=2 and I_f=2 the matrix element is related to the quadrupole moment :

$$\langle 2||M(E2)||2\rangle = \frac{1}{0.7579}Q_2 \tag{2.35}$$

where Q_2 (= the *spectroscopic* quadrupole moment) is related to the *intrinsic* quadrupole moment $Q_2=\frac{3K^2-I(I+1)}{(I+1)(2I+3)}Q_0$ in the case of a rotational nucleus. In Fig. 2.17 the effect of Q_2 on the differential cross section is plotted for ^{74}Zn on ^{120}Sn (for conditions see tab. 5.19). Both cross sections are calculated for the same B(E2) but different quadrupole moments (0. and 0.152 eb). The ratio of the integrated cross section over two different CM ranges (σ_{CM1} and σ_{CM2}) depends on the quadrupole moment. Assuming a positive quadrupole moment, this ratio increases 3%. This feature will be utilized further in this work.

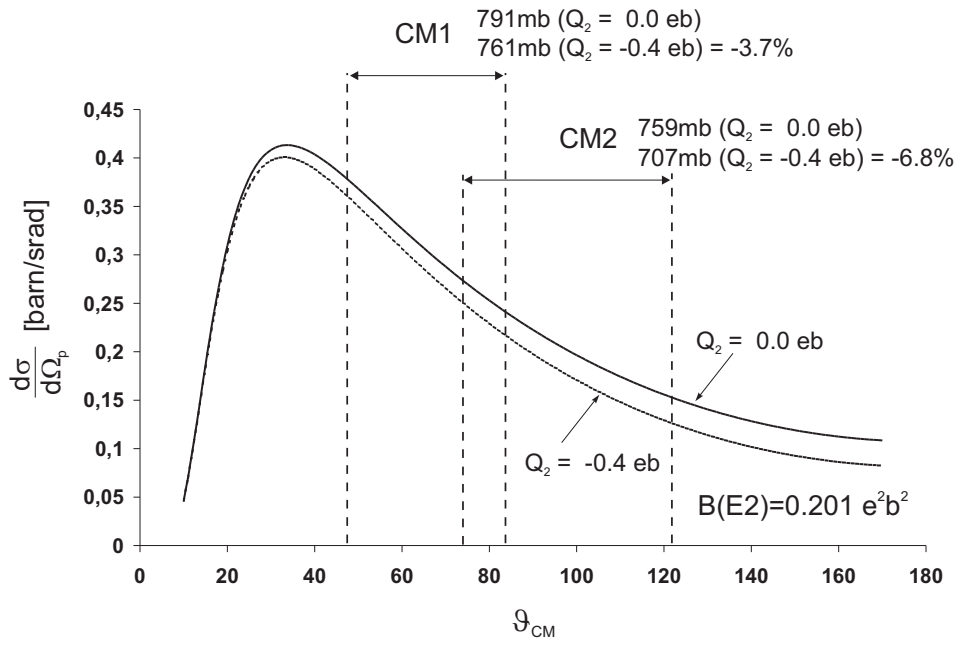

Figure 2.17: *Illustration of the effect of the quadrupole moment on the differential cross section, calculated with the classical coulex code "CLX" (see par. 4.6.2). Input parameters are given in the figure. The input B(E2) value was the same for both the Q_2=0 eb and 0.4 eb results.*

Double excitations

Another second order effect is that of a double E2 excitation to a final state which cannot be reached by a single step E2 excitation. The order of magnitude of the cross section for such a double excitation is approximately given by :

$$\sigma_{E2,E2} \sim \sigma_{E2}(I_i \rightarrow I_z) \cdot \sigma_{E2}(I_z \rightarrow I_f). \tag{2.36}$$

A typical example in these experiments is a double excitation to the 4_1^+ state, where I_i=0_1^+ , I_z=2_1^+ and I_f=4_1^+ (see Fig. 2.16). A direct E4 excitation to this level is strongly hindered (see Fig. 2.15). An explicit calculation of the second order terms gives [Ald56] :

$$\begin{aligned} \frac{\sigma_{E2,E2}}{\sigma_{E4}} &= 2.1 \frac{A_1 Z_1^2}{E_{MeV}} \frac{B(E2,0 \rightarrow 2) B(E2,2 \rightarrow 4)}{e^2 B(E4,0 \rightarrow 4)} \\ &\approx 10^3 \frac{B(E2,0 \rightarrow 2) B(E2,2 \rightarrow 4)}{e^2 B(E4,0 \rightarrow 4)} \end{aligned} \tag{2.37}$$

for A_1=120, Z_1=50 and E=212.4MeV (^{74}Zn case). B(E2) values are expressed in e^2fm^4 and B(E4) in e^2fm^8, cross sections in barn. Thus, E4 excitations are approximately hindered by a factor of 10^3.

2.2.5 Application to experiments

The parameters described in paragraph 2.2.3 are summarized in table 2.1 for the three experiments described in this work. A summary of the experimental conditions is given in Chapter 6, table 5.19. Recalling the conditions for the validity of the first order

approach : $\eta \gg 1$ and $\xi \leq 1$, it is seen from table 2.1 that this approach is valid for the considered experiments.

A	$\xi \leq 1$	$\eta \gg 1$	$\chi_{0,2}$
74	0.323	139	0.649
76	0.321	140	0.560
78	0.362	128	0.416

Table 2.1: *The Coulomb excitation parameters ξ, η and $\chi_{0,2}$ for the considered $0_1^+ \rightarrow 2_1^+$ excitation in $^{74,76,78}Zn$. For further experimental parameters, see table 5.19 in Chapter 6.*

2.2.6 Relative measurement

The number of inelastically scattered particles (beam or target nuclei) in a Coulomb excitation experiment is a measure for the excitation probability to a state n (P_n) (see eq. 2.22). Experimentally, the number of inelastically scattered beam or target nuclei may be determined from the gamma decay of the state n in the considered nucleus. In this work, the de-excitation gamma rays following Coulomb excitation of the beam and target nuclei were detected by the Germanium Gamma Detector Array MINIBALL (see par. 3.4). The number of detected $2_1^+ \rightarrow 0_1^+$ de-excitation γ-rays, associated with the de-excitation of the 2_1^+ state of the incoming beam particles (even-even ^{74,76,78}Zn) is given by :

$$N_\gamma^{Zn}(2_1^+ \rightarrow 0_1^+) = \epsilon_{MB,Zn} \cdot \sigma_{E2,Zn} \cdot \frac{\rho d N_A}{A} I_{Zn}, \tag{2.38}$$

where $\epsilon_{MB,Zn}$ is the total isotropic photopeak efficiency of the MINIBALL array at the energy of the 2_1^+ state in ^{74,76,78}Zn, $\sigma_{E2,Zn}$ is the total detected cross section for de-excitation from the 2_1^+ state, ρd is the target thickness in mg/cm^2, N_A Avogadro's number, A the target mass number and I_{Zn} the total incoming beam intensity. The latter is in the special case of Radioactive Ion Beams not accurately known. The total inelastic cross section should therefore be measured relative to a known inelastic cross section in the same experiment, i.e. the known cross section for target excitation. The total number of $2_1^+ \rightarrow 0_1^+$ de-excitation gamma's from the even-even target nucleus ($^{120}_{50}$Sn or $^{108}_{46}$Pd) is related to the known de-excitation cross section ($\sigma_{E2,Target}$) :

$$N_\gamma^{Target}(2_1^+ \rightarrow 0_1^+) = \epsilon_{MB,Target} \cdot \sigma_{E2,Target} \cdot \frac{\rho d N_A}{A} I_{Zn} \tag{2.39}$$

Dividing 2.38 by 2.39 results in a relative comparison of target and beam excitation cross sections :

$$\frac{N_\gamma^{Zn}(2_1^+ \rightarrow 0_1^+)}{N_\gamma^{Target}(2_1^+ \rightarrow 0_1^+)} = \frac{\epsilon_{MB,Beam}}{\epsilon_{MB,Target}} \cdot \frac{\sigma_{E2,Zn}}{\sigma_{E2,Target}} \tag{2.40}$$

It should be noted that in 2.39 the target is excited *only* by incoming Zn isotopes, neglecting possible other isotopes in the beam. Corrections to eq. 2.39, related to possible beam contamination will be treated in paragraph 4.2. In equation 2.40 an explicit dependence on the angular distribution of the gamma rays should be included, of the form $\frac{W_\gamma^{Zn}}{W_\gamma^{Target}}$ where $W_\gamma^{Zn/Target}$ is the integrated angular distribution of the de-excitation gamma rays over the detector solid angles. The angular distribution differs

for target and beam de-excitation gamma's, so the detection efficiency needs to be corrected for this non-isotropic distribution. This additional correction to eq. 2.40 will be treated in paragraph 4.5.

Chapter 3

The Experimental Setup

3.1 Introduction

In the exploration of the nuclear chart far off the line of beta stability ("exotic" regions), the main limitation is put by the low beam intensities. Therefore (on-going) developments in the *selectivity*, *efficiency* and *intensity* of the production techniques are required at the several Radioactive Ion Beam Facilities (RIBF). The two main production techniques of exotic nuclei are : the 'In-Flight' (IF) method and the Isotope Separation On Line (ISOL).
The IF production technique makes use of a intermediate to relativistic heavy ion beam (from 30 MeV/u-1.5 GeV/u) which impinges on a thin primary production target. With a combination of magnetic and electrical fields[1], atomic processes to identify the nuclei[2] and making use of the reaction kinematics, the isotopes of interest are selected from the primary beam, or other isotopes produced in the reaction [Van06,Mor04]. The ISOL technique relies on the availability of the radioactive species produced in a target and thermalized in a catcher consisting of solid, liquid or gas material, from which the isotopes are extracted and ionized in an ion source. After extraction from the ion source the isotopes are mass analyzed and accelerated to the required energy [Van06]. The latter might consist of a preparation stage of the ions for post-acceleration up to MeV/u energies.
The ultimate goal of both methods is to transport the nuclei of interest away from their place of production, where a large background from nuclear reactions is present, to a well shielded experimental setup where their properties can be explored. The following experimental conditions should be met by both methods : 1- High production rate, 2- Efficient (all stages in the production process should be efficient), 3- Fast (short lived isotopes should survive the whole production process) and 4- Selective (unwanted -in general more stable- isotopes should be avoided in the final RIB as much as possible). Depending whether neutron rich or proton rich nuclei are under investigation, different mechanisms for populating the isotope of interest are dominating. Proton rich nuclei are best produced by *fusion(-evaporation)* reaction of projectile and target nuclei. Neutron rich nuclei are well produced by *fission* or *spallation* of neutron rich heavy nuclei. Proton(-neutron) induced fission of U was employed in this work to produce neutron rich ^{74,76,78}Zn at the ISOL facility ISOLDE(CERN).
ISOLDE has been over 40 years the leading low-energy ISOL facility, providing beams of more than 60 elements (Z=2-88) and more then 600 isotopes [ISO06]. By coupling

[1] E.g.: B·ρ=m·v/q, where Bρ is referred to as the *magnetic rigidity* of an IF-separator and ρ is the bending radius of the trajectory

[2] E.g.: Atomic energy loss dependence on Z.

the existing low energy facility with a post-accelerator, the REX-project (see par. 3.3 and [Hab94]), the laboratory has now the possibility to accelerate a wealth of stable and radioactive isotopes up to 3 MeV/u. The first successful experiment with a post accelerated Radioactive Ion Beam was performed in 2002 (^{30}Mg). Other facilities incorporating post-acceleration are Oak Ridge National Laboratory (ORNL, U.S.), SPIRAL (France) and Triumf (Canada). IF facilities where similar experiments are performed are GSI (Germany) and MSU (US). It should be emphasized that ISOLDE is currently the only RIB facility where post-accelerated radioactive Zn beams are available with appreciable intensity for A>74. Experiments at GANIL have been performed on ^{70,72,74}Zn [Lee02, Per06]. In the same region of the nuclear chart, ORNL produces intense Ge beams [Pad05] and at GANIL successful RIB experiments have been performed on Kr isotopes [Kor05].
In the following, the ISOL facility ISOLDE will be discussed at length. First, the isotope production technique (par. 3.2) will be discussed with the emphasize on the unique selectivity offered by laser ionization. Secondly, the several steps necessary for post-acceleration of the extracted and mass separated isotopes are described (par. 3.3). Finally, the detection system for the nuclear radiation and scattered particles is elaborated upon (par. 3.4).

3.2 The Radioactive Ion Beam (RIB) facility ISOLDE

3.2.1 Isotope Production technique

Proton induced fission and release from the target

The investigated nuclei (^{74,76,78}Zn) are situated at the neutron rich side of the chart of nuclides. Neutron-rich isotopes of medium mass are well produced by fission [Kos05]. At ISOLDE, up to 4 μA of 1.4 GeV protons are delivered by the four coupled synchrotrons of the PS[3]-booster, which is part of the CERN accelerator complex (see Fig. 3.1). With this energetic proton beam impinging on a $\sim$50 mg/cm^2 $^{238}UC_x$ target, over 10^{13} fission products are produced per second. To illustrate the proton induced fission of ^{238}U, isotope production cross sections of fission fragments are plotted in Fig. 3.2. These cross sections were measured at the fragment separator at GSI. The isotopes were produced in an inverse kinematics[4] spallation reaction of ^{238}U + p (1 AGeV) [Ber03]. The plots illustrate the order of magnitude of the production cross sections of Zn and the main contaminants in the final RIB at ISOLDE (see further).
The produced fission products are stopped in the target material and move towards a transfer line by diffusion and effusion[5] transport processes. Both the target and the transfer line are electrically heated up to about 2000 °C to reduce the diffusion times, to avoid too long "sticking" times of the atoms on the surface and to ensure sufficient electron emission to provide conditions for ion repelling from the surface. The speed of the transport process depends strongly on 1- the target geometry, 2- the target material (or coating on the walls of the target container) and 3- the specific element. The element dependent release time from the primary target is exploited in cases where the unwanted isobaric contaminant has a significant different release characteristics then the investigated isobar. Examples of this technique in the Pb region

[3] **P**roton **S**ynchrotron

[4] The term *Inverse Kinematics* is utilized when the target (a) is the lighter element of X and a in the reaction a(X,Y)b.

[5] *Diffusion* is the spontaneous spreading of matter, heat or momentum, whereas *effusion* is the process where individual particles flow through a hole, which is smaller then their mean free path.

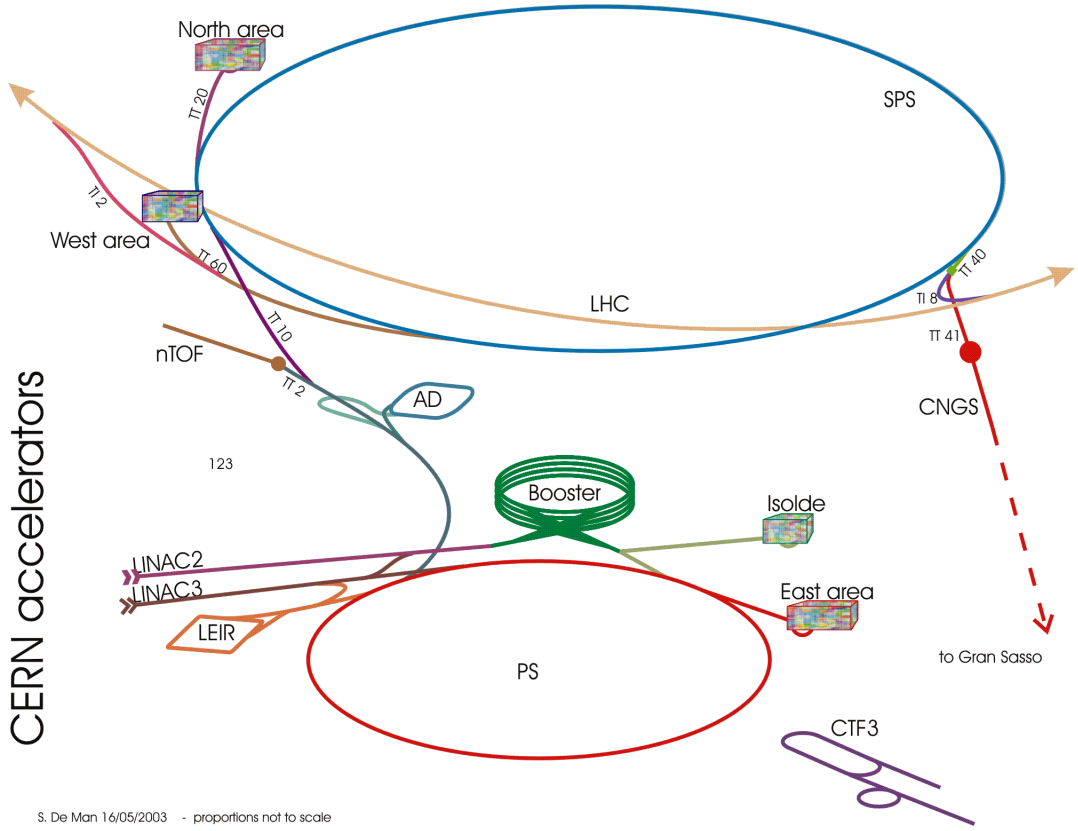

Figure 3.1: *The CERN accelerator complex. ISOLDE utilizes the "(PS-)Booster" and "Linac2".*

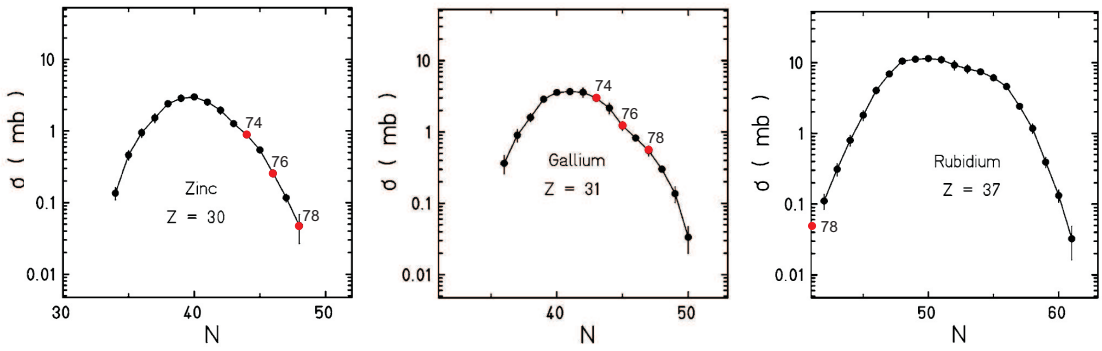

Figure 3.2: *Isotope production cross sections in the spallation reaction ^{138}U + p (1AGeV), measured in inverse kinematics at the Fragment Separator in GSI. Plots are taken from [Ber03]. $^{74,76,78}Zn, Ga$ and Rb are shown, which are the main contaminants in the RIB in ISOLDE.*

are discussed in [Dew04, Van98] and a first application in the Ni region is discussed in [Bre06]. The element dependent release function P(t) is defined as the probability density for an atom generated at t=0 of a given element to be released at at time t. Since the decay and release probabilities are independent, the release function for

element i is given by :

$$P_i(t, \lambda_i) = P_{\lambda_r,\lambda_f,\lambda_s,\alpha}(t) exp(-\lambda_i t), \tag{3.1}$$

where λ_i is the decay constant of the radioactive element i. The function $P_{\lambda_r,\lambda_f,\lambda_s,\alpha}(t)$ was observed to be best fitted by a four parameter function given by [Let97]:

$$P_{\lambda_r,\lambda_f,\lambda_s,\alpha}(t) = N(1 - exp(-\lambda_r t)) \cdot [\alpha exp(-\lambda_r t) + (1 - \alpha) exp(-\lambda_s t)], \tag{3.2}$$

where N is a normalization constant. This release curve was measured for Zn and Ga isotopes and is given in Fig. 3.3 (right), the parameters can be found in [Kos05]. In the left part of Fig. 3.3 the observed particle rate in the CD detector is plotted as a function of time elapsed since the last proton pulse. In black, the particle rate during laser on periods is plotted, while the open triangles show the particle rate during laser off periods is shown (same time interval). The solid circles represent the difference in particle rate (laser on minus laser off). The release functions $P_{Zn}(t)$, $P_{Ga}(t)$ and their sum are plotted on the graph as well. (A time delay in the release function $P_{\lambda_r,\lambda_f,\lambda_s,\alpha}$ of 90 msec was assumed because of the trapping and charge breeding time - the decay time was *not* shifted by this amount.) The main contaminant (Ga) diffuses out of the target rather constant in time, whereas the Zn beam content falls down to the same level as the contaminant after ∼800 ms. This different release behavior will be utilized in par. 3.3.5.

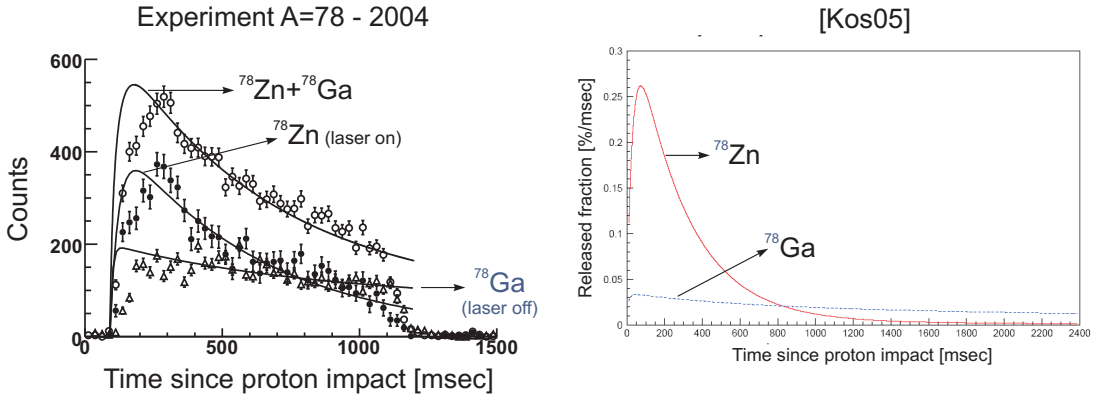

Figure 3.3: *Left : Particle rate in the CD detector, as a function of time elapsed since the proton impact, during the A=78 laser on/off runs (2004 experiment) : laser on (Zn+Ga, open circles), laser off (Ga, open triangles), (laser on minus laser off) (Zn, solid circles). The release functions from [Kos05] are plotted as well. Right : Release functions as they are measured right after the ISOLDE mass separator, taken from [Kos05]*

.

Selectivity in the transfer line [Kos05]

From the wealth of produced fission products, only the investigated element should be extracted from the target ion source, therefore an element selective mechanism is needed. One element selective mechanism was touched upon in the previous paragraph, namely the element dependent diffusion times. The "volatility" of the element

is of importance in this case. Elements with high volatility have a shorter "sticking time" on the surface. The group 12 elements, like Zn, have an atomic subshell closure $d^{10}10s^2$ and have a higher volatility then the neighboring elements. Keeping the temperature of the transfer line just high enough to allow the transport of short lived Zn isotopes will retain other, less volatile elements by condensing them on the surface of the transfer line. Cu, Ni, Ga, Ge, As and Se are retained in this way in the Zn beams.

Laser Ionization [Fed00]

The transmitted ions effuse through a thin tube (referred to as 'line') where ionization takes place. A powerful element selective ionization process is governed by the resonance laser ionization technique. The atomic excitation energy is provided by pulsed laser light tuned to strong atomic transitions of the element of interest. For other elements the laser light is out of resonance and there will be only negligible amount of ionization and excitation. In the case of Zn the laser ionization is a 3-step ionization scheme [Let98]. Frequency tripled dye laser light at 213.86 nm excites the atomic ground state $3d^{10}4s^2{}^1S_0$ to $3d^{10}4s4p{}^1P_0^1$. The second transition is performed with dye laser light at 636.23 nm to the $3d^{10}4s4d{}^1D_2$ state from whereon the atoms are ionized non-resonantly to the continuum with the green copper vapor laser light at 511 nm. Because only pulsed lasers can provide sufficient peak power to saturate the atomic excitations, the atoms have to be 'stored' for the time between two laser pulses to have at least one chance to interact with the laser light. This is achieved in the long thin tube through which the atoms effuse. The ionized elements are extracted from the RILIS by an extraction electrode of 60 kV. This combination of a heated, long tube and laser light is called the RILIS (Resonant Ionization Laser Ion Source) and is sketched in Fig. 3.4, where the several parts are indicated together with the proton beam direction.

Surface Ionization

Due to the high temperature of the tube thermal ionization of atoms occurs next to laser ionization, depending on the ionization potential of the element. Some of these ionization potentials are plotted in fig 3.5. The atom loses an electron by hitting the ion source wall (the heated thin tube) and is re-evaporated as an ion. This 'surface ionization' is very efficient when the ionization potential is lower then the work function of the ionizer. From Fig. 3.5 it is clear that Kr and Br are strongly suppressed due to their low ionization potential, while Rb, Ga and Sr are possible sources of surface ionized contamination.

Neutron induced fission

In the case of ^{74,76}Zn beams (proton induced fission of U) the main beam contamination stems from Ga (others are chemically retained or the production cross section is much lower in the proton induced fission reaction). In the A=78 beam a Rb contamination was observed as well, due to the higher production cross section at A=78 (see Fig. 3.2) and the low ionization potential. An additional selectivity was obtained by the use of low energy neutron induced fission of UC_x, which suppresses the amount of produced Sr and Rb. Compared to proton induced fission, the neutron induced fission cross section is more peaked at the neutron rich side. The low energy neutrons were

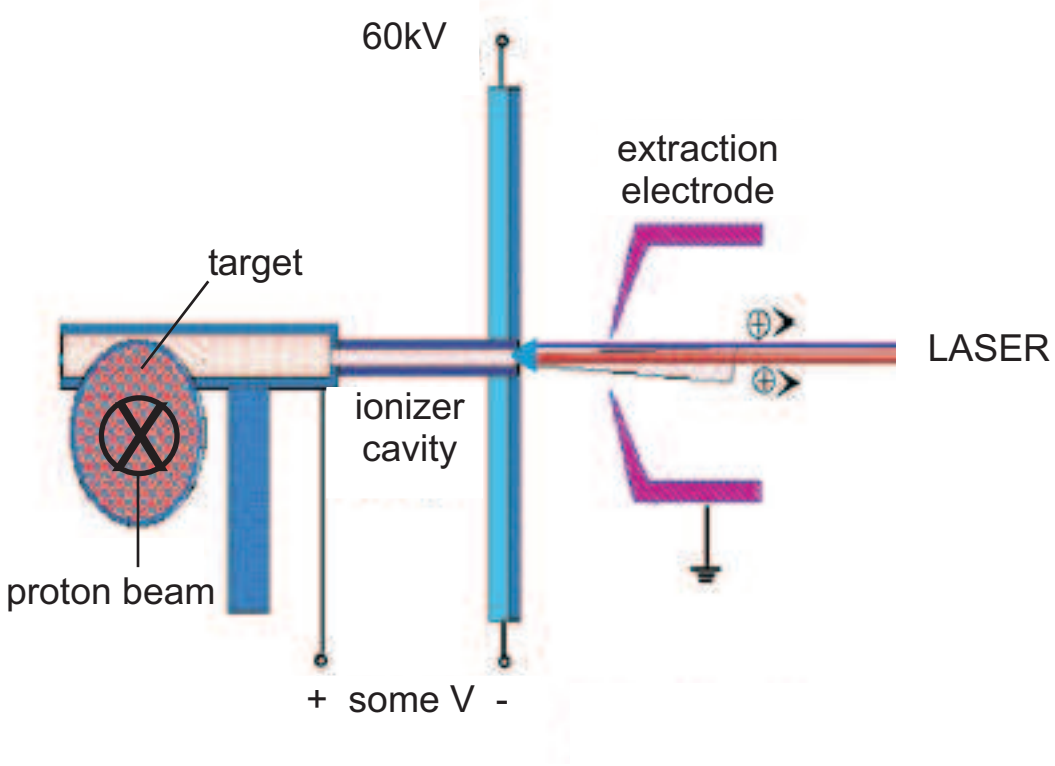

Figure 3.4: *The ISOLDE target and the Resonance Ionization Laser Ion Source.*

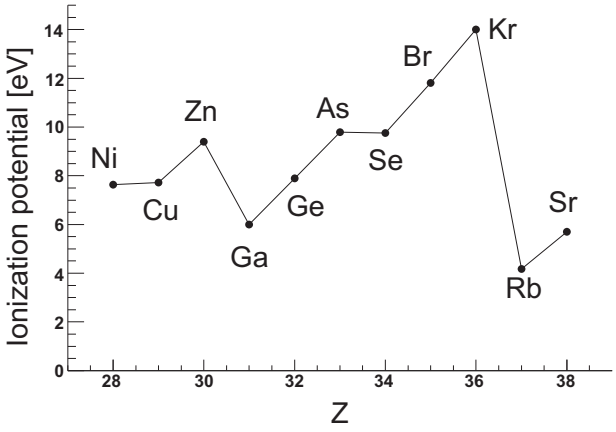

Figure 3.5: *Ionization potentials of elements near Zn (Z=30). The strong contamination from Ga stems from its low ionization potential.*

produced by sending the proton beam on a heavy metal rod (ex. Ta, referred to as the neutron-to-proton convertor). Low energy spallation neutrons emitted at large angles hit the UC container. The direct proton beam and higher energy spallation neutrons are strongly forward peaked and do not hit the UC target (Fig. 3.6). A measurement of the beam content at the end of the post-accelerator shows the improvement in beam contamination with and without the neutron convertor (see Fig. 4.3).

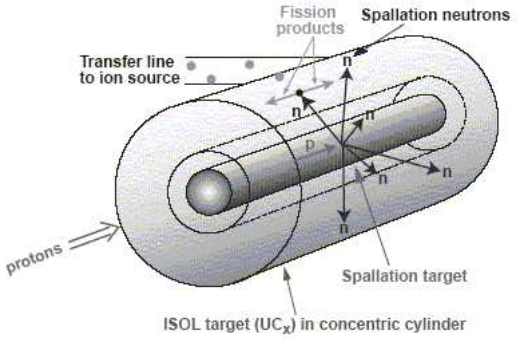

Figure 3.6: *Spallation target.*

Conclusion

In conclusion, the innovative target ion source developments at ISOLDE have made it possible to produce high intensity Zn beams. Due to the selective laser ionization, the presence of non laser ionized contaminants, such as Ga, can be identified in the final RIB. Other isobaric contaminants should be reduced below the % level. A careful investigation of particle and gamma spectra will be performed in par. 4.2 in order to establish the beam content.

Mass separation and Yields

After the extraction of the single charged ions from the ion source, the radioactive beam is mass separated by either the General Purpose Separator (GPS) or the High Resolution Separator (HRS) which have a mass resolving power of resp. ΔM/M=2400 and 5000. The GPS was used in the experiments described in this work. After the GPS an "on-line" yield measurement is done prior to each experiment with Radioactive Ion Beams, in order to evaluate the feasibility of the experiment. In table 3.1 the on-line yield for the considered isotopes are given for the experiment in 2004 and additionally (between brackets) values are given from 2005. Yields are expressed in ions/μC, which can be converted to ions/sec depending on the incoming proton beam intensity (e.g. : 3.0E13 protons$\times$1.6E-19C /2.4sec = 2μA).

	YIELDS [ions/μC]					
	proton induced			neutron induced		
A	Zn	Ga	Rb	Zn	Ga	Rb
74	2.0E7	-	-	2.0E6	2.8E5	-
76	5.0E6	-	-	9.2E5	-	-
78	5.7E5	1.2E6	$\gg$1.2E6	3.9E5(1.3E5)[1]	1.5E5	$\ll$
80	(3.4E4)[1]			3.0E4(1.6E4)[1]	6.7E4	1.1E5

Table 3.1: *Online yield measurements after the GPS, in ions/μC for ^{74,76,78}Zn,Ga and Rb from 2004. Between brackets new values from 2005 are given. ([1]=the transfer line material is quartz instead of Thallium.)*

3.3 REX-ISOLDE

The **R**adioactive beam **EX**periment in ISOLDE was proposed in 1994, as a pilot experiment to bunch, charge breed and post-accelerate already existing mass separated singly charged radioactive ions in an efficient and cost effective way [Hab94]. The bunching of the RIB is necessary because of 1- the charge breeding times which are typically 20 msec (lighter ions, e.g. Mg) $\rightarrow$ 200 msec (heavier ions, e.g. Cd), 2- the duty cycle of the linear accelerator and 3- to increase the signal-to-noise ratio in measurements with low RIB intensity.

3.3.1 Penning Trap (REXTRAP)

The continuous RIB is injected into a Penning Trap [6] where the ions are decelerated by the high voltage of the Penning Trap from 60 kV to some eV. Further deceleration (or *cooling*) occurs through collisions with the Ar or Ne buffer gas in the trap at a pressure of 10^{-3} mbar (see Fig. 3.7B for an illustrative sketch of the process). By the cooling in the buffer gas the transverse emittance[7] of the extracted beam improves. Further improvement of the emittance and additional purification of the extracted beams might be achieved by applying a sideband cooling technique ([Ame05]). The intensity limitation of the Penning Trap is given by the Brilloin limit for the charge density in a magnetic field. The limit depends on the mass of the stored ions and is typically $\approx 10^8/\mathrm{cm}^3$ [Ame05]. The ions are extracted from the trap in short bunches of 10-50 μsec by lowering of the potential and re-accelerated to 60 kV. The extracted ions are transported through a vertical beam line to the EBIS ion source. The Penning Trap is illustrated in Fig. 3.7D. [Ame05]

3.3.2 Electron Beam Ion Source (EBIS)

The Electron Beam Ion Source (EBIS) is intended to charge breed ions by electron impact ionization, prior to injection into the compact linear accelerator. An electron gun delivers mono-energetic electrons of 3-6 kV with a beam current of 100-500mA. The electron beam is confined by a 2T superconducting solenoid magnet to $150\mathrm{A}/\mathrm{cm}^2$ (see Fig. 3.7E). A radial confinement of the ions is obtained by the potential depression of the negative space charge of the electrons, while the longitudinal confinement is arranged by potential barriers established by cylindrical electrodes surrounding the electron gun (see Fig. 3.7C). The breeding efficiency is large when there is a phase space overlap between the confined electron beam and the injected ions. The limitation on the number of stored ions in the EBIS is given by the space charge of the electron beam, which is typically $\sim 10^{10}$ charges. In general this is not the limiting factor in the Trap-EBIS combination. The vacuum inside the EBIS must be 10^{-11}mbar so a several differential pumping stations are installed on the vertical beam line. Still, rest-gas atoms from the Penning Trap buffer gas are injected in the EBIS and occur as contaminants in the final RIB delivered by the EBIS. [ISO06, Rex06]
The charge breeding time in EBIS, which is identical to the trapping time in the REXTRAP, was 78 msec for the experiments described in this work (A=74,76,78 in 2004). At a rate of $\sim$13 Hz, the EBIS injects bunches of particles in the REX linac.

[6] A cylindrical trap which captures ions by applying electromagnetic fields.

[7] Emittance is defined as a figure of merit for the divergence of a particle beam. It expresses the extent occupied by the particles in the space and momentum (phase-)space. Good emittance improves the charge breeding efficiency, see par. 3.3.2.

The release from the EBIS lasts for $\sim$ 150-300μsec, as shown in Fig. 3.8B2 and Fig. 3.21. [Ame04]

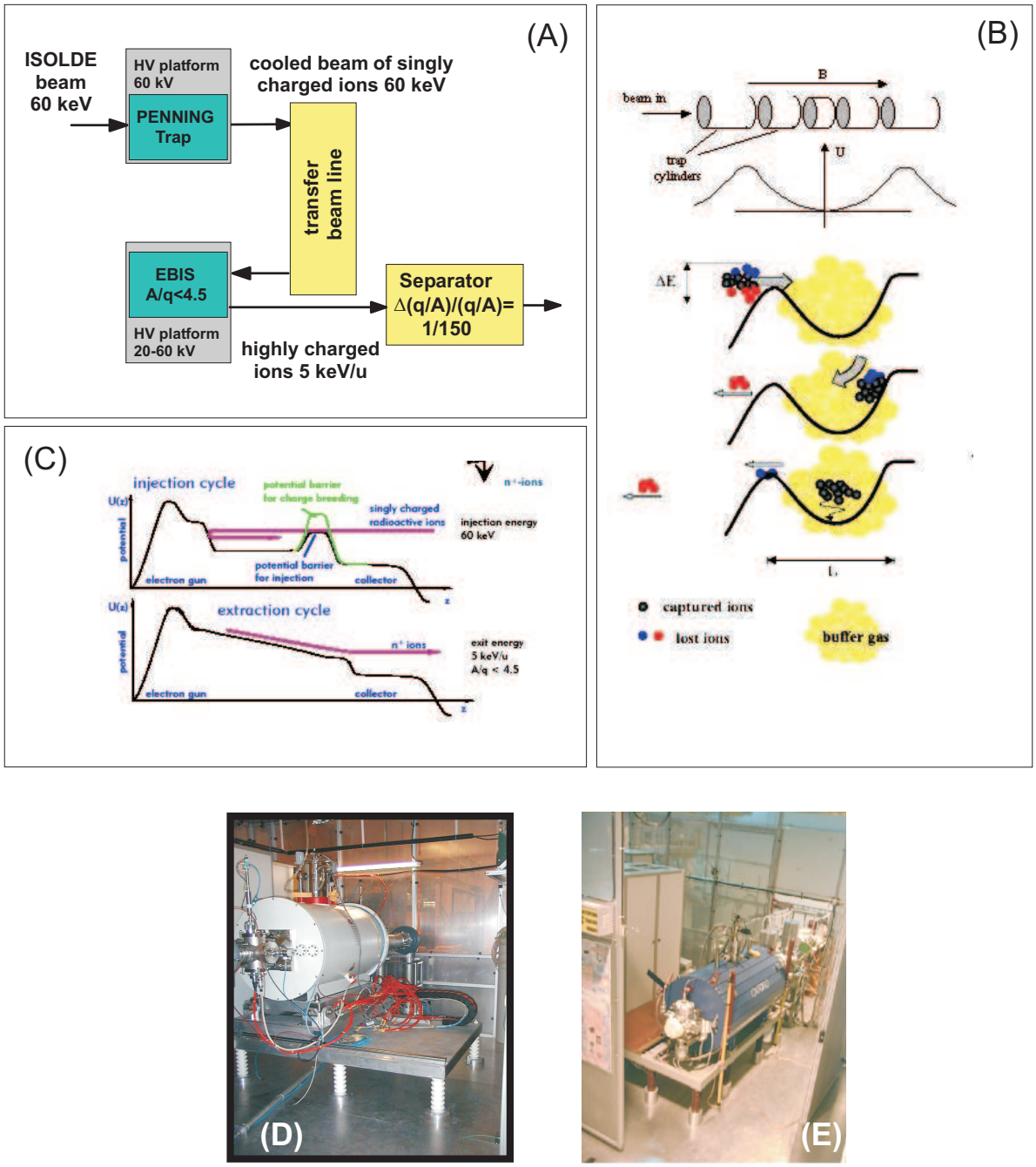

Figure 3.7: *(A) The Trap-EBIS combination. (B) Sketch of the bunching process in the Penning Trap : cooling of the incoming RIB is done through collisions with the buffer gas. (C) Sketch of charge breeding process in the EBIS : after bunching in the Penning Trap, the ions are re-accelerated to 20-60 kV and confined within potential barriers in the EBIS. (D) Picture of the Penning Trap. (E) Picture of the EBIS, the cylinder contains the liquid He for cooling of the superconducting magnet. Pictures taken from [ISO06].*

3.3.3 The A/q separator

The beam delivered by EBIS consists of the required radioactive ions originating from the ISOLDE primary target and residual gas ions from the REX-TRAP combination. Therefore an additional mass separation according to the A/q ratio is required. Due to the (wide) potential depression of the electron beam, the extracted ions have a large energy spread. In an S-shaped combination of deflectors, a first separation performs an electrostatic separation to energy, irrespective of the mass. The second separation stage contains a magnetic deflector where the optimum A/q ratio can be selected in the focal plane. Prior to any experiment a scan is made over A/q (see tab.3.2) in order to determine the A/q setting with the least contamination from the REX-EBIS combination (rest-gas). It should be emphasized that at this stage the isobaric contamination originating from the primary ISOLDE target is still present. In Fig. 3.8A an example of such a scan is given for mass 74, obtained during the experimental campaign of 2003 [8]. The main contaminants being rest-gas atoms (^{20,22}Ne and ^{40}Ar) With the (REX-)Trap closed (no RIB is injected) the rest-gas particles are present, while with the (REX-)Trap opened, the RIB is separated as well. In 2003 an A/q setting of 4.11 was set for A=74 ($^{74}Zn^{18+}$), important contamination was present from stable $^{66}Zn^{(16+)}$ (A/q=4.13) and $^{40}Ar^{(10+)}$ (A/q=4.00). In 2004, better vacuum conditions in the EBIS source reduced the stable contaminants in the RIB considerably (see par. 4.2). In Fig. 3.8B an EBIS time release curve is plotted for the A=74 (2003) experiment, for periods when the ISOLDE beam gate is open (RIB ON) and closed (RIB OFF). Note that in 2003, the ISOLDE beam gate was ∼0.6 sec, whereas in 2004 this was 1 sec. A remarkable difference is observed for the "early" and "late" EBIS times. The total extraction pulse including A=74 isotopes lasts ∼150-300μsec, while the lighter contaminating particles are extracted already after 60μsec ("early EBIS"). This is illustrated in the particle identification plots of Fig. 3.8C. In this way, stable contaminants can be identified by gating on the status of the ISOLDE beam gate. The EBIS release curve for A=74, obtained in 2004, is given in Fig. 3.21.

	^{20}Ne	^{22}Ne		^{40}Ar	^{36}Ar		^{74}Zn	^{76}Zn	^{78}Zn
q	*90.48%*	*9.25%*	*q*	*99.6%*	*0.34%*	*q*	-	-	-
3	6.67	7.33	8	5.00	4.50	17	4.35	4.47	4.59
4	5.00	5.50	9	4.44	4.00	18	4.11	4.22	4.33
5	4.00	4.40	10	4.00	3.60	19	3.89	4.00	4.11
6	3.33	3.67	11	3.64	3.27	20	3.70	3.80	3.90
7	2.86	3.14	12	3.33	3.00	21	3.52	3.62	3.71

Table 3.2: *A/q values for possible beam particles (incl. beam contaminants). The natural abundances for each stable isotopes are given as well.*

[8] The experiments described in this work originate from 2004. The A/q scan from 2004 is similar to the scan from 2003 in Fig. 3.8

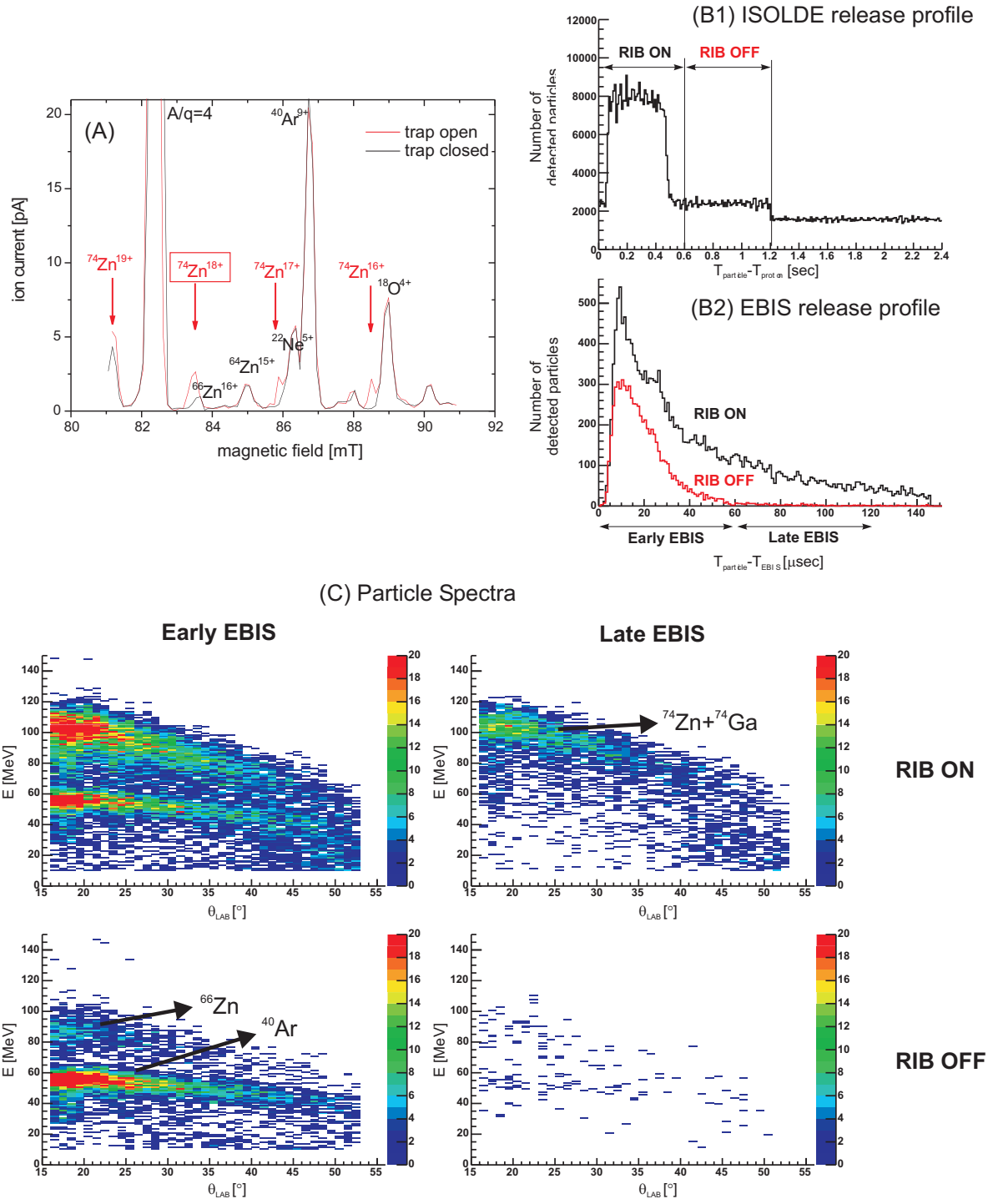

Figure 3.8: *(A) A/q scan (2003 campaign) at the exit of the mass separator after the EBIS ion source with "trap closed" (no RIB) and "trap open" (with RIB). The A=74 beam was delivered at A/q=4.11 (18^+). (B1) Release profile of the RIB out of the ISOLDE primary target. A beam gate of ∼500 msec was applied after the proton impact. (B2) Release profile of the EBIS as detected by the CD detector at the MINIBALL setup. (C) The identification of the contaminants is based on the energy versus scattering angle plots. Contamination from ^{66}Zn and ^{40}Ar was observed. The first column represents the "Early EBIS" (0-60 µsec) after the extraction started, the second column represents the "Late EBIS" (60-120 µsec) after the extraction started. The first row is acquired 0-600 msec after the proton impact (RIB present), the second row 600-1200 msec after the proton impact (no RIB present, since the ISOLDE beam gate is closed).*

3.3.4 The REX-Linac

Due to the limited space in the ISOLDE hall (prior to 2004) and to reduce costs, the linac was designed as compact as possible. The design A/q acceptance of the linac is 4.5. In order to keep the possibility open for accelerating heavier masses, the isotopes should be brought to a charge state higher then one. Therefore the bunching and charge breeding concept for REX-ISOLDE was developed. The highly charged ions are accelerated over 4 different resonator sections, each adjustable over a certain energy range. The different parts of the linac are shown in Fig. 3.9. The first type of resonator is an RFQ structure (not visible in Fig. 3.9) which accelerates the extracted particles from the EBIS from 5 keV/u to 300 keV/u. The next IH-structure further accelerates the ions to an adjustable energy of 1.1-1.2 MeV/u. The final acceleration stages consist of three 7-gap resonators delivering energies over the range 0.8-2.25 MeV/u, and a 9-gap resonator, installed in early 2004 which brings the highest energy up to 3.0 MeV/u. The resonance frequencies are 101.28 MHz (7-gap) and 202.56 MHz (9-gap). The ion bunching in the REX-Trap is synchronized with the linac operation. The ratio of the time over which the linac is 'ON' (RF power is transmitted to the cavities) over the total time between EBIS pulses is called the *duty cycle* and amounts 10%. The injection rate of ion bunches from the EBIS into the linac is called the repetition rate and is maximal 50 Hz. The Zn Coulomb excitation experiments in 2004 were performed at a repetition rate of $\sim$13 Hz (charge breeding and bunching $\approx$80 msec). The energy upgrade of the last 9=gap resonator section is crucial for the feasibility of the Coulomb excitation experiments, since due to the low beam intensities, high cross sections are needed. As exemplified for ^{74}Zn in Fig. 3.10, the total cross section is a factor of 2 higher at 2.8 MeV/u compared to 2.2 MeV/u, indicating the importance of the 9-gap resonator. [Kes03]

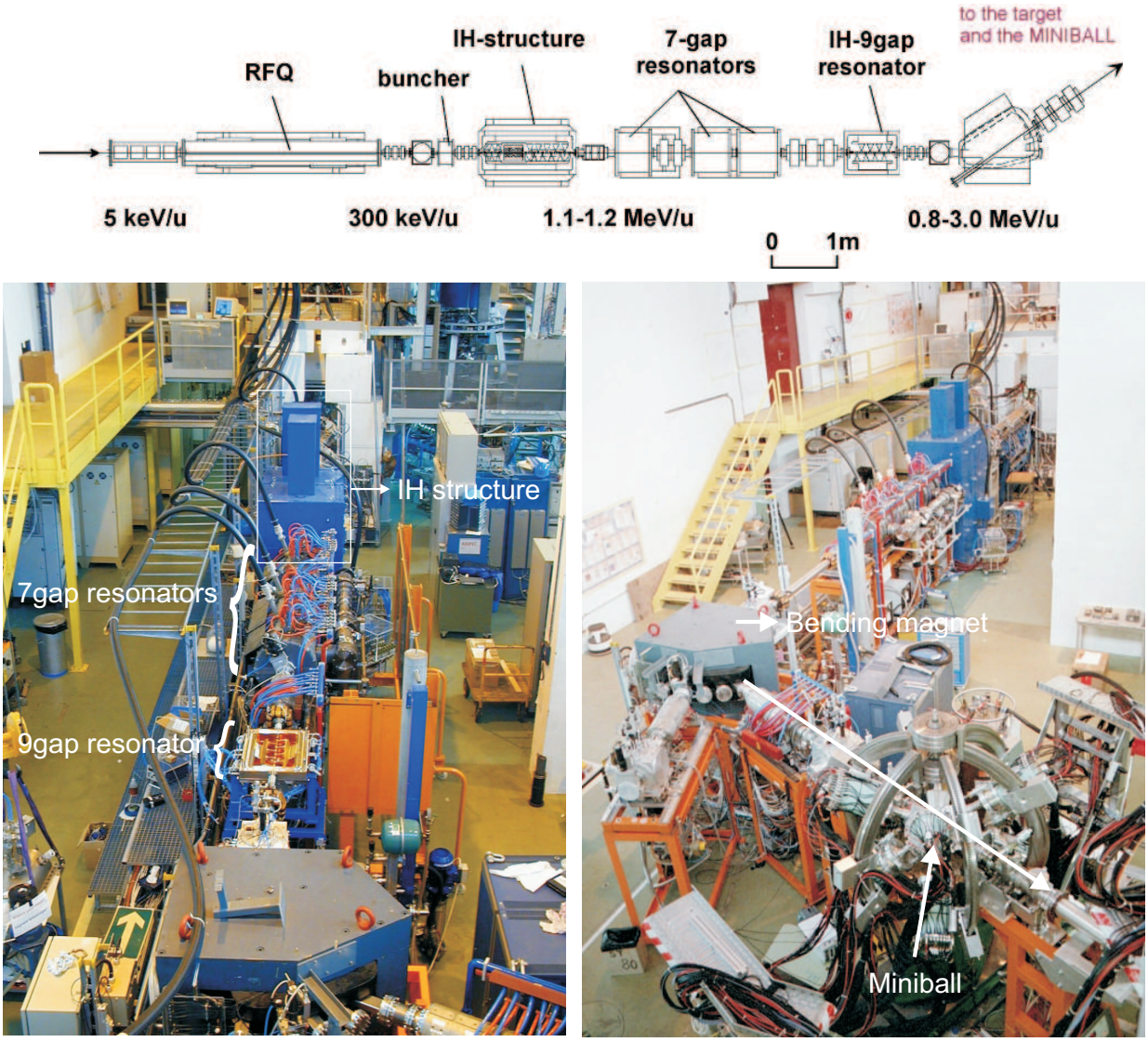

Figure 3.9: *Layout of the REX linac in 2004. (Pictures taken from [Nie05])*

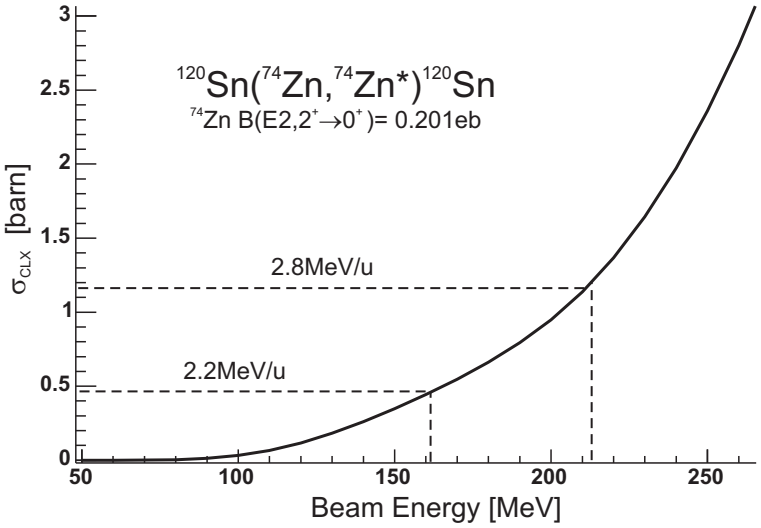

Figure 3.10: *Energy dependence of the total (detected) cross section $\sigma_{CLX}(0_1^+ \rightarrow 2_1^+)$ for ^{74}Zn ($B(E2) = 0.201\ e^2b^2$).*

3.3.5 Time structure of (REX-)ISOLDE

In Fig. 3.11 the relevant timing signals related to the REX-ISOLDE operation are given. In table 3.3 the three main time signals are summarized with their periodicity and their usage in the analysis.
The first periodic time signal in Fig. 3.11 is the time pulse issued at the beginning of a new supercycle of the PS booster. The periodicity is always a multiple of 1.2sec, in the considered experiments this was 14×1.2sec (A=74,76) and 21×1.2sec (A=78). The signal is used to drive a laser shutter which blocks the laser light towards the thin ionization tube. In the data acquisition the status of this shutter is stored in a pattern unit, which is read out after each On and Off Beam window.
The second time pulse is the T1 proton pulse, generated each time the ISOLDE HV is switched off. This indicates the proton beam will impinge on the primary target. [9] Every other second proton pulse was sent to the ISOLDE target in 2004. From the time T1 on, the radioactive ions will diffuse out of the target as discussed in par. 3.2.1. The usage of the proton time information was already demonstrated in Fig. 3.3 and Fig. 3.8. By imposing conditions on the time difference between particle arrival and proton impact, the ISOLDE beam gate information is exploited. Closely related to T1, is the T2 signal which indicates the rise of the HV after the proton impact. This signal was not used in the current experiments.
The third time information is related to the EBIS injection into the linac. The signal is used to trigger the data acquisition for an "In Beam" measurement ("BEAM ON" in Fig. 3.11). The same time information is send to the linac to synchronize the accelerator with the ejected particle bunches. The usage of this time information was demonstrated in Fig. 3.8. The "In Beam" window is crucial in the operation and data

[9] The proton beam ionizes the air in the target area, because it is not conducted through a high vacuum beam line towards the ISOLDE primary target. The HV needs to be switched off because the highly ionized air might cause sparking in the target area.

acquisition of the REX-MINIBALL setup. During the "In Beam" window, the post-accelerated isotopes reach the MINIBALL setup and the measurement of the nuclear properties is performed only then. The "In Beam" window lasts for ∼780 μsec which is long enough to cover the full EBIS release curve. The "Off Beam" window will be discussed in par. 3.5.

Time Information	Periodicity	Analysis
PS supercycle	12-21×1.2 sec	laser ON/OFF cycle
T1 proton pulse	every 2.4 sec	beam gate ISOLDE
EBIS pulse	every ∼40 msec	In Beam measurement

Table 3.3: *The different time signals relevant for MINIBALL experiments and their usage in the analysis.*

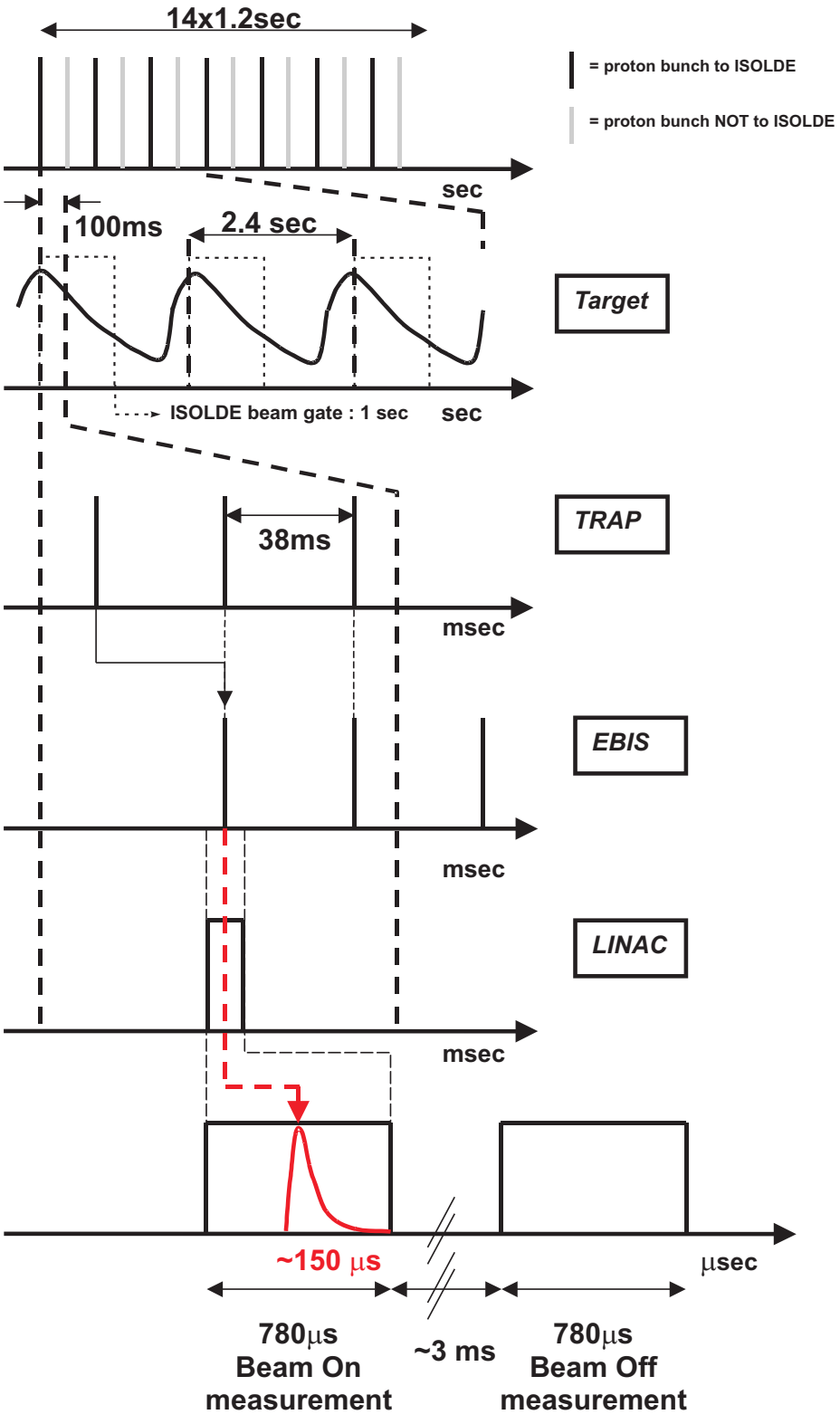

Figure 3.11: *The time structure of the different stages in the ISOLDE laboratory : 1- The supercycle (PS booster, sec), 2- The proton impact time (sec), 3- The Trap and EBIS trapping and charge breeding time (msec), 4- The EBIS release time (μsec).*

3.4 The MINIBALL setup

Integrated in the original REX-ISOLDE design [Hab94], a high resolution gamma spectrometer was envisaged in order to perform nuclear structure experiments on low intensity post-accelerated radioactive ion beams. This idea has been elaborated since 1996 and resulted in the fully operational MINIBALL detector array in 2001. The MINIBALL array is a high resolution Ge detector array in a close geometry to increase the total efficiency. Advanced segmentation of the Ge crystals and pulse shape processing increases the granularity of the detector and provides the possibility for Doppler correction of the in-flight emitted gamma rays. In Fig. 3.12A the present MINIBALL setup is shown at the end of the REX-linac, around a 60° beamline. The MINIBALL detectors surround the secondary target as shown in Fig. 3.12B.

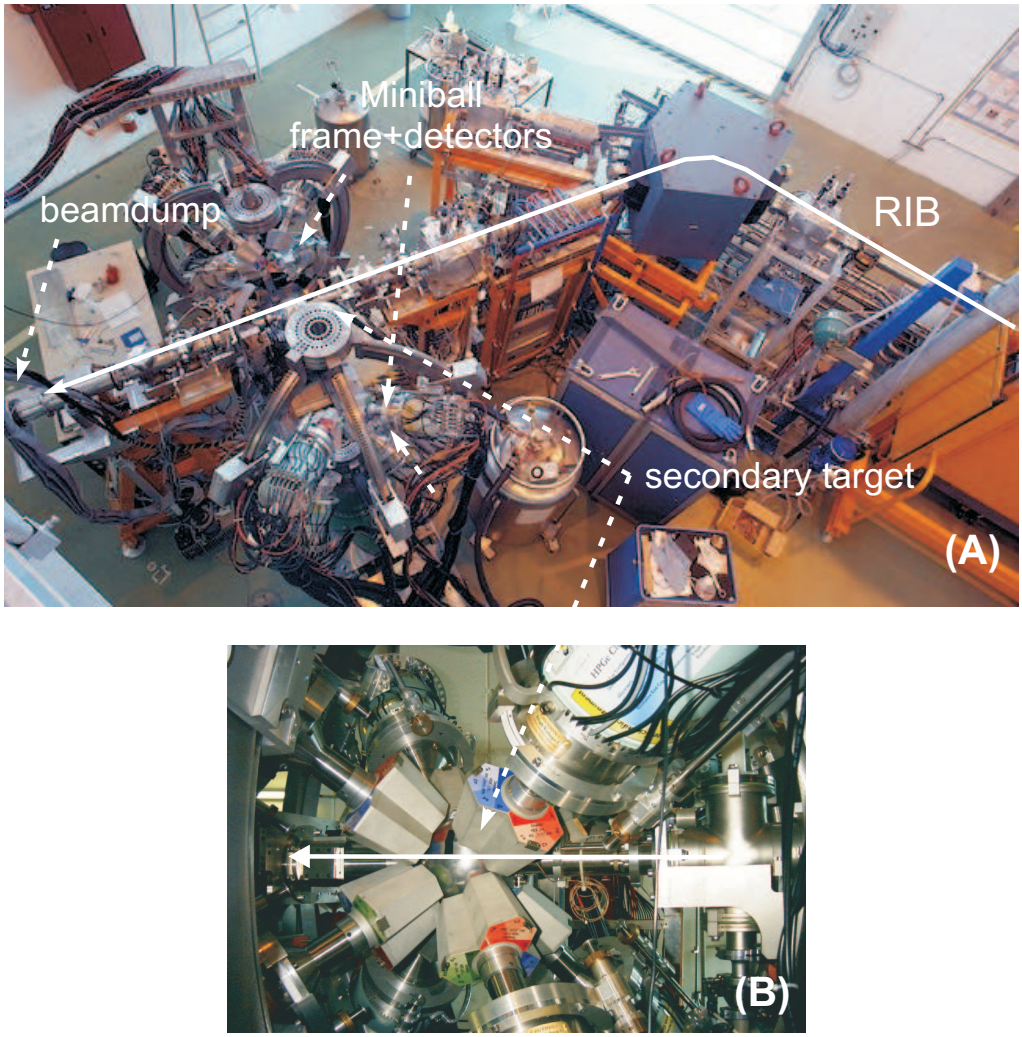

Figure 3.12: *A. The full setup at the end of the REX-linac. B. Detail of the secondary target, contained inside the spherical target chamber. The HPGe detectors are placed in "close geometry" around the target chamber.*

3.4.1 The Germanium Detector Array MINIBALL

Introduction

The MINIBALL detector array consists of 8 cluster detectors, where each cluster contains 3 individually encapsulated Hyper Pure Germanium (HPGe) crystals, surrounded by an aluminium cap. Each crystal is electrically segmented[10] in 6 parts (=segments) along the crystal side, as depicted in Fig. 3.13. The central electrode, where the depletion High Voltage is applied, is referred to as the "core". Typical depletion voltages for a MINIBALL HPGe crystal are 2.5-4.5 kV. The individual cores of MINIBALL assure a "granularity" of 24 (3x8) individual parts, the 6 fold segmentation brings the "electrical granularity" to 8x3x6=146. The three crystals are mounted on a cold finger and are kept at LN2 temperature. The 8 clusters with their attached dewar, containing the liquid nitrogen (LN2), are mounted on 4 flexible aluminum arms. The clusters can be positioned in theta (angle with the beam axis), phi (cone around the beam axis) and alfa (spin around the cluster center) direction (see Fig. 4.13). The solid angle coverage of the 8 clusters at a target-cluster distance of ∼11 cm is ∼60% of 4π. The average γ resolution of each core is 2.3 keV at 1.3 MeV, for the segments this is 2.8 keV.

Electronics

The pre-amplified signals from all 24 cores and the 146 segments are send to the "Digital Gamma Finder" (DGF, X-ray Instruments Associates). Two DGF modules are used per crystal, where the pre-amplified signal from the core is send to a "master trigger" channel, while the remaining 7 inputs on the DGF modules are used for the 6 segment signals (1 remains empty). This layout of the signals is used for Pulse Shape Analysis on the several segments and is illustrated in Fig. 3.13. The core contact *always* detects an interacting γ-ray, while it depends on the interaction point in the crystal if a segment detects the signal or not. The concept of mirror charges, discussed in [Gun00], is used for pulse shape analysis (PSA), but this feature of the MINIBALL is not used in this work. The DGF channel containing the core signal serves as a trigger to read out the accompanying segment channels on the crystal. In this way, a direct correlation exists between the detected core energy and the segment energy. The segment information is used in the Doppler correction of in-flight emitted γ-rays. It is assumed that the first interaction of the γ ray (which determines the emission direction of the γ-quantum) coincides with the 'main' interaction (=the interaction where the highest energy is deposited in a Compton event). This is a reasonable assumption in the energy range of the relevant γ rays in this work (600-1172 keV). In the add-back mode (where coincident gamma-ray energies in neighboring cores on the same cluster are summed), the segment number correlated with the core where the highest energy was detected is assumed to be the first interaction point.
The DGF module is the first fully operational digital module used in γ ray spectroscopy. In the current MINIBALL setup (2004) the particle branch (see par. 3.4.2) is not read out in digital modules, so a link must be established between the analogue particle branch and the digital γ branch. This will be discussed in par. 3.4.2.

[10] The electrical segmentation is achieved by shielding part of the HPGe crystal-sides during implantation of Boron n-type impurities. In this way, only parts of the crystal are electrically contacted and they can be read out separately.

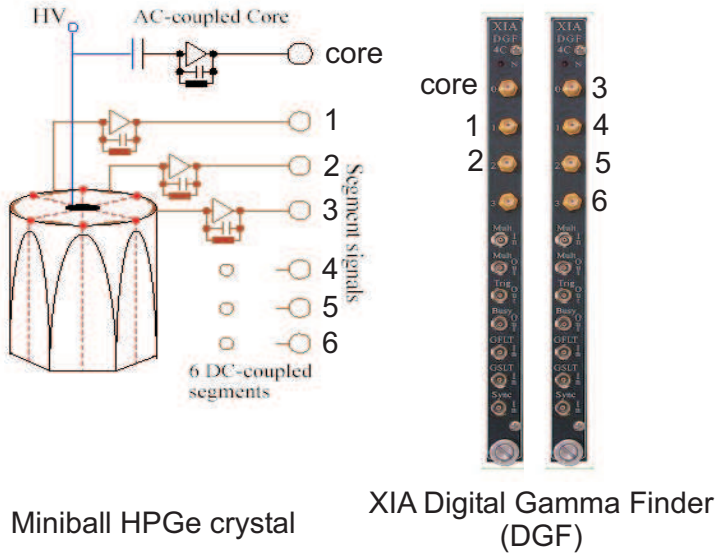

Figure 3.13: *The HPGe crystal and its segmentation. 24 of these crystals are mounted in groups of 3 on 8 clusters. The core and the 6 accompanying segments are read by 2 XIA DGF modules.*

Photopeak efficiency and calibration

The photo-peak efficiency for the full MINIBALL array was determined with a ^{152}Eu ($T_{1/2}$=13.537(6) y) source positioned inside the target chamber on the central target position. In table 3.4 the highest intensity lines are given, together with their branching ratio. The absolute efficiency was determined by gating on the 744 keV gamma line which is part of a gamma cascade together with the line at 345 keV in the β-decay of ^{152}Eu. The absolute efficiency is then the number of counts in the gated 345 keV line over the number of counts in the singles 744 keV line. The absolute efficiency curve, when the clusters are operated in add-back mode, is reproduced by a GEANT4 simulation of the full MINIBALL Ge array [11]. The resulting experimental and simulated ^{152}Eu spectra are shown in Fig. 3.14 together with the absolute efficiency for each calibration point. It should be pointed out that the main analysis in this work relies on a relative comparison of two gamma energies in the interval ∼400-1200 keV, so the absolute determination of photopeak efficiencies is of minor importance.
The absolute efficiencies, with and without add-back, were fitted with a function consisting of a sum over logarithms :

$$ln(\epsilon_\gamma) = \sum_{i=0}^{4} A_i (ln(E_{keV}))^i, \tag{3.3}$$

with A_0=-31.01, A_1=19.61, A_2=-4.73, A_3=0.49, A_4=-0.02. The accuracy of the fit was tested by comparing the simulated and experimental "add-back factor", which is defined as the ratio of the absolute efficiency with add-back over the absolute efficiency without add-back : $\epsilon_\gamma^{withAB}/\epsilon_\gamma^{withoutAB}$ (AB=Add-Back). In Fig. 3.15 the solid line represents the ratio of the fitted efficiency curves (eq. 3.3). The experimental points

[11] GEANT4 code provided by the Heidelberg group [Boi05]

in Fig. 3.15 originate from the ^{152}Eu calibration (eight points) and the experimental yields from the Coulomb excitation measurement. The simulated add-back factor is higher then the observed add-back factor, which might originate from increased low energy background (up to ∼300 keV). Though, the overall trend in the add-back factor is accurately reproduced by the simulation.

$E_\gamma[keV]$	I_γ [%]
121.7817(3)	28.58(6)
244.6975(8)	7.583(19)
344.2785(12)	**26.5(4)**
778.9040(18)	**12.942(19)**
964.079(18)	14.605(21)
1085.869(24)	10.207(21)
1112.074(4)	13.644(21)
1408.006(3)	21.005(24)

Table 3.4: *γ-decay lines from the β-decay of ^{152}Eu, only the used energies and γ-intensities are listed. In bold, the cascade γ's used to normalize the experimental relative efficiencies to absolute efficiencies. Values taken from [Lun06].*

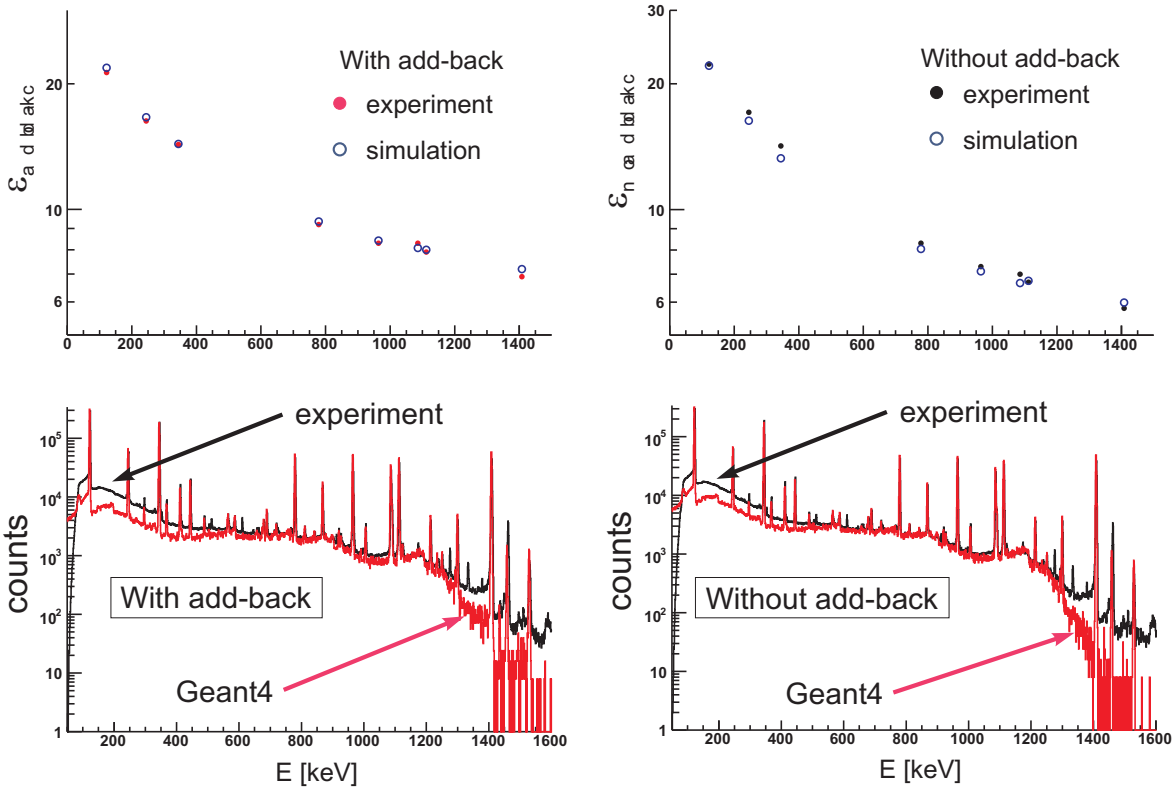

Figure 3.14: *Top : Experimental and simulated photopeak efficiency for a ^{152}Eu source, with and without cluster add-back. Bottom : Simulated (red) and experimental (black) ^{152}Eu spectrum, with and without cluster add-back.*

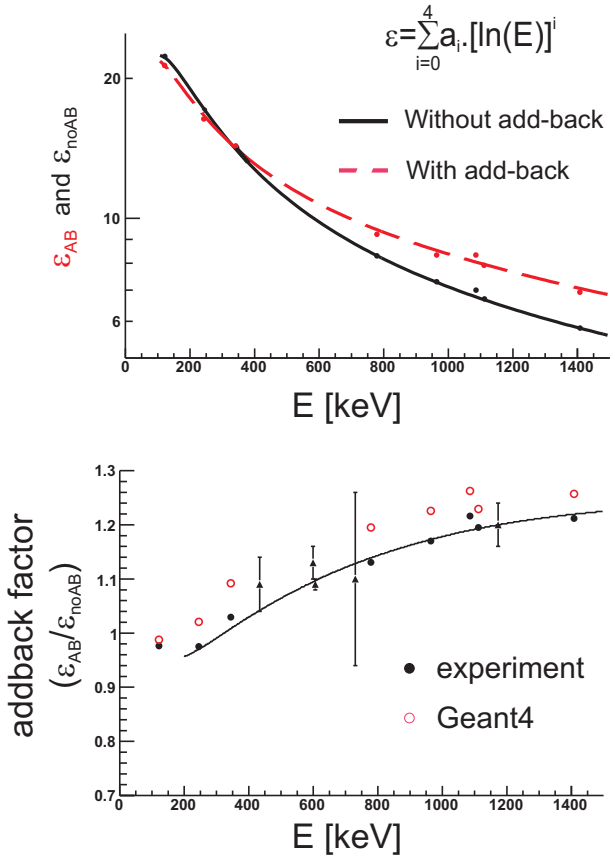

Figure 3.15: *Top : Fit of photopeak efficiencies for a ^{152}Eu to experimental points, with and without cluster add-back. Bottom : The add-back factor $\epsilon_{withadd-back}/\epsilon_{withouadd-back}$, ratio of the fitted functions from Fig. 3.14 (solid black line) and ratio's of the experimental points in Fig. 3.14. The points with large error bars are experimental yields from the Coulomb excitation spectrum.*

3.4.2 Particle Detector

Introduction

Inside the target chamber, a double sided silicon strip detector is mounted, 30.5 mm after the secondary target. This segmented Si detector [Ost02] consists of 4 identical and independent quadrants. The 4 segmented Si detectors have a Si wafer thickness between 476 μm and 481 μm. Each quadrant consists of 16 annular strips (θ - front plane) and 24 sector strips (ϕ - back plane). The front side annular strips have a width of 1.9 mm and a pitch of 2 mm, the sector strips have a 3.4° pitch. In Fig. 3.16 a schematic front view of the CD detector is shown, together with a picture of one quadrant. To reduce the high instantaneous particle flux in the center strips of the CD, a plug was inserted in the central hole. The plug limits possible radiation damage to the inner strips of the CD detector during the high intensity A=74,76 runs. It completely shields the inner three strips, while in the analysis the four inner strips were left out because the 4th strips was partly shielded. The loss in cross section when shielding strips 0-i (i=0...15) is plotted in Fig. 3.17 for the A=74 experiment, where the ratio of the detected integrated Rutherford(Coulomb excitation) cross section for the shielded CD over the full CD range is plotted. Shielding strips 0-3 reduces the Rutherford cross section to ∼22%, while the Coulomb excitation cross section is only reduced to ∼68%. This shielding thus reduces considerably the huge elastic scattered particle flux in the CD, while the Coulomb excitation yield is only partly reduced.

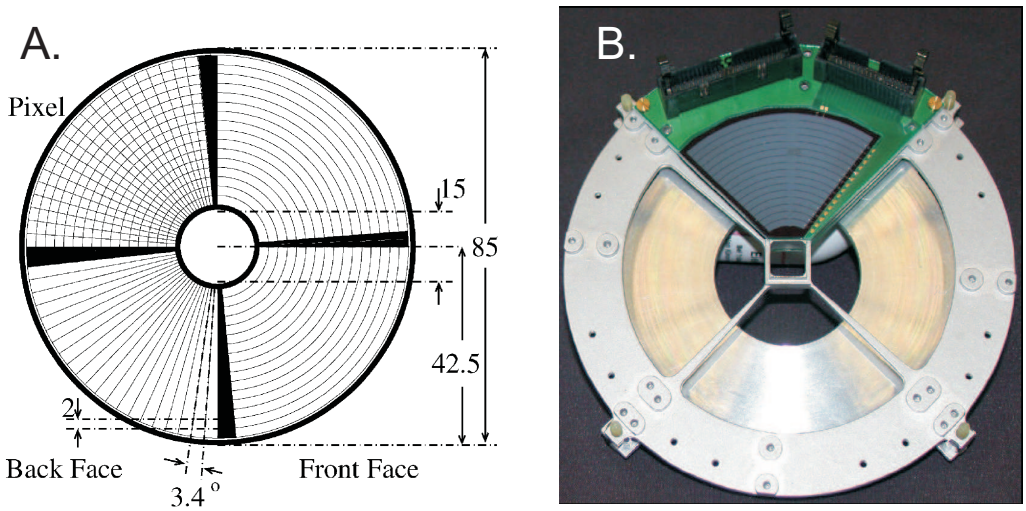

Figure 3.16: *The Particle Detector : Left = schematic drawing of the CD (taken from [Ost02]) - Right = picture of 1 quadrant of the CD with the area indicated used in the experiment.*

Calibration

The annular strips were calibrated with a triple alpha source, consisting of ^{239}Pu, ^{241}Am and ^{244}Cm with alpha energies of (resp.) 5.156 MeV, 5.486 MeV and 5.805 MeV. The raw and calibrated spectra are shown in Fig. 3.18 for the 4th inner strip in 1 quadrant, in Fig. 3.18A,C for the alpha calibration runs and in Fig. 3.18B,D for the ^{76}Zn on ^{120}Sn target at 2.83 MeV/u. In the spectrum the two lower energy peaks

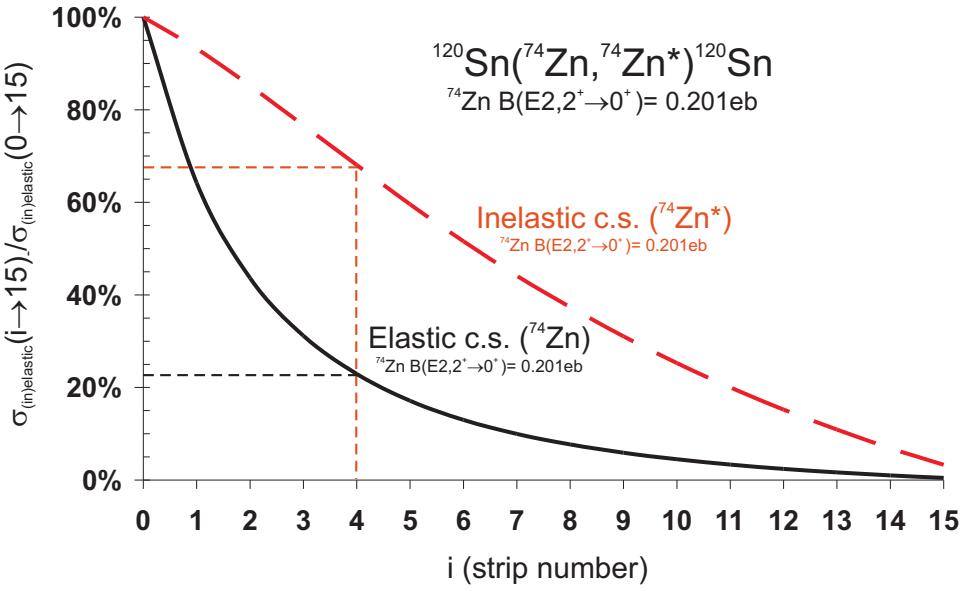

Figure 3.17: *Reduction of the detected cross section (c.s.) if a plug shields strips 0 to i (i=0...15).*

correspond to contaminating beam particles. These can be identified by their kinematics and the limit put on their mass to fit the A/q setting (=3.8 in 2004). The most probable candidates are then ^{22}Ne and ^{40}Ar (see tab.3.2) as contaminating particles. The extrapolation from ∼5-6 MeV, where the alpha calibration is performed, to higher energies assumes perfect linearity of the CD system and ADC response. The simulated energy position of the ^{76}Zn and ^{22}Ne peaks (dashed line in Fig. 3.18 D) differ 5-10 MeV from the (alpha-)calibrated CD energy peaks (black line in Fig. 3.18D). In order to improve the calibration, the simulated energy position for ^{76}Zn and ^{22}Ne were included in the calibration. The position of the small ^{40}Ar peak, which is not used as a calibration point, fits the improved calibration with triple alpha, ^{22}Ne and ^{76}Zn (small peak ∼80MeV in Fig. 3.18D).
The energy information of the CD detector is used to identify the scattered particle in an energy versus scattering angle plot (for example Fig. 3.20 for A=76) and to determine the velocity of the in-flight decaying nucleus for use in the Doppler correction formula (see eq. 4.26). In Fig. 3.19, the impact of the detected energy on the resolution of the Doppler corrected photopeak for the ^{76}Zn Doppler broadened Coulomb excitation peak is illustrated. ΔE=0 corresponds to the rough calibration with the triple alpha source, while higher and lower ΔE values correspond to energy offsets added to the detected energy. The minimum FWHM of the Doppler corrected photopeak is obtained when ∼5-10 MeV is added to the detected energy, in correspondence with the more accurate calibration discussed above.
If there is no need for identification or Doppler correction the energy information is ignored. The final result in this work relies on the timing information rather then on the detected energy (see Chapter6).

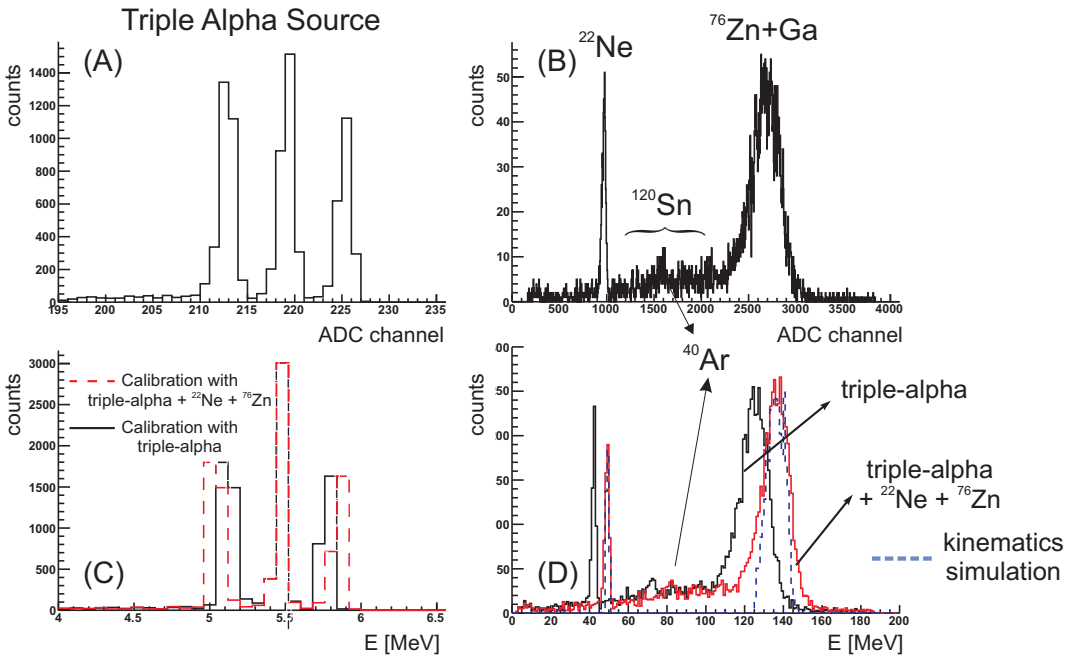

Figure 3.18: *Calibration of the CD detector with a triple α source, with energies at 5-6MeV, compared to a calibration where a higher energy point is included.*

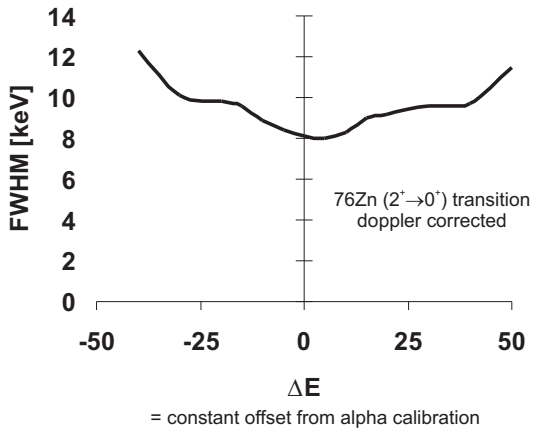

Figure 3.19: *FWHM of the Doppler corrected ^{76}Zn Coulomb excitation peak, as a function of an offset on the detected energy of the scattered ^{76}Zn particle.*

Electronics

As was already mentioned in par. 3.4.1, the particle branch is not fully digital read out. In order to join particle and γ information, the timing of the CD energy signals was performed with DGF modules. The energy signal from the CD was sent to analogue peak sensing CAEN ADC's. The four ADC's operate independently from each other [12]. With every accepted particle (see par. 3.5.2), which is send to the CAEN ADC, a block pulse is send to an input channel of a DGF module. In this way the time of the particle is stored as a digital "timestamp" in a dedicated DGF module. The time

[12]Before 2004 this was not the case : the four quadrants were read out at the same time. The decoupling of the four quadrants increases the detection efficiency of the CD, because the detection of a particle 1 quadrant does not "blind" the other quadrant !

correlation between γ's and particles is in the offline analysis limited to a comparison of digital time stamps.

3.5 Data Acquisition

3.5.1 Synchronization with REX-ISOLDE

Each timing signal related to (REX-)ISOLDE, discussed in par. 3.3.5, is digitally time stamped in a dedicated DGF module. The EBIS time stamp is used to synchronize the data acquisition with the EBIS extraction and the linac operation. With every EBIS extraction, an *"In Beam"* window is opened of ∼780 μsec during which data is taken. Only during ∼150 μsec (the EBIS pulse length) particles arrive at the MINIBALL setup. After this "In Beam" measuring window, all the modules are read out by the Marabou data acquisition system [Lut06]. Reading and transferring the data stream takes ∼3-5 μsec. "Scalers" are read at a rate of 1 Hz, which increases the readout time considerably (up to 10 μsec). These scalers give an overall counting rate per second of the particle and γ detection systems, this information will be used in Chapter6. If there is sufficient time between the "In Beam" readout and the next EBIS pulse an "Off Beam" window is opened, during which the γ background in the MINIBALL area is measured. During the "Off Beam" window no beam is present, so the CAEN ADCs contain no data. It was observed that an important amount of bremstrahlung from the 7- and 9-gap resonators is present in the "In Beam" spectrum. This important low-energy background is not observed in the "Off Beam" window, when the resonators are off. This will be illustrated in Fig. 4.10,4.11 and 4.12 in Chapter 4.
The use of the proton pulse related T1 signal (see 3.3.5) is illustrated in Fig. 3.20 for the A=76 run of 2004 (the experiments from 2005 are similar). The ISOLDE beam gate is opened for one second, ∼7 msec after the proton impact. As was illustrated in Fig. 3.3, most of the Zn isotopes are released from the target after this period. The one second beam gate will be referred to as 'RIB ON', because the radioactive Zn and Ga isotopes are injected into the Penning Trap. Outside this gate, only rest-gas from the Penning Trap and EBIS is detected and will be referred to as 'RIB off'. The rest-gas beam is only a small fraction of the total beam intensity during the RIB on periods (see 4.2). From a simulation of the elastic scattering in the CD, a mass determination can be done for this rest-gas beam. The natural abundant ^{22}Ne is identified, together with a negligible amount of ^{40}Ar. During the A=74 and A=78 runs no rest-gas contaminants were present, due to a different A/q setting of the mass separator after the EBIS.

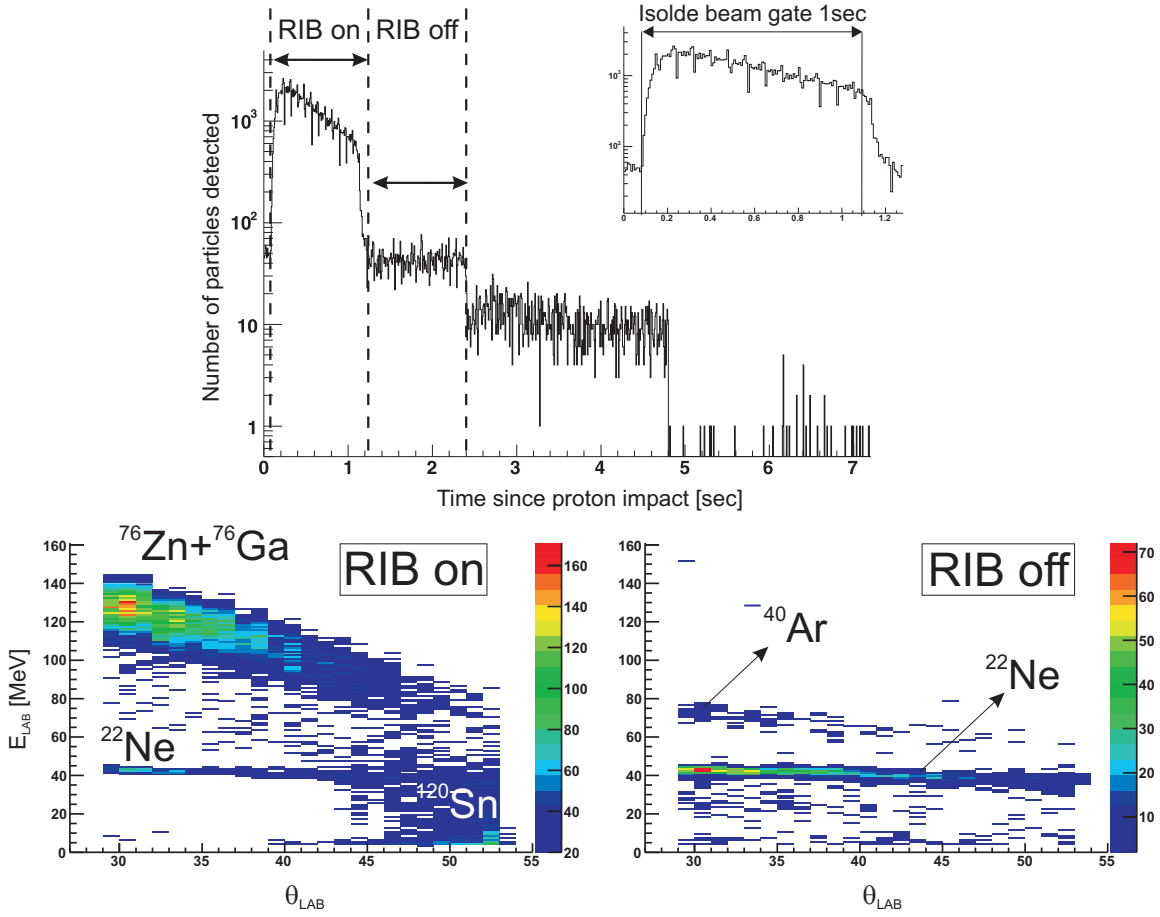

Figure 3.20: *The A=76 timing properties illustrated by the particle rate as a function of time elapsed since the proton impact. The 2 dimensional energy versus scattering angle spectra identify the beam content during periods when the ISOLDE beam gate is opened (RIB ON) and closed (RIB OFF). Rest-gas related beam content can easily be identified.*

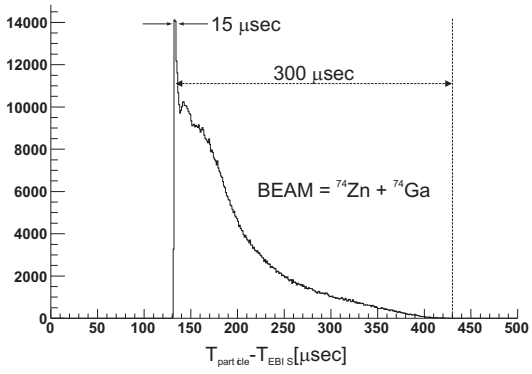

Figure 3.21: *Release profile from the EBIS for A=74 beam in 2004.*

3.5.2 The coincidence condition

The beam pulse from the EBIS lasts for about 300 μsec (see Fig. 3.21 for A=74), with most of the particles arriving in the first 150 μsec. The sharp peak at $T_{particle}$-T_{EBIS}=130 μsec lasts for 15 μsec (Fig. 3.21), corresponds to the constant dead time of the particle detection ADC. Particles arriving within 15 μsec after the first detected particle are not "seen" by the ADC. The dead time induced by the detection of the (overwhelming) elastic scattered particles (Rutherford cross section) should be limited since the nuclear information is contained in the inelastic cross section. Therefore, a particle-γ coincidence was constructed on the detector level, which limits the detection of elastically scattered particles.
The relevant signals are shown in Fig. 3.22. The signals from the 16 front and 12 back strips [13] of each quadrant are send to "Edinburgh/RAL108" pre-amplifiers, and from there on send to "Edingburgh/RAL109" shaping amplifiers where both a constant fraction timing (CFT) and gaussian-like shaping is performed to produce the fast timing and energy signals ((1 and 2) in Fig. 3.22). The 16 timing signals from the front strips are OR'ed and the resulting quadrant timing signal((2) in Fig. 3.22) is send to a delay unit where it is delayed by ∼500 ns ((4) in Fig. 3.22). The back strip timing signals (12) are send to TDC channels. The delay of the quadrant (front strips) timing signal is necessary because of the slower fast timing signals generated by the DGF modules (∼200 ns, leading edge timing on the digital pre-amp pulse), compared to the RAL CFT. A logical OR of all fast timing signals from the cluster cores (24 time signals[14],(6) in Fig. 3.22) opens a coincidence gate of 500 ns ((7) in Fig. 3.22). A coincidence trigger for each quadrant is generated if the delayed particle trigger falls within the 500 ns gate. If a coincidence trigger is generated, the particle is detected without any further condition and an ADC gate ((3) in Fig. 3.22) is generated to detect the energy signal of the particle ((1) in Fig. 3.22). If there was no coincidence trigger, 1 out of 64 of these events are recorded as well. It is important to note that in the current MINIBALL setup γ ray detection is not conditioned ! Only the particle detection is conditioned by the coincidence with a γ. The conditioned particle detection will be referred to as "downscaling", while the γ data can be referred to as "singles" data.

[13] In fact, 24 back strip signals were send to the electronics, the joining of 2 neighboring backstrips was done at the level of the RAL-amplifiers. A better solution would be to join the 2 signals at the detector level.

[14] The fast timing signals referred to at this point are in fact the "MULT OUT" signals, available on the front panel of a DGF module, see [XIA]. An additional shaping of this output signal is required to improve the timing properties of the γfast timing signal, this is done with a dedicated NIM module designed by the Cologne group.

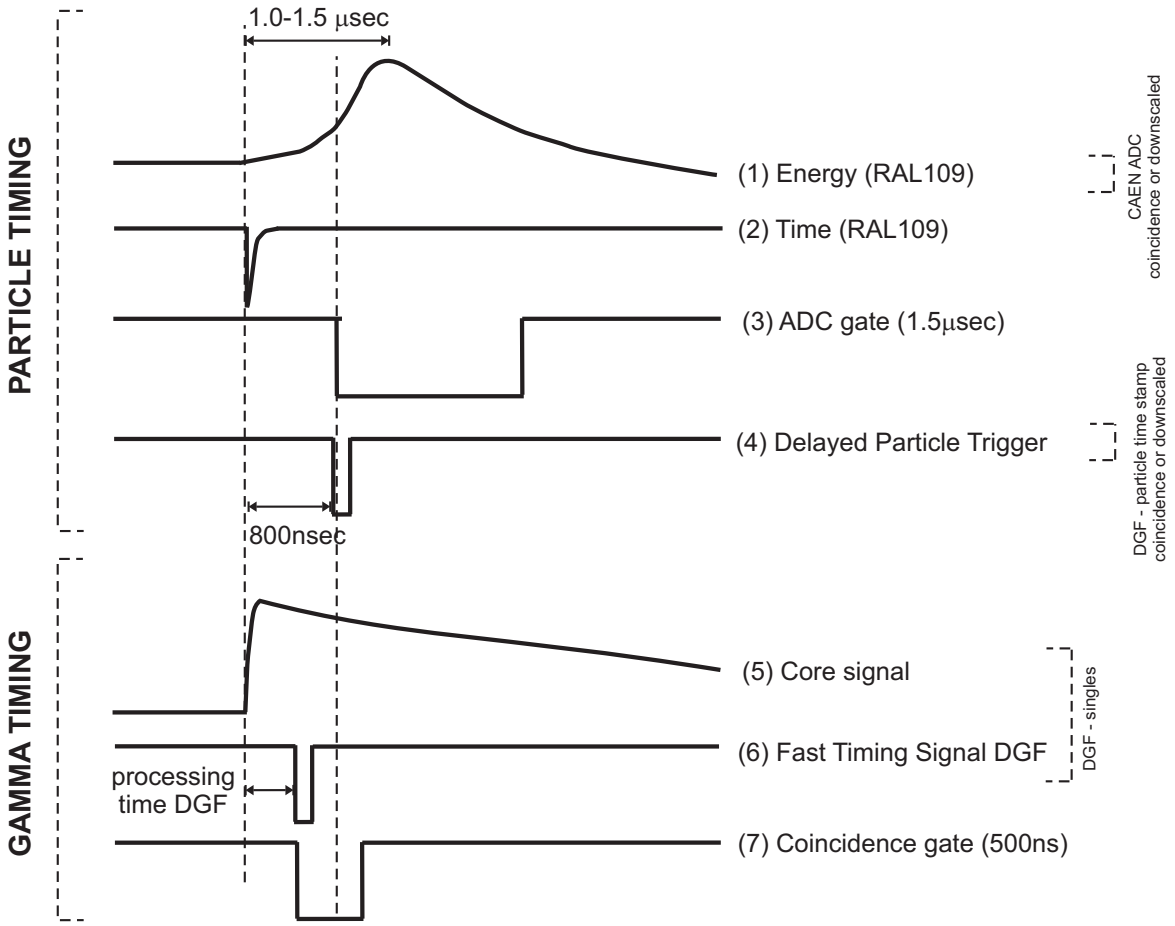

Figure 3.22: *The coincidence timing - for details : see text.*

3.5.3 Event structure

The raw data is written to an array of hard disks in the 'med' format [Lut05]. The format is based on the GSI MBS (sub)event structure. A C++ code to translate the raw data in the 'med'-file to a user friendly format containing energy, time and position information of particles and gamma's was developed by the MPI, Heidelberg. The further sorting of the raw data can be divided into 3 steps :
STEP 1 : calibration of ADC channels and threshold settings + matching of time stamps in TDGF's with particles in CAEN ADC's. If there is a mismatch this ADC is ignored. All detected gamma's in the DGF core channels are calibrated and the segment number with the highest detected energy is correlated with it.
STEP 2 : All detected particles with their associated timestamp are written to separate entries of a ROOT tree. The gamma's in a window of 4 μsec around the particle timestamp are correlated to this particle. This ROOT tree (referred to as 'rt' in the following) is most suitable to analyze particle spectra.
STEP 3 : During STEP 2 it is possible that the same gamma is correlated to two particles. This can be either by random coincidences or by the 'real' kinematical case of target and projectile detection in opposite quadrants. In this step of the analysis, the ROOT tree created during step 2 is taken as input. First an add-back routine is imposed on the gamma's correlated in the 4 μsec window around a particle. Then, these add-back gamma's are written to individual entries of a separate ROOT tree and

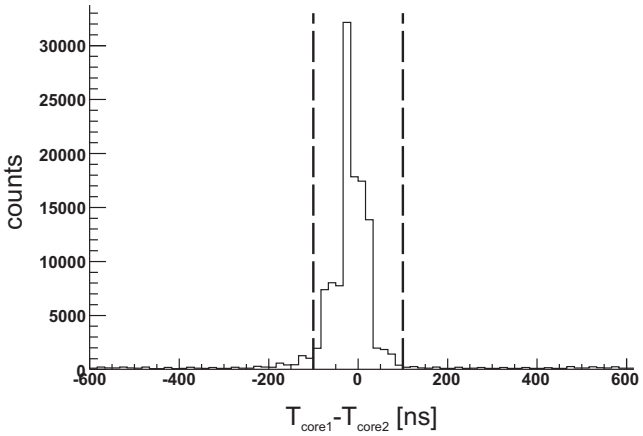

Figure 3.23: *Time difference spectrum between 2 γ's in neighboring cores.*

particles are correlated to them, with a flag indicating whether they came in prompt or random coincidence with the gamma. In this root tree, one gamma is correlated with several particles. The add-back routine sums up the energy in two neighboring core channels (two cores on the same cluster) when both of them detected a gamma in prompt coincidence. The time difference spectrum for two such gamma's arriving in two neighboring cores is shown in Fig. 3.23. The 'prompt' time condition to reconstruct an add-back event (sum of the two energies) ranges from -100 ns to +100 ns. The segment number of the highest energy gamma is attached to the add-back gamma.

Chapter 4

The Coulomb Excitation Experiment

4.1 Kinematics considerations

The relation between the scattering angle in the laboratory frame (LAB) and the scattering angle in the center of mass system (CM) is given by

$$tan(\theta_{LAB}) = \frac{sin(\vartheta_{CM})}{cos(\vartheta_{CM}) + \tau} \tag{4.1}$$

where ϑ_{CM},θ_{LAB} is the scattering angle of the projectile in the CM, LAB system respectively and τ=A_p/A_t with A_p the mass of the projectile (beam) and A_t the mass of the ejectile (target). The kinematics for A=74 (τ=0.617) is given in Fig. 4.1A and B. The solid lines correspond to the "pure" kinematics case, without energy loss through the target. The scatter plot is a simulation of the kinematics taking into account energy loss through the target material, a random interaction depth in the target and a beam spot of 4 mm FWHM. The simulation was done with an isotropic distribution of CM angles and electronic and nuclear energy losses are taken from SRIM2003 [SRI]. Over a certain CM range (A=74 : ϑ_{CM}=83°-106°), both the target-like as the beam-like particles are detected in the CD detector. In Fig. 4.2 the simulated (top) and detected (bottom) energy versus lab angle is plotted. The separation between the two CM regions is not always clear in the experimental spectrum. In Chapter 5 the three CM ranges defined in Fig. 4.1 will be used to check the consistency of the B(E2) value. In Fig. 4.1C the calculated cross section is shown for the $0_1^+ \rightarrow 2_1^+$ excitation in ^{74}Zn. The differential cross section is calculated with the Coulomb excitation code "CLX" (see par. 4.6.2) and with a B(E2,$2_1^+ \rightarrow 0_1^+$) = 0.201 eb. No higher spin states nor a quadrupole moment were assumed in this calculation.

BEAM	TARGET	ENERGY [MeV/u]	ϑ_{CM1}	ϑ_{CM2}	ϑ_{CM3}	ϑ_{CM4}
^{74}Zn	^{120}Sn	2.87	46.6	73.1	82.9	121.7
^{76}Zn	^{120}Sn	2.83	47.1	73.1	83.9	121.7
^{78}Zn	^{108}Pd	2.87	49.7	73.2	88.8	121.7

Table 4.1: *Experimental details for the ^{74,76,78}Zn experiments : CM angles covered by the particle detector, the beam energy and the target.*

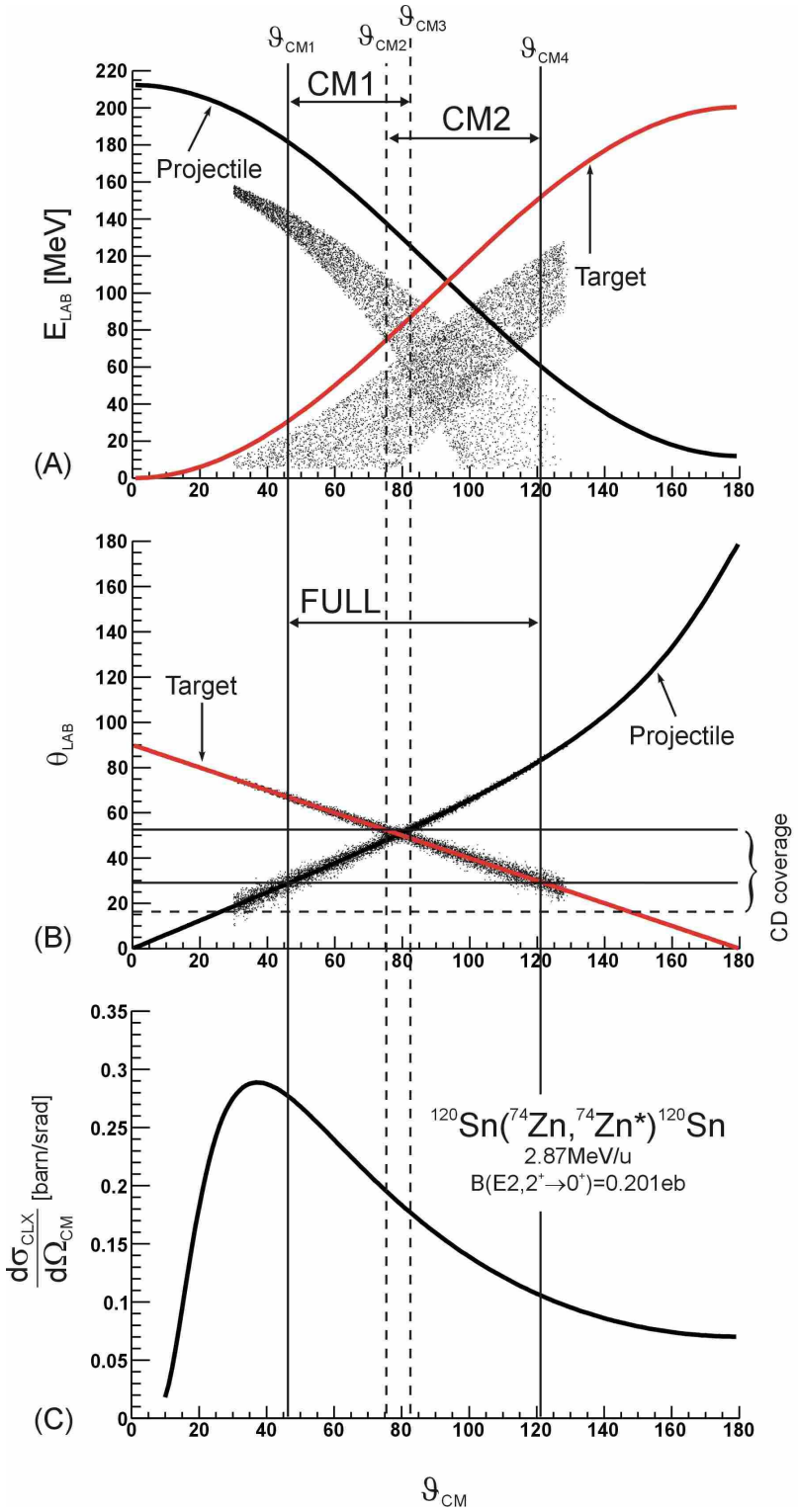

Figure 4.1: *A./B. Kinematics relations (energy/lab angle versus CM angle) between projectile (beam,^{74}Zn) and ejectile (target,^{120}Sn). The scatter plot is a simulation, taking into account a beam spot of 4 mm FWHM and energy loss through the target. C. Differential Coulomb Excitation cross section of ^{74}Zn ($0^+ \rightarrow 2^+$ excitation). The angular range of the CD detector, used in the analysis is indicated by the solid lines. The region where both target and projectile are detected in the CD is indicated by the dashed lines.*

The kinematics for ^{76}Zn on ^{120}Sn and ^{78}Zn on ^{108}Pd is completely analogue to the above discussed A=74 case, the only difference being the incident beam energy and the angular limits of the CM ranges (CM1,CM2 and FULL in Fig. 4.1A and B). In table 4.1 the limiting angles are summarized for the three cases. These values depend on the exact CD-target distance, which was determined to be 30.5 mm.

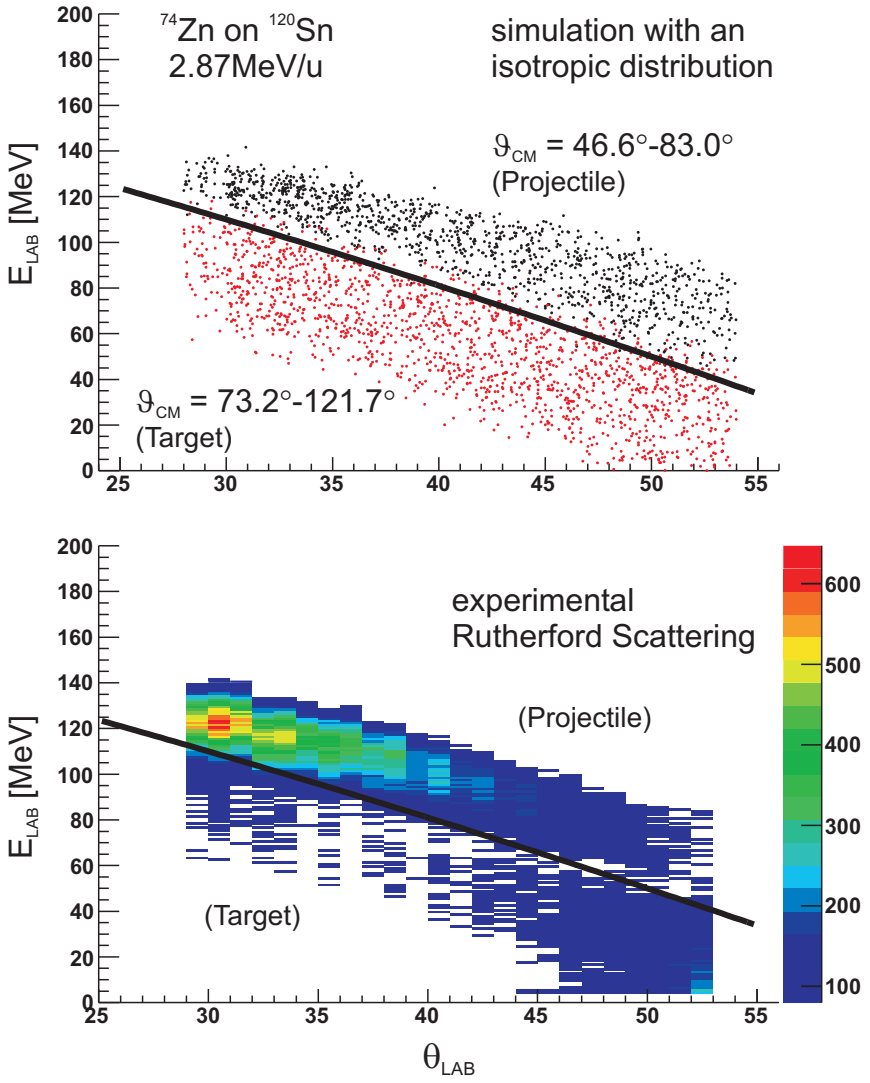

Figure 4.2: *Bottom : experimental energy versus scattering angle plot for the A=74 experiment. The black line indicates the separation between CM1 and CM2. Top : simulated energy versus scattering angle plot of projectile (Zn) and ejectile (target). In the simulation, a beam spot with FWHM of 4 mm was assumed. The separation between target and projectile is possible. Though, small overlap is observed for higher laboratory angles and a higher then expected intensity at the lower laboratory angles in the CM2 region indicates contributions from CM1 particles in the CM2 region.*

4.2 Beam Contamination

The normalization of the discussed Coulomb excitation experiments is given by the amount of target excitation (see eq. 2.39). Since the contaminating particles excite the target as well, it is of prime importance to know the ratio of Zn to Ga (and Trap/EBIS-) particles in the beam. In the following paragraphs an overview will be given how the 'Zn-to-total' ratio (R) can be extracted from the experimental data.
So far it was assumed that the only isobaric contaminant in the A=74,76,78 beams is Ga, as was discussed in the section on the RIB production (3.2). An explicit identification of the beam content was performed before the A=78 run (settings for A=78) by sending the post-accelerated beam into an ionization chamber, where a Z-dependent ΔE(gas)-E(Si) measurement provides identification. With protons send directly onto the primary ISOLDE target the contaminants are Ga and Rb (see Fig. 4.3A). Sending the protons on the "convertor" (see par. 3.2.1), the isotopes are produced by low energy neutron induced fisson and the ^{78}Rb contamination is drastically reduced (see Fig. 4.3B). The Rb contamination in the A=74,76 beams (proton induced fission) is expected to be much lower, because the production cross section for ^{74,76}Rb is much lower (see Fig. 3.2). Other possible isobaric contamination can be traced by their char-

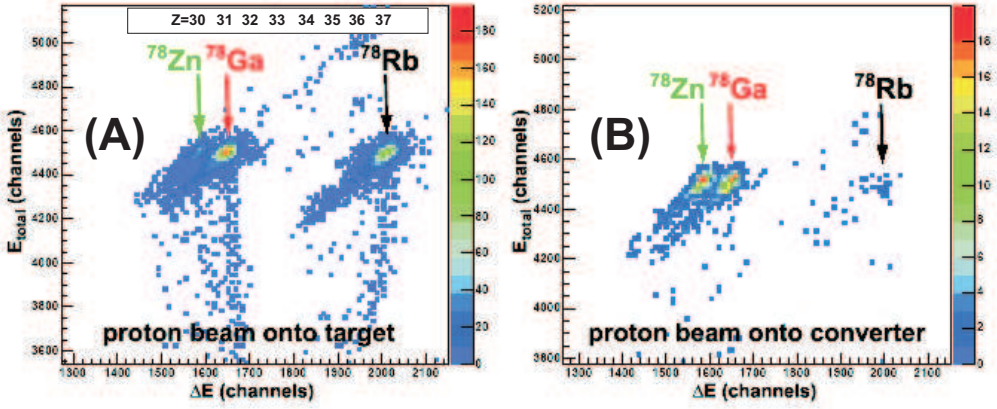

Figure 4.3: *Δ-E spectrum obtained during the preparation of the A=78 experiment. The purest RIB was obtained with the usage of the proton to neutron convertor (neutron induced low energy fission instead of high energy proton induced fission).*

acteristic radioactivity (unstable contaminants) and by observed Coulomb excitation of these nuclei (both stable and unstable contaminants). Traces of Coulomb excitation of isobaric even-even nuclei should be observed in the laser off spectra if these isotopes are present in the RIB. For A=74,76 the Doppler corrected Coulomb excitation spectra are shown in Fig. 4.4. The 2_1^+ energies are indicated for neighboring even-even isobars. No evidence for Doppler corrected $0_1^+ \rightarrow 2_1^+$ Coulomb excitation yield from these even-even isobars is observed.
Another source of contamination is the rest-gas from the (REX-)Trap. It will be shown that corrections to the target yield are particularly small for these light contaminants.
Eq. 2.39 must be adapted to account for the target excitation by Ga and possible

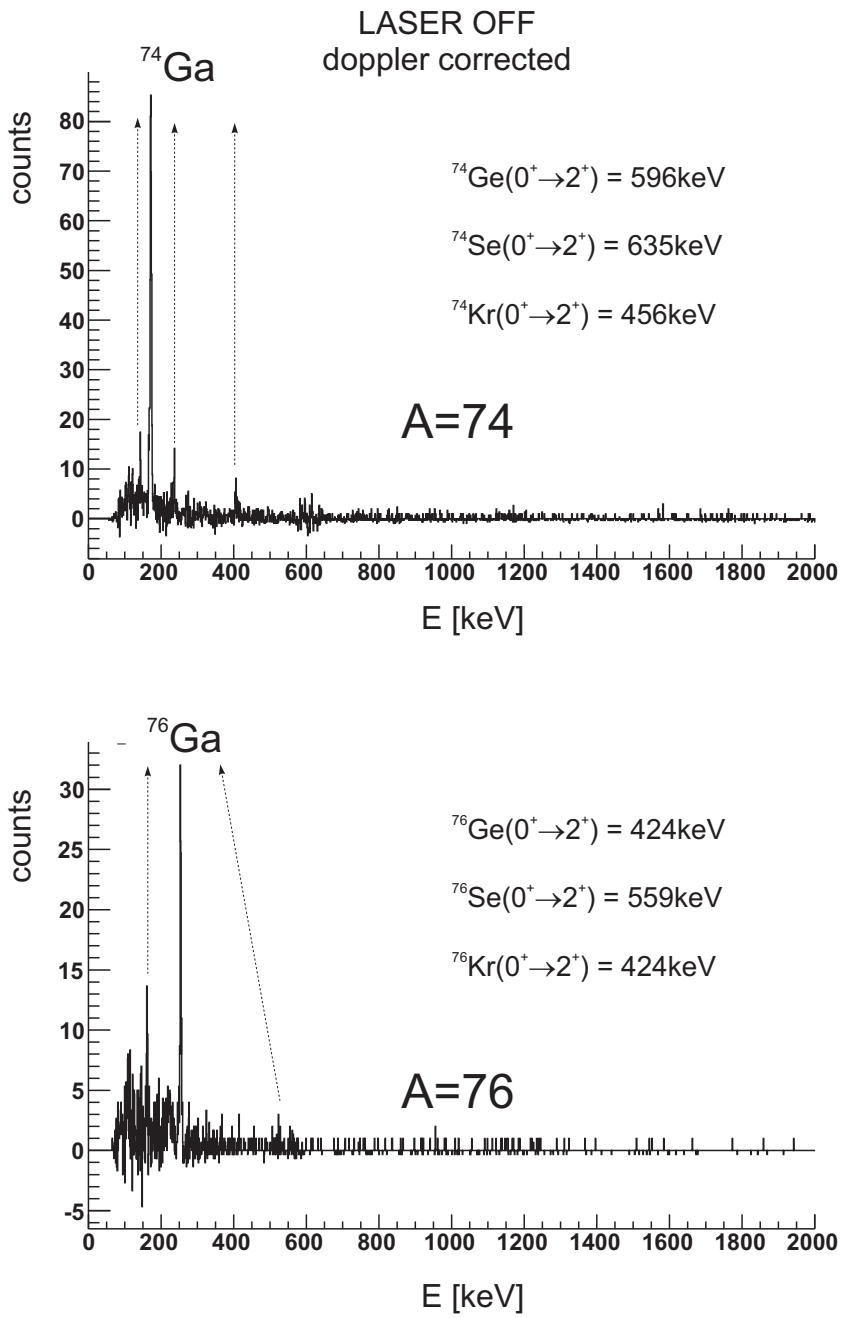

Figure 4.4: *Prompt coincident γ spectrum (coulex spectrum) during laser off periods for both A=74 and A=76. No sign for Coulomb excitation to the first excited 2^+ state is observed for possible even-even isobaric contaminants.*

other contaminants (labelled X).

$$
\begin{aligned}
N^{Target,total}_{\gamma,2^+\to 0^+} &= N^{Target,Zn}_{\gamma,2^+\to 0^+} + N^{Target,Ga}_{\gamma,2^+\to 0^+} + N^{Target,X}_{\gamma,2^+\to 0^+} \\
&= \epsilon_{MB,Target} \cdot (\sigma^{Zn}_{E2,Target} I_{Zn} + \sigma^{Ga}_{E2,Target} I_{Ga} + \sigma^{X}_{E2,Target} I_X) \cdot \tfrac{\rho d N_A}{A} \\
&= \epsilon_{MB,Target} \cdot \sigma^{Zn}_{E2,Target} I_{Zn} \cdot (1 + r \cdot \tfrac{\sigma^{Ga}_{Target}}{\sigma^{Zn}_{Target}} + r_X \cdot \tfrac{\sigma^{X}_{Target}}{\sigma^{Zn}_{Target}})) \\
&= N^{Target,Zn}_{\gamma,2^+\to 0^+} \cdot (1 + r \cdot \tfrac{\sigma^{Ga}_{Target}}{\sigma^{Zn}_{Target}} + r_X \cdot \tfrac{\sigma^{X}_{Target}}{\sigma^{Zn}_{Target}}))
\end{aligned}
$$

$$N^{Target,Zn}_{\gamma,2^+\rightarrow 0^+} = \frac{N^{Target,total}_{\gamma,2^+\rightarrow 0^+}}{(1+r\cdot\frac{\sigma^{Ga}_{Target}}{\sigma^{Zn}_{Target}}+r_X\cdot\frac{\sigma^{X}_{Target}}{\sigma^{Zn}_{Target}}))} \tag{4.2}$$

where r=I_{Ga}/I_{Zn} and r_X=I_X/I_{Zn}. The following paragraphs will describe how the ratios r and r_X are deduced from the experiment.

4.2.1 Laser On/Off runs

The laser ionization offers a unique tool to disentangle the Zn and Ga contribution in the final RIB. Recalling that Ga is surface ionized in the RILIS while Zn is selectively laser ionized, the Zn beam can be cut off by switching off the laser light. Two modes of data taking were used during the experiment : laser ON (constant laser ionization) and laser ON/OFF (periodically laser ionization on and off). A good time base for the periodicity during the laser on/off runs is governed by the supercycle of the PS booster (14.4-21.6 sec). Averaged over a typical measuring time in this laser on/off mode (0.5-1 hour), the laser on and laser off time periods are roughly equal and the difference in particle scattering is directly linked to the R ratio (see eq. 4.5, below). As a rule of thumb, a laser on/off run was performed during 1 hour in between two laser on runs (typically 2 hours for each laser on run). Fluctuations in laser power and ionization efficiency (and, accordingly, the Zn content) over time are thus taken into account by measuring the R ratio during well separated time intervals. The total measuring time in laser on/off mode is summarized in table 5.19 together with the total measuring time "laser on" for the three investigated Zn isotopes.
In this paragraph the following conventions will be used for beam intensities during laser on/off runs :
Zn :

$$\begin{aligned} I^{tot}_{Zn} = & \int_{t_{start}}^{t_{stop}} \left(i^{ON}_{Zn} + i^{OFF}_{Zn}\right) dt \\ = & \int_{t_{start}}^{t_{stop}} i^{ON}_{Zn} dt \\ = & < i^{ON}_{Zn} > \cdot \frac{(t_{stop}-t_{start})}{2} \\ = & I^{ON}_{Zn} \end{aligned} \tag{4.3}$$

where i^{ON}_{Zn} is the varying incoming Zn intensity when the laser is on and i^{OFF}_{Zn} is obviously 0.
Ga :

$$\begin{aligned} I^{tot}_{Ga} = & \int_{t_{start}}^{t_{stop}} \left(i^{ON}_{Ga} + i^{OFF}_{Ga}\right) dt \\ = & \int_{t_{start}}^{t_{stop}} i^{ON}_{Ga} dt + \int_{t_{start}}^{t_{stop}} i^{OFF}_{Ga} dt \\ = & < i^{ON}_{Ga} > \cdot \frac{(t_{stop}-t_{start})}{2} + < i^{OFF}_{Ga} > \cdot \frac{(t_{stop}-t_{start})}{2} \\ = & I^{ON}_{Ga} + I^{OFF}_{Ga} \\ = & 2 \cdot I^{ON}_{Ga} \end{aligned} \tag{4.4}$$

where i^{ON}_{Ga}(i^{OFF}_{Ga}) is the in time fluctuating incoming Ga intensity when the laser is ON(OFF). Equal time intervals ((t_{stop}-t_{start})/2) are assumed for laser ON and laser OFF periods.
Additional definitions are as follows :

$$R = \frac{I^{ON}_{Zn}}{I^{ON}_{Total}} \tag{4.5}$$

$$r = \frac{I^{ON}_{Ga}}{I^{ON}_{Zn}} \tag{4.6}$$

The relation between R and r is given by :

$$R = \frac{1}{1+r} \tag{4.7}$$

$$r = \frac{1-R}{R}. \tag{4.8}$$

First, the Zn-to-total ratio R will be determined for the laser on/off runs during the A=74, 76 and 78 experiments. For A=78 the ΔE-E measurement provided an additional tool to measure the R-value, prior to the actual experiment. Afterwards, extrapolation methods will extend the Zn-to-total ratio ("R") to the total laser on period, this ratio will be labelled R_{ON}.

"R"-value from Ionization Chamber

During the A=78 experiment, a ΔE-E detector was mounted on a second beamline after the REX-linac. The ΔE detector is a gas filled ionization chamber, the E detector is a Si detector. The gas detector is operated with P10 gas (90% Argon, 10% Methan). The identification of the beam particles depends on their atomic number Z. Since the differential energy loss is proportional to Z^2, the identification is based on the ΔE value. The Z resolution of the ΔE-E combination is governed by the gas pressure. The relation between the gas pressure and the average Z of the beam particles is given by an empirically formula, derived during the summer 2004 campaign :

$$P = \frac{12.764}{Z}[bar]. \tag{4.9}$$

From Fig. 4.3 the amount of Zn and Ga can be determined by gating on the respective particles. This detector setup was used in the beginning of the A=78 experiment to identify the RIB content with different primary target conditions (temperature dependence, neutron convertor, ...). The optimal setting for A=78, which yielded the purest RIB was obtained with a line temperature of ∼2000 °C (>1960 °C, see [Kos05]) and with the usage of the proton to neutron convertor.

"R"-value from scattered beam fraction

The R value can be determined from the scattered beam fraction in the particle detector. During laser on periods of the laser on/off runs :

$$N_{ON}^{sc} = (I_{Zn}^{ON} \cdot \sigma_{Zn}^{Rutherford} + I_{Ga}^{ON} \cdot \sigma_{Ga}^{Rutherford}) \cdot \frac{\rho d N_A}{A} \tag{4.10}$$

and during laser off periods :

$$N_{OFF}^{sc} = (I_{Ga}^{OFF} \cdot \sigma_{Ga}^{Rutherford}) \cdot \frac{\rho d N_A}{A} \tag{4.11}$$

where equal time intervals for laser on and off periods were supposed (based on the oscillating supercycle) : I_{Ga}^{ON}=I_{Ga}^{OFF}. Dividing eq. 4.10 by eq. 4.11 yields :

$$r = \frac{\sigma_{Zn}^{Rutherford}}{\sigma_{Ga}^{Rutherford}} \cdot \frac{1}{(N_{ON}^{sc}/N_{OFF}^{sc}) - 1} \tag{4.12}$$

where $\frac{\sigma_{Zn}^{Rutherford}}{\sigma_{Ga}^{Rutherford}} = (\frac{Z_{Zn}}{Z_{Ga}})^2$. In Fig. 4.5 the energy versus scattering angle spectra are shown for the three isotopes, for both laser on as laser off periods. The integration of

the number of particles in these spectra yields N^{sc}_{ON} and N^{sc}_{OFF}. The spectra in Fig. 4.5 are the sum of all laser On/Off runs on the same mass. In Fig. 4.6 the final R-value is shown for each mass (labelled by "run nr 10"), together with the R values obtained from the individual laser on/off runs. It is clear from Fig. 4.6 that the laser ionization fluctuates over time, especially during the A=76 run the ionization efficiency appeared to be unstable. The error on the final R-value is determined by the statistical error on the number of scattered particles in the two-dimensional spectra of Fig. 4.5.

"R"-value from target excitation

The R value can as well be extracted by the difference in target excitation during laser on and laser off periods. The amount of target excitation during laser off periods is due to excitation by Ga ($N_\gamma^{Target,OFF}$), while during laser on periods, the target is excited by both Zn and Ga ($N_\gamma^{Target,ON}$).

$$\frac{N_\gamma^{Target,ON}}{N_\gamma^{Target,OFF}} = \frac{I_{Zn}^{ON}\cdot\sigma_{Zn}^{Target} + I_{Ga}^{ON}\cdot\sigma_{Ga}^{Target}}{I_{Ga}^{OFF}\cdot\sigma_{Ga}^{Target}} \tag{4.13}$$

where again $I_{Ga}^{ON}=I_{Ga}^{OFF}=\frac{1}{2}I_{Ga}^{tot}$ and $\sigma_{Zn,Ga}^{Target}$ is the cross section for target excitation ($0^+ \rightarrow 2^+$) by either Zn or Ga. Eq. 4.13 can now be rewritten as :

$$R = \frac{N_\gamma^{Target,ON}/N_\gamma^{Target,OFF} - 1}{N_\gamma^{Target,ON}/N_\gamma^{Target,OFF} + \sigma_{Zn}^{Target}/\sigma_{Ga}^{Target} - 1}. \tag{4.14}$$

The error is in this case determined by the amount of target excitation. The statistics is rather limited for A=74,76 (target=^{120}Sn, $\sigma_{E2,Sn}^{^{74}Zn}$=148mb,$\sigma_{E2,Sn}^{^{74}Ga}$=131mb), while sufficient target excitation is present for A=78 (target=^{108}Pd, $\sigma_{E2,Pd}^{^{78}Zn}$=2.11b,$\sigma_{E2,Pd}^{^{78}Ga}$=2.13b). The results of this approach are summarized in table 4.2. In Fig. 4.7 the difference in target excitation is shown during laser on and laser off periods for A=78. This spectrum is the sum of the 9 individual laser on/off runs obtained during the A=78 experiment. The $0_1^+ \rightarrow 2_1^+$ excitation in ^{78}Zn is observed at 730 keV. The line at 434 keV is the $0_1^+ \rightarrow 2_1^+$ excitation in ^{108}Pd.

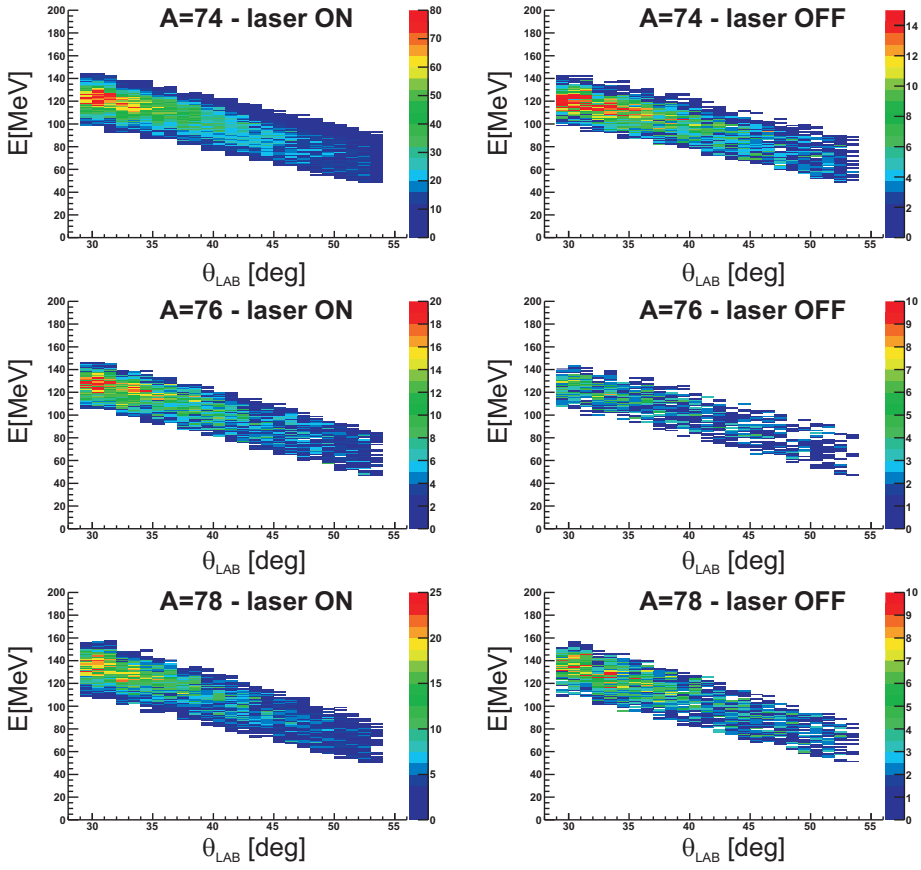

Figure 4.5: *Energy versus scattering angle spectra during laser on/off runs, for the three masses. A gate is applied in these figures on the kinematical region where Zn and Ga are detected.*

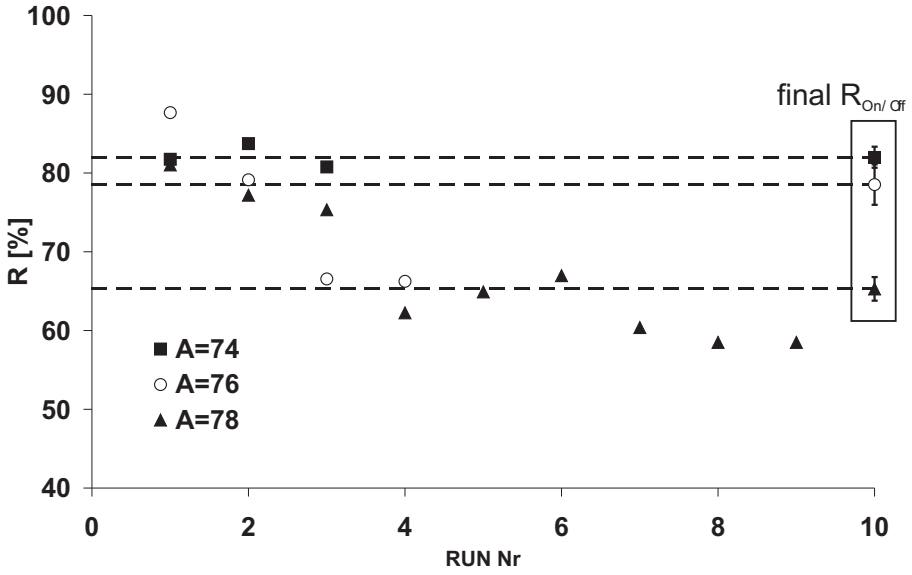

Figure 4.6: *Evolution of the R-value, obtained during individual laser on/off runs for the three masses (A=74 : 3 runs, A=76 : 4 runs, A=78 : 9 runs). Run number 10 indicates the sum of all laser on/off runs.*

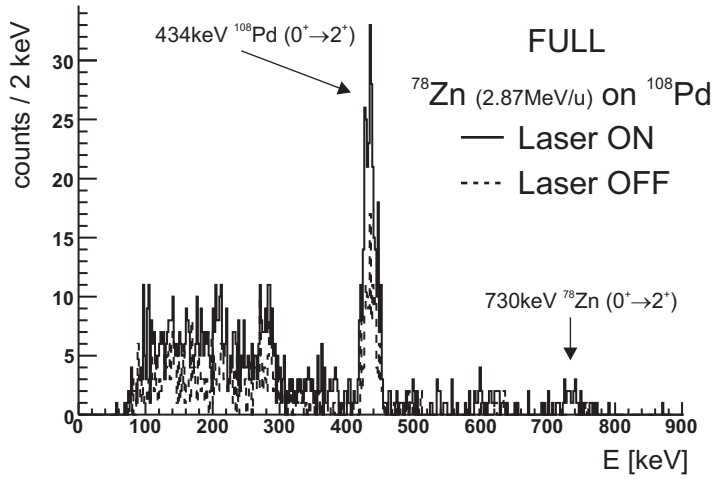

Figure 4.7: *Coulomb excitation spectrum obtained during the 9 laser on/off runs on mass A=78. At 434keV the $0_1^+ \rightarrow 2_1^+$ excitation in the target ^{108}Pd is observed, while the $0_1^+ \rightarrow 2_1^+$ transition in ^{78}Zn is observed at 730 keV, only during laser on periods.*

Parameters for extrapolation

In the next paragraph, the R_{ON} value for the laser on runs will be extracted from the data, utilizing the "parameters for extrapolation" which will be derived in this paragraph.

Zn and Ga Coulomb Excitation In the first method Coulomb excitation yields from Zn and Ga are used to extrapolate the parameter R (or r) to R_{ON}. This can be seen as an analysis of "prompt radiation" from individual components (Zn and Ga) in the beam. The number of Zn excitation gamma's during laser on/off runs is given by :

$$N_\gamma^{Zn} = I_{Zn}^{ON} \cdot \sigma_{Zn} \cdot \epsilon_{MB,Zn} \tag{4.15}$$

$$N_\gamma^{Ga} = 2I_{Ga}^{ON} \cdot \sigma_{Ga} \cdot \epsilon_{MB,Ga} \tag{4.16}$$

Introducing the parameter $\Re_{CLX,1}$ as :

$$\begin{aligned} \Re_{CLX,1} &= \frac{\sigma_{Ga}}{\sigma_{Zn}} \cdot \frac{\epsilon_{MB,Ga}}{\epsilon_{MB,Zn}} \\ &= \frac{N_\gamma^{Ga}}{N_\gamma^{Zn}} \cdot \frac{1}{2r} \end{aligned} \tag{4.17}$$

where the parameter r is determined by the methods discussed above. The error on $\Re_{CLX,1}$ is determined by the intensity in the Ga and Zn Coulomb excitation peaks, which is sufficient in A=74,76.

Target and Ga Coulomb excitation The second method compares target and Ga Coulomb excitation yield to extrapolate the R-value to laser on periods. The number of target excitation gamma's during laser on/off runs is given by :

$$\begin{aligned} N_\gamma^{Target} &= (I_{Zn}^{ON} \cdot \sigma_{Target}^{Zn} + I_{Ga}^{tot} \cdot \sigma_{Target}^{Ga}) \cdot \epsilon_{MB,Target} \\ &= (I_{Zn}^{ON} \cdot \sigma_{Target}^{Zn} + 2I_{Ga}^{ON} \cdot \sigma_{Target}^{Ga}) \cdot \epsilon_{MB,Target} \end{aligned} \tag{4.18}$$

and the amount of gamma's from Ga excitation is given by 4.16. After some manipulation of the ratio of 4.18 and 4.16 the parameter $\Re_{CLX,2}$ can be defined as :

$$\begin{aligned} \Re_{CLX,2} &= \frac{\sigma_{Ga} \cdot \epsilon_{MB,Ga}}{\sigma_{Target}^{Zn} \cdot \epsilon_{MB,Target}} \\ &= (\frac{\sigma_{Target}^{Ga}}{\sigma_{Target}^{Zn}} + \frac{1}{2r}) \cdot \frac{N_\gamma^{Ga}}{N_\gamma^{Target}} \end{aligned} \tag{4.19}$$

where the error is determined by the statistics in target and Ga yield.

4.2.2 Extrapolation to laser on runs

The ratio of Zn and Ga particles in the beam is only exactly known during laser on/off runs. In the preceding paragraphs it was shown how the R value can be determined from these laser on/off runs. Then, extrapolation parameters were determined, based on a relative comparison of Zn-Ga excitation ($\Re_{CLX,1}$) and Ga-Target excitation ($\Re_{CLX,2}$). Now these parameters will be used to determine the R_{ON} value for the laser on runs. This method takes into account that in between laser on/off runs the ionization efficiency might change[1], by utilizing the detected "prompt" Coulomb

[1]The ionization efficiency changes because of 1- drop of the laser power; 2- a shift of the laser beam; 3- distortion of the thin ionization tube due to heating might cause a slight shift of the tube.

excitation radiation characteristic for each beam particle. In this paragraph (laser ON) the definitions from 4.3 and 4.4 need to be adjusted :

$$I_{Zn}^{tot} = I_{Zn}^{ON} \tag{4.20}$$
$$I_{Ga}^{tot} = I_{Ga}^{ON} \tag{4.21}$$

since Ga and Zn are produced over the same amount of time. The relations 4.5 and 4.6 remain the same.
Utilizing $\Re_{CLX,1}$ (see eq. 4.17), the parameter r during a laser ON run is extracted as follows :

$$r = \frac{N_\gamma^{Ga}}{N_\gamma^{Zn}} \cdot (1/\Re_{CLX,1}) \tag{4.22}$$

where $\frac{N_\gamma^{Ga}}{N_\gamma^{Zn}}$ is the number of detected de-excitation gamma's from Ga and Zn during a laser ON run. The efficiencies and cross sections are absorbed in the parameter $\Re_{CLX,1}$.
Utilizing $\Re_{CLX,2}$ (see eq. 4.19), the parameter r during a laser ON run is extracted as follows :

$$r = 1/(\Re_{CLX,2} \cdot \frac{N_\gamma^{Target}}{N_\gamma^{Ga}} - \frac{\sigma_{Target}^{Ga}}{\sigma_{Target}^{Zn}}) \tag{4.23}$$

The results of this extrapolation (R_{ON}), together with the determined R values during the laser on/off runs are summarized in tab. 4.2 [2]. In Fig. 4.8 the results for the three masses are summarized. The solid black line indicates the sum of all laser on runs, extrapolated with the method which gives the smallest error bar. The error bar is indicated by the dashed lines. The thin solid black line line indicates the R value deduced from the sum of all laser on/off runs.

A	**R** [%]			**Extrapolation**		**R_{ON}** [%]	
	CD[1]	Target[2]	IC[3]	$\Re_{CLX,1}$	$\Re_{CLX,2}$	$\Re_{CLX,1}$	$\Re_{CLX,2}$
74	82.0(1.3)	82(21)	-	1.20(0.06)	17.3(1.5)	**82.9(4.4)**	84.5(7.9)
76	78.5(1.8)	66(27)		1.34(0.13)	12.9(1.8)	**72.6(7.3)**	71.8(10.7)
78	65.3(1.5)	61.5(7.3)	∼50	3.3(0.8)	0.49(0.08)	63(19)	**64(13)**

Table 4.2: *Columns 2-4 present the R values extracted from the laser on/off runs, [1]=elastic scattering in the CD detector; [2]=target excitation; [3]=Ionisation chamber. Columns 5-6 present the extrapolation parameters $\Re_{CLX,1}$ and $\Re_{CLX,2}$. The last 2 columns give the final value for the full laser on period. The value with the smallest error bar is taken in the further analysis.*

[2] At this point, the results from Chapter 5 are used for $N_\gamma^{Zn,Ga,Target}$

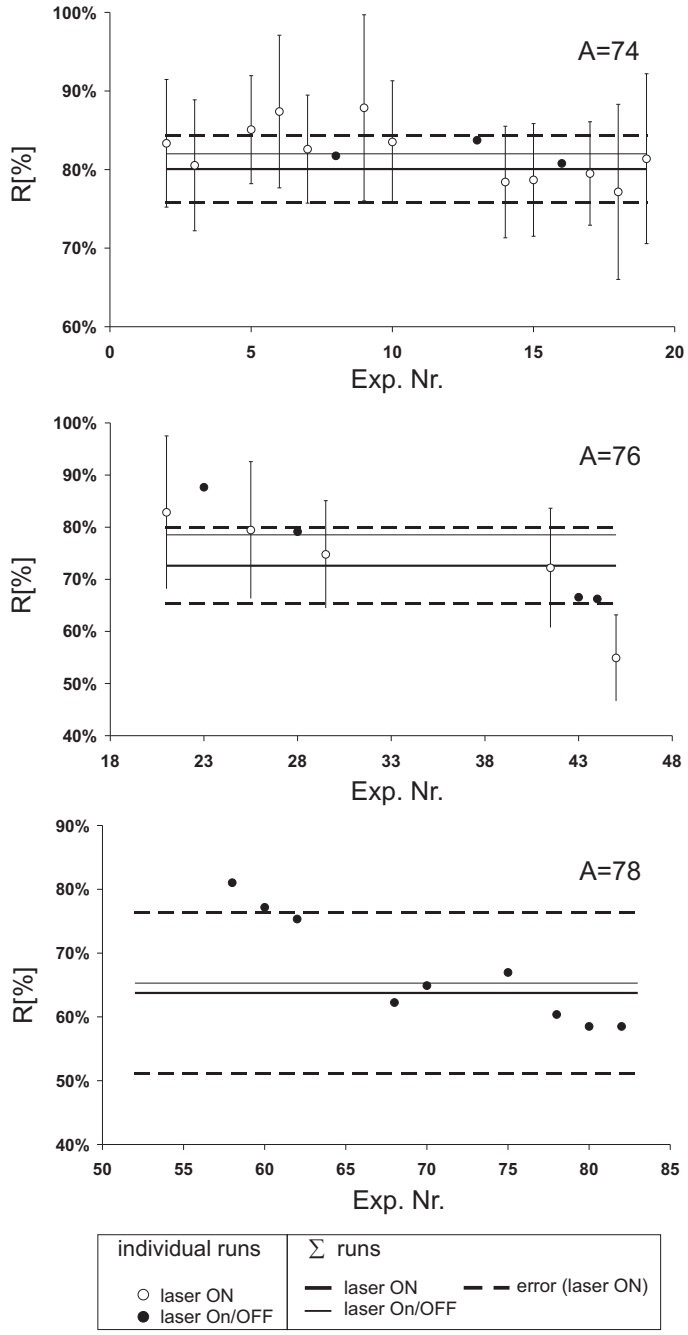

Figure 4.8: *Summary of the $R_{(ON)}$ values for the three masses. The solid circles are the individual laser on/off results (particle scattering), while the open circles are the extrapolated values to individual laser on runs, with the method which gives the smallest error bar. For A=78, these marks are left out because of the limited statistics in the individual laser on runs. The black line is the final extrapolated value for the sum of all laser on runs, while the dashed black line indicates the error bar on the final (extrapolated) R-value.*

4.2.3 Beam gate for RIB

In the A=76 experiment, an additional contamination from stable rest-gas isotopes was present. The target excitation yield needs to be corrected for possible excitation induced by these lighter isotopes. It was concluded in par. 3.4.2 that the contaminants are ^{22}Ne and ^{40}Ar, based on the following arguments : 1- the rest-gas in the (REX-)Trap consists mainly of natural abundant Ne and Ar gas ; 2- the simulated and detected energy versus scattering angle spectrum fits with the A=22 and A=40 assignment ; 3- the A/q setting of 3.8 for ^{76}Zn fits A/q values for these contaminants (see tab. 3.2). Since ^{22}Ne is by far the most intense contaminant, the correction will be limited to this isotope. The number of scattered Zn and Ga particles during 'RIB on' periods is given by :

$$\begin{aligned} N^{Zn+Ga}_{sc,RIBon} &= I_{Zn} \cdot \sigma^{Rutherford}_{Zn} + I_{Ga} \cdot \sigma^{Rutherford}_{Ga} \\ N^{Zn+Ga}_{sc,RIBoff} &= 0 \end{aligned} \tag{4.24}$$

while the number of scattered ^{22}Ne particles during 'RIB on' and 'RIB off' periods is given by [3]:

$$N^{Ne}_{sc,RIBoff} = N^{Ne}_{sc,RIBon} = I_{Ne} \cdot \sigma^{Rutherford}_{Ne}. \tag{4.25}$$

Combining these two formula, the ratio r_{Ne}=I_{Ne}/I_{Zn} can be extracted :

$$r_{Ne} = \frac{\sigma^{Rutherford}_{Zn}}{\sigma^{Rutherford}_{Ne}} \cdot \frac{1 + r \cdot (\sigma^{Rutherford}_{Ga} / \sigma^{Rutherford}_{Zn})}{N^{Zn+Ga}_{sc,RIBon} / N^{Ne}_{sc,RIBon}}.$$

In conclusion, by extracting the number of scattered ^{22}Ne particles during 'RIB off' periods, the ratio r_{Ne} can be determined, which must be included in eq. 4.2 where X=Ne. The importance of this correction then depends on the ratio $\sigma^{Ne}_{E2,Target}/\sigma^{Zn}_{E2,Target}$. In tab. 4.3, the parameters are given for the A=76 RIB, resulting in r_{Ne}=0.084(0.007) (r=0.377(0.031), see table 4.2). The ratio of the Coulomb excitation cross section for target excitation is $\sigma^{Ne}_{E2,Target}/\sigma^{Zn}_{E2,Target}$ = 0.105. The total, additional correction to the target excitation in eq. 4.2 becomes 0.105*0.084 = 0.0088(0.0007), thus, less than 1%.

$N^{Ne}_{sc,RIBoff}/N^{Zn}_{sc,RIBon}$	$\sigma^{Rutherford}_{Ne}$	$\sigma^{Rutherford}_{Zn}$	$\sigma^{Ne}_{E2,Sn}$	$\sigma^{Zn}_{E2,Sn}$
13.69	12.96 b [1]	10.7 b [1]	16 mb [2]	149 mb [3]

Table 4.3: *The different terms in eq. 4.26 and eq. 4.2. ([1]) = integrated over the angular range where Ne is detected (ϑ_{CM}=34.2°-61.8°) - ([2]) = integrated over the "CM1" range (Zn gated - see tab. 4.1) - ([3]) = integrated over the CM angular range labelled "FULL".*

4.3 β-decay background

During the RIB experiments, the MINIBALL reaction chamber accumulates radioactive isotopes which are scattered into the target chamber walls or the CD detector. The β-decay of these isotopes can be seen in random coincidence with detected particles. This random coincident gamma spectrum needs to be subtracted from the prompt

[3] Assuming the EBIS operation is not influenced by RIB injection !

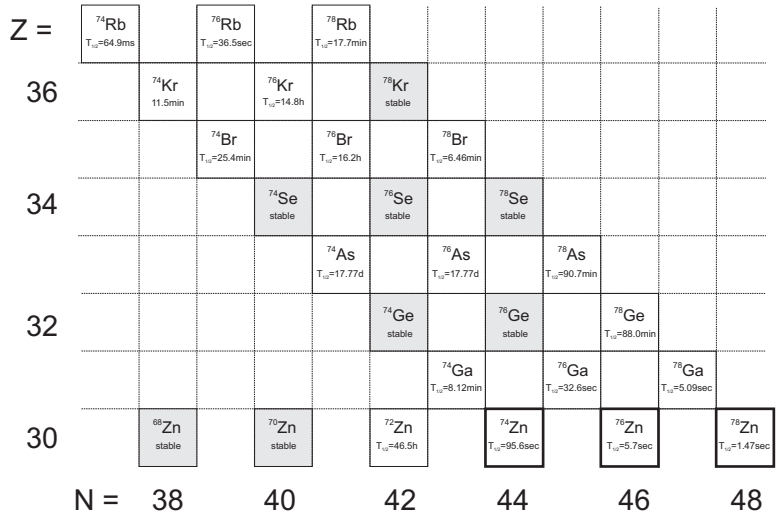

Figure 4.9: *Detail of the nuclear chart for A=74,76 and 78. β-decay lines of daughter products of ^{74,76,78}Zn are observed in the background spectrum.*

coincident (Coulomb excitation-)spectrum. In the following chapter this subtraction will be elaborated upon for the three masses separately. The counting rate in the MINIBALL detectors depends mainly on this accumulated radioactivity during the RIB experiment. For the three masses these counting rates for the full MINIBALL array (24 cores) are : 103kHz (A=74), 47kHz (A=76) and 8kHz (A=78). The decreasing counting rate for the three masses is due to the decreasing beam intensities. In par. 4.2, the isobaric contamination was discussed, based on production mechanisms and the "prompt" Coulomb excitation radiation characteristic for each of them. In this paragraph, the β-decay spectra are shown in Fig. 4.10(A=74), 4.11(A=76) and 4.12(A=78), characterizing the radioactive beam content by its β-decay. The possible radioactive isobars for the three masses are shown in Fig. 4.9. The most intense β-decay lines are identified in Fig. 4.10,4.11 and 4.12. No clear evidence is found for the presence of an appreciable amount of isobaric radioactive contaminants next to Ga. The increased low energy background during 'In Beam' periods is due to the bremstrahlung from the REX linac (7- and 9-gap resonators), illustrating the need for an adequate shielding of the linac.

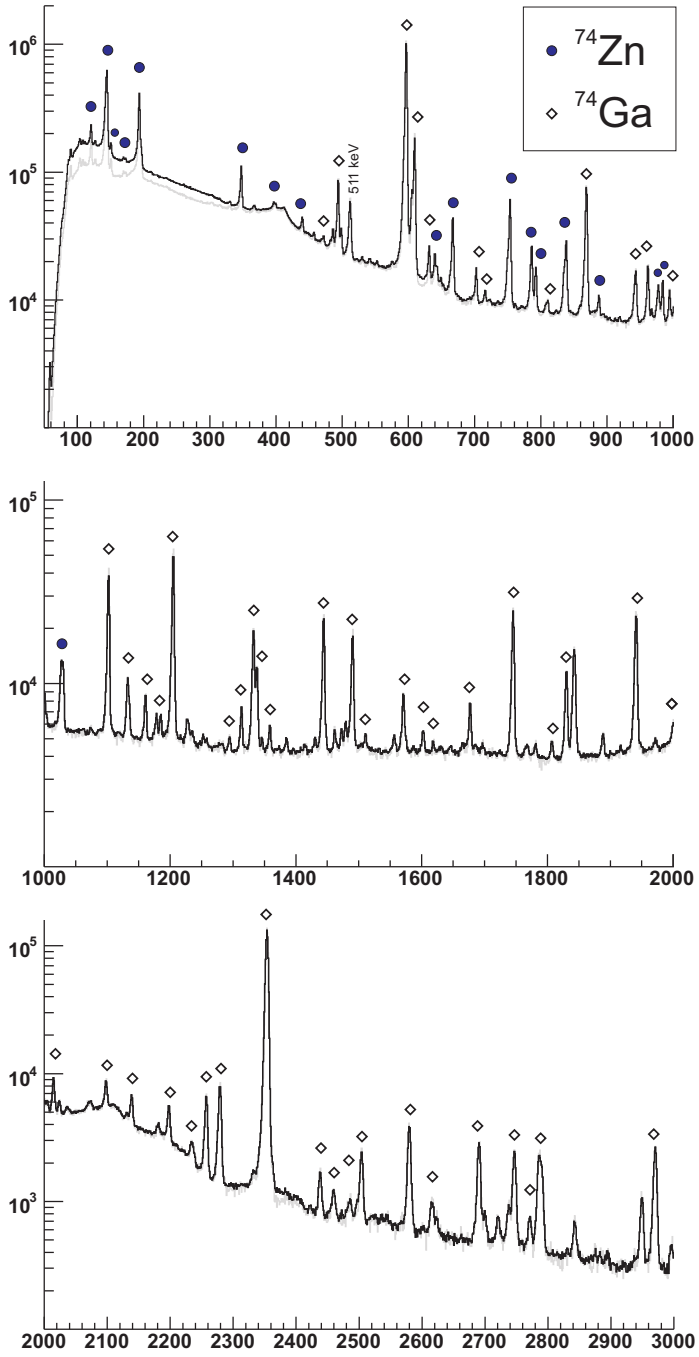

Figure 4.10: *The full singles spectrum, measured by the 8 MINIBALL clusters. The spectrum is dominated by β-decay of A=74 radioactive isobars. The highest intensity decay lines are identified. The grey line corresponds to the measured singles spectrum during "RIB OFF" periods, this is when the linac is off and the resonators do not induce low energy bremstrahlung. The black line is the "RIB ON" singles spectrum.*

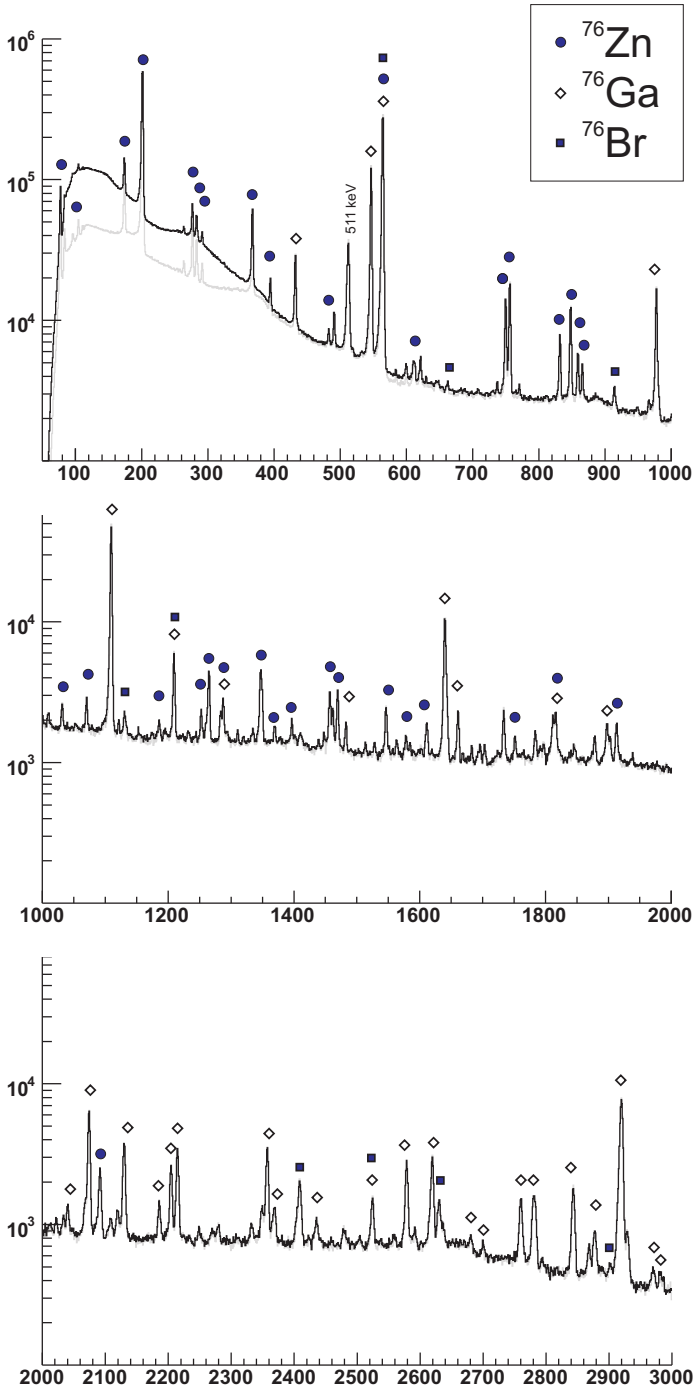

Figure 4.11: *The full singles spectrum, measured by the 8 MINIBALL clusters. The spectrum is dominated by β-decay of A=76 radioactive isobars. The highest intensity decay lines are identified. The grey line corresponds to the measured singles spectrum during "RIB OFF" periods, this is when the linac is off and the resonators do not induce low energy bremstrahlung. The black line is the "RIB ON" singles spectrum.*

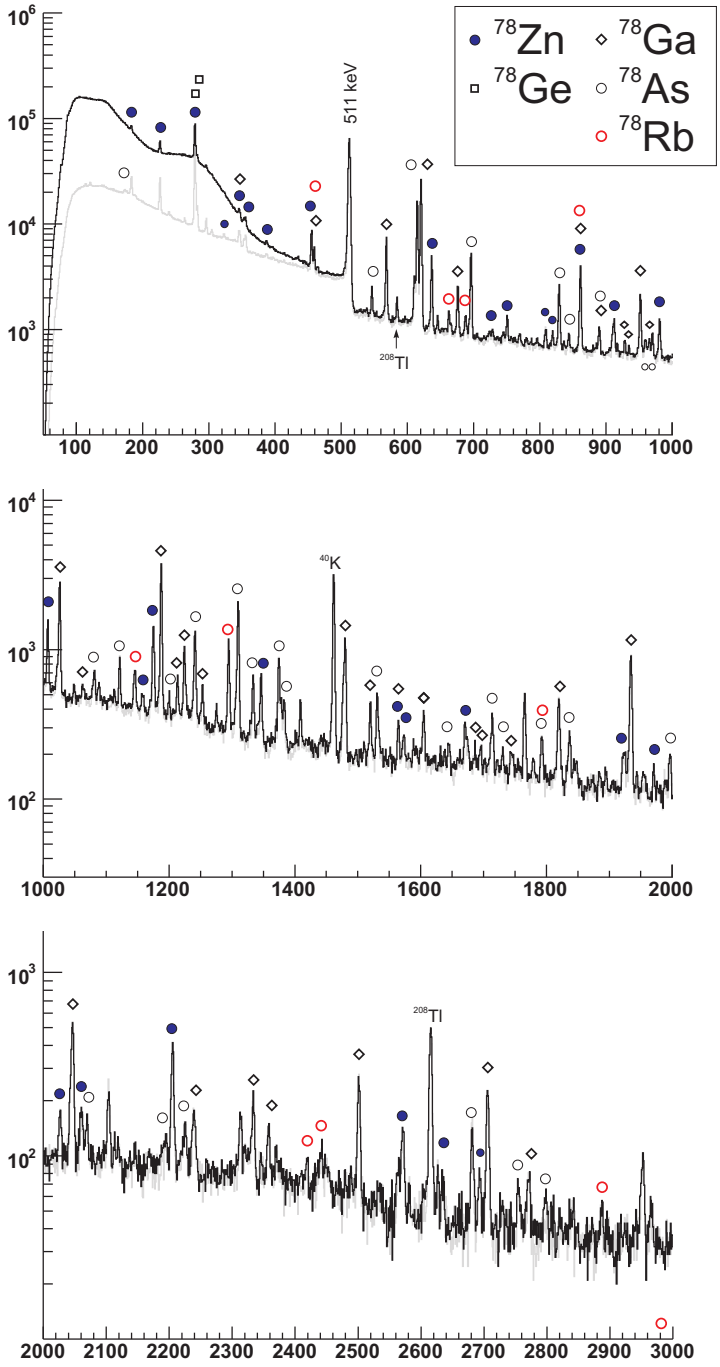

Figure 4.12: *The full singles spectrum, measured by the 8 MINIBALL clusters. The spectrum is dominated by β-decay of A=78 radioactive isobars. The highest intensity decay lines are identified. The grey line corresponds to the measured singles spectrum during "RIB OFF" periods, this is when the linac is off and the resonators do not induce low energy bremstrahlung. The black line is the "RIB ON" singles spectrum.*

4.4 Doppler Correction

4.4.1 Introduction

The typical life time of the excited 2^+ states in the considered experiments (^{74,76}Zn on ^{120}Sn and ^{78}Zn on ^{108}Pd) is in the order of psec (10^{-12} sec). The flight time from the end of the target to the CD detector is typically in the order of magnitude ns (10^{-9} sec) [4], for v/c ranging from ∼0.01 (target detection) to ∼0.06 (projectile detection) and a target-detector distance of 30.5 mm. This assures that the excited nucleus will have decayed in flight before it is stopped in the CD detector. Consequently, all $2_1^+ \rightarrow 0^+$ de-excitation gamma rays will be Doppler shifted by the in-flight decay, where the Doppler shift is given by :

$$E_{lab} \quad = \quad \gamma E_0/(1 - \beta cos(\vartheta)), \tag{4.26}$$

where E_0 is the original energy of the γ-ray in the rest frame of the emitting nucleus, E_{lab} is the detected, Doppler shifted energy, γ is the relativistic factor $1/\sqrt{(}1 - \beta^2)$, β=v/c and ϑ is the angle between the de-exciting nucleus and the emitted γ-ray. With the knowledge of the position coordinates of the gamma ray and the de-exciting nucleus, a Doppler correction can be applied to the detected gamma ray energy by using eq. 4.26. In the case where the de-exciting nucleus is detected in the CD detector, ϑ is correlated with the detected angles for the particle (θ_p, ϕ_p) and the gamma ray $(\theta_\gamma, \phi_\gamma)$:

$$cos(\vartheta) = sin(\theta_p)sin(\theta_\gamma)cos(\phi_p - \phi_\gamma) + cos(\theta_p)cos(\theta_\gamma). \tag{4.27}$$

The detected energy is used to determine β=$\sqrt{2E_{lab}/A[u]}$. The resolution of the Doppler corrected photo-peak is slightly influenced by the accuracy of the CD calibration, as was illustrated in Fig. 3.19.

4.4.2 Gamma angle optimization

The eight triple clusters of the MINIBALL array are mounted on a flexible frame. They can be moved in 3 angular directions : θ, ϕ and α, as defined in Fig. 4.13. The angular coordinates of the clusters can be estimated from the MINIBALL frame, though not accurately. In order to determine the coordinates more precise a position calibration is necessary. This was done using the 1-neutron pickup reaction ^{2}H(^{22}Ne,^{23}Ne)p at a ^{22}Ne beam energy of 2.25MeV/u and making use of a 10μm deuterated polyethylene target. The ^{22}Ne beam is available as a rest-gas beam from the EBIS in several charge states (see Fig. 3.8). In the neutron pick-up reaction the first excited $\frac{1}{2}^+$ state in ^{23}Ne at 1017 keV is populated. The lifetime of this level is 178(10) ps [nndc], so ^{23}Ne de-excites 'in flight'. The Doppler shifted transition is shown in Fig. 4.14A and this ($\frac{1}{2}^+ \rightarrow \frac{5}{2}^+$) transition in ^{23}Ne will be used for the position calibration. Another Doppler shifted transition is present in this spectrum, coming from the 1-proton pickup channel ^{2}H(^{22}Ne,^{23}Na)n where the $\frac{5}{2}^+$ state at 440 keV is populated in ^{23}Na.
Two criteria are used during the position optimization : 1- minimization of the Doppler corrected FWHM of 1 cluster and 2- alignment of the Doppler corrected peak in the 6 segments. The angular coordinates are varied recursively until the two criteria are optimized. The result of such an optimization is shown in Fig. 4.14B. The 'Full Width at Half Maximum' (FWHM) of the Doppler corrected line after optimization is 15.5

[4] The only exception being isomeric states in ^{76}Ga which are not Doppler shifted in the detected Coulomb excitation spectrum. The lifetime of these states exceeds the typical flight time target-CD.

keV on the core level and 11.0 keV on the segment level. The Doppler correction was performed *without* kinematical reconstruction of the ^{23}Ne scattering direction. The maximum scattering angle of the excited ^{23}Ne is 4.3° and the scattered proton is detected in the CD detector. The spectra in Fig. 4.14 and Fig. 4.15 are singles spectra and the Doppler correction is performed assuming $(\theta_p,\phi_p)=(0,0)$. The angle ϑ in eq. 4.27 is then identical to θ_γ which is the lab angle of the core/segment where the gamma is detected.
The criterium of alignment of the Doppler corrected segment energies is shown in the bottom part of Fig. 4.15. Before Doppler correction, the Doppler shift in each segment is slightly different (right series and line marked "NOT doppler corrected" in bottom part of Fig. 4.15). When the cluster is accurately positioned, the Doppler corrected peak in the 6 segments will be aligned (left series and line marked "doppler corrected" in bottom part of Fig. 4.15). The lines in the bottom part of Fig. 4.15 presents the fitted mean energy detected in the segment minus the fitted mean energy on the core, without(with) Doppler correction.

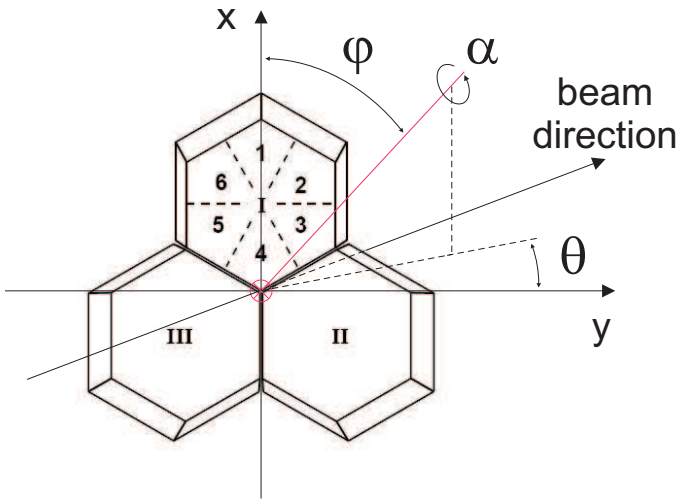

Figure 4.13: *The reference system for positioning of the clusters.*

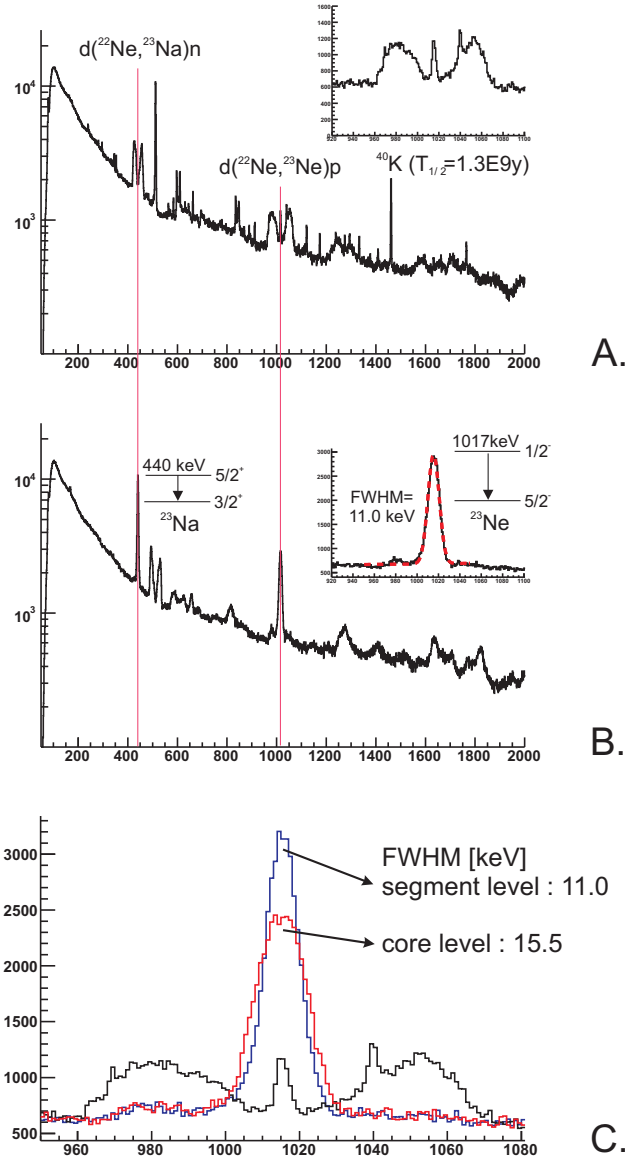

Figure 4.14: *A. Full uncorrected singles spectrum obtained during the ^{22}Ne beam on a 10μm PE target measurement. - B. Doppler corrected singles spectrum (on the core level). - C. Detail on the Doppler corrected 1017 keV line. No kinematical reconstruction of the emitting particles is performed.*

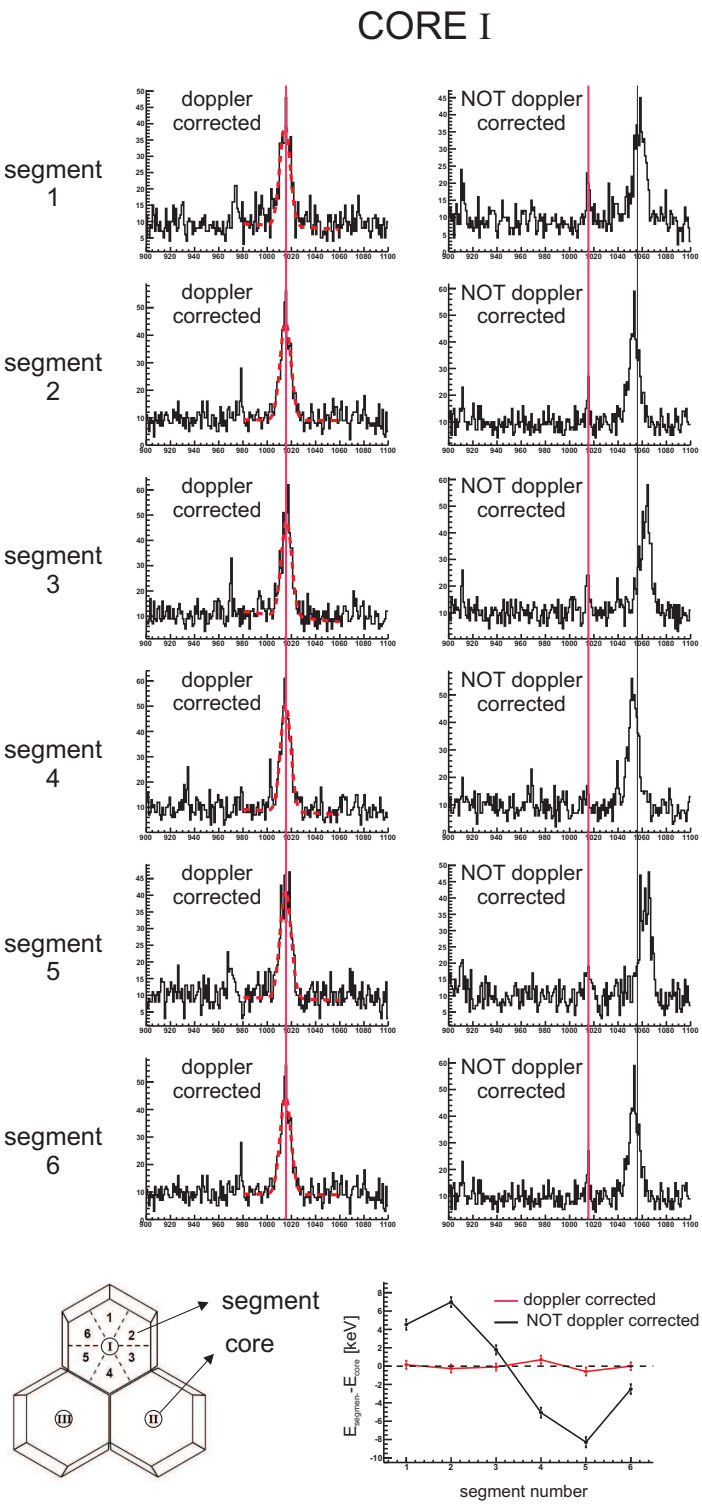

Figure 4.15: *The photopeak events in the different segments are correctly Doppler corrected after position optimization of the cluster.*

4.4.3 Limitations for ^{120}Sn

The lifetime of the first excited 2^+ state ($\tau_{2_1^+}$) in ^{120}Sn is 0.916(19) ps [Ram01]. This is short, compared to the lifetime of e.g. $\tau_{2_1^+}(^{108}\text{Pd})$=23.9(7) ps and (in this experiments measured) $\tau_{2_1^+}(^{74,76,78}\text{Zn})$=25-30 ps (see Chapter 5). The short lifetime limits the possibility to Doppler correct the detected gamma-ray energy of the $2_1^+ \rightarrow 0_1^+$ transition. This will be shown in the following paragraph for the case of ^{74}Zn on a 2.3 mg/cm^2 ^{120}Sn target (=3.16 μm).
With the detected scattering angle and energy of the projectile (=Zn), the kinematics of the considered reaction and taking into account the energy loss in the target material, a kinematical reconstruction of the not-detected ejectile (=Sn) is possible. The reconstructed Sn coordinates can then be used in eq. 4.26/4.27 to Doppler correct the $2_1^+ \rightarrow 0_1^+$ transition in Sn. Though, if the de-excitation occurs before the Sn nucleus has reached its final velocity, these reconstructed coordinates are not applicable. The time it takes the Sn nucleus to 'travel' from an initial velocity β_i ($=\sqrt{2E_{Sn}/120u}$ with E_{Sn} the transferred energy in the reaction) to a final velocity β_f ($=\sqrt{2(E_{Sn}-E_{loss})/120u}$ with $E_{Sn} \geq E_{loss} \geq 0$ the energy loss in the target material) is given by :

$$t_\beta = mc \int_{\beta_i}^{\beta_f} \frac{d\beta'}{dE/dx} \tag{4.28}$$

where m is the mass of the retarding nucleus (in this case 120u) and dE/dx is the stopping power in MeV/cm [Fyn03]. In case β_f=0, $t_{\beta=0}$ is called the 'stopping time', while $t_{\beta\neq 0}$ is referred to as the 'exit' time. In Fig. 4.16 this time is plotted as a function of the detected CM angular range. The open dots correspond to the 'stopping time' ($t_{\beta=0}$, Sn is stopped in the target material), whereas the full dots correspond to the 'exit time' (t_β, Sn leaves the target material). Circles and triangles correspond to two cases where (1,triangles) Sn is scattered from the front of the target and (2,circles) Sn is scattered from the middle of the target. In case (1,triangles), the target nucleus travels through more target material and looses more energy then in case (2,circles). For the lower CM angles, the energy transfer to Sn is lower than for the higher CM angles (see Fig. 4.1), so stopping occurs merely for the lower CM angles. The dashed line indicates the lifetime of the 2_1^+ state in ^{120}Sn. If the retardation to β_f takes $\geq \tau_{2_1^+}$, $\geq$50% of the excited Sn nuclei will have decayed before they reach their final velocity. In Fig. 4.16 the detected CM ranges CM1 and CM2 are indicated as well (see par. 4.1). Interestingly, 50-85% of the Sn nuclei which are scattered from the front of the target and are detected in the CD over the range $\sim$75-85° have already decayed before they exit the target material. This is much less for the Sn nuclei detected in the same CM range but scattered from the middle of the target. In general, most of the exit times are below $\tau_{2_1^+}$ over CM2 range, so the detected Sn coordinates are applicable in eq. 4.26/4.27. In conclusion, it can be stated that over the CM1 range, the coordinates (E,θ_p) of Sn, obtained from a kinematical reconstruction, are not adequate to Doppler correct the detected Sn excitation over the same CM region. This due to the dependence of the stopping/exit time on the interaction depth in the target.

4.4.4 Application in the final result

The full detected CM range and the correlated Coulomb excitation gamma spectrum will be used to determine the B(E2) value with the best statistical error. In this case, the CD detector is merely used as a time trigger to indicate a prompt or random gamma (or particle) event. When selecting CM1 or CM2, the detected energy in the

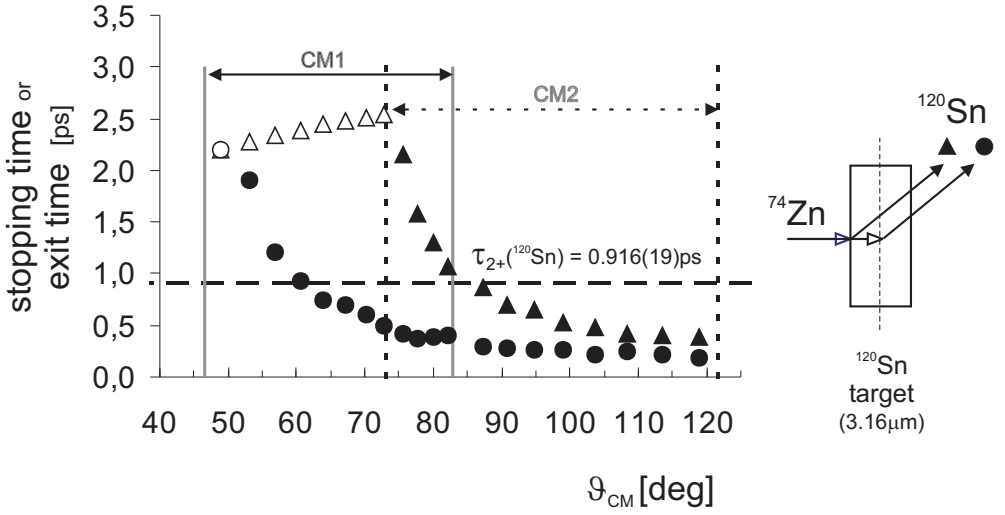

Figure 4.16: *The stopping time (open symbols) or exit time (filled symbols) of the scattered Sn nuclei as a function of CM scattering angle. The triangles correspond to Sn scattering in the beginning of the target, circles to Sn scattering at the middle of the target. The detected CM ranges are indicated (CM1=Zn detection, CM2=Sn detection).*

CD is used as well. From the discussion in par. 4.1 it is clear that the 2 CM ranges are not always as clearly separated. Therefore, the B(E2,$2_1^+ \rightarrow 0_1^+$) value derived from the measured Coulomb excitation yields over CM1 and CM2 will be used as a consistency check of the first method. The possibility to Doppler correct the Doppler shifted Zn Coulomb excitation peak when selecting CM1 puts an additional selectivity on the gamma spectrum. Only the "true" Zn Coulomb excitation events will contribute to the Doppler corrected photopeak. This selectivity is not available for the Sn Coulomb excitation yields over the CM1 range, since no Doppler correction can be performed (see previous paragraph). Therefore, because of the scattered border between the two CM ranges, it remains possible that 'contaminating' Sn yield from CM2 contributes to the Sn yield in CM1.

4.5 Gamma angular distribution

In eq. 2.40 an explicit dependence on the gamma angular distribution should be included. The angular distribution in the CM frame of the nucleus can be derived in first order perturbation theory approach [Ald56]. From a detailed derivation [Ald56] it is concluded that the angular distribution can always be written in the form :

$$W(\vartheta_\gamma, \varphi_\gamma) = \sum_{k,k'} A^*_{kk'}(\vartheta) Y_{k,k'}(\vartheta_\gamma, \varphi_\gamma) \tag{4.29}$$

$$with\ A_{kk'}(\vartheta) = \sum_{\kappa,\kappa'} \rho^C_{\kappa\kappa'}(\vartheta) K_{kk',\kappa\kappa'} \tag{4.30}$$

where $(\vartheta_\gamma, \varphi_\gamma)$ are the polar coordinates of the emitted gamma quantum, ϑ is the scattering angle of the emitting particle and $Y_{k,k'}$ are the spherical harmonics. $\rho^C_{\kappa\kappa'}$ is the statistical tensor evaluated in a coordinate frame where the z-axis is parallel to the beam direction (details are found in [Ald75]). The coefficients $K_{kk',\kappa\kappa'}$ may partly describe the effects of unobserved gamma quanta, conversion electrons and other attenuation effects. The angle ϑ_γ is the angle between the z-axis (=the beam axis) and the propagation direction of the emitted gamma quantum in the rest system of the γ-emitting nucleus. The angular distribution has a reflection symmetry around ϑ_γ=90°. In the special case of an E2 transition, the angular distribution can be written as [Ald56] :

$$W_{E2}(\vartheta_\gamma) = 1 + a_2 P_2(cos(\vartheta_\gamma)) + a_4 P_4(cos(\vartheta_\gamma)) \tag{4.31}$$

where $P_{k=2,4}$ are the Legendre polynomials. If the excited nucleus decays in flight a distortion of the symmetric angular distribution will take place. The distortion is evaluated in the lab system where the emitted γ quantum is detected. The original reference system is moving with speed v (β) parallel to the beam axis. The relation between the angular distribution in the rest frame ($W(\vartheta_\gamma, \varphi_\gamma)$) and the laboratory frame ($W_{lab}(\theta_\gamma, \phi_\gamma)$) is

$$W_{lab}(\theta_\gamma, \phi_\gamma) = W(\vartheta_\gamma(\theta_\gamma), \varphi_\gamma) \frac{d\Omega_\gamma}{d\omega_\gamma} \tag{4.32}$$

where $d\Omega_\gamma$ = the solid angle in the rest system and $d\omega_\gamma$ = the solid angle in the LAB-system. The solid angle ratio is given by

$$\frac{d\Omega_\gamma}{d\omega_\gamma} = \frac{1-\beta^2}{(1-\beta cos(\theta_\gamma))^2} \tag{4.33}$$

and ϑ_γ is related to θ_γ through :

$$tan(\frac{1}{2}\vartheta_\gamma) = \sqrt{\frac{1+\beta}{1-\beta}} tan(\frac{1}{2}\theta_\gamma) \tag{4.34}$$

In Fig. 4.17 the angular distribution is plotted for the $2^+_1 \rightarrow 0^+_1$ transitions in both ^{74}Zn and ^{120}Sn in the laboratory frame (dashed line). The angular distributions were calculated with the coupled channels Coulomb excitation code GOSIA [Czo]. One gamma counter was assumed in the GOSIA code at angles (θ_{det}=0...180°,ϕ_{det}=0). An integration over the detected scattering angle ϑ (in eq. 4.29) and an integration over energy loss through the target was included. A circular particle detector was assumed. The calculated distribution $W_{lab}(\theta_\gamma, \phi_\gamma = 0)$ was transformed to the rest frame by applying eq. 4.34 and 4.32. The result of this transformation to the CM system is shown in Fig. 4.17 (full line). The β-value in eq. 4.34 is not well defined, since the yields were integrated over energy loss through the target (the β-value varies along the energy loss path). An 'average' value for β was determined by requesting a symmetric $W_{E2}(\vartheta_\gamma)$ distribution around 90°.
The absolute efficiency was determined in par. 3.4.1 with a ^{152}Eu source, yielding an isotropic efficiency for the MINIBALL. The radiation pattern from the $2^+_1 \rightarrow 0^+_1$ transition is not isotropic. This is taken into account by folding the isotropic efficiency (ϵ_{iso}) with the (normalized) angular distribution function :

$$\epsilon_W = \epsilon_{iso} \cdot \frac{\int_\Omega W_{lab} d\Omega}{\frac{1}{4\pi}\int_\Omega d\Omega} \tag{4.35}$$

where $\int_{4\pi} W_{lab} d\Omega$=1. Defining $W_\gamma^{Zn} = \frac{\int_\Omega W_{lab}^{Zn} d\Omega}{\frac{1}{4\pi}\int_\Omega d\Omega}$ for the angular distribution of Zn and similar for the target (W_γ^{Target}). In eq. 2.38 and 2.39, the efficiencies are the isotropic efficiencies determined in par. 3.4.1. In table 4.4 these relative coefficients are given for the three isotopes.

A	W_γ^{Zn}	W_γ^{Target}	Ratio
74	0.943	0.952	**0.990**
76	0.813	0.817	**0.995**
78	0.952	0.948	**1.004**

Table 4.4: *Corrections to the isotropic MINIBALL efficiencies due to the angular distribution of the $2^+ \rightarrow 0^+$ transition in the Zn and target nuclei.*

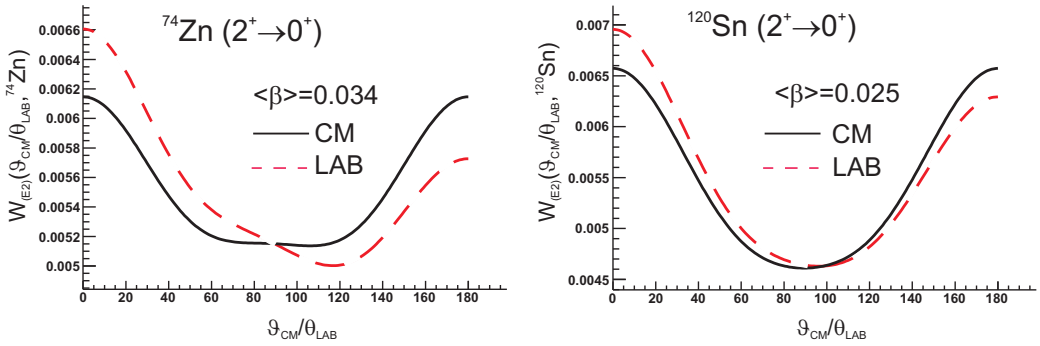

Figure 4.17: *The angular distribution in the rest frame of the emitting nucleus (black) and in the laboratory frame (dashed grey). A distortion of the angular distribution is observed in the lab frame because of the moving of the emitting nucleus.*

4.6 Calculation of Cross Sections

4.6.1 GOSIA

The inelastic cross section for Coulomb excitation to excited states n can be calculated with the coupled channels code GOSIA, which was developed at Rochester university by Czosnyka et al. [Czo] as a data analysis software package. GOSIA performs a "least squares" fit (χ^2 method) of calculated transition yields to experimentally observed transition yields. During the fitting procedure, the nuclear matrix elements are modified within borders specified by the user and consistent with known experimental data (such as M1/E2 mixing ratio's, lifetimes,...). Inputs to the code are divided in 4 parts : (1) kinematics input (masses, energy, ...) (2) nuclear structure input (3) detector geometry (particles and gamma's) and (4) integration options.

Theory

GOSIA calculates the double differential cross section for gamma de-excitation of state I to state I_f :

$$\frac{d^2\sigma}{d\Omega_p d\Omega_\gamma} = \sigma_R(\vartheta) \sum_{\lambda\mu} R_{\lambda\mu}(I, I_f) Y_{\lambda\mu}(\theta_\gamma, \phi_\gamma) \tag{4.36}$$

where σ_R is the rutherford cross section and

$$R_{\lambda\mu}(I, I_f) = \frac{1}{2\gamma(I)\sqrt{\pi}} G_\lambda \rho_{\lambda\mu} \sum_{\kappa\kappa'} \delta_\kappa \delta^*_{\kappa'} F_k(\kappa\kappa' I_f I) \tag{4.37}$$

with δ_L the transition amplitude of multipolarity L, $\gamma(I)$ the emission probability, $F_k(\kappa\kappa' I_f I)$ the γ-γ correlation coefficients and G_λ the attenuation coefficients. The factor $\rho_{\lambda\mu}$ is the polarization tensor of level I after single step Coulomb excitation to this state from initial state I_0 :

$$\rho_{\lambda\mu} = \frac{\sqrt{2I+1}}{2I_0+1} \sum_{M_0 M M'} (-1)^{I-M'} \begin{pmatrix} I & \lambda & I \\ -M' & \mu & M \end{pmatrix} a^*_{IM',I_0M_0} a_{IM,I_0M_0} \tag{4.38}$$

The result is output as the "integrated yield" of each γ de-excitation from each excited state I. The *integrated yield* is expressed in units $\left[\frac{mb}{srad} \cdot \frac{mg}{cm^2}\right]$ where the srad refers to the solid angle of γ-emission. It incorporates an integration over particle scattering angles (θ_p, ϕ_p) and over the energy loss $\frac{dE}{dx}$ through the target :

$$Y(I \to I_f) = \int_{E_{min}}^{E_{max}} dE \frac{1}{\frac{dE}{dx}} \int_{\theta_{p,min}}^{\theta_{p,max}} sin(\theta_p) \int_{\phi_p} \frac{d^2\sigma(I \to I_f)}{d\Omega_\gamma d\Omega_p} d\phi_p d\theta_p \tag{4.39}$$

where E_{min} and E_{max} refer to the initial beam energy and the final beam energy after passage through the target material.

Minimization

GOSIA, in its original form, fits a number of calculated transition yields to a set of experimental yields, by adjusting (=fitting) the transition matrix elements. In the case of multiple Coulomb excitation, the number of experimental data points (e.g. transition yields and lifetimes) is large enough, to ensure a proper normalization of the final result (all data points are normalized to one yield, the same as in the calculated yield). In the case where only one experimental data point is known, e.g. the $2_1^+ \to 0_1^+$ transition yield, there is no normalization possible. Therefore, a new version of GOSIA was developed [GOS2] that includes a simultaneous calculation of the target yield. In the simplest case, there is one experimental yield from the target and one experimental yield from the (unknown) beam particle. The target in this case has known spectroscopic information, and the target data point can serve as a normalization point. GOSIA then minimizes the matrix element(s) of the beam nucleus, according to the χ^2 method. This method of minimization is similar to the straightforward comparison in eq. 2.40, where the unknown normalization constant of the incoming particle intensity is divided out.

Inputs

In appendix A an example GOSIA input file is given for the case ^{74}Zn on ^{120}Sn.

Kinematics : Energy losses for the Zn isotopes when passing through the Sn(or Pd) targets are calculated with SRIM2003 [SRI]. The stopping powers are input to the code for integration and are used to calculate the integration limits E_i and E_f.

Nuclear structure : Possible excitations in the considered Zn Coulomb excitation experiment are limited to $0_1^+ \rightarrow 2_1^+$, $2_1^+ \rightarrow 4_1^+$ excitations, all of E2 character. Other transition multipolarities are not considered in these experiments. The Zn matrix elements to be minimized by GOSIA are : $\langle 0_1^+||E2||2_1^+\rangle$,$\langle 2_1^+||E2||2_1^+\rangle$ and $\langle 2_1^+||E2||4_1^+\rangle$. Since for none of the three Zn isotopes lifetimes are known for the 2_1^+ and 4_1^+ states, nor are quadrupole moments measured for the 2_1^+ states, no additional spectroscopic information could be input to GOSIA. The $\langle 2_1^+||E2||2_1^+\rangle$ matrix element was fixed, but varied over a certain range, see Chapter 5. Internal conversion coefficient for Zn isotopes were taken from [nndc].
For the targets, known spectroscopic information was input (see Chapter 5). The target matrix elements were fixed during the minimization.

Detector geometry : The particle detector is considered to have a circular geometry and is placed symmetric around the beam axis. The MINIBALL array is implemented in GOSIA as 24 separate Ge detectors, where the (θ_c, ϕ_c) angles from the ^{23}Ne optimization are input. The experimental yields are input as the sum of the yields in the individual detectors. A parameterized efficiency curve is given as well to correct the calculated yields.

Detector clusters

An option in GOSIA provides the possibility to define clusters of individual γ-detectors. The MINIBALL array was implemented as 24 individual γ-detectors (8 cluster with each 3 crystals) together with their θ and ϕ angles from the position optimization. The transition yield was input as the **NOT** efficiency corrected sum of all core yields. With the option "RAW" in GOSIA the not efficiency corrected yield of a whole detection array can be calculated, provided the efficiency curve of each individual detector is input. The isotropic efficiency curve for the whole MINIBALL array was divided by 24 and input as the individual efficiency curve for each crystal. GOSIA outputs the experimental transition yield, taking into account the detection efficiency and the γ angular distribution. The relative comparison of target and projectile yields, expressed in eq. 2.40 reduces then simply to :

$$\frac{N_\gamma^{Zn}(2^+ \rightarrow^+)}{N_\gamma^{Target}(2^+ \rightarrow 0^+)} = \frac{Y_{Zn}(2^+ \rightarrow 0^+)}{Y_{Sn}(2^+ \rightarrow 0^+)} \tag{4.40}$$

where the integrated yields $Y_{Zn,Sn}$ are calculated with the option "RAW" in GOSIA.

4.6.2 CLX

The Coulomb excitation code "CLX", written by H. Ower and adapted by J. Gerl, calculates the excitation cross sections according to the first order perturbation theory of Alder and Winther [Ald56]. Input parameters to the code involve 1- all matrix elements connecting the populated states, 2- the (average) beam energy, 3- (Z,A) for beam and target nuclei and 4- the angular range of the center of mass scattering angles. CLX outputs the differential cross section at the specified angular mesh points and the excitation cross section to each nuclear level (including the ground state, which is the

elastic scattering cross section). No angular distribution of the gamma rays is taken into account, since CLX calculates the single differential cross section to solid angle of the scattered particles.
CLX was used in this work to calculate the differential and integrated excitation cross sections, whereas GOSIA was used to calculate the de-excitation yields for target and projectile. The unknown matrix elements in ^{74,76,78}Zn were fitted to the de-excitation yields calculated by GOSIA. The resulting matrix elements were used in CLX to calculate the differential excitation cross sections, which will be used in the following chapter.

Chapter 5

Results

In this chapter the results of the Coulomb Excitation experiments on ^{74,76,78}Zn are presented. Results on the Coulomb Excitation of the isobaric ^{74,76,78}Ga contaminant are given in Appendix B.

5.1 ^{74}Zn

5.1.1 Data analysis of the relative measurement

In the current MINIBALL setup for Coulomb Excitation, the B(E2,$2_1^+ \rightarrow 0_1^+$) strength in radioactive ^{74}Zn is obtained through a relative comparison to the B(E2,$2_1^+ \rightarrow 0_1^+$) excitation strength of the target nucleus. This data analysis is discussed below.

Data reduction

The several steps in data reduction are illustrated in Fig. 5.1. The MINIBALL detectors are read in 'singles' mode during the 'In Beam' periods. In Fig. 5.1A , this 'In Beam' spectrum is shown. After offline sorting of the gamma's and particles, prompt and random spectra are generated. A typical time difference spectrum T_γ-$T_{particle}$ is given in Fig. 5.2 for A=74 and one CD quadrant. The prompt and random coincidence time-windows are not equal in time, so a scaling of the random spectrum is necessary. The prompt spectrum in Fig. 5.1C is generated without a condition on the detected particle energy and with *at least one prompt particle* attached to the gamma ray. No energy condition on the particle is imposed in the random spectrum (5.1B) neither, and *at least one random and no prompt coincident particle* is requested.

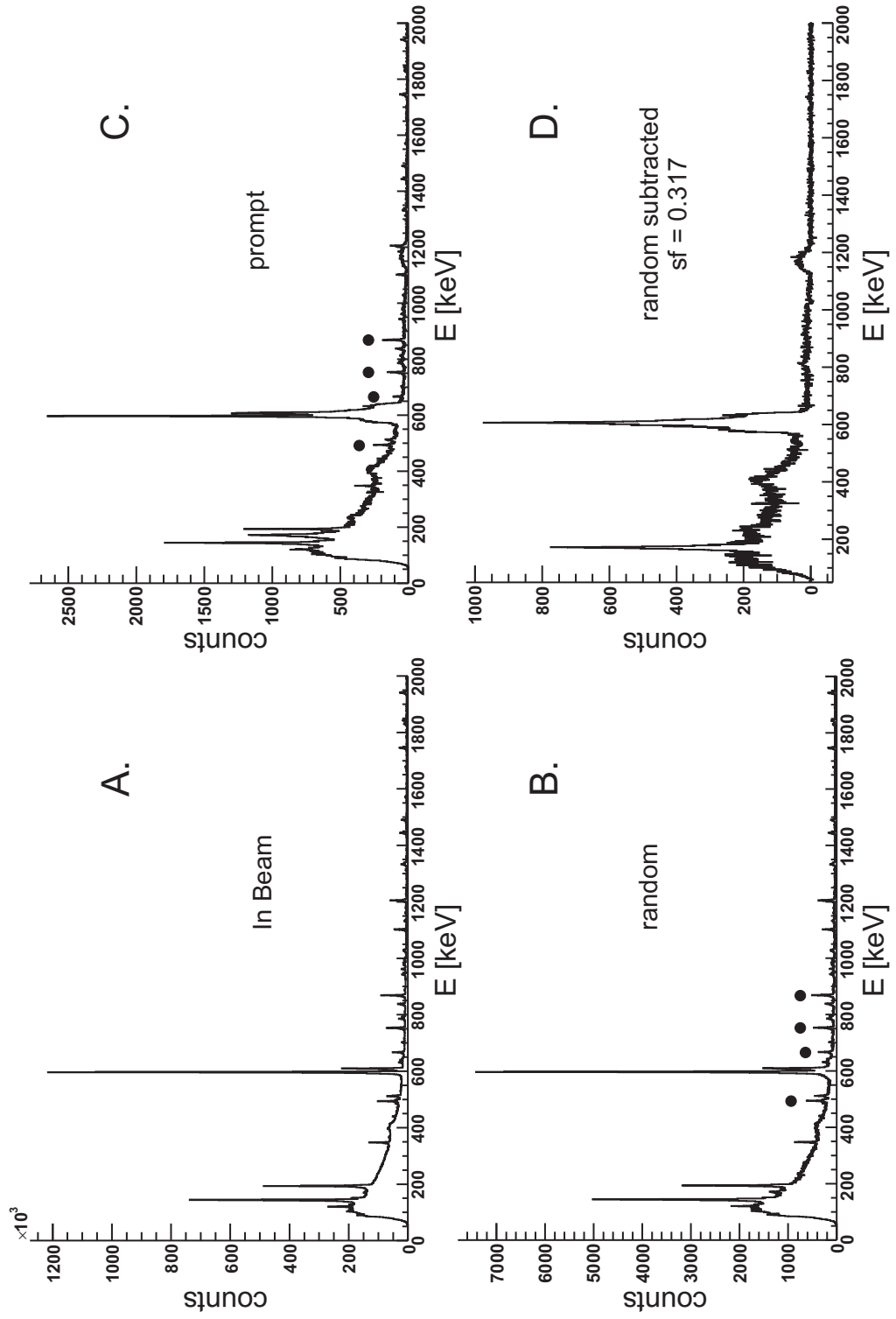

Figure 5.1: *A. The 'In Beam' singles spectrum. B. The random coincident spectrum. C. The prompt coincident spectrum. D. Random subtracted prompt spectrum. The β-decay lines used to scale the random spectrum are indicated with •. The additional line at 2353 keV and the range [2 MeV - 5 MeV] are not indicated.*

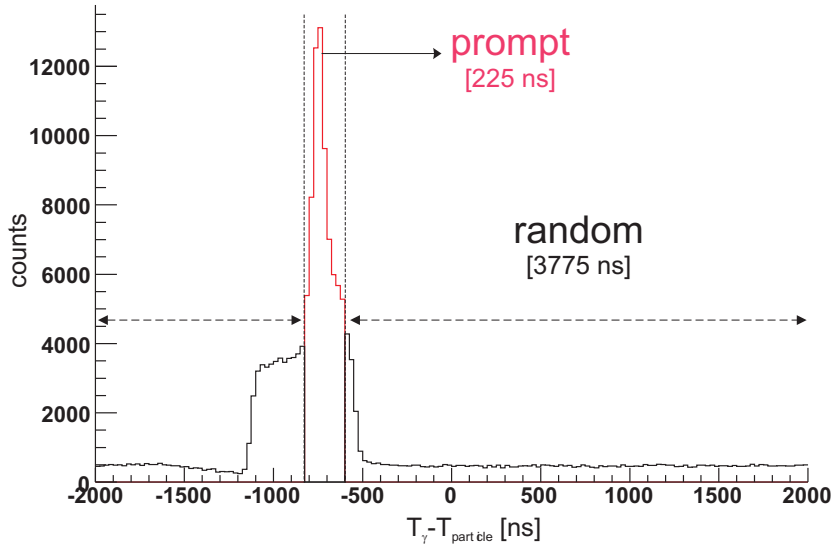

Figure 5.2: *Time difference between offline sorted γ's and particles. The time window of 4 μsec is divided in a prompt window of 225 ns and a random window of 3775 ns.*

Random subtraction

In table 5.1 $N_\gamma^{prompt}/N_\gamma^{random}$ is given for some intense beta decay lines, which are indicated in Fig. 5.1B,C, together with the number of counts over the energy range between 2 and 5 MeV. An average subtraction factor (sf) is taken as final number. The random subtracted spectrum is plotted in Fig. 5.1D.

N_γ	E [keV]						
	493*	666$^+$	753$^+$	868*	2353*	2000-5000	
prompt	429	283	487	580	1777	3715813	
random	1300	967	1519	1786	5852	11198698	
sf[1]	0.330	0.293	0.321	0.325	0.304	0.332	**0.317(0.021)**

Table 5.1: *β-decay lines used to scale the random to the prompt spectrum. The last column corresponds to the number of counts over the full range 2 MeV - 5 MeV (*:^{74}Ga, $^+$:^{74}Zn) and ^{1}:subtraction factor).*

Doppler correction

By requesting an additional condition on the detected particle energy, two CM ranges can be selected (see paragraph 4.1). In Fig. 5.3 three spectra are shown corresponding to the full detected CM range, CM1 (=beam detection) and CM2 (=target detection) (Fig. 5.3A is identical to 5.1D). The subtraction factor for the random coincidence correction is the same in the three cases. In the CM1 spectrum, the Doppler broadened $2^+ \rightarrow 0^+$ transition in ^{74}Zn can be Doppler corrected with the detected particle and gamma angles and energies (see 4.26 and 4.27). The same can be done in CM2 spectrum

for the detected target particle. The Doppler corrected spectra for beam(target) are shown in Fig. 5.4B(5.5B), the corresponding detected particles are shown in Fig. 5.4C(5.5C).

Beam contamination

In the previous chapter the number of counts during the laser on/off runs were already used to deduce the R_{ON} value (see tab.4.2). These numbers are explicitly given in table 5.2, while the ratio of the cross sections, used in eq. 4.2 are given in table 5.3. After random subtraction, the prompt coincident spectrum displays the Coulomb excitation excitation lines from ^{74}Zn,^{74}Ga and ^{120}Sn. No contaminating lines are present at the position of the $2_1^+ \rightarrow 0_1^+$ transition in ^{74}Zn, as shown by the laser on and laser off Doppler corrected, random subtracted spectra (CM1) in Fig. 5.6.

^{74}Zn		^{74}Ga - 171 keV		^{120}Sn		R_{ON}	*error*	r_{ON}	*error*
counts	*error*	counts	*error*	counts	*error*	[%]			
1228	39	683	38	102	12	82.9	4.4	0.207	0.011

Table 5.2: *In the first 3 columns, the total number of counts observed during all laser on/off runs on mass A=74 are given. These integrals were used in the previous chapter to deduce the extrapolation parameters $\Re_{CLX,1}$ and $\Re_{CLX,2}$. In the last 2 columns the result from the previous chapter is repeated.*

Integration

The integration of the Coulomb excitation peaks in the spectrum is performed with the procedure described in [Coe85]. The counts in the Coulomb excitation transitions are given in table 5.4 for the three CM ranges : FULL, CM1 and CM2, where the latter two ranges require additional energy information in the CD. In the last row, the corrected target yield is given, according to 4.2 with the parameters r and $\sigma^{Ga}_{E2,Sn}/\sigma^{Zn}_{E2,Sn}$ given in tables 5.2 and 5.3. The error on the corrected target yield is given by :

$$\frac{\Delta N^{Zn}_{\gamma,Target}}{N^{Zn}_{\gamma,Target}}^2 = \sqrt{\frac{\Delta N^{Total}_{\gamma,Target}}{N^{Total}_{\gamma,Target}}^2 + \frac{\Delta R_{ON}}{R_{ON}}^2} \tag{5.1}$$

The ratio of target excitation yield in CM1 over CM2 is 99(9)%, which is consistent with the GOSIA2 calculated yield ratio over the 2 CM ranges : 92.0%. The integration limits of the $4_1^+ \rightarrow 2_1^+$ transition in ^{74}Zn were fixed by a simulation of the Doppler shift in each crystal. The result of the simulation together with the experimental spectrum is given in Fig. 5.7.

	FULL	CM1	CM2
$\frac{\sigma^{Ga}_{E2,Sn}}{\sigma^{Zn}_{E2,Sn}}$	0.883	0.877	0.889

Table 5.3: *Ratio of the cross section for target excitation by Ga over Zn, used in eq. 4.2.*

	Energy [keV]	$J_i \rightarrow J_f$	FULL counts	FULL error	CM1 counts	CM1 error	CM2 counts	CM2 error
Zn	606	$2_1^+ \rightarrow 0_1^+$	22528	*165*	10249	*106*	9102	*105*
Zn	814	$4_1^+ \rightarrow 2_1^+$	363	*52*	153	*20*	218	*36*
Ga	171	?	5600	*124*	2503	*83*	2531	*83*
Sn	1173	$2_1^+ \rightarrow 0_1^+$	2052	*51*	876	*33*	903	*35*
	corrected		1736	*102*	734	*46*	763	*48*

Table 5.4: *Summary of the number of counts integrated over the three CM ranges (FULL,CM1 and CM2). In the last row, the corrected number of target excitation counts is given.*

GOSIA2 calculations

The input to GOSIA2, using the option "RAW" (see 4.6.1), requires the not efficiency corrected transition yields of the $2_1^+ \rightarrow 0_1^+$ and $4_1^+ \rightarrow 2_1^+$ transitions in Zn and the "corrected" $2_1^+ \rightarrow 0_1^+$ yield for the target excitation, given by 4.2. The minimization routine fits the unknown transition ME('s) for Zn. The ME's of the target ^{120}Sn were fixed to their adopted values :

$$ME(0_1^+ \rightarrow 2_1^+) = 0.4494(40)eb \quad (5.2)$$

$$ME(2_1^+ \rightarrow 2_1^+) = 0.029(13)eb \quad (5.3)$$

taken from [Ram01], [Sto05] (resp.). In the first minimization the unknown "re-orientation" matrix element ME_{22} was fixed to 0. The result of this minimization is summarized in table 5.5 for the three CM ranges. In a second step, the re-orientation ME was varied from 0.6 to -0.6 ($Q_{2_1^+}$=±0.455 eb). The result is summarized in Fig. 5.8. The error bar is limited to the statistical error bar, excluding the error on the R-value (beam contamination). The R-value determines the absolute value of the $B(E2,2_1^+ \rightarrow 0_1^+)$ value, whereas the relative behavior of the $B(E2,2_1^+ \rightarrow 0_1^+)$ value as a function of the assumed quadrupole moment does not significantly change with R. Thus, the error bar in Fig. 5.8 is solely determined by the number of counts in the projectile and target transitions. For comparison, the shell model prediction (SMII) is given in Fig. 5.8 as well. The influence of the quadrupole moment is most prominent over the CM2 range, as was already highlighted in Chapter 3 (see par.2.2.4). Even though the result in Fig. 5.8 hints a better consistency over the three CM ranges when a small negative quadrupole moment is assumed, no clear evidence can be given for this negative quadrupole moment. The systematics of quadrupole moments in the Zn isotopes and neighboring isotopes, together with shell model results indicate a negative quadrupole moment as well, this will be discussed in the following chapter.

Error determination

Statistical error : The statistical error on the final ME('s) is dominated by the statistics in the $2_1^+ \rightarrow 0_1^+$ and $4_1^+ \rightarrow 2_1^+$ transitions (column Zn($2_1^+ \rightarrow 0_1^+$) and Zn($4_1^+ \rightarrow 2_1^+$) in table 5.5) and the "corrected" $2_1^+ \rightarrow 0_1^+$ target yield (column Sn($2_1^+ \rightarrow 0_1^+$)+R_{ON} in table 5.5). The latter includes the error on the beam contamination (R_{ON}), given by eq. 5.1. The statistical error was deduced by subsequent GOSIA minimizations

with $N_x \pm dN_x$ where N_x indicates the number of de-excitation gamma's from particle x and dN_x is the error on this number of counts.

Systematics error : The systematical error is determined by the uncertainty on the ME's of the target and by the beam energy. The error on the beam energy was assumed to be 1% [Sie05]. Subsequent GOSIA minimization were performed with one of the parameters (the ME('s) or the energy) varied by their error bar. It is seen from table 5.5 that a 1% lower beam energy decreases the B(E2,$0_1^+ \rightarrow 2_1^+$) by ≈3%, while it increases the B(E2,$2_1^+ \rightarrow 4_1^+$) value by ≈6%, because the excitation of the 4_1^+ state is a double excitation (2-step process) it depends more strongly on the beam energy.

Final B(E2,$2_1^+ \rightarrow 0_1^+$) and B(E2,$4_1^+ \rightarrow 2_1^+$) values :

For the following three reasons, the final result for the B(E2,$2_1^+ \rightarrow 0_1^+$) value is the value obtained over the CM range labeled "FULL". First, over this region, the statistical error is the smallest. Second, since there is no gating on particle energy needed (no CM selection), systematical errors due to the detected particle energy are not present. Finally, the integration of the Coulomb excitation yields is reliable due to the high statistics and the clean spectrum around the transitions.
Contrary for B(E2,$4_1^+ \rightarrow 2_1^+$) the most reliable integration of the Coulomb excitation yield is over CM1. This is due to the low statistics in the $4_1^+ \rightarrow 2_1^+$ transition. Over the CM range "FULL", the Doppler smeared $4_1^+ \rightarrow 2_1^+$ yield can be hardly disentangled from the background counts. Over CM1, the Doppler corrected $4_1^+ \rightarrow 2_1^+$ yield is the most clearly observed and integration limits can be the most clearly defined.
The final B(E2,$0_1^+ \rightarrow 2_1^+$) and B(E2,$2_1^+ \rightarrow 4_1^+$) values are :

$$B(E2, 0_1^+ \rightarrow 2_1^+) = 0.2006^{+175}_{-151} e^2b^2 \quad (5.4)$$

$$B(E2, 2_1^+ \rightarrow 4_1^+) = 0.0857^{+126}_{-122} e^2b^2. \quad (5.5)$$

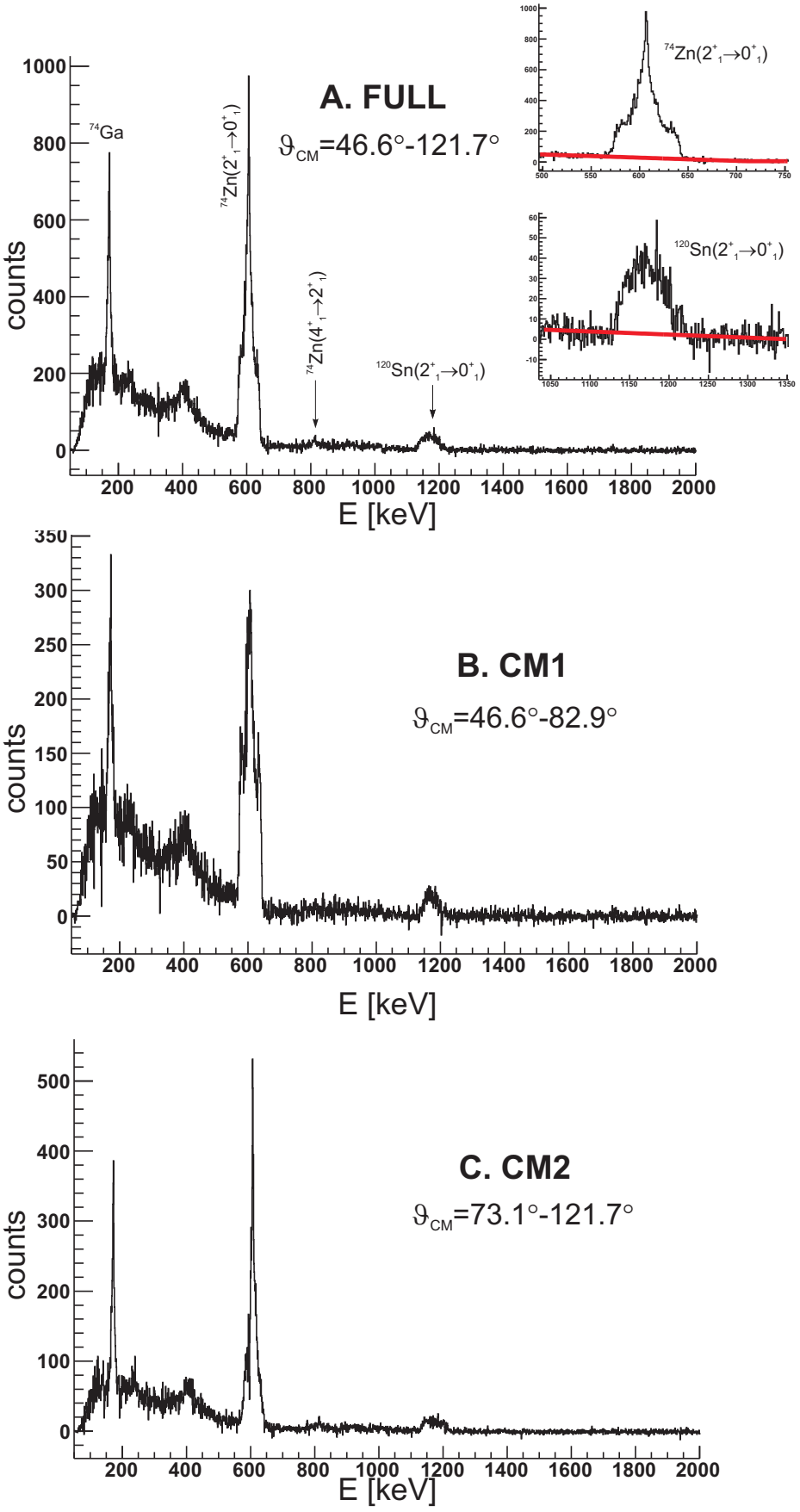

Figure 5.3: *A. The random subtracted prompt gamma spectrum over the full detected CM range. B. The random subtracted prompt gamma spectrum over CM1 range (beam detection). C. The random subtracted prompt gamma spectrum over CM2 range (target detection).*

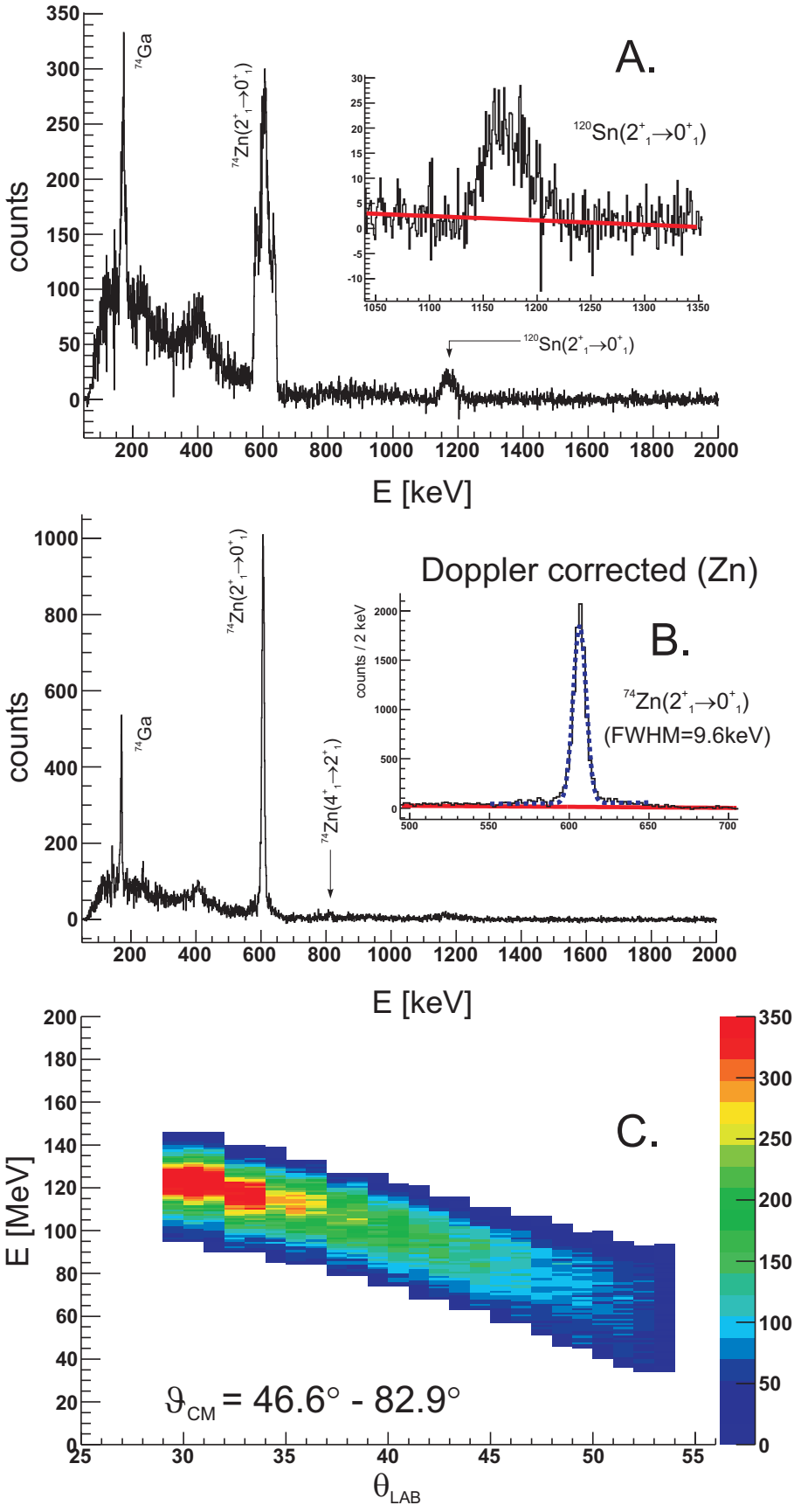

Figure 5.4: *A. The random subtracted prompt gamma spectrum over the CM1 range. B. The* **Doppler corrected** *random subtracted prompt gamma spectrum over CM1 range (beam detection). C. The detected particle detection (energy versus lab angle) over the considered CM range.*

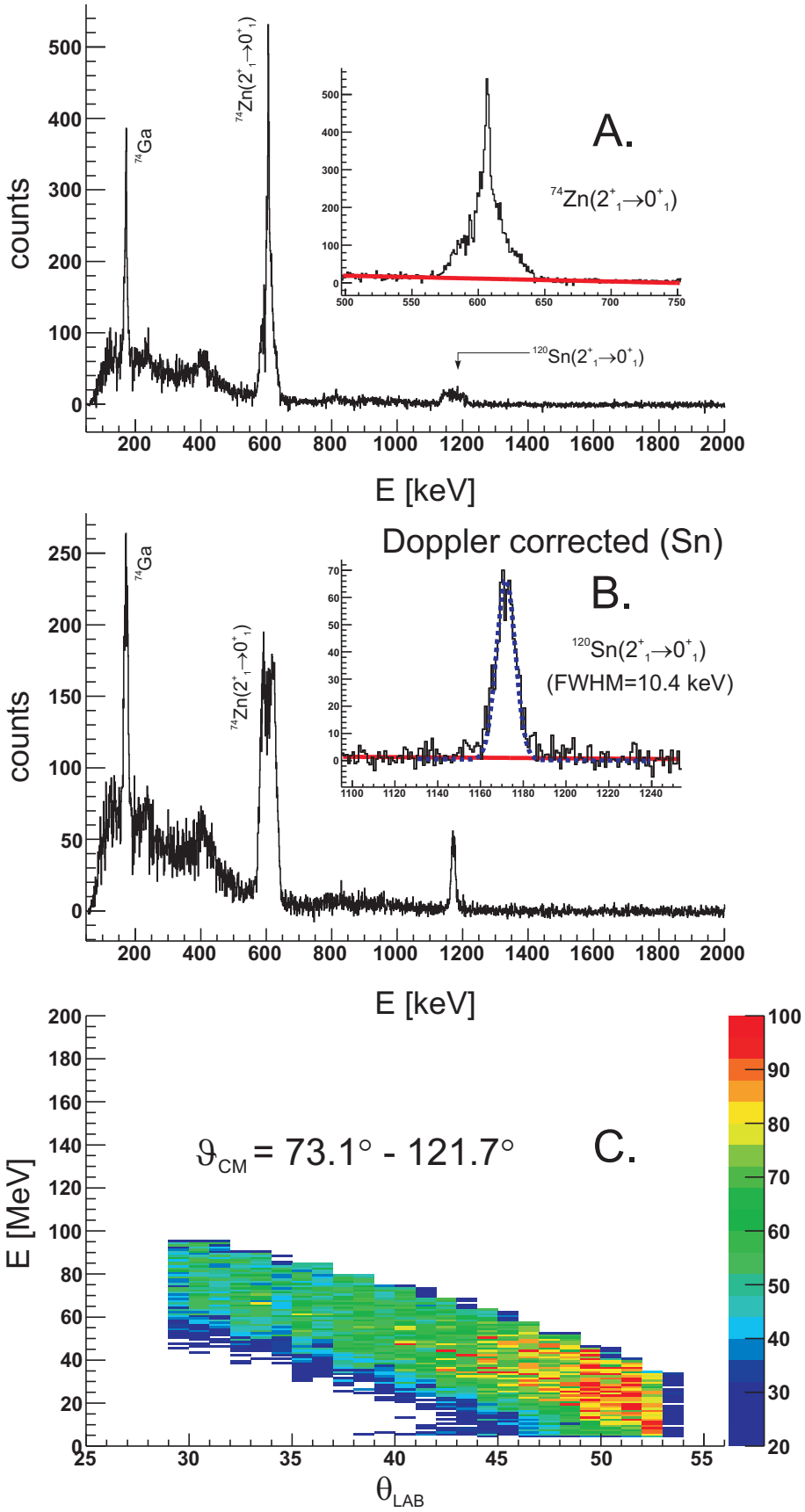

Figure 5.5: *A. The random subtracted prompt gamma spectrum over the CM2 range. B. The* **Doppler corrected** *random subtracted prompt gamma spectrum over CM2 range (target detection). C. The detected particle detection (energy versus lab angle) over the considered CM range.*

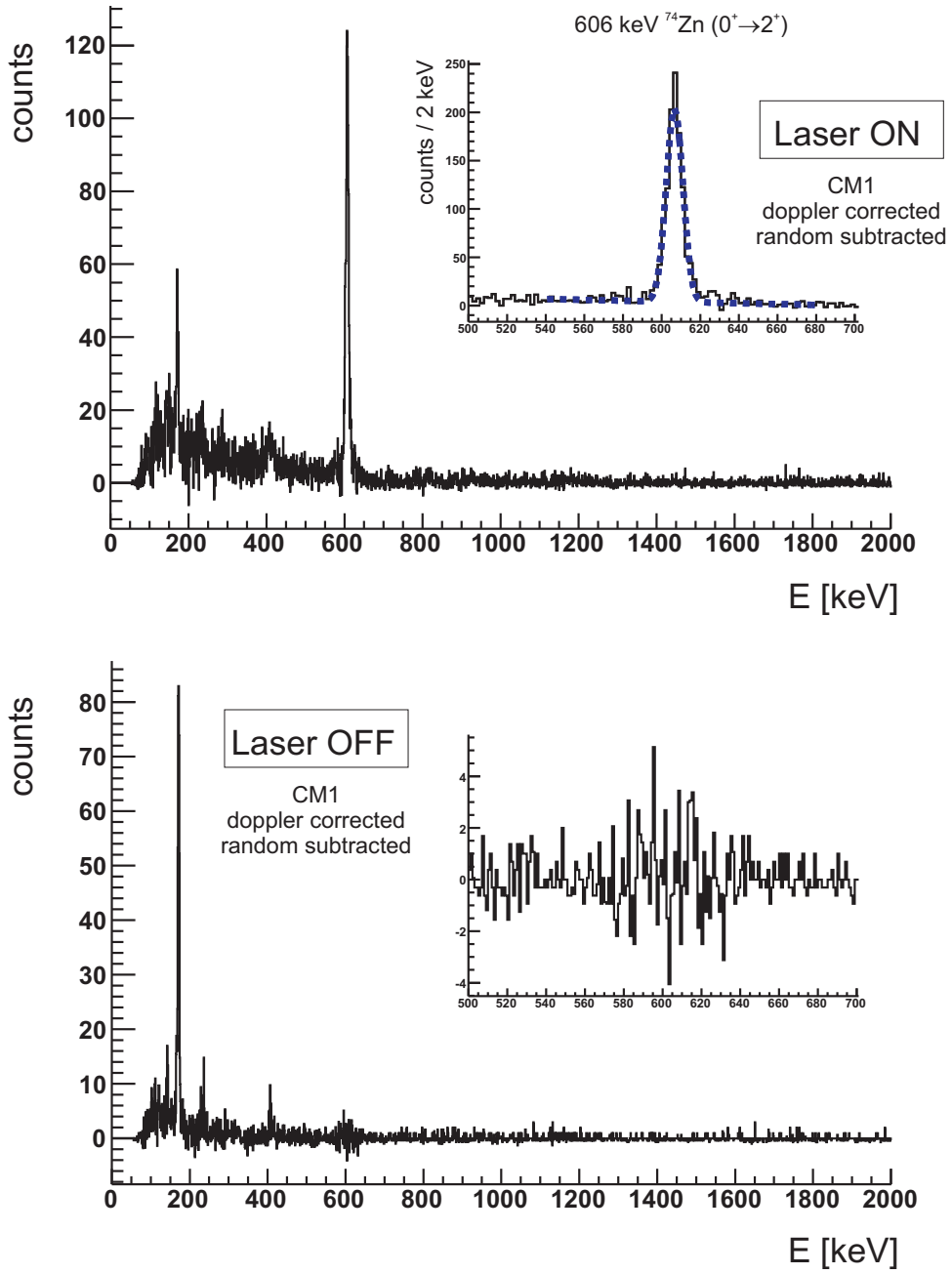

Figure 5.6: *Doppler corrected, random subtracted Coulomb excitation spectrum during laser ON(Top)/OFF(Bottom) periods of the laser on/off runs.*

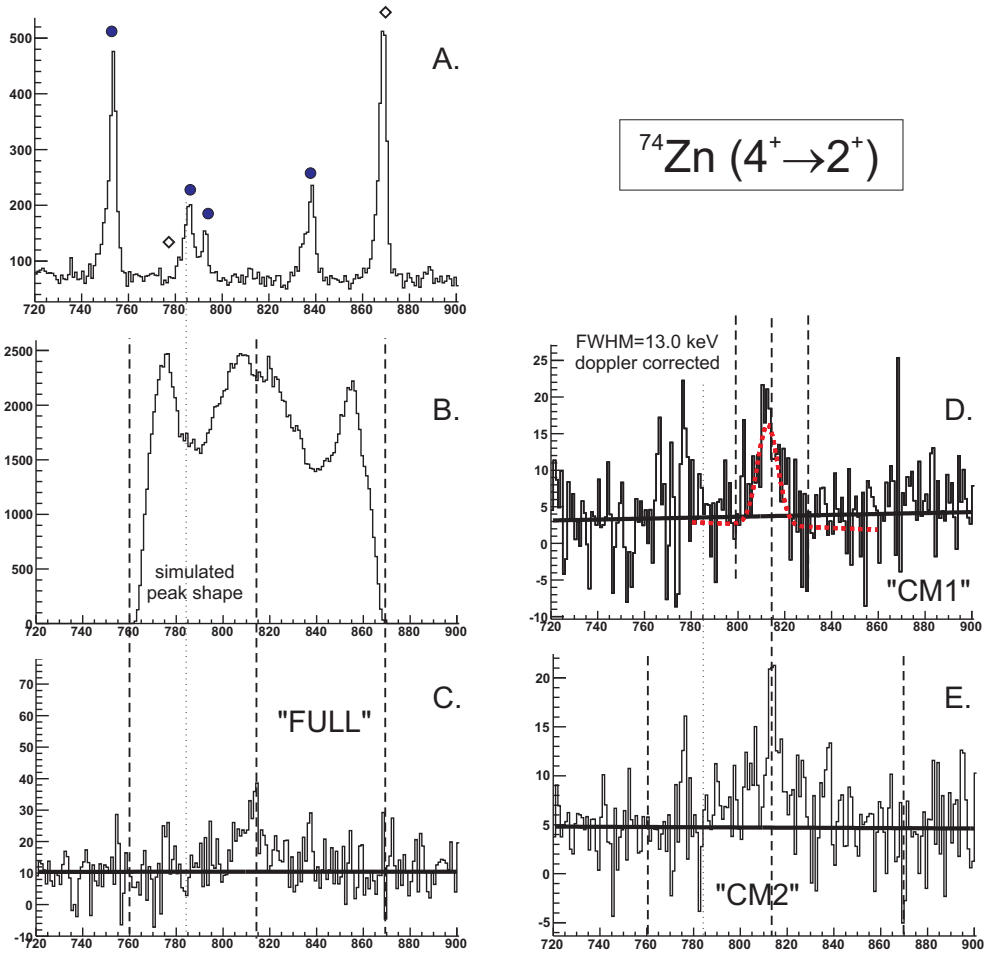

Figure 5.7: *A. Singles spectrum in the region of the 814 keV $4_1^+ \rightarrow 2_1^+$ transitions. Full circles indicate β-activity from ^{74}Zn, whereas open diamonds indicate β-activity from ^{74}Ga. B. The calculated Doppler shift of the 814 keV $4_1^+ \rightarrow 2_1^+$ transition (sum of all crystals). C. Random subtracted prompt spectrum : detail of the 814 keV line in the FULL CM range spectrum. No spurious β-decay activity is apparent in the random subtracted spectra. D. Detail of the Doppler corrected 814 keV transition in the CM1 range spectrum. E. Detail of the Doppler broadened 814 keV transition in the CM2 range spectrum.*

B(E2,$J_i \rightarrow J_f$)			Stat. Error				Syst. Error		
J_i	J_f	[e^2b^2]	$Zn(2_1^+ \rightarrow 0_1^+)$	$Zn(4_1^+ \rightarrow 2_1^+)$	$Sn(2_1^+ \rightarrow 0_1^+)$ + R_{ON}	**TOTAL**	ME Sn	Beam Energy	**TOTAL**
				FULL					
0_1^+	2_1^+	0.2006	$^{+0.0016}_{-0.0016}$	<0.1%	$^{+0.0144}_{-0.0122}$	$^{+0.0145}_{-0.0123}$	$^{+0.0040}_{-0.0040}$	$^{+0.0088}_{-0.0076}$	$^{+0.0097}_{-0.0086}$
2_1^+	4_1^+	0.0554	$^{+0.0004}_{-0.0004}$	$^{+0.0083}_{-0.0072}$	$^{+0.0001}_{-0.0002}$	$^{+0.0083}_{-0.0072}$	$^{+0.0002}_{-0.0002}$	$^{+0.0035}_{-0.0028}$	$^{+0.0035}_{-0.0028}$
				CM1					
0_1^+	2_1^+	0.2046	$^{+0.0020}_{-0.0020}$	<0.1%	$^{+0.0149}_{-0.0129}$	$^{+0.0151}_{-0.0130}$	$^{+0.0041}_{-0.0041}$	$^{+0.0090}_{-0.0078}$	$^{+0.0099}_{-0.0088}$
2_1^+	4_1^+	0.0857	$^{+0.0008}_{-0.0008}$	$^{+0.0114}_{-0.0114}$	$^{+0.0002}_{-0.0002}$	$^{+0.0114}_{-0.0114}$	$^{+0.0003}_{-0.0003}$	$^{+0.0054}_{-0.0043}$	$^{+0.0054}_{-0.0043}$
				CM2					
0_1^+	2_1^+	0.1964	$^{+0.0026}_{-0.0026}$	<0.1%	$^{+0.0167}_{-0.0145}$	$^{+0.0169}_{-0.0148}$	$^{+0.0039}_{-0.0039}$	$^{+0.0086}_{-0.0075}$	$^{+0.0095}_{-0.0084}$
2_1^+	4_1^+	0.0706	$^{+0.0008}_{-0.0008}$	$^{+0.0103}_{-0.0103}$	$^{+0.0004}_{-0.0004}$	$^{+0.0103}_{-0.0103}$	$^{+0.0003}_{-0.0003}$	$^{+0.0044}_{-0.0035}$	$^{+0.0045}_{-0.0035}$

Table 5.5: *Results from GOSIA2 calculations over the three different CM ranges, including an overview of the different error contributions (statistical and systematic).*

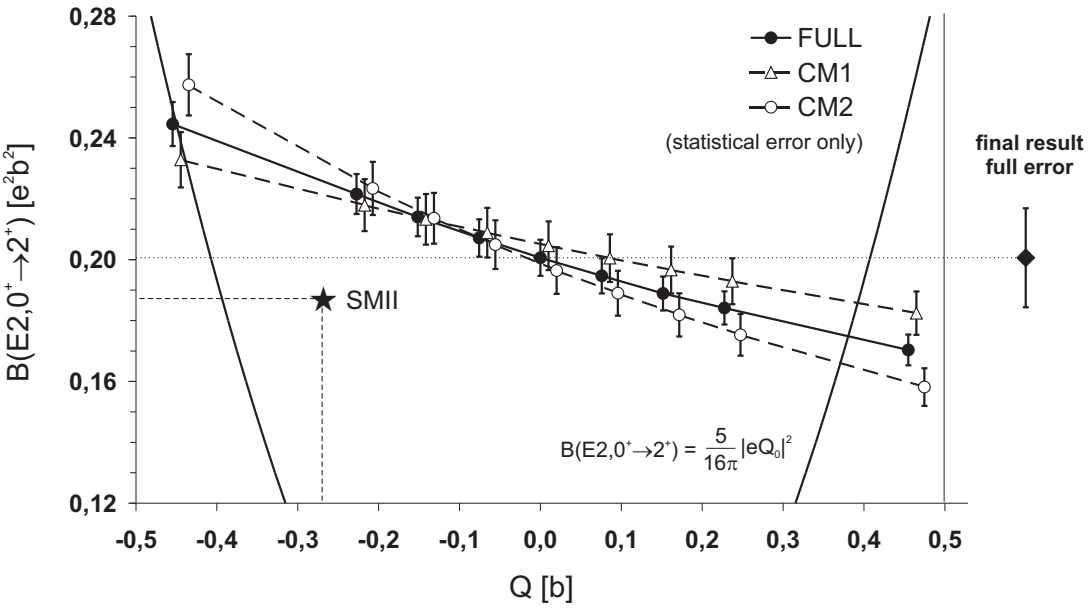

Figure 5.8: *^{74}Zn : Dependence of the resulting B(E2,$0_1^+ \rightarrow 2_1^+$) value on the (unknown) quadrupole moment of the 2_1^+ state, obtained for the three considered CM ranges in GOSIA2. The star represents the SMII prediction for ^{74}Zn. The point at the right side is the final B(E2) value for ^{74}Zn, including all statistical and systematical errors. The solid black lines indicate the rotational quadrupole moment, related to the B(E2,$0_1^+ \rightarrow 2_1^+$) as $|Q^{rot}_{2_1^+}|=0.91\sqrt{B(E2, 0_1^+ \rightarrow 2_1^+)}$.*

5.1.2 Data analysis of the absolute measurement

In the previous section the B(E2,$2_1^+ \rightarrow 0_1^+$) value was deduced from a relative comparison of target and beam excitation. Therefore, a new version of GOSIA was utilized which treats target and beam excitation simultaneous. The knowledge of the incoming beam intensity was circumvented in that way and the full -integrated- statistics over the full CD could be used in the analysis. In this section, the result from the previous section will be applied to check the absolute cross section, determined from the inelastic scattered particles in the individual annular CD strips.
The total incoming beam intensity can be determined from the detected elastic scattered particles. As discussed in Chapter 4, the *unconditioned* detection of the elastic scattered particles is reduced, i.e. 1 out of 64 scattered particles is detected without any condition [1]. If the particle is coincident with a gamma ray, it is detected anyhow. The time difference between gamma and particle is given in Fig. 5.9, where the "coincident" region is indicated (particles coming within the gamma gate, see Fig. 3.22), divided in equal time windows prompt and random coincident [2]. The particle times outside this coincidence window are marked "downscaled".
The total incoming beam intensity is detected in "scalers", which count the amount of fast triggers in each CD quadrant. The scalers detect at the same time the number

[1] This particle can be either prompt (or random) coincident with a gamma *or* it is really an elastic scattered particle !

[2] This definition is different from the definition in Fig. 5.2!

trigger type	delayed	delayed/64	coincident	accepted
	1254857	19607	150464	167479

Table 5.6: *Scaler information for the A=74 run.*

of coincident particles (particles within the coincident window). From this scaler information it is deduced that the *detected downscaled (1/64) elastic scattered particles* constitute 11.3% of the detected coincident particles. In table 5.6 the scaler information for A=74 is given. The accepted triggers are -irrespective of possible deadtime effects- the number of detected particles. The accepted triggers minus the coincident triggers should in principle give the number of elastic scattered particles : 17015 particles. This is close to the number of downscaled delayed triggers (delayed/64) = 19607 particles. The small discrepancy comes from downscaled particles which are at the same time coincident with a gamma! [3] The 17015 elastic detected elastic scattered particles are 11.3% of the total detected coincident particles. This factor of 11.3% is then applied as a scaling factor to the detected particles in the region "downscaled", to make this number of particles consistent with the number of detected coincident particles. The main reason for this scaling is that originally coincident particles might loose there correlation with the gamma ray in the offline sort due to loss in detection efficieny of the gamma ray (dead time in the DGF module, time shift of the gamma ray of >100ns,...). The profile of the elastic scattering cross section is given by the particles detected in the region marked "downscaled", while the absolute number of *detected elastic scattered particles in each strip* is governed by appropriate scaling of the number of counts in each strip by :

$$(\frac{N_{strip} \times 0.113 \times N_{coin}}{N_{downsc}} - \frac{(1-\epsilon_{Zn})N_{Zn}}{64 \cdot \epsilon_{Zn}} - \frac{(1-\epsilon_{Sn})N_{Sn}}{64 \cdot \epsilon_{Sn}})/(1 + r \cdot \frac{\sigma_{Ga}^{Ruth}}{\sigma_{Zn}^{Ruth}}) \qquad (5.6)$$

where N_{strip} is the number of detected downscaled particles in each strip, $N_{coin/downsc}$ in the number of coincident/downscaled particles detected in the **full** CD, $N_{Zn/Sn}$ the number of particles detected in prompt coincidence with a gamma ray which is detected in the region of the $2_1^+ \rightarrow 0_1^+$ energy. This number is corrected, again for the beam contamination, since the interest is in elastically scattered Zn particles. The differential cross section is then given by :

$$\frac{d\sigma_{Ruth}}{d\Omega_{strip}} = \frac{N_{strip} \times 64 \cdot A_{target} \cdot 10^4}{I_{inc} \cdot \rho d \cdot N_A \cdot 2\pi \cdot sin\vartheta \cdot \Delta\vartheta} \qquad (5.7)$$

expressed in barn, where $d\Omega_{strip}$ is the solid angle in the CM covered by the CD strip, I_{inc} the incoming beam intensity, ρd the target thickness in mg/cm^2, N_A Avogadro's number and $\Delta\vartheta$ the angular coverage of the CD strip. Using this formula, the parameter I_{inc} can be fitted to the elastic scattered particles and to the known target excitation cross section. Both approaches result in an incoming beam intensity of 1.38E10 particles (elastic cross section) and 1.44E10 particles (target excitation cross section), where an average value is taken of 1.41(0.03)E10 in the following. For comparison, the detected fast triggers in the scalers give an incoming intensity of 5.6E10 particles. The lower "detected" value can be understood from the dead time induced by the CAEN ADC's. The scalers have a dead time less then 100 ns, while the CAEN

[3] The downscaling is on ALL particles, irrespective if they came in coincident with a gamma or not!

ADC's have a fixed dead time of 15 μsec after each detected particle.
Once the incoming beam intensity is determined, the unknown differential inelastic cross section of Zn can be plotted, using the number of counts in each strip detected in prompt coincidence with a gamma ray in the region of the $2_1^+ \rightarrow 0_1^+$ transition. For the CM1 region a more stringent condition can be put by requesting a proper Doppler correction. It should be noted that in the outer regions of the CD, the 2 CM ranges are difficult to separate, since the energies of the detected particles (Zn or Sn) might overlap. In Fig. 5.10 the resulting differential cross section are given together with calculated differential cross sections (CLX calculation, $Q_{2_1^+}$=0 eb and the B(E2,$2_1^+ \rightarrow 0_1^+$) value for the FULL CM range = 0.2011 e^2b^2). In Fig. 5.11 a detail of the inelastic cross sections is given for Zn and Sn excitation. The Zn differential cross section in red is calculated with $Q_{2_1^+}$=0. eb and B(E2,$0_1^+ \rightarrow 2_1^+$) =0.201 e^2b^2. The black dashed lines correspond to $Q_{2_1^+}$=+0.23 eb (top figure) and $Q_{2_1^+}$=-0.23 eb (bottom figure). The three B(E2,$2_1^+ \rightarrow 0_1^+$) values obtained over "CM1","CM2" and "FULL" ranges, associated to these quadrupole moments (see Fig. 5.8), were used in the calculation of the differential cross section. The data points were integrated over three strips in order to decrease the statistical fluctuations. The one point in the CM2 region is the average scattering angle for detection in the inner three CD strips.
The steeper trend over the "CM1" range and the low "CM2" data point are better reproduced when a negative quadrupole moment is assumed.

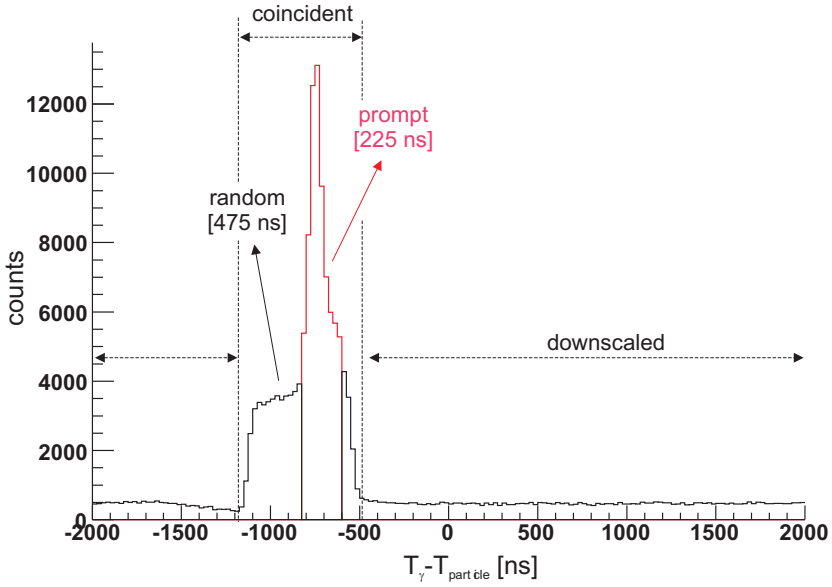

Figure 5.9: *Definition of time regions : coincident, downscaled, prompt and random in the T_γ-$T_{particle}$ spectrum of one CD quadrant and the full MINIBALL array.*

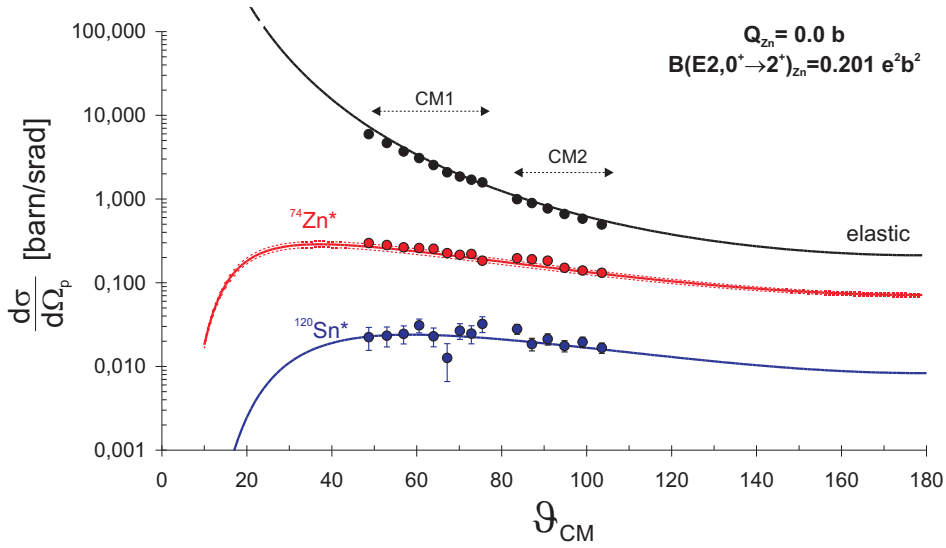

Figure 5.10: *Calculated differential cross sections for elastic scattering and inelastic scattering where either ^{74}Zn or ^{120}Sn are excited together with the experimental data points. The data points correspond to the CM1 and CM2 regions. Part of the overlapping region is taken out. The dashed lines corresponds to the differential cross section, taking into account the total (statistical+systematical) error on the matrix element 0_1^+-2_1^+ in ^{74}Zn (see table 5.5).*

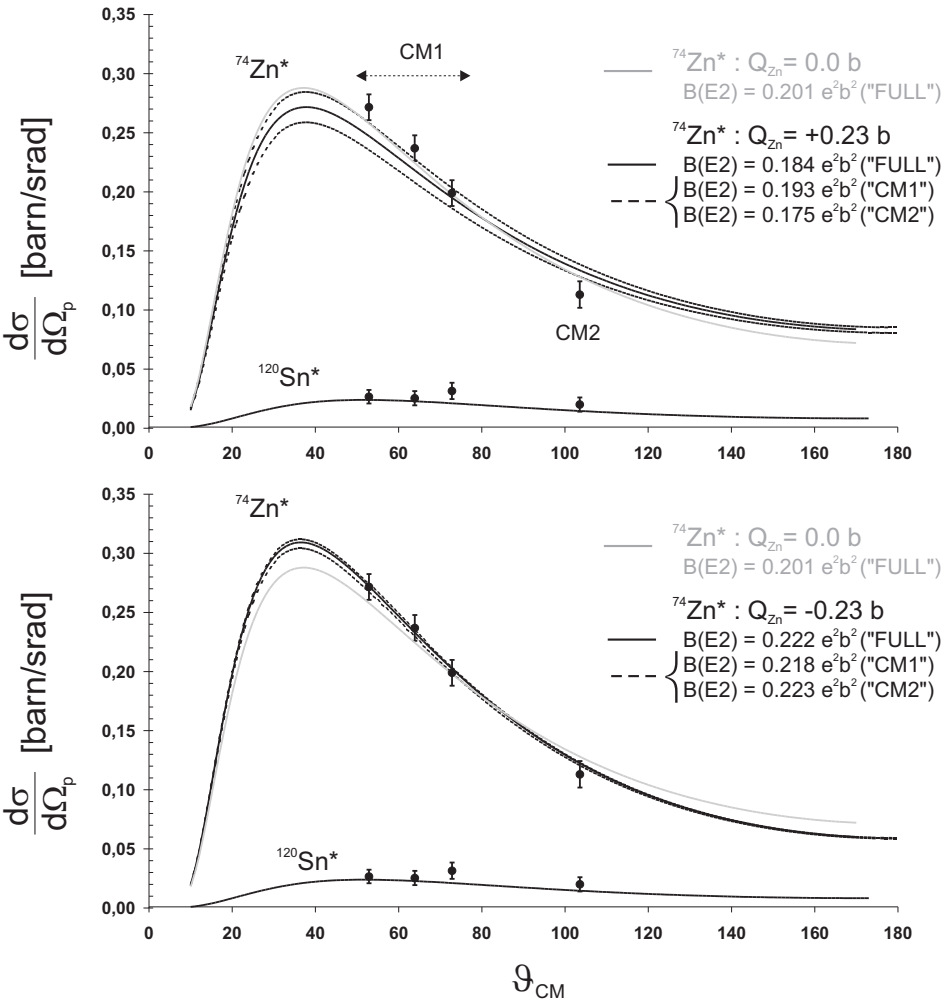

Figure 5.11: *Calculated differential cross sections for inelastic scattering of ^{74}Zn and ^{120}Sn, utilizing the B(E2) value for $Q_{2_1^+}$=0.0 eb over the FULL CM range (grey, top and bottom), the B(E2) value assuming $Q_{2_1^+}$=+0.23 eb for the three CM ranges (see Fig. 5.8, top) and the B(E2) value assuming $Q_{2_1^+}$=-0.23 eb for the three CM ranges (see Fig. 5.8, bottom). The one experimental point in the CM2 region (sum of three annular strips) can be reproduced only when assuming a negative quadrupole moment.*

5.2 ^{76}Zn

The data analysis of the A=76 measurement is analogue to the A=74 analysis. The same analysis steps, figures and tables are discussed in the following paragraphs.

5.2.1 Data analysis of the relative measurement

Data reduction

The several steps in data reduction are illustrated in Fig. 5.12. The MINIBALL detectors are read in 'singles' mode during the 'In Beam' periods. In Fig. 5.12A , this 'In Beam' spectrum is shown. After offline sorting of the gamma's and particles, prompt and random spectra are generated. The time difference spectrum for A=76 is equivalent to Fig. 5.2 for A=74. The prompt and random coincidence time-windows are not equal in time, so a scaling of the random spectrum is necessary. The prompt spectrum in Fig. 5.12C is generated without a condition on the detected particle energy and with *at least one prompt particle* attached to the gamma ray. No energy condition on the particle is imposed in the random spectrum (5.12B) neither, and *at least one random and no prompt coincident particle* is requested.

Random subtraction

In table 5.7 $N_\gamma^{prompt}/N_\gamma^{random}$ is given for some intense beta decay lines, which are indicated in Fig. 5.12B,C. An average subtraction factor (sf) is taken as final number. The random subtracted spectrum is plotted in Fig. 5.12D.

N_γ	E [keV]						
	199^+	366^+	546^*	563^+	1108^+	1500-2500	
prompt	1129	129	223	575	128	1023	
random	3787	339	683	1885	372	2936	
sf[1]	0.298	0.381	0.327	0.305	0.344	0.348	**0.334(0.031)**

Table 5.7: *β-decay lines used to scale the random to the prompt spectrum. The last column corresponds to the number of counts over the full range 1.5 - 2.5 MeV (*:^{76}Ga, $^+$:^{76}Zn and ^{1} = subtraction factor.*

Doppler correction

By requesting an additional condition on the detected particle energy, two CM ranges can be selected (see paragraph 4.1). In Fig. 5.13 three spectra are shown corresponding to the full detected CM range, CM1 (=beam detection) and CM2 (=target detection). Fig. 5.13A corresponds to 5.12D. The subtraction factor for the random coincidence correction is the same in the three cases. In the CM1 spectrum, the Doppler broadened $2^+ \rightarrow 0^+$ transition in ^{76}Zn can be Doppler corrected with the detected particle and gamma angles and energies (see 4.26 and 4.27). The same can be done in CM2 spectrum for the detected target particle. The Doppler corrected spectra for beam(target), respectivily, are shown in Fig. 5.14B(5.15B), the corresponding detected particles are shown in Fig. 5.14C(5.15C).

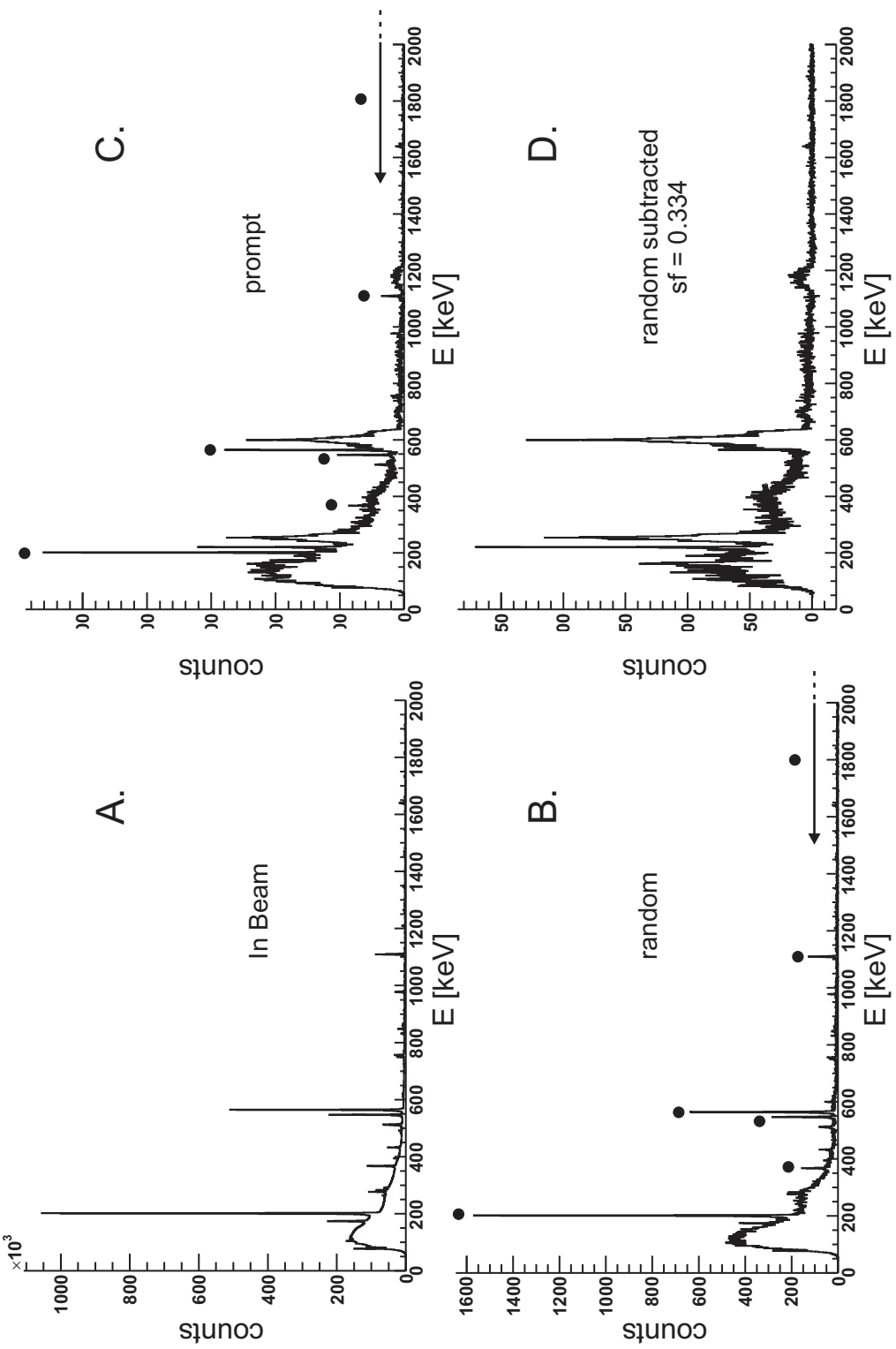

Figure 5.12: *A. The 'In Beam' singles spectrum. B. The random coincident spectrum. C. The prompt coincident spectrum. D. Random subtracted prompt spectrum. The β-decay lines used to scale the random spectrum are indicated with •. The range [1.5 - 2.5 MeV] is partially indicated.*

Beam contamination

In the previous chapter the number of counts during the laser on/off runs were already used to deduce the R_{ON} value (see tab.4.2). These numbers are explicitly given in table 5.8, while the ratio of the cross sections, used in eq. 4.2 are given in table 5.9. After random subtraction, the prompt coincident spectrum displays the Coulomb excitation lines from ^{76}Zn,Ga and ^{120}Sn. No contaminating lines are present at the position of the $2_1^+ \rightarrow 0_1^+$ transition in ^{76}Zn, as is proven by the laser on and laser off Doppler corrected, random subtracted spectra (CM1) in Fig. 5.16.

^{76}Zn		^{76}Ga - 253keV		^{120}Sn		R_{ON}	*error*	r_{ON}	*error*
counts	*error*	counts	*error*	counts	*error*	[%]			
510	26	375	27	79	10	72.6	7.3	0.377	0.038

Table 5.8: *In the first 3 columns, the total number of counts observed during all laser on/off runs on mass A=76 are given. These integrals were used in the previous chapter to deduce the extrapolation parameters $\Re_{CLX,1}$ and $\Re_{CLX,2}$. In the last 2 columns the result from the previous chapter is repeated.*

Integration

The integration of the Coulomb excitation peaks in the spectrum is performed with the procedure described in [Coe85]. The counts in the Coulomb excitation peaks are given in table 5.10 for the three CM ranges : FULL, CM1 and CM2, where the latter 2 ranges require additional energy information in the CD. In the last row, the corrected target yield is given, according to 4.2 with the parameters r, $\sigma^{Ga}_{E2,Sn}/\sigma^{Zn}_{E2,Sn}$ and $\sigma^{Ne}_{E2,Sn}/\sigma^{Zn}_{E2,Sn}$ given in tables 5.8 and 5.9. The error on the corrected target yield is analogue to eq. 5.1. The integration limits of the $4_1^+ \rightarrow 2_1^+$ transition in ^{76}Zn were fixed by a simulation of the Doppler shift in each crystal. The result of the simulation together with the experimental spectrum is given in Fig. 5.17.

GOSIA2 calculations

The input to GOSIA2, using the option "RAW" (see 4.6.1), requires the not efficiency corrected transition yields of the $2_1^+ \rightarrow 0_1^+$ transition in Zn and the "corrected" $2_1^+ \rightarrow 0_1^+$ yield for the target excitation, given by 4.2. The minimization routine fits the ME(0_1^+-2_1^+) of ^{78}Zn transition to the experimental yield. The ME's of the target ^{120}Sn were fixed to the adopted values eq. 5.2 and eq. 5.3. In a first calculation the unknown "re-orientation" matrix element (ME) ME_{22} was fixed to 0. The results of these calculation are summarized in table 5.11. In a second step, the re-orientation ME_{22} was varied

	FULL	CM1	CM2
$\frac{\sigma^{Ga}_{E2,Sn}}{\sigma^{Zn}_{E2,Sn}}$	0.887	0.883	0.885
$\frac{\sigma^{Ne}_{E2,Sn}}{\sigma^{Zn}_{E2,Sn}}$	0.106	-	0.173

Table 5.9: *Ratio of the cross section for target excitation by Ga/Zn and Ne/Zn, used in eq. 4.2. Ne only contributes in the full CM range and CM2 range.*

	Energy [keV]	$J_i \rightarrow J_f$	FULL counts	FULL error	CM1 counts	CM1 error	CM2 counts	CM2 error
Zn	599	$2_1^+ \rightarrow 0_1^+$	4848	*78*	2353	*52*	2351	*55*
Zn	697	$4_1^+ \rightarrow 2_1^+$	80	*29*	40	*12*	53	*21*
Ga	254	?	2459	*73*	1077	*49*	1112	*48*
Ga	220	?	718	*43*	280	*26*	399	*29*
Ga	160	?	643	*57*	309	*37*	305	*37*
Sn	1173	$2_1^+ \rightarrow 0_1^+$	656	*28*	278	*17*	373	*20*
	corrected		488	*53*	208	*25*	276	*32*

Table 5.10: *Summary of the number of counts integrated over the three CM ranges (FULL,CM1 and CM2). In the last row, the corrected number of target excitation counts is given according to eq. 4.2*

from 0.6 to -0.6 ($Q_{2_1^+}$=±0.455 eb). The result is summarized in Fig. 5.18. The error bar in the figure is limited to the statistical error bar, excluding the error on the R-value (beam contamination). As in the ^{74}Zn experiment, the error bars are limited to the statistical errors. The consistency between the three CM ranges is less clear, due to the limited target excitation yield over the CM1 and CM2 ranges, which increases the statistical error bar. No conclusion can be drawn on the sign of the quadrupole moment. For comparison, the shell model prediction (SMII) is given in Fig. 5.18 as well.

Error determination

Statistical error : The statistical error on the final ME('s) is determined by the statistics in the $2_1^+ \rightarrow 0_1^+$ (and $4_1^+ \rightarrow 2_1^+$ transitions) in Zn (column Zn($2_1^+ \rightarrow 0_1^+$) and Zn($4_1^+ \rightarrow 2_1^+$) in table 5.11) and the "corrected" $2_1^+ \rightarrow 0_1^+$ target yield (column Sn($2_1^+ \rightarrow 0_1^+$)+R_{ON} in table 5.11). The latter includes the error on the beam contamination (R_{ON}), given by eq. 5.1.

Systematics error : The systematical error is determined by the uncertainty on the ME's of the target and by the beam energy. The error on the beam energy was assumed to be 1%. It is seen from table 5.11 that a 1% lower beam energy decreases the B(E2,$0_1^+ \rightarrow 2_1^+$) by ≈3%, while it increases the B(E2,$2_1^+ \rightarrow 4_1^+$) value by ≈5%, because the excitation of the 4_1^+ state is a double excitation (2-step process) it depends more strongly on the beam energy.

Final B(E2,$2_1^+ \rightarrow 0_1^+$) and B(E2,$4_1^+ \rightarrow 2_1^+$) values :

For the following three reasons, the final result for the B(E2,$2_1^+ \rightarrow 0_1^+$) value is the value obtained over the CM range labeled "FULL". First, over this region, the statistical error is the smallest. Second, since their is no gating on particle energy needed (no CM selection), systematical errors due to the detected particle energy are not present. Finally, the integration of the peaks is reliable due to the high statistics and the clean spectrum around the transitions.
Contrary, due to the low statistics in the $4_1^+ \rightarrow 2_1^+$ transition, the most reliable integration of the peak is over CM1, where the Doppler corrected $4_1^+ \rightarrow 2_1^+$ yield is the most

clearly observed. Over the CM range "FULL", the Doppler smeared $4_1^+ \rightarrow 2_1^+$ yield can hardly be disentangled from the background counts. The final B(E2,$0_1^+ \rightarrow 2_1^+$) and B(E2,$2_1^+ \rightarrow 4_1^+$) values are :

$$B(E2, 0_1^+ \rightarrow 2_1^+) = 0.1452^{+208}_{-161} e^2b^2 \quad (5.8)$$

$$B(E2, 2_1^+ \rightarrow 4_1^+) = 0.0576^{+163}_{-163} e^2b^2. \quad (5.9)$$

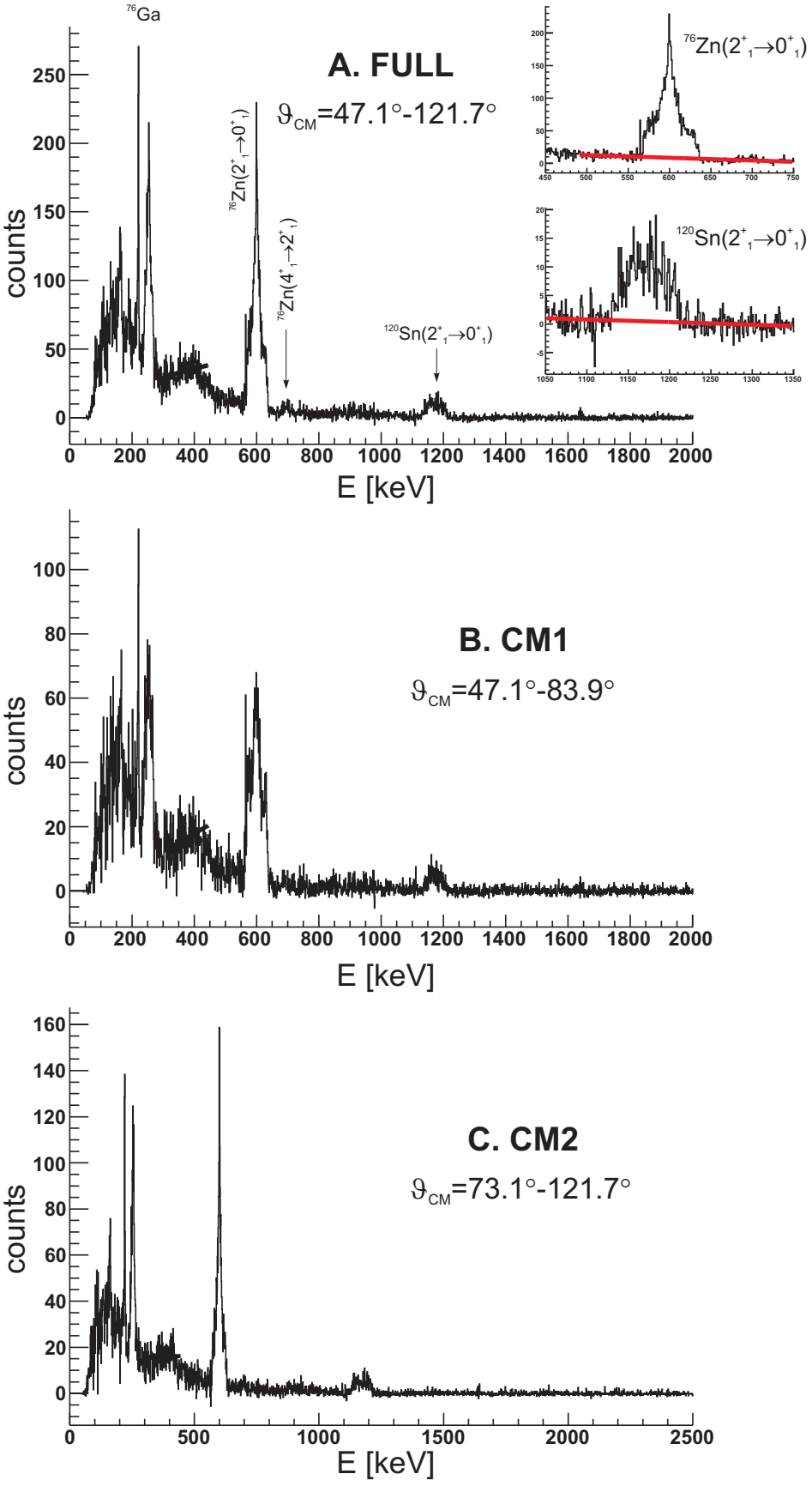

Figure 5.13: *A. The random subtracted prompt gamma spectrum over the full detected CM range. B. The random subtracted prompt gamma spectrum over CM1 range (beam detection). C. The random subtracted prompt gamma spectrum over CM2 range (target detection).*

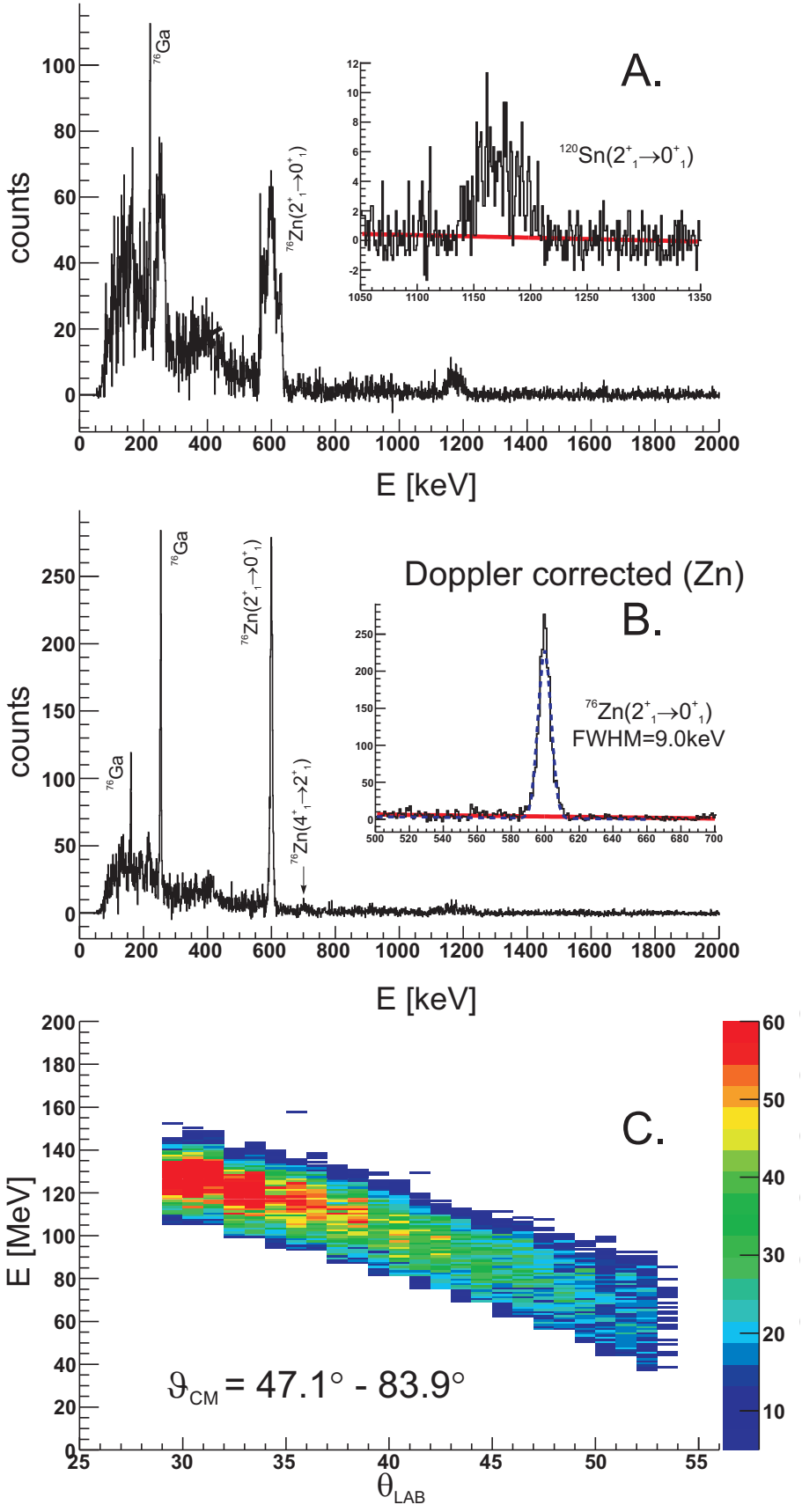

Figure 5.14: *A. The random subtracted prompt gamma spectrum over the CM1 range. B. The* **Doppler corrected** *random subtracted prompt gamma spectrum over CM1 range (beam detection). C. The detected particle detection (energy versus lab angle) over the considered CM range.*

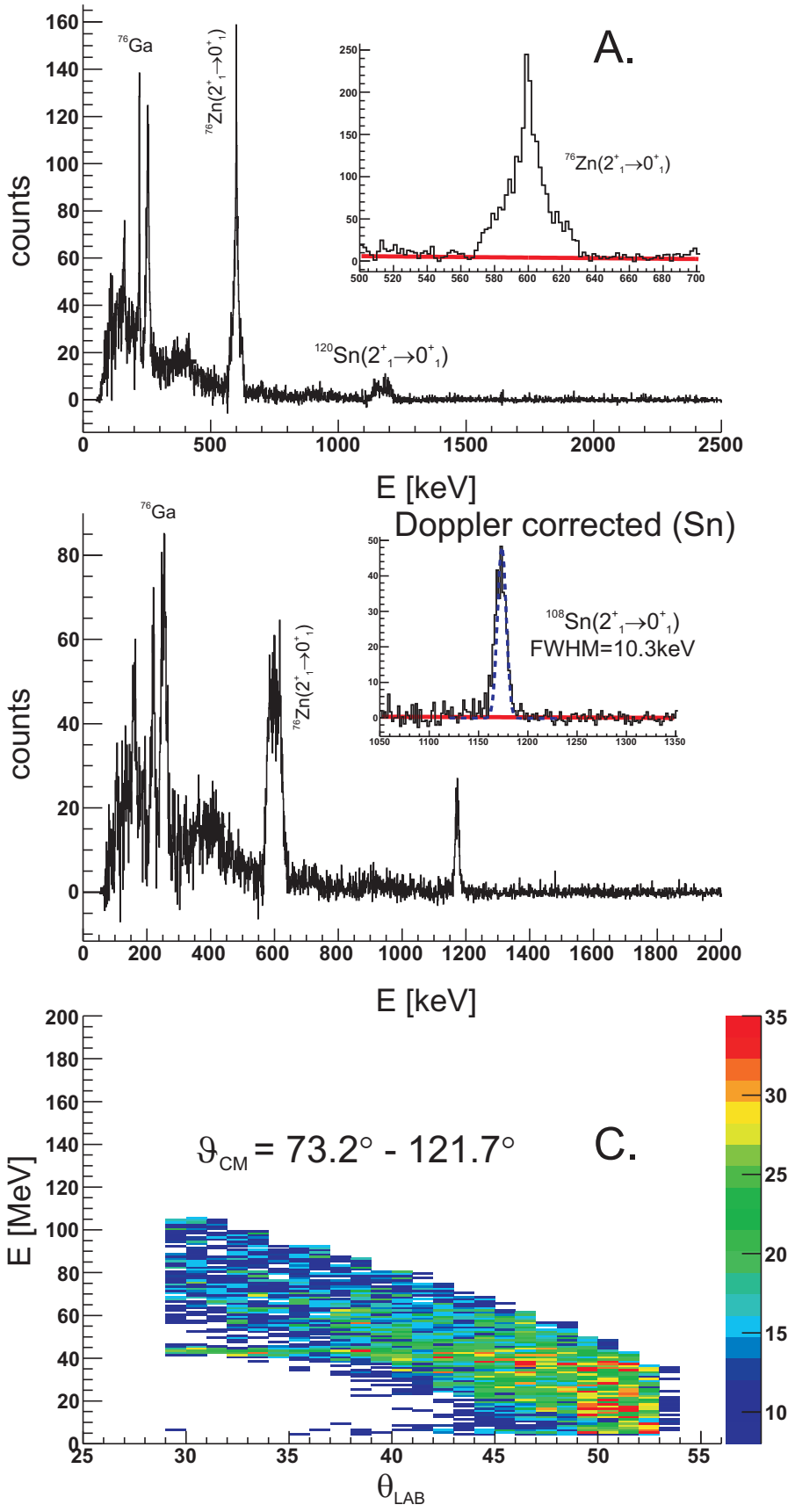

Figure 5.15: *A. The random subtracted prompt gamma spectrum over the CM2 range. B. The* **Doppler corrected** *random subtracted prompt gamma spectrum over CM2 range (target detection). C. The detected particle detection (energy versus lab angle) over the considered CM range.*

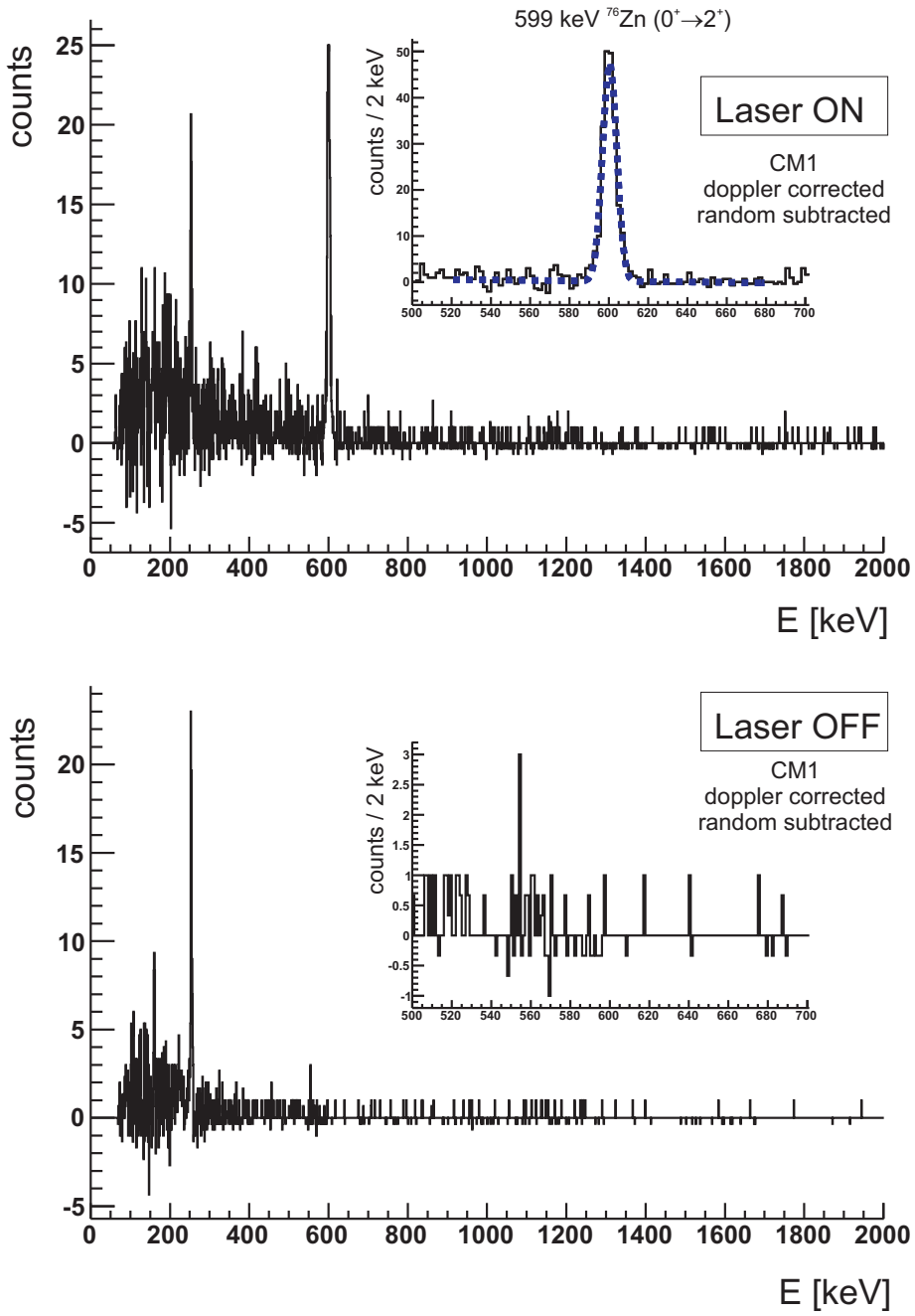

Figure 5.16: *Doppler corrected, random subtracted Coulomb excitation spectrum during laser ON(Top)/OFF(Bottom) periods of the laser on/off runs.*

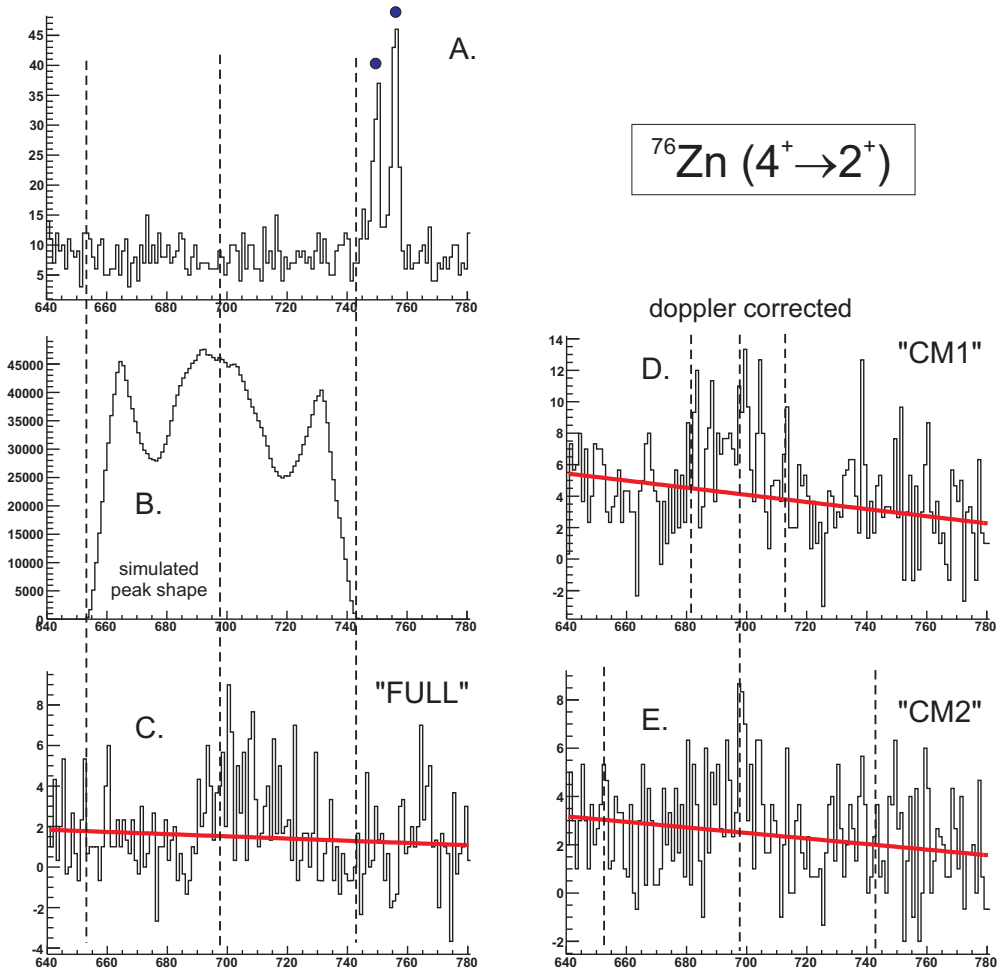

Figure 5.17: *A. Singles spectrum in the region of the 697 keV $4_1^+ \rightarrow 2_1^+$ transitions. No β-decay activity contaminates this region. Full circles indicate β-activity from ^{76}Zn. B. The calculated Doppler shift of the 814 keV $4_1^+ \rightarrow 2_1^+$ transition (sum of all crystals). C. Random subtracted prompt spectrum : detail of the 697 keV line in the FULL CM range spectrum. No spurious β-decay activity is apparent in the random subtracted spectra. D. Detail of the Doppler corrected 697 keV transition in the CM1 range spectrum. E. Detail of the Doppler broadened 697 keV transition in the CM2 range spectrum.*

B(E2,$J_i \to J_f$)			Stat. Error				Syst. Error		
J_i	J_f	[e^2b^2]	$Zn(2_1^+ \to 0_1^+)$	$Zn(4_1^+ \to 2_1^+)$	$Sn(2_1^+ \to 0_1^+)$ + R_{ON}	**TOTAL**	ME Sn	Beam Energy	**TOTAL**
FULL									
0_1^+	2_1^+	0.1452	$^{+0.0025}_{-0.0025}$	<0.1%	$^{+0.0198}_{-0.0154}$	$^{+0.0199}_{-0.0156}$	$^{+0.0028}_{-0.0026}$	$^{+0.0052}_{-0.0029}$	$^{+0.0059}_{-0.0039}$
2_1^+	4_1^+	0.0424	<0.1%	$^{+0.0096}_{-0.0094}$	$^{+0.0002}_{-0.0003}$	$^{+0.0096}_{-0.0094}$	$^{+0.0001}_{-0.0001}$	$^{+0.0022}_{-0.0022}$	$^{+0.0022}_{-0.0022}$
CM1									
0_1^+	2_1^+	0.1592	$^{+0.0038}_{-0.0035}$	<0.1%	$^{+0.0234}_{-0.0178}$	$^{+0.0237}_{-0.0182}$	$^{+0.0029}_{-0.0029}$	$^{+0.0057}_{-0.0032}$	$^{+0.0064}_{-0.0043}$
2_1^+	4_1^+	0.0740	<0.1%	$^{+0.0206}_{-0.0206}$	$^{+0.0001}_{-0.0001}$	$^{+0.0206}_{-0.0206}$	$^{+0.0001}_{-0.0001}$	$^{+0.0038}_{-0.0038}$	$^{+0.0038}_{-0.0038}$
CM2									
0_1^+	2_1^+	0.1298	$^{+0.0035}_{-0.0036}$	<0.1%	$^{+0.0192}_{-0.0148}$	$^{+0.0195}_{-0.0152}$	$^{+0.0023}_{-0.0023}$	$^{+0.0047}_{-0.0026}$	$^{+0.0052}_{-0.0035}$
2_1^+	4_1^+	0.0460	<0.1%	$^{+0.0224}_{-0.0220}$	$^{+0.0002}_{-0.0002}$	$^{+0.0224}_{-0.0220}$	<0.1%	$^{+0.0023}_{-0.0024}$	$^{+0.0023}_{-0.0024}$

Table 5.11: *Results from GOSIA2 calculations over the three different CM ranges, including an overview of the different error contributions (statistical and systematic).*

trigger type	delayed	delayed/64	coincident	accepted
	265197	4144	25247	28978

Table 5.12: *Scaler information for the A=76 run.*

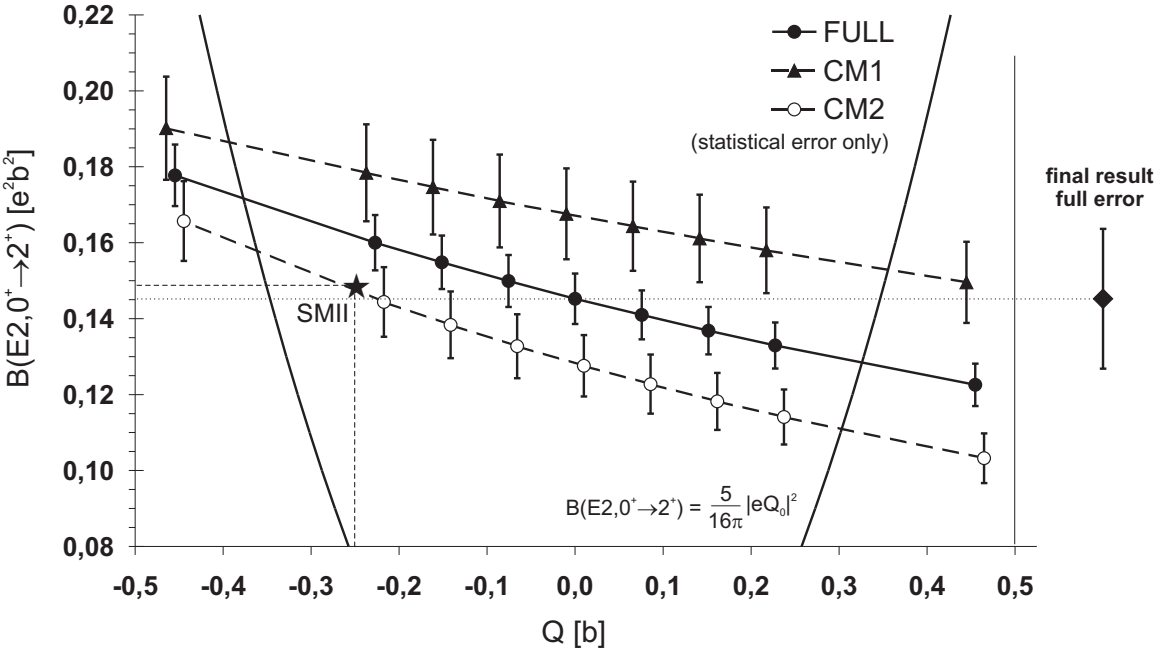

Figure 5.18: ^{76}Zn *: Dependence of the resulting B(E2,*$0_1^+ \rightarrow 2_1^+$*) value on the (unknown) quadrupole moment of the* 2_1^+ *state, obtained for the three considered CM ranges in GOSIA2. The star represents the SMII prediction for* ^{76}Zn*. The point at the right side is the final B(E2) value for* ^{76}Zn*, including all statistical and systematical errors. The solid black lines indicate the rotational quadrupole moment, related to the B(E2,*$0_1^+ \rightarrow 2_1^+$*) as* $|Q^{rot}_{2_1^+}|=0.91\sqrt{B(E2, 0_1^+ \rightarrow 2_1^+)}$.

5.2.2 Data analysis of the absolute measurement

Analogue to the A=74 analysis, the result from the relative measurement will be used in the calculation of the differential cross section. The result is compared to the observed differential cross section, which is a crucial confirmation of the validity of the first method.

The procedure to acquire the correctly scaled elastic and inelastic cross section is analogue to the procedure explained for A=74. The downscaled elastic events constitute 14.8% of the total number of coincident events, deduced from the scaler information, given in table 5.12.

The result is shown in Fig. 5.19. The B(E2,$2_1^+ \rightarrow 0_1^+$) value for the FULL CM range was used : 0.1452 e^2b^2, for $Q_{2_1^+}$=0 eb. The dashed lines correspond to the calculated differential cross sections taking into account the total (statistical+systematical) error bar on B(E2,$2_1^+ \rightarrow 0_1^+$) from table 5.11 (4th column).

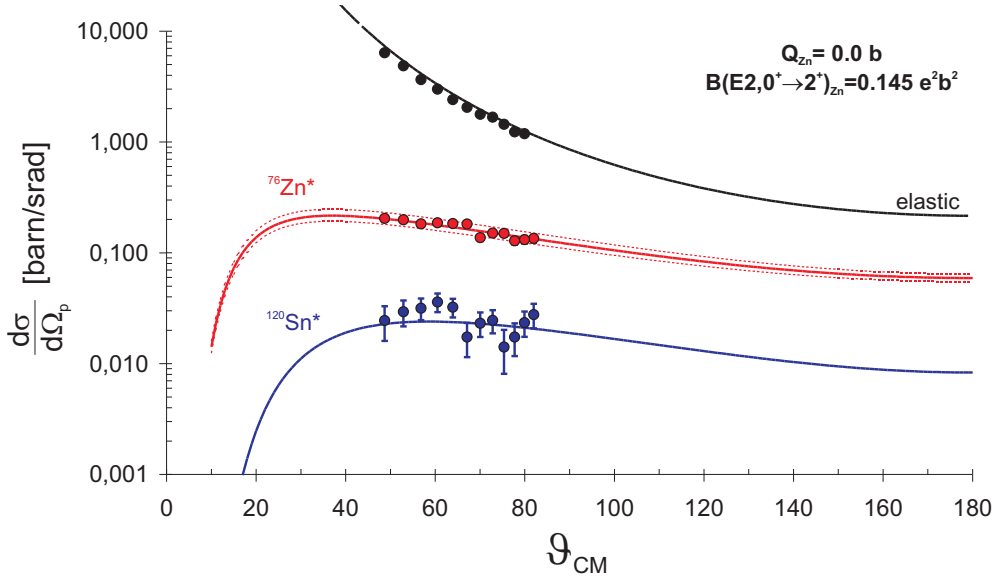

Figure 5.19: *Calculated differential cross sections for elastic scattering and inelastic scattering where either ^{76}Zn or ^{120}Sn are excited together with the experimental data points. The data points correspond to the CM1 region. The dashed lines corresponds to the differential cross section, taking into account the total (statistical+systematical) error on the matrix element 0_1^+-2_1^+ in ^{76}Zn (see table 5.11).*

5.3 ^{78}Zn

5.3.1 Data analysis of the relative measurement

The data analysis of the A=78 measurement is analogue to the A=74,76 analysis.

Data reduction

The several steps in data reduction are illustrated in Fig. 5.20. The MINIBALL detectors are read in 'singles' mode during the 'In Beam' periods. In Fig. 5.20A , this 'In Beam' spectrum is shown (black) together with the 'Off Beam' spectrum (grey). As pointed out before, during the 'In Beam' period, a huge amount of low energy bremstrahlung (<500 keV) is present, originating from the REX linac. After offline sorting of the gamma's and particles, prompt and random spectra are generated. The time difference spectrum T_γ-$T_{particle}$ for A=78 is shown in Fig. 5.21. No downscaling was applied on the scattered particles (the not downscaled window of Fig. 5.2 has disappeared) because the beam intensity was sufficiently low for A=78. The prompt and random coincidence windows are not equal in time, so a scaling of the random spectrum is necessary. The prompt spectrum in Fig. 5.20C is generated without a condition on the detected particle energy and with *at least one prompt particle* attached to the gamma ray. No energy condition on the particle is imposed in the random spectrum (5.20B) neither, and *at least one random and no prompt coincident particle* is requested.

Random subtraction

The random coincident spectrum is dominated by the low energy tail from the bremstrahlung originating from the REX-linac. This is as well apparent from the comparison of the "In Beam" (black) and "Off Beam" (grey) (singles) spectrum in Fig. 5.20A. The ^{78}Ga decay lines at 619.4 keV (I_γ=77(4)%) and 567 keV (I_γ=18.2(9)%) are seen in the random spectrum, but are overwhelmed by the target excitation lines in the prompt spectrum. The random subtraction is based on the ratio prompt to random over the range from 1.5 - 2.5 MeV, which is 0.15. The random subtracted spectrum is plotted in Fig. 5.20. The random subtracted spectrum contains seven net counts above 1.0 MeV. The highest energy transition which can be seen with an appreciable number of counts is the $2_2^+ \rightarrow 0_1^+$ transition in ^{108}Pd at 931 keV (4(2) counts). The excitation of the 4_1^+ state at 1.048 MeV decays through the emission of 2 gamma rays of 434 keV and 614 keV in cascade. A simulation of this gamma ray cascade (including the angular distribution of the 2 gamma's) shows that 0.4% of these cascade events should be seen at 1.048 MeV in the spectrum (where the clusters are operated in add-back mode) and 10.1% are seen in the 614 keV photopeak. In the current experiment 93 counts are detected in the 614+619 keV region, where from the calculated yield ratio 90% belongs to the 614 keV transition (84 counts), so 3 counts are expected at 1.048 MeV. Higher energy gamma rays might come from random summing of bremstrahlung gamma's or β-decay activity.

Doppler correction

By requesting an additional condition on the detected particle energy, two CM ranges can be selected (see paragraph 4.1). In Fig. 5.22 three spectra are shown corresponding to the full detected CM range, CM1 (=beam detection) and CM2 (=target detection). Fig. 5.22A corresponds to 5.20D. The subtraction factor for the random coincidence

correction is the same in the three cases. In the CM1 spectrum, the Doppler broadened $2_1^+ \rightarrow 0_1^+$ transition in ^{78}Zn can be Doppler corrected with the detected particle and gamma angles and energies (see 4.26 and 4.27). The same can be done in CM2 spectrum for the detected target particle. The Doppler corrected spectra for beam(target), respectivily, are shown in Fig. 5.23B(5.24B), the corresponding detected particles are shown in Fig. 5.23C(5.24C).

Beam contamination

In the previous chapter the number of counts during the laser on/off runs were already used to deduce the R_{ON} value (see tab.4.2). These numbers are explicitly given in table 5.13, while the ratio of the cross sections, used in eq. 4.2 are given in table 5.14. After random subtraction, the prompt coincident spectrum displays the Coulomb excitation lines from ^{78}Zn,Ga and ^{108}Pd. No contaminating lines are present at the position of the $2_1^+ \rightarrow 0_1^+$ transition in ^{78}Zn, as is proven by the laser on and laser off Doppler corrected, random subtracted spectra (CM1) in Fig. 5.25.

Integration

The integration of the de-excitation peaks in the spectrum is performed with the procedure described in [Coe85]. The counts in the Coulomb excitation peaks are given in table 5.15 for the three CM ranges : FULL, CM1 and CM2, where the latter two ranges require additional energy information in the CD. In the last row, the corrected target yield is given, according to 4.2 with the parameters r and $\sigma^{Ga}_{E2,Sn}/\sigma^{Zn}_{E2,Sn}$ given in tables 5.13 and 5.14. The error on the corrected target yield is analogue to eq. 5.1.

GOSIA2 calculations

The input to GOSIA2, using the option "RAW" (see 4.6.1), requires the not efficiency corrected transition yields of the $2_1^+ \rightarrow 0_1^+$ transition in Zn and the "corrected" $2_1^+ \rightarrow 0_1^+$ yield for the target excitation, given by 4.2. The minimization routine fits the unknown transition ME($2_1^+ \rightarrow 0_1^+$) for Zn. The ME's of the target ^{108}Pd were fixed to the following adopted values :

$$\begin{aligned}
ME(0_1^+ \rightarrow 2_1^+) &= 0.872(0.011)eb \\
ME(0_1^+ \rightarrow 2_2^+) &= -0.098(0.005)eb \\
ME(2_1^+ \rightarrow 2_1^+) &= -0.81(^{+0.04}_{-0.09})eb \\
ME(2_1^+ \rightarrow 2_2^+) &= -0.88(0.04)eb \\
ME(2_1^+ \rightarrow 4_1^+) &= 1.42(0.07)eb \\
ME(2_1^+ \rightarrow 0_2^+) &= 0.40(0.02)eb \\
ME(2_2^+ \rightarrow 2_2^+) &= 0.73(^{+0.09}_{-0.07})eb
\end{aligned}$$

where the matrix element 0_1^+-2_1^+ and its error bar are calculated from the adopted B(E2,$0_1^+ \rightarrow 2_1^+$) =0.761(23) e^2b^2 in [nndc]. The remaining matrix elements are taken from [Sve95]. The level scheme of ^{108}Pd is shown in Fig. 5.26. Only the levels used in the GOSIA2 calculations are shown. The de-excitation yields for the indicated transitions in Fig. 5.26 are summarized in table 5.16, together with the yields calculated by GOSIA2. The calculated yields were normalized to the experimental $2_1^+ \rightarrow 0_1^+$ yield and incorporate the yields from excitation by Zn and Ga. The error on the calculated yields stems from the error on the corresponding ME. The latter are all ∼5% (except

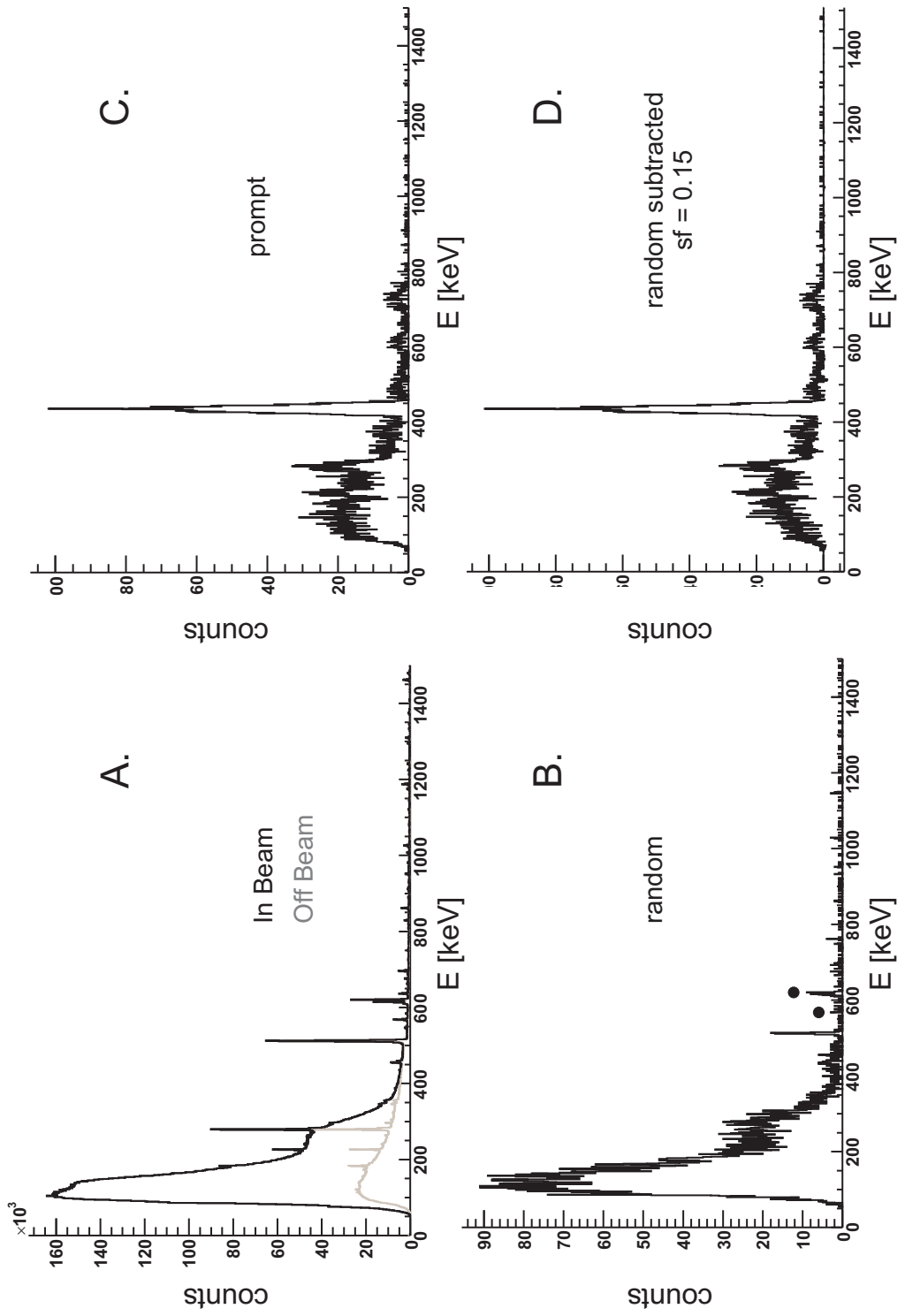

Figure 5.20: *A. The 'In Beam' singles spectrum. B. The random coincident spectrum. C. The prompt coincident spectrum. D. Random subtracted prompt spectrum.*

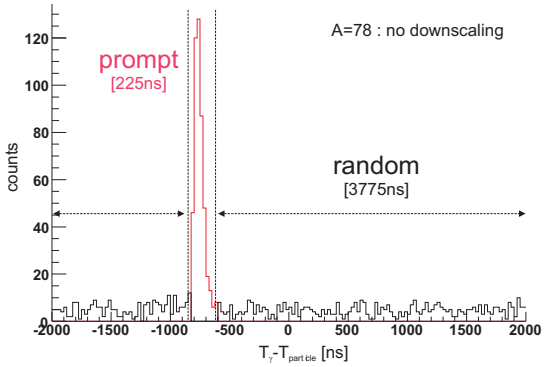

Figure 5.21: *Time difference between offline sorted γ's and particles. The time window of 4 μ sec is divided in a prompt window of 225ns and a random window of 3775 ns. No downscaling was applied in the A=78 experiment.*

^{78}Zn		^{78}Ga - 283 keV		^{108}Pd		R_{ON}	*error*	r_{ON}	*error*
counts	*error*	counts	*error*	counts	*error*	[%]			
29	6	100	15	389	22	64	13	0.568	0.112

Table 5.13: *In the first three columns, the total number of counts observed during all laser on/off runs on mass A=78 are given. These integrals were used in the previous chapter to deduce the extrapolation parameters $\Re_{CLX,1}$ and $\Re_{CLX,2}$. In the last two columns the result from the previous chapter is repeated.*

ME($2_2^+ \rightarrow 2_2^+$) : 12% and ME($0_1^+ \rightarrow 2_1^+$) : 1.3%). The errors on all ME's, except ME(0_1^+ -2_1^+), affect the calculated $2_1^+ \rightarrow 0_1^+$ yield by less then 0.2%, indicating that the major systematical error is due to the uncertainty on the (0_1^+ -2_1^+) ME in ^{108}Pd. The experimental Doppler corrected de-excitation yields for ^{108}Pd are in fair agreement with the calculated yields.

In a first calculation the unknown "re-orientation" matrix element (ME) ME_{22} in ^{78}Zn was fixed to 0. The result of these minimizations for the three CM ranges are summarized in table 5.17. In a second step, the re-orientation ME was varied from 0.6 to -0.6 ($Q_{2_1^+}$=$\pm$0.455 eb). The result is summarized in Fig. 5.27. The error bar is limited to the statistical error bar, *excluding* the error on the R-value (beam contamination). Due to the large error bars no conclusive evidence can be given for the sign of the quadrupole moment. For comparison, the shell model prediction (SMII) is given in Fig. 5.27 as well.

	FULL	CM1	CM2
$\frac{\sigma^{Ga}_{E2,Sn}}{\sigma^{Zn}_{E2,Sn}}$	0.995	0.989	1.001

Table 5.14: *Ratio of the cross section for target excitation by Ga/Zn, used in eq. 4.2. Ne only contributes in the full CM range and CM2 range.*

	Energy [keV]	$J_i \rightarrow J_f$	FULL counts	FULL error	CM1 counts	CM1 error	CM2 counts	CM2 error
Zn	730	$2_1^+ \rightarrow 0_1^+$	145	*15*	72	*9*	61	*11*
Ga	283	?	279	*30*	141	*17*	132	*22*
Pd	434	$2_1^+ \rightarrow 0_1^+$	1536	*44*	878	*32*	688	*30*
	corrected		982	*196*	561	*113*	439	*89*

Table 5.15: *Summary of the number of counts integrated over the three CM ranges (FULL,CM1 and CM2). In the last row, the corrected number of target excitation counts is given according to eq. 4.2*

Energy [keV]	$J_i \rightarrow J_f$	CM2 exp	CM2 calc
434	$2_1^+ \rightarrow 0_1^+$	688(30)	-
497	$2_2^+ \rightarrow 2_1^+$	22(7)	29(3)
614	$4_1^+ \rightarrow 2_1^+$	63(8)	77(7)
619	$0_2^+ \rightarrow 2_1^+$		9(1)
931	$2_2^+ \rightarrow 0_1^+$	7(3)	6

Table 5.16: *Comparison of the experimental number of counts observed in the ^{108}Pd transition yields and the calculated transition yields (GOSIA2) relative to the experimental $2_1^+ \rightarrow 0_1^+$ yield. The error bars on the calculated yields are related with the uncertainty on the matrix elements.*

Error determination

Statistical error : The statistical error on the final ME('s) is determined by the statistics in the $2_1^+ \rightarrow 0_1^+$ (and $4_1^+ \rightarrow 2_1^+$ transitions) in Zn (column Zn($2_1^+ \rightarrow 0_1^+$) in table 5.17) and the "corrected" $2_1^+ \rightarrow 0_1^+$ target yield (column Pd($2_1^+ \rightarrow 0_1^+$)+R_{ON} in table 5.17). The latter includes the error on the beam contamination (R_{ON}), given by eq. 5.1.

Systematics error : The systematical error is determined by the uncertainty on the ME's of the target and by the beam energy. The error on the beam energy was assumed to be 1%. Since no counts were observed corresponding to the $4_1^+ \rightarrow 2_1^+$ transition, no B(E2,$4_1^+ \rightarrow 2_1^+$) value can be obtained from the current data.

Final B(E2,$2_1^+ \rightarrow 0_1^+$) and B(E2,$4_1^+ \rightarrow 2_1^+$) values :

The final result for the B(E2,$2_1^+ \rightarrow 0_1^+$) value is obtained over the CM range labeled "FULL", for the same reasons mentioned above for A=74,76. The final B(E2,$0_1^+ \rightarrow 2_1^+$) value is :

$$B(E2, 0_1^+ \rightarrow 2_1^+) \quad = \quad 0.0770^{+209}_{-166} e^2 b^2 \tag{5.10}$$

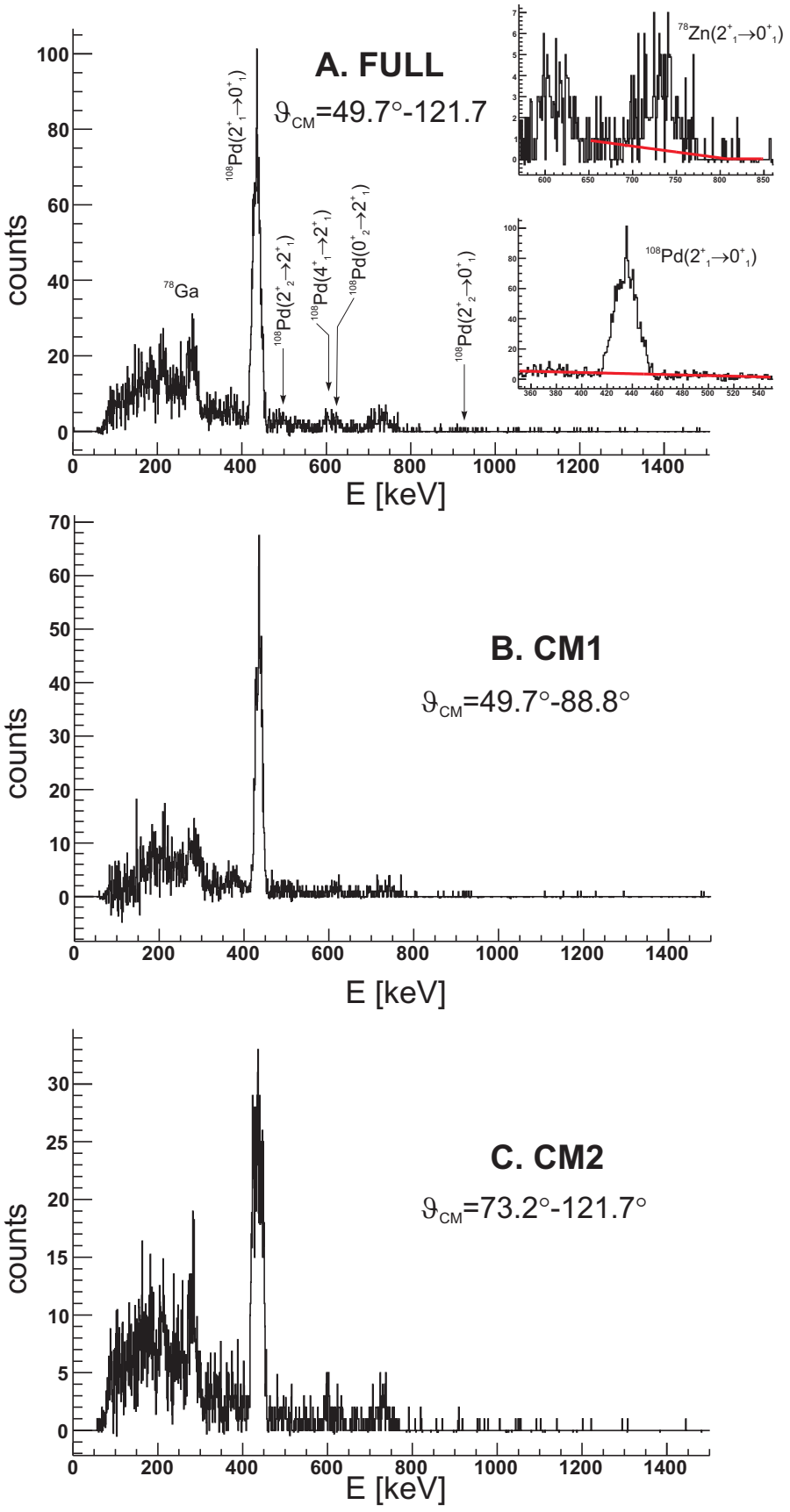

Figure 5.22: *A. The random subtracted prompt gamma spectrum over the full detected CM range. B. The random subtracted prompt gamma spectrum over CM1 range (beam detection). C. The random subtracted prompt gamma spectrum over CM2 range (target detection).*

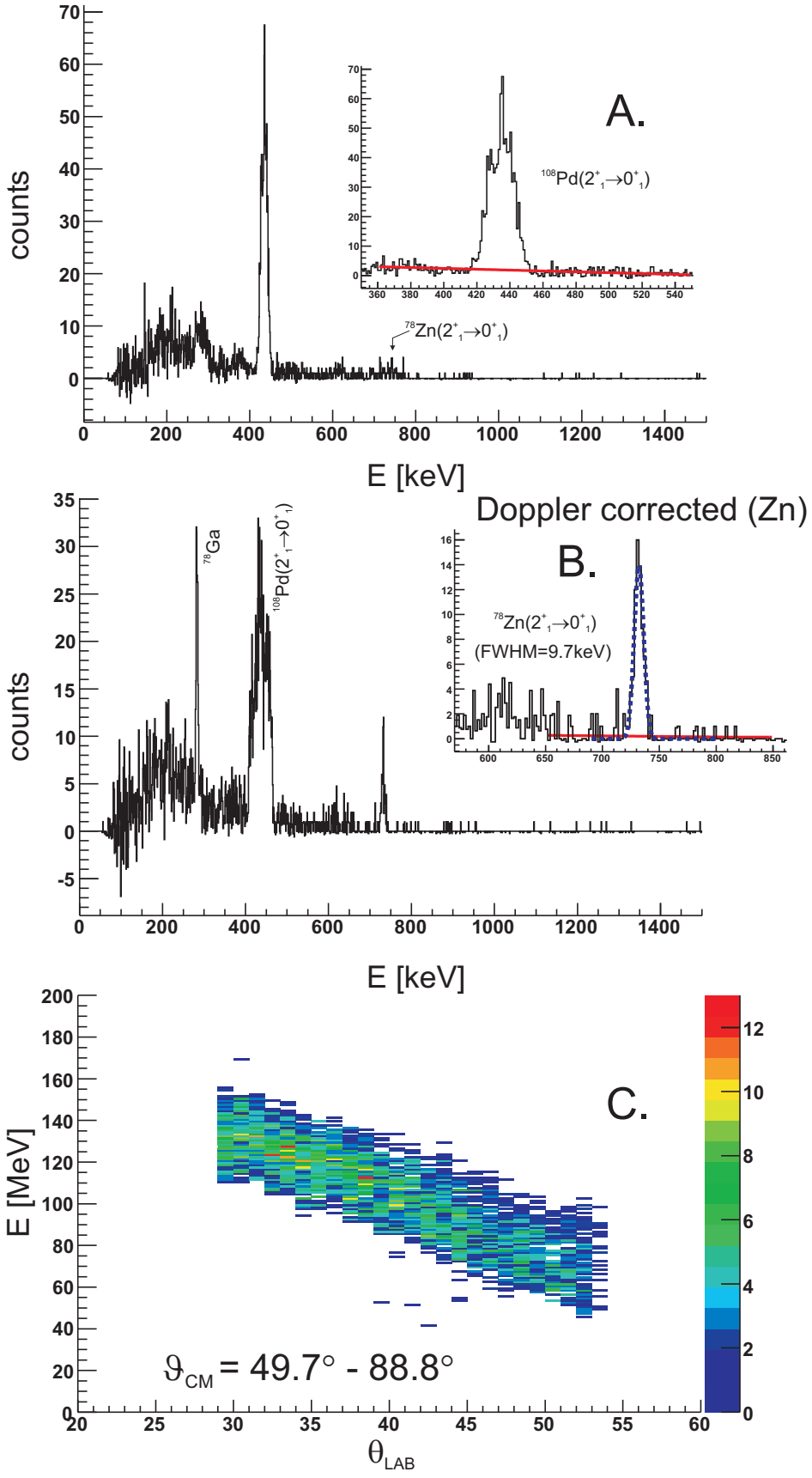

Figure 5.23: *A. The random subtracted prompt gamma spectrum over the CM1 range. B. The* **Doppler corrected** *random subtracted prompt gamma spectrum over CM1 range (beam detection). C. The detected particle detection (energy versus lab angle) over the considered CM range.*

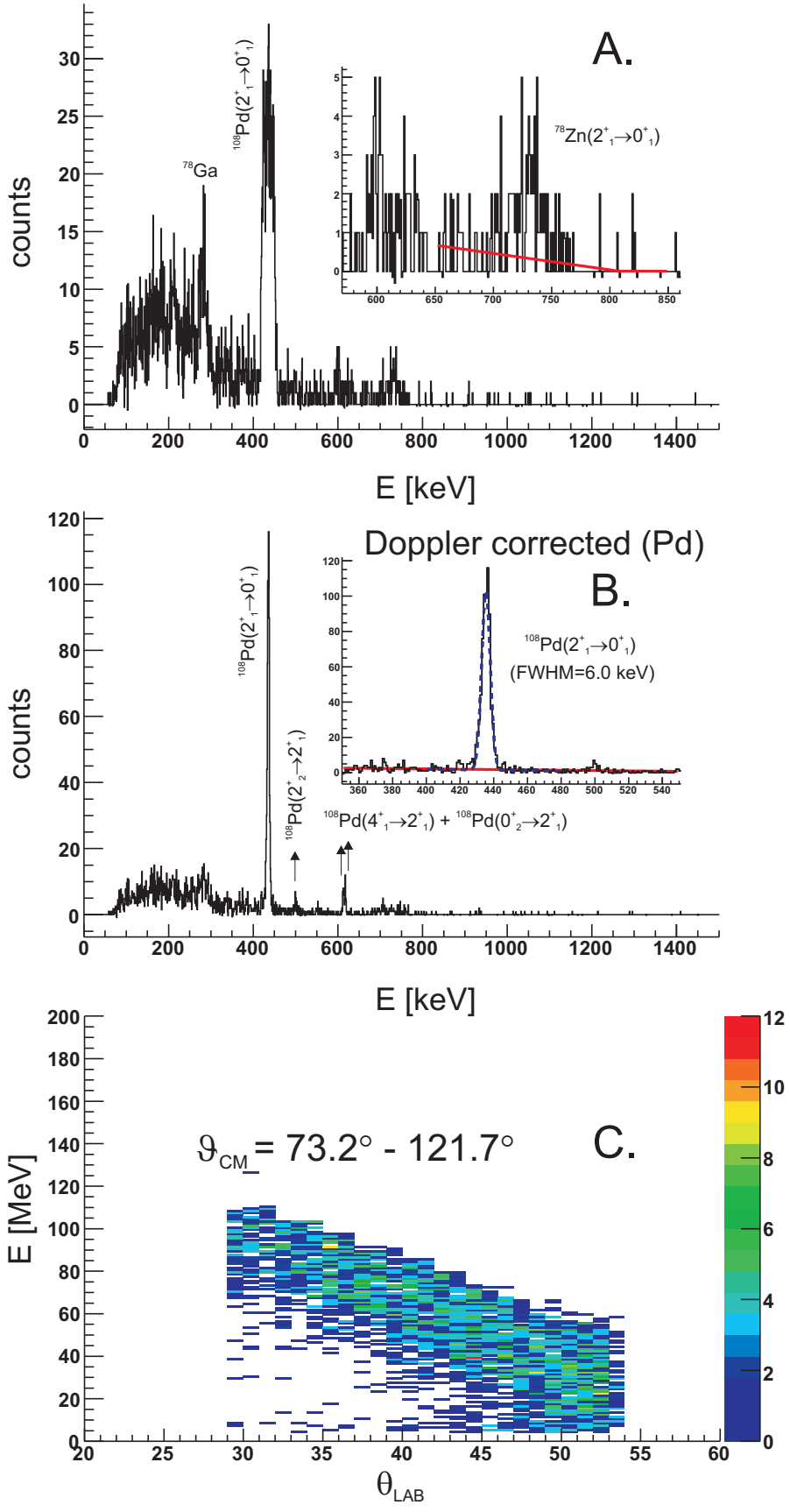

Figure 5.24: *A. The random subtracted prompt gamma spectrum over the CM2 range. B. The* **Doppler corrected** *random subtracted prompt gamma spectrum over CM2 range (target detection). C. The detected particle detection (energy versus lab angle) over the considered CM range.*

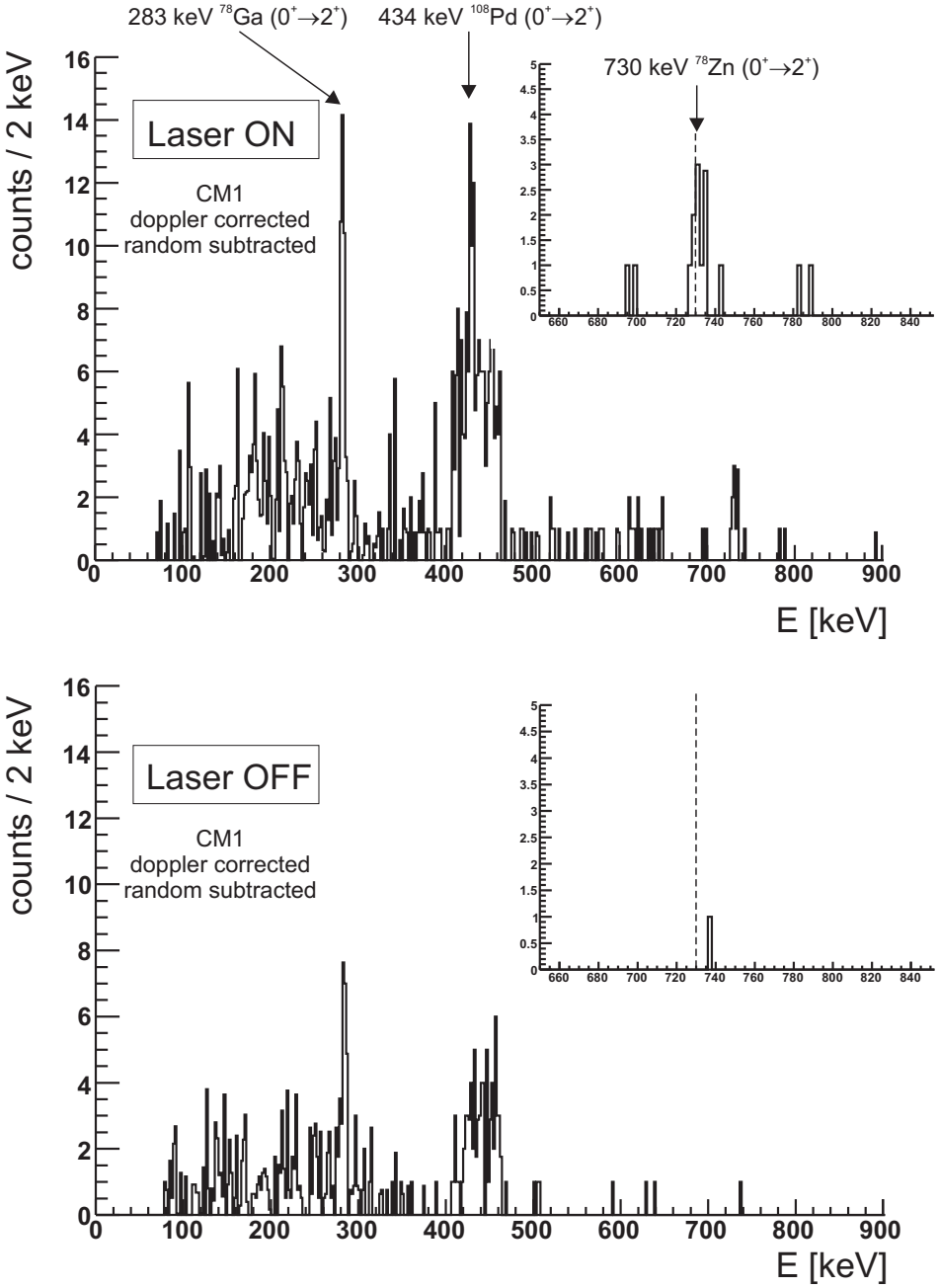

Figure 5.25: *Doppler corrected, random subtracted Coulomb excitation spectrum during laser ON(Top)/OFF(Bottom) periods of the laser on/off runs.*

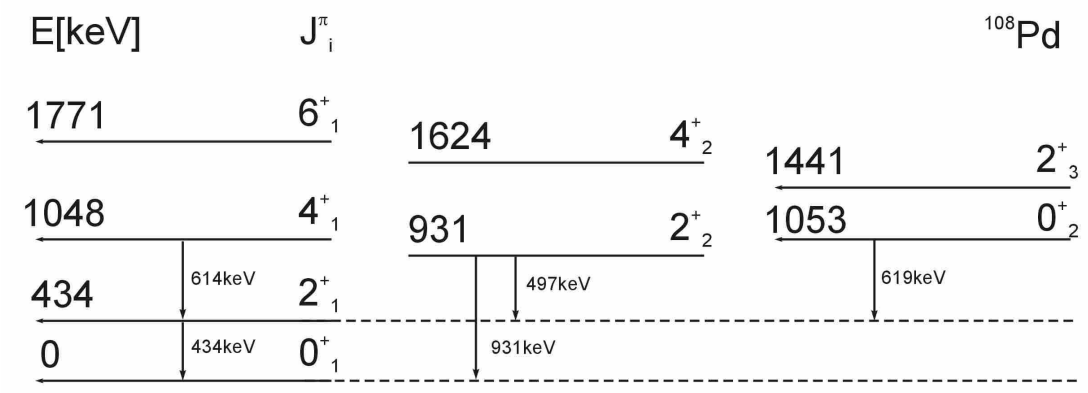

Figure 5.26: *Partial level scheme of ^{108}Pd. Only the levels below 1800 keV are shown and the transitions which are observed experimentally.*

B(E2,$J_i \rightarrow J_f$)			Stat. Error			Syst. Error		
J_i	J_f	[e^2b^2]	Zn($2_1^+ \rightarrow 0_1^+$)	Pd($2_1^+ \rightarrow 0_1^+$) + R_{ON}	**TOTAL**	ME's Pd	Beam Energy	**TOTAL**
				FULL				
0_1^+	2_1^+	0.770	$^{+0.0082}_{-0.0081}$	$^{+0.0066}_{-0.0056}$	$^{+0.0105}_{-0.0099}$	$^{+0.0044}_{-0.0041}$	$^{+0.0013}_{-0.0007}$	$^{+0.0046}_{-0.0041}$
				CM1				
0_1^+	2_1^+	0.0743	$^{+0.0105}_{-0.0106}$	$^{+0.0160}_{-0.0107}$	$^{+0.0191}_{-0.0150}$	$^{+0.0016}_{-0.0018}$	$^{+0.0013}_{-0.0007}$	$^{+0.0021}_{-0.0019}$
				CM2				
0_1^+	2_1^+	0.0633	$^{+0.0123}_{-0.0120}$	$^{+0.0087}_{-0.0069}$	$^{+0.0152}_{-0.0139}$	$^{+0.0026}_{-0.0024}$	$^{0.0011}_{-0.0006}$	$^{+0.0028}_{-0.0025}$

Table 5.17: *Results from GOSIA2 calculations over the three different CM ranges, including an overview of the different error contributions (statistical and systematic).*

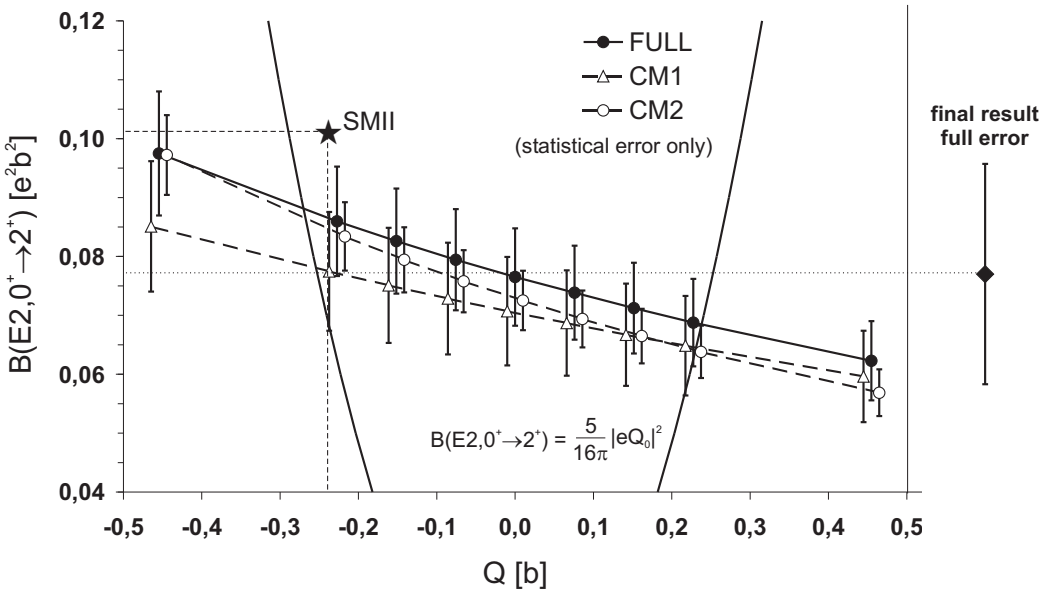

Figure 5.27: *^{78}Zn : Dependence of the resulting B(E2,$0_1^+ \rightarrow 2_1^+$) value on the (unknown) quadrupole moment of the 2_1^+ state, obtained for the three considered CM ranges in GOSIA2. The star represents the SMII prediction for ^{78}Zn. The point at the right side is the final B(E2) value for ^{78}Zn, including all statistical and systematical errors. The solid black lines indicate the rotational quadrupole moment, related to the B(E2,$0_1^+ \rightarrow 2_1^+$) as $|Q^{rot}_{2_1^+}|=0.91\sqrt{B(E2,0_1^+ \rightarrow 2_1^+)}$.*

5.3.2 Data analysis of the absolute measurement

In this section, the result from the previous section will be applied to check the absolute differential cross section, determined from the inelastic scattered particles in the individual annular CD strips.
The procedure to acquire the correctly scaled elastic and inelastic cross section is analogue to the procedure explained for A=74, except for the overall downscaling factor which was in the A=74 case 64, while during the A=78 experiment, this downscaling factor was 1 (no downscaling, all scattered particles are detected without any condition). The factors 0.113 and 1/64 in eq. 5.6 are replaced by 1 since no downscaling was applied and the offline non-coincident particles are assumed to be true non-coincident events.
The result is shown in Fig. 5.28. A $Q_{2_1^+}$=0 eb and the B(E2,$2_1^+ \rightarrow 0_1^+$) value for the FULL CM range were assumed (0.0770 e^2b^2). The dashed lines correspond to the calculated differential cross sections taking into account the quoted statistical and systematical error bar in table 5.17.

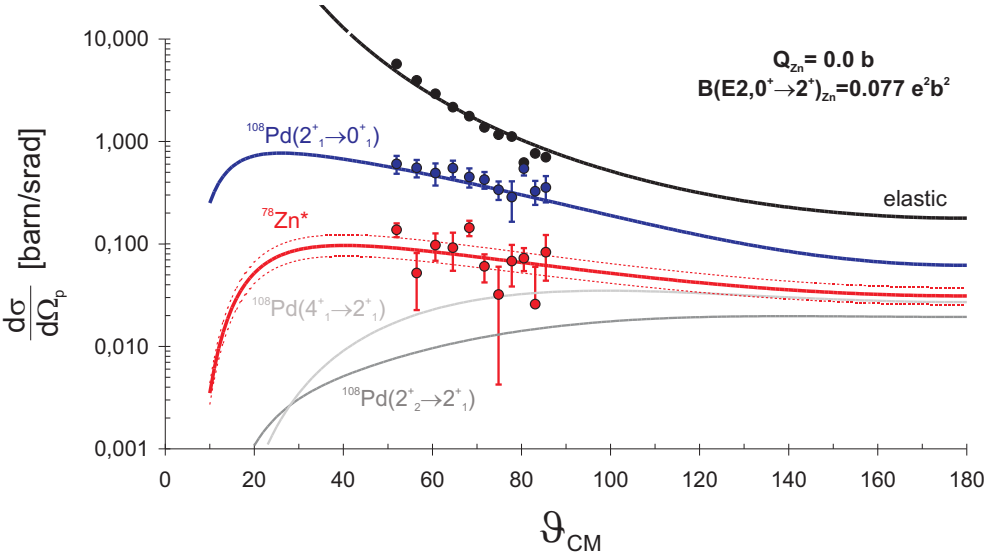

Figure 5.28: *Calculated differential cross sections for elastic scattering and inelastic scattering where either ^{78}Zn or ^{108}Pd are excited together with the experimental data points. The data points correspond to the CM1 region. The grey lines correspond to the excitation of higher spin states in ^{108}Pd. The dashed lines corresponds to the differential cross section, taking into account the total (statistical+systematical) error on the matrix element 0_1^+-2_1^+ in ^{78}Zn (see table 5.17).*

5.4 Summary

In table 5.18 the experimental results are summarized together with the related quantities : $\tau_{(2^+)}$, β, β/β_{sp}, EWSRI and EWSRII [4]. The deformation parameter β is related to the B(E2,$0_1^+ \rightarrow 2_1^+$) value in the framework of the collective nuclear models :

$$\beta = \frac{4\pi}{3ZR_0^2}\sqrt{B(E2, 0_1^+ \rightarrow 2_1^+)}. \tag{5.11}$$

The single particle deformation parameter β_{sp} is the value obtained with the single particle estimate for B(E2,$0_1^+ \rightarrow 2_1^+$) . The ratio β/β_{sp} is an indication of collective quadrupole motion in nuclei [Ram01].
The "Energy Weighted Sum Rule" (EWSR) expresses how much total transition strength there is in a particular nucleus and is given by :

$$EWSR = \sum E \times B(E2, 0_1^+ \rightarrow 2_1^+) \tag{5.12}$$

$$= 30e^2(\hbar^2/8\pi m)AR_0^2 \tag{5.13}$$

where m is the nucleon mass and $(3/5)R_0^2$ is the single particle mean square radius. The parameter EWSRI in table 5.18 is the the ratio E(2_1^+)×B(E2,$0_1^+ \rightarrow 2_1^+$)/EWSR in percentage. EWSRII is the "isoscalar" part of EWSR, given by EWSR·$(Z/A)^2$.
For comparison, the quantities are given for ^{70}Zn in the first row. In table 5.19 an overview is given of the experimental conditions. The Yield in [μC^{-1}] refers to the number of produced Zn ions per μC proton beam (in the considered experiments :

[4] The review article [Ram01] on B(E2,$0_1^+ \rightarrow 2_1^+$) and E(2^+) values in even-even nuclei contains the same table for all known data up to 2001.

2μA). The yield was measured prior to the experiment and might have decreased with the aging of the target (due to distortion, drop in release efficiency, etc...). I_{in} refers to the number of incident Zn isotopes at the MINIBALL setup. This quantity was inferred from the target Coulomb Excitation yield :

$$\epsilon_{REX} \cdot I_{in} = \frac{N^{Zn}_{E2,Sn} \cdot A}{\epsilon_{MB} \cdot \sigma^{Zn}_{E2,Sn} \cdot N_A \rho d} \tag{5.14}$$

where ρd is the target thickness in mg/cm^2, N_A Avogadro's number and the total REX efficiency ϵ_{REX} is explicitly written. The REX efficiency is deduced from the ratio of Zn intensity per second at the MINIBALL setup over the Zn Yield at the primary target. Values close to 1% are obtained for all three masses, which is the standard value for the REX efficiency. The actual REX efficiency consists of three main components : ϵ_{REX}=$\epsilon_{TRAP,EBIS} \cdot \epsilon_{linac} \cdot \epsilon_{detection}$. The incoming Zn beam intensity (I_{in}) deduced from the target excitation is only 22% of the intensity deduced from the scaler information (counting of the delayed CD triggers). This big difference might have different sources, such as noise in the scaler channels or a lower then expected $\epsilon_{detection}$ [5]. In conclusion, the $\epsilon_{linac} \cdot \epsilon_{TRAP,EBIS}$ might be higher then 1%. The quoted cross sections in table 5.19 are calculated with the Coulomb excitation code CLX, using the matrix elements deduced from table 5.18. These cross sections are integrated single differential cross sections (particle solid angle). The big difference between "In Beam" measuring time and total "Laser ON Beam Time" originates from the pulsed beam structure at ISOLDE. The EBIS injects the radioactive ions at a rate of 25 Hz in the linac and the particles arrive at the MINIBALL setup within 300 μsec. Thus, the actual time the relevant nuclear information can be measured at the setup is much lower then the actual beam time. The big "instantaneous" incoming beam intensity during an EBIS output pulse increases the "signal-to-noise" ratio in the experiment [Hab94].
In Fig. 5.29 the B(E2,$2^+_1 \rightarrow 0^+_1$) values obtained in this work are plotted in W.u. together with adopted B(E2,$2^+_1 \rightarrow 0^+_1$) values ([nndc]) for Zn isotopes. The interpretation of these results is the subject of the next chapter.

[5] This might be attributed to the known problem of "time stamp mismatch", i.e. the mismatch between detected particle energy signals and timing signals.

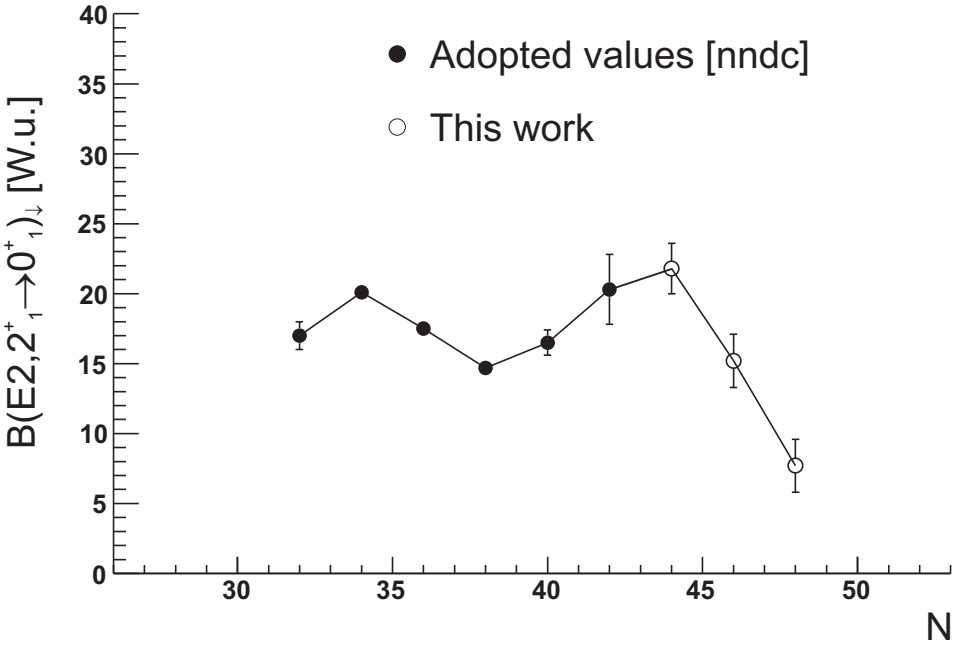

Figure 5.29: *The open circles represent the B(E2,$2_1^+ \rightarrow 0_1^+$) values obtained in this work (^{74,76,78}Zn). The full circles are adopted values for Zn isotopes from [nndc].*

	$E(2_1^+)$ [keV]	$E(4_1^+)$ [keV]	$B(E2,0_1^+ \rightarrow 2_1^+)$ [e^2b^2]	[W.u.]	$B(E2,2_1^+ \rightarrow 4_1^+)$ [e^2b^2]	[W.u.]	τ [ps]	β	β/β_{sp}	EWSRI %	EWSRII %
^{70}Zn	885	1787	0.160(14)	18.7(3.3)	-	-	4.74(42)	0.228(10)	4.30(19)	1.67(15)	9.1(8)
^{74}Zn	606	1419	0.2006^{175}_{151}	$21.7^{1.9}_{1.6}$	0.0857^{126}_{122}	26(4)	24.9(1.7)	0.246(10)	4.65(19)	1.31(11)	0.22(2)
^{76}Zn	599	1296	0.1452^{208}_{161}	$15.2^{2.2}_{1.7}$	0.0576^{163}_{163}	17(5)	36.4(4.6)	0.206(14)	3.9(3)	0.89(11)	0.14(2)
^{78}Zn	730	$(1621)^1$	0.0770^{209}_{166}	$7.8^{2.1}_{1.7}$	-	-	25.6(6.2)	0.147(19)	2.8(4)	0.55(13)	0.08(2)

Table 5.18: *Summary of the experimental results for ^{74,76,78}Zn. (^{1} The 4^+ level in ^{78}Zn was not confirmed in the current experiment, the value is taken from [Van05].) τ is the lifetime of the 2_1^+ state (see eq. 2.5), $\beta_{(sp)}$ is the (single particle) deformation parameter. EWSRI(I) is the ratio $E(2_1^+)\times B(E2,0_1^+ \rightarrow 2_1^+)$/EWSR, where EWSR is given in eq. 5.13.*

Isotope	Yield	I_{in}	Beam Time		"In Beam"	ϵ_{REX}	E_{beam}	Target	ρd	$\sigma^{Target}_{E2,0^+_1\rightarrow 2^+_1}$	$\sigma^{Zn}_{E2,0^+_1\rightarrow 2^+_1}$	$\sigma^{Zn}_{E2,2^+_1\rightarrow 4^+_1}$
			Laser ON	Laser OFF	Time							
	[ions/μC]	[pps]	[sec]	[sec]	[sec]	[%]	[MeV/u]		[mg/cm^2]	mb	mb	mb
^{74}Zn	2.0E7	3.0E5	49221	5100	431	0.75	2.87	^{120}Sn	2.3	148(1)	1321(109)	36(5)
^{76}Zn	5.0E6	1.1E5	37408	4560	321	1.10	2.83	^{120}Sn	2.3	149(1)	1009(145)	24(7)
^{78}Zn	3.9E5	4.3E3	91644	15990	739	0.56	2.87	^{108}Pd	2.0	2113(27)	464(126)	(10^1)

Table 5.19: *Overview of the experimental conditions during the august 2004 runs and excitation cross sections calculated with the Coulomb excitation code CLX. Results from table 5.18 are utilized. The quoted error bar is the total error, statistical + systematic. The sum of Beam Time Laser ON and Beam Time Laser OFF is the actual time the experiment was running. The "In Beam" Time is the total time the radioactive isotopes were actually arriving at the MINIBALL setup. ϵ_{REX} is the REX efficiency (the transmission efficiency from the mass separator to the MINIBALL setup). (^{1} = cross section if the vibrational relation between B(E2,$4^+_1 \rightarrow 2^+_1$) and B(E2,$2^+_1 \rightarrow 0^+_1$) is used.)*

Chapter 6

Discussion, Summary and Outlook

6.1 Shell model description

A shell model description of the new experimental data points is provided by two shell model calculations, which will be labelled SMI and SMII, performed in the full $pf_{5/2}$-$g_{9/2}$ shell outside a ^{56}Ni closed core. SMI calculations were performed by N. Smirnova (UGent, [Smi04,Smi06]) with the ANTOINE shell model code, whereas SMII calculations were performed by A. Lisetskiy (GSI, [Lis04, Lis05, Lis06]) with the shell model code OXBASH. The emphasize is on results for Zn isotopes with N$\geq$40. In the following a brief description of the utilized residual interactions will be given, followed by a discussion of the results for Zn isotopes, the neighboring Ni and Ge isotopes and N=48,N=50 isotones. For comparison, shell model results from literature, for N$\leq$40 are shown in order to highlight the insight obtained in the nuclear structure of the lighter ^{60,62}Zn and stable ^{64,66,68,70}Zn isotopes.
A comparison of experimental and calculated energy levels and transition strengths for N$\geq$40 Zn isotopes is made in Fig. 6.1, 6.2 and 6.3.

6.1.1 The effective residual interaction

The configuration space considered in the shell model calculations is the full $pf_{5/2}$-$g_{9/2}$ shell ($2p_{3/2}$,$2p_{1/2}$,$1f_{5/2}$ and $1g_{9/2}$ orbitals) outside an inert ^{56}Ni core. Two effective residual interaction were used and compared to experimental data. The first and second interaction will be referred to as SMI and SMII respectively. Both interactions depart from the same realistic effective nucleon-nucleon interaction based on G-matrix theory. This realistic interaction includes possible polarization effects due to the inert ^{56}Ni core [Hjo95]. SMI uses the original "Two Body Matrix Elements" (TBME) deduced by Hjorth-Jensen *et al.* [Hjo95] with a further modification of the monopole term [Smi04]. SMII departs from the same TBME's, where the original TBME's for protons and neutrons have been fitted to new experimental data. The experimental input for the fitting procedure consisted of Ni isotopes (closed proton shell at Z=28) from A=57 to A=78 (the ^{78}Ni data point being the theoretical Hartree-Fock binding energy [Lis04]) and for protons data on the N=50 isotones from ^{79}Cu to ^{100}Sn was taken. Additional recent nuclear data on N=48,49 isotones and Cu isotopes (N=41-44) were included as well in fitting of the TBME [Lis06].
In Chapter 3 both shell model calculations were already mentioned in the context of the monopole variation in Cu isotopes. The calculated $J^{\pi}=5/2^{-},3/2^{-}$ energy levels in

odd-even Cu isotopes (see Fig. 2.9 in Chapter 3) indicated the accurate description of the proton single particle properties by SMII, which reproduces the observed near degeneracy of the $2p_{3/2}$ and $1f_{5/2}$ levels in $^{73}_{29}$Cu. Though it should be noted that the experimental spins of the two close lying levels at A=73 remain uncertain.
The T=1 part of the SMII interaction is symmetric in proton and neutrons, though it has been shown that an asymmetric T=1 interaction reproduces Ni and N=50 $E(2^+_1)$ states much better [Lis04]. A listing of these T=1 TBME's for protons and neutrons, together with the original G-matrix TBME's can be found in [Lis04]. An interesting feature of this asymmetric T=1 residual interaction is the strong enhancement of the $1g^2_{9/2}$ $J^\pi=2^+$ TBME for the neutron-neutron interaction. The difference between the $J^\pi=2^+$ and $J^\pi=0^+$ neutron TBME is 0.373 MeV, compared to 0.727 MeV for the proton-proton TBME, whereas in the original G-matrix TBME this difference is 0.538 MeV (no distinction between neutron and proton TBME is made). The asymmetry is assumed to mimic the effect of proton excitations over the Z=28 shell, which are outside the model space [Lis04]. The influence of these TBME's on the excitation energies is nicely illustrated when comparing the calculated $E(2^+_1)$ in Ni isotopes (N=42-46) and N=50 isotones (Z=42-46) with the experimental $E(2^+_1)$. As seen in Fig. 6.8 (Bottom), the energy of the 2^+_1 state in Ni is systematically lower than in the N=50 isotones. The calculation labelled SMIIT1 reproduces the $E(2^+_1)$, though with an isospin dependent residual interaction. The breaking of the Z=28 closed core due to the repulsive monopole interaction between $\nu 1g_{9/2}$ and $\pi f_{7/2}$ was suggested in several recent publications ([Lis04,Ots05,Maz05,Les05a,Ken01,Per06]) and might explain the overall decrease of the 2^+_1 state in Ni, and possibly Zn isotopes. The results from SMII calculations in this work were calculated with a symmetric T=1 interaction, which is a compromise between accurate $E(2^+_1)$ description and a universal isospin independent residual interaction in this valence space.

6.1.2 Effective charges

Effective charges are determined by adjusting the calculated $B(E2,2^+_1 \rightarrow 0^+_1)$ and $B(E2,8^+_1 \rightarrow 6^+_1)$ values for singly π/ν closed shell nuclei with two ν/π outside the N/Z=40 shell (resp.). In both cases the B(E2) values depend solely on one type of nucleon since no nucleons of the opposite type are available in the restricted model space. The nuclei considered are $^{92}_{42}$Mo (closed neutron shell N=50 + $\pi 1g^2_{9/2}$) and ^{70}Ni (closed proton shell Z=28 + $\nu 1g^2_{9/2}$) with following known B(E2) values : for $^{92}_{42}$Mo $B(E2,2^+_1 \rightarrow 0^+_1)$ =8.4(5) W.u. and $B(E2,8^+_1 \rightarrow 6^+_1)$=1.31(2) W.u. [nndc], for ^{70}Ni $B(E2,2^+_1 \rightarrow 0^+_1)$ =10(2) W.u. [Per06] and $B(E2,8^+_1 \rightarrow 6^+_1)$=0.66(2) W.u. [nndc]
The effective neutron and proton charges in the SMI calculations were (e_ν=0.9e,e_π=1.9e). The proton effective charge which should be used to reproduce the experimental $B(E2,2^+_1 \rightarrow 0^+_1)$ value in $^{92}_{42}$Mo of 8.4(5) W.u. is 1.7e [nndc, Smi06], though the effect of assuming e_π=1.9e on the Zn results is minor.
In the SMII calculations effective charges (e_ν=1.00e,e_π=1.56e) were used. For ^{70}Ni the calculated $B(E2,8^+_1 \rightarrow 6^+_1)$is 0.65 W.u., which compares well with the experimental value. The $B(E2,2^+_1 \rightarrow 0^+_1)$ value in the same ^{70}Ni is calculated to be 4.2 W.u., which deviates from the recent experimental value. It should be noted that the current theoretical value is closer to the theoretical value in [Sor02] : 4.8 W.u. The calculated $B(E2,2^+_1 \rightarrow 0^+_1)$ value for ^{68}Ni is 2.97 W.u., which compares very well to the recent experimental value of 3.09(73) e^2fm^4 [Sor02]. For $^{92}_{42}$Mo the calculated $B(E2,2^+_1 \rightarrow 0^+_1)$ value is 7.2 W.u. (experimental value = 8.4(5) W.u. [nndc]).

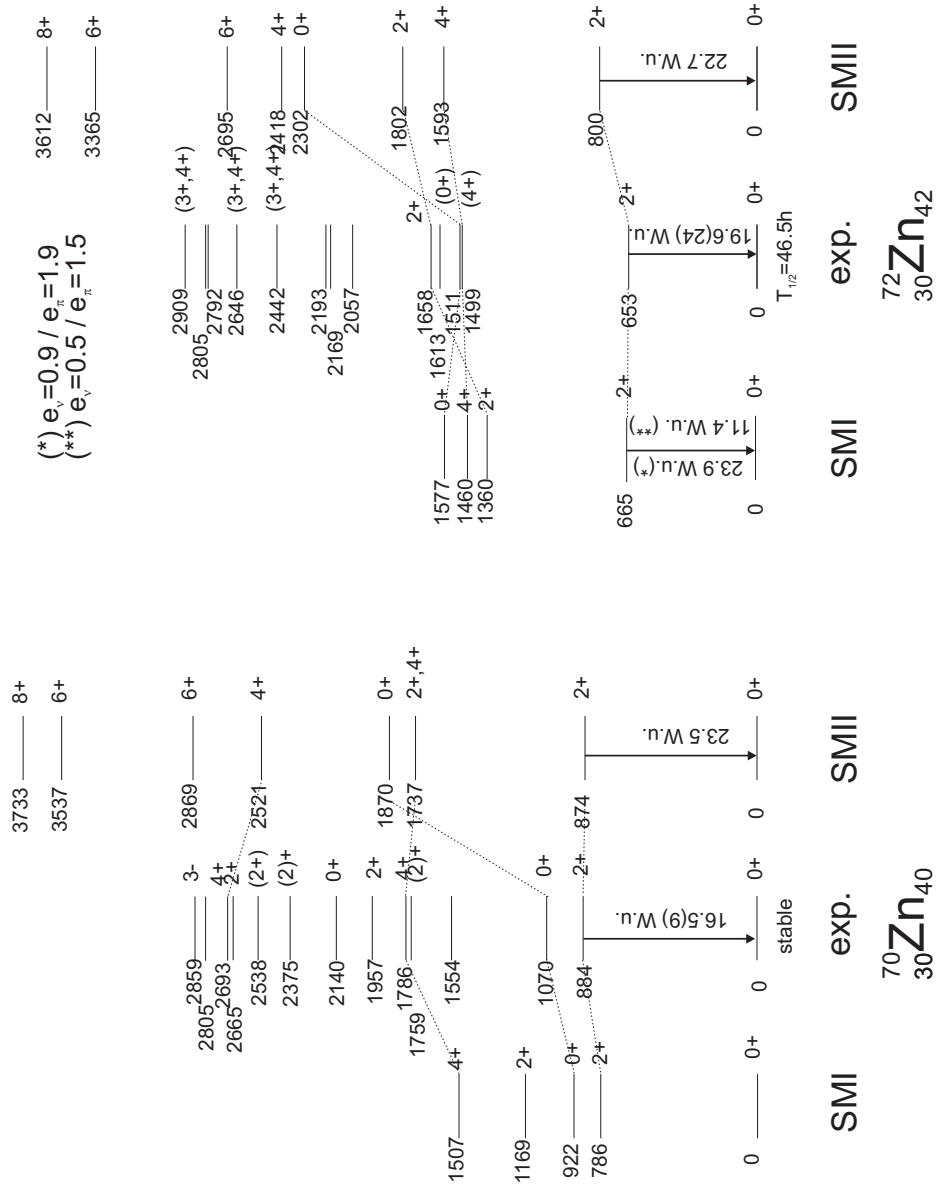

Figure 6.1: *Comparison of the experimental level scheme, $B(E2,2_1^+ \to 0_1^+)$ and $B(E2,4_1^+ \to 2_1^+)$ values with shell model calculations (SMI,SMII) for $^{70,72}Zn$.*

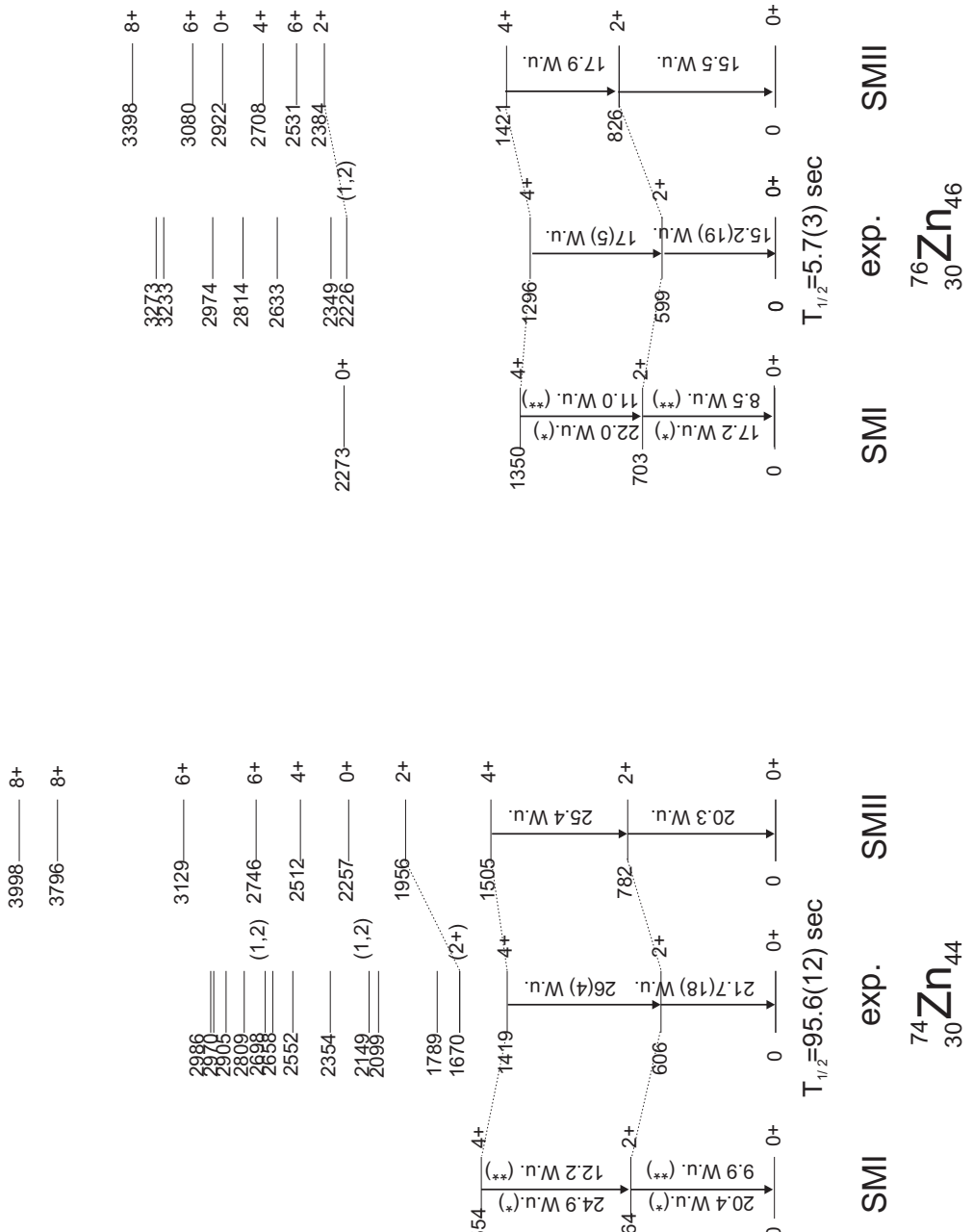

Figure 6.2: *Comparison of the experimental level scheme, $B(E2;2_1^+ \rightarrow 0_1^+)$ and $B(E2;4_1^+ \rightarrow 2_1^+)$ values with shell model calculations (SMI,SMII) for $^{74,76}Zn$.*

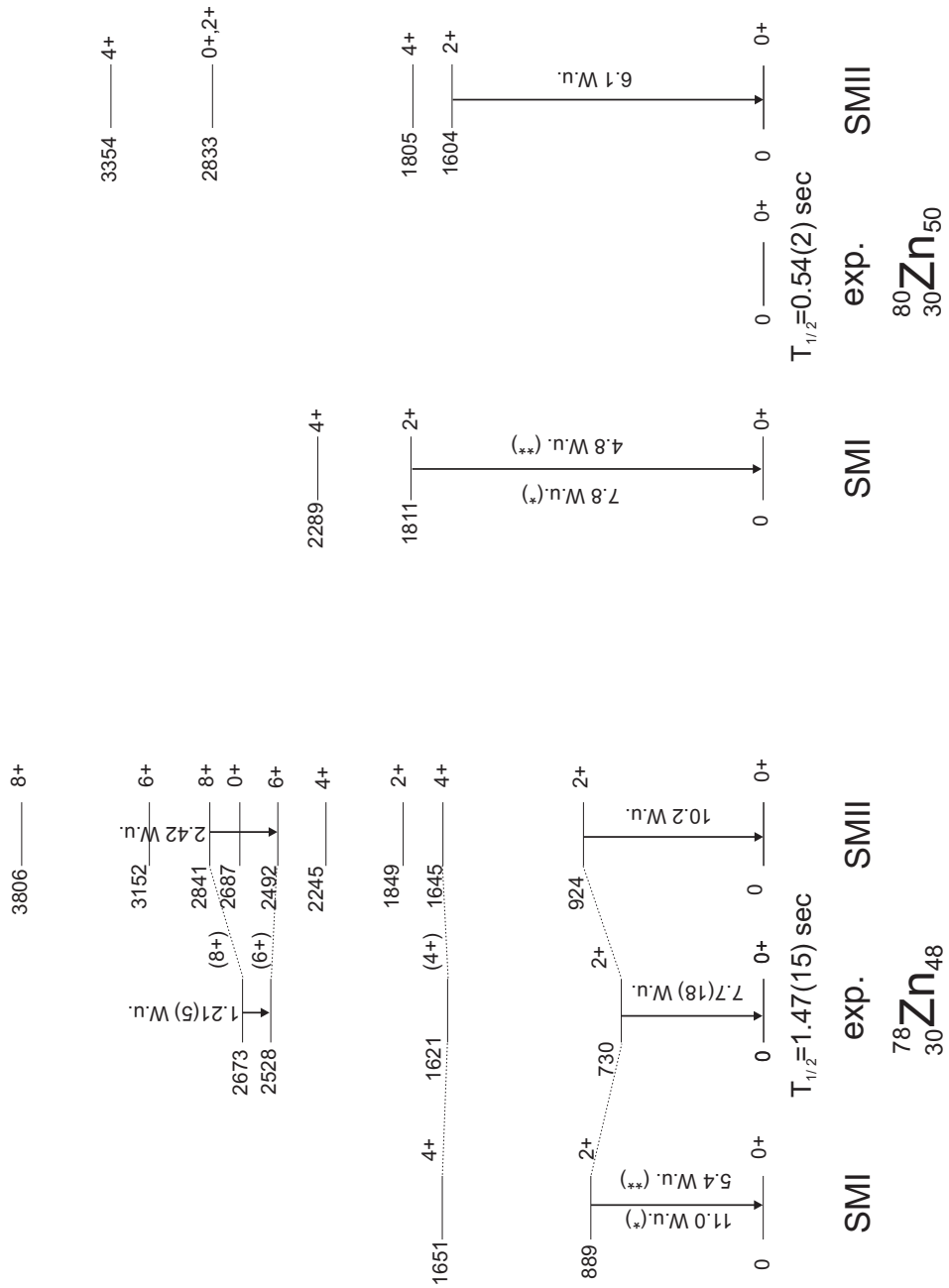

Figure 6.3: *Comparison of the experimental level scheme, $B(E2,2_1^+ \rightarrow 0_1^+)$ and $B(E2,4_1^+ \rightarrow 2_1^+)$ values with shell model calculations (SMI,SMII) for $^{78,80}Zn$.*

6.1.3 Evolution of the $E(2_1^+)$,$E(4_1^+)$,$E(2_2^+)$ and $E(0_2^+)$ states

First, it should be noted that the 2_1^+ level in ^{78}Zn and the 4_1^+ level in ^{76,78}Zn were firmly established in this work due to the selective E2 excitation probability in low energy coulomb excitation of even-even nuclei. In Fig. 6.5 the evolution of the 2_1^+,4_1^+,0_2^+ and 2_2^+ energy levels is shown over the full $pf_{5/2}$-$g_{9/2}$ shell together with the SMI and SMII calculations.

The monopole migration

From the proton occupation numbers in the ground state 0_1^+ wave function the effect of the monopole migration is apparent as shown in Fig. 6.4. The occupancy of the two protons over the $pf_{5/2}$-$g_{9/2}$ shell shows a change from predominantly $2p_{3/2}$ to predominantly $1f_{5/2}$ occupancy in between A=72 and A=74. This increased proton occupancy of the $1f_{5/2}$ orbit might increase the importance of the attractive monopole residual interaction between $\pi 2f_{5/2}$-$\nu 1g_{9/2}$ orbitals. Even though SMI and SMII significantly differ in the description of this proton single particle energy evolution, the calculated $E(2_1^+)$ levels do not differ significantly, indicating that the $E(2_1^+)$ state is dominated by neutron excitations in(to) the $1g_{9/2}$ orbit, as will be shown in the following.

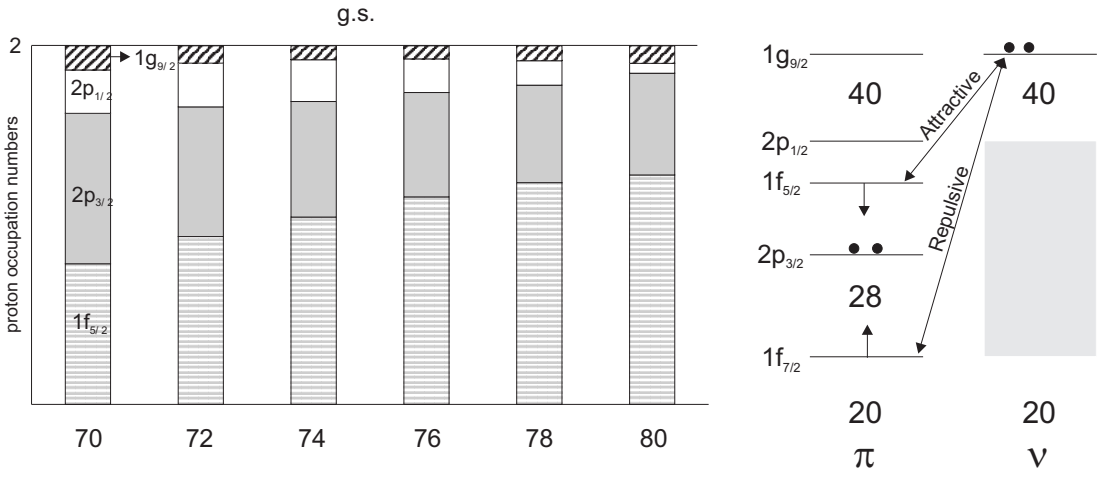

Figure 6.4: *Distribution of the two protons over the $pf_{5/2}$-$g_{9/2}$ orbitals, as calculated by SMII. Due to the monopole migration, the $1f_{5/2}$ is gradually filled more.*

$\mathbf{E(2_1^+)}$ systematics

The overall decrease of the 2_1^+ and 4_1^+ levels is reproduced by both shell model calculations, though the magnitude is underestimated by both SMI and SMII for the $E(2_1^+)$ level. Experimentally, the $E(2_1^+)$ decreases by ∼400 keV over the range N=42-46, while both shell model calculations predict an overall decrease of roughly 150 keV, indicating the need for more collectivity in the shell model.
In table 6.1 the amount of $1g_{9/2}^{N-40}$ component in the ground state 0_1^+ wave function is given for Zn isotopes (SMII calculation). The $1g_{9/2}^{N-40}$ component increases with increasing neutron number, whereas the amount of the 2p-2h component decreases with increasing neutron number. Neutron pair scattering from $1f_{5/2}$ to $1g_{9/2}$ peaks in ^{72}Zn and decreases strongly in ^{76,78}Zn.
The near constancy of the Zn $E(2_1^+)$ over the range N=42-46 indicates a seniority like behavior for this state in the $1g_{9/2}$ orbit. The same situation is observed in Ni isotopes (N=42-48) and the N=50 isotones (Z=42-48) (see Fig. 6.8). For the N=50 isotones, it has long been recognized that seniority is a good quantum number within the identical nucleon $1g_{9/2}$-$2p_{1/2}$ configurations ([Lis04], [Xia88],).
The dominance of the $1g_{9/2}^n$ wave function in Ni isotopes was established in a shell model study ([Maz05]) utilizing the same interaction as in SMII and is given for comparison in table 6.1. In the Ni isotopic chain, the $E(2_1^+)$ decreases ≈300 keV over the range N=42 (^{70}Ni) to N=48 (^{76}Ni) (Fig. 6.8). The amount of pure $1g_{9/2}^n$ wave function in the ground state varies from 46% in ^{70}Ni to 86% in ^{76}Ni (see table 6.1). The decreased configuration mixing in the ground state decreases in turn the pairing and thus the 0_1^+ is lowered less in ^{76}Ni, compared to ^{70}Ni ([Maz05]). For Zn isotopes a similar increasing $1g_{9/2}^{(N-40)}$ J=0 component is apparent in the ground state (from 10% in A=72 to 87% in A=78, see table 6.1), indicating decreased mixing in the ground state when more and more neutrons are added to $1g_{9/2}$. Though, the $E(2_1^+)$ state remains roughly constant and increases again at N=48, contrary to the $E(2_1^+)$ in ^{76}Ni. An alternative explanation for the further decrease of $E(2_1^+)$ in ^{76}Ni (N/Z=1.71) is given by a reduced neutron pairing interaction for N/Z>1.60 nuclei [Wal06]. The reduced $E(2_1^+)$ at this N/Z ratio was noticed before in $^{136}_{52}$Te$_{84}$ (N/Z=1.62, see fig. 2.7) and was explained by a reduced neutron pairing gap at N=84 (QRPA calculations [Ter02]).
The unknown energy of the $E(2_1^+)$ state in ^{80}Zn (N=50) is predicted to be 1810 Mev by SMI and 1604 MeV by SMII. Since N/Z=1.67 in this nucleus, the energy might be expected lower then these predictions. The N/Z ratio's for some isotopes where this effect might be expected are indicated in Fig. 6.8.

$\mathbf{E(2_2^+)}$ systematics

Experimentally a decrease of the 2_2^+ state is observed over the range N=40-46, though the decrease is less pronounced compared to the 2_1^+ state (this is seen from the $E(2_2^+)$ /$E(2_1^+)$ ratio). The nature of this different behavior might be clarified by investigating the corresponding neutron wave function (table 6.1).
The main difference between both states is the dominance of 2p-2h (4p-4h) excitations in the 2_1^+ wave function where the two (neutron) holes are situated in the same orbital, whereas the 2_2^+ wave function has a more pronounced amount of 2p-2h excitations where the two neutron holes are situated in two different orbitals. The dominance of pair scattering in the 2_1^+ wave function is possibly a reflection of the erosion of the N=40 shell gap, which enhances pair scattering. The latter can be attributed to the

0_1^+						
	$1g_{9/2}^{N-40}$	$1f_{5/2}^{-2}1g_{9/2}^{N-40+2}$	$2p_{1/2}^{-2}1g_{9/2}^{N-40+2}$	$1f_{5/2}^{-1}2p_{1/2}^{-1}1g_{9/2}^{N-40+2}$	[Lis04]	$1g_{9/2}^{N-40}$
$^{70}Zn_{40}$	3%	25%	10%	-		
$^{72}Zn_{42}$	10%	47%	12%	1%	^{70}Ni	44%
$^{74}Zn_{44}$	32%	44%	12%	1%	^{72}Ni	53%
$^{76}Zn_{46}$	71%	16%	7%	-	^{74}Ni	67%
$^{78}Zn_{48}$	87%	7%	-	-	^{76}Ni	83%
2_1^+						
	$1g_{9/2}^{N-40}$	$1f_{5/2}^{-2}1g_{9/2}^{N-40+2}$	$2p_{1/2}^{-2}1g_{9/2}^{N-40+2}$	$1f_{5/2}^{-1}2p_{1/2}^{-1}1g_{9/2}^{N-40+2}$	-	
$^{70}Zn_{40}$	-	21%	-	2%	-	
$^{72}Zn_{42}$	5%	51%	13%	3%	-	
$^{74}Zn_{44}$	27%	52%	12%	2%	-	
$^{76}Zn_{46}$	77%	16%	-	1%	-	
$^{78}Zn_{48}$	97%	1%	-	-	-	
2_2^+						
	$1g_{9/2}^{N-40}$	$1f_{5/2}^{-2}1g_{9/2}^{N-40+2}$	$2p_{1/2}^{-2}1g_{9/2}^{N-40+2}$	$1f_{5/2}^{-1}2p_{1/2}^{-1}1g_{9/2}^{N-40+2}$	-	
$^{70}Zn_{40}$	-	16%	3%	14%	-	
$^{72}Zn_{42}$	4%	27%	4%	42%	-	
$^{74}Zn_{44}$	11%	27%	3%	46%	-	
$^{76}Zn_{46}$	73%	8%	1%	11%	-	
$^{78}Zn_{48}$	97%	2%	-	-	-	

Table 6.1: *Analysis of the 0_1^+ ,2_1^+ and 2_2^+ neutron wave functions in terms of $1g_{9/2}^{N-40}$ component and 2p-2h components (limited to $1f_{5/2}^{-2}1g_{9/2}^{N-40+2}$,$2p_{1/2}^{-2}1g_{9/2}^{N-40+2}$ and $1f_{5/2}^{-1}2p_{1/2}^{-1}1g_{9/2}^{N-40+2}$) in % of the total wave function. Results are for SMII calculations [Lis06].*

strong attractive monopole residual interaction between $\pi 1f_{5/2}$-$\nu 1g_{9/2}$ orbitals.

$\mathbf{E(0_2^+)}$

Experimentally the 0_2^+ state decreases with increasing neutron number and reaches a minimum at N=40. A similar behavior was observed in N=48,50 isotones and the neighboring even-even Ni and Ge isotopes (see as well Fig. 6.8), where it even becomes the first excited state at N=40 in Ni and Ge. The reason for this behavior can be attributed to the superfluid character of the neutron shell at N=40 ([Sor02, Van05]). The 0_2^+ state might be a mixture of different 0^+ orbitals, where pairs of nucleons are located in different orbitals. From the occupation numbers n($1g_{9/2}$) of the $1g_{9/2}$ orbit in the ground state, relative to the "normal" occupation (N-40) : $n_{extra}(1g_{9/2})$=n($1g_{9/2}$)-(N-40) over the range N=30-50 it can be seen that at N=40 the pair scattering across N=40 is enhanced. This fact was pointed out in [Sor02] for Ni isotopes and is plotted in Fig. 6.6 for the 0_1^+ ground state in Ni and Zn isotopes (current SMI and SMII results). The enhanced filling of the $\nu 1g_{9/2}$ orbit in Zn sets in earlier then in the Ni

isotopes, and decreases more rapidly at N=46,48. This observation has been reported in [Per06] as well. At N=46, the enhanced filling of the $1g_{9/2}$ is strongly reduced. This is indicated by both SMI and SMII calculations. The overall higher occupation in SMII is due to restrictions on the number of possible excitations to the $1g_{9/2}$ in SMI for computational reasons.

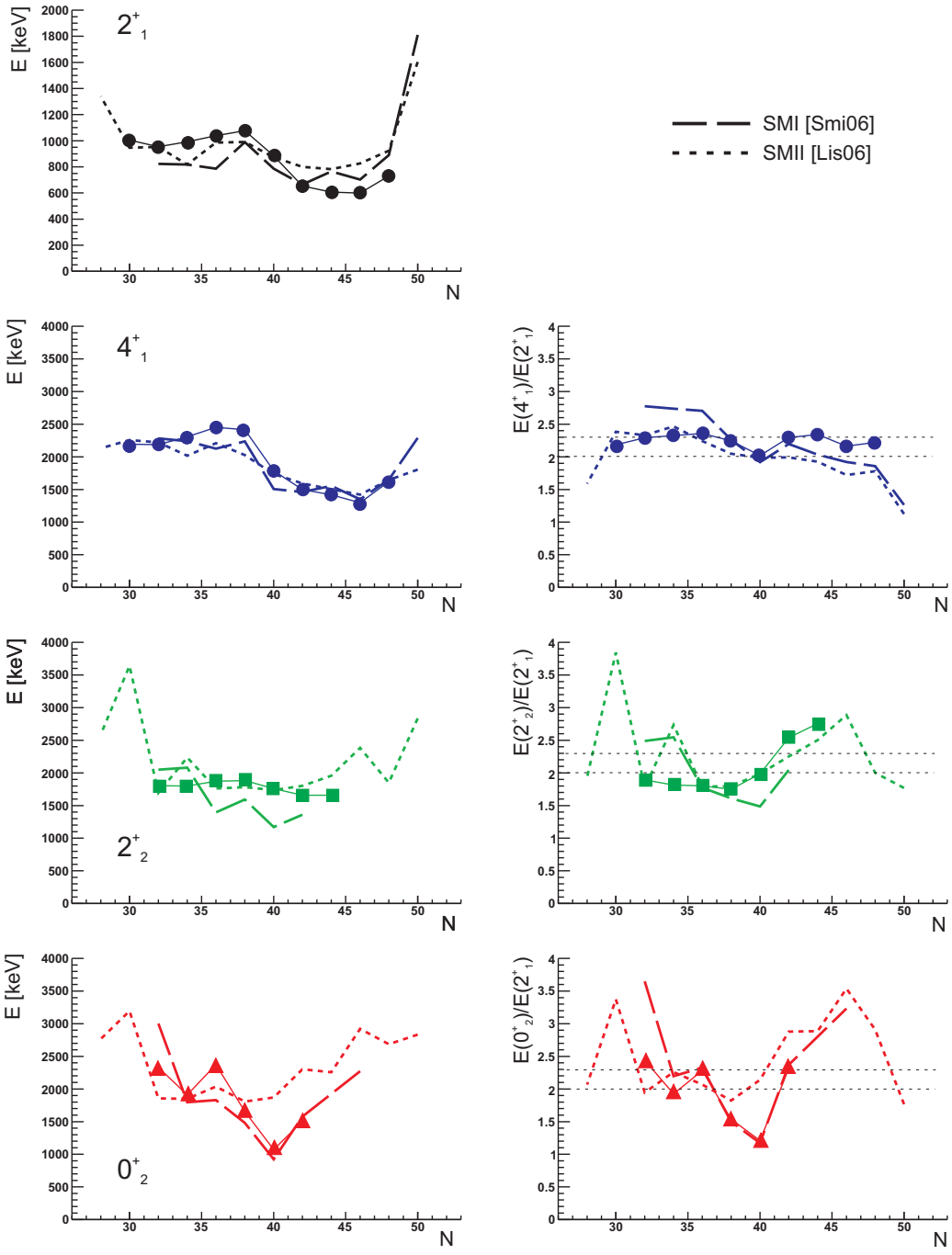

Figure 6.5: *Systematics of $E(2_1^+)$, $E(4_1^+)$, $E(2_2^+)$ and $E(0_2^+)$ compared to SMI and SMII calculations.*

[t]

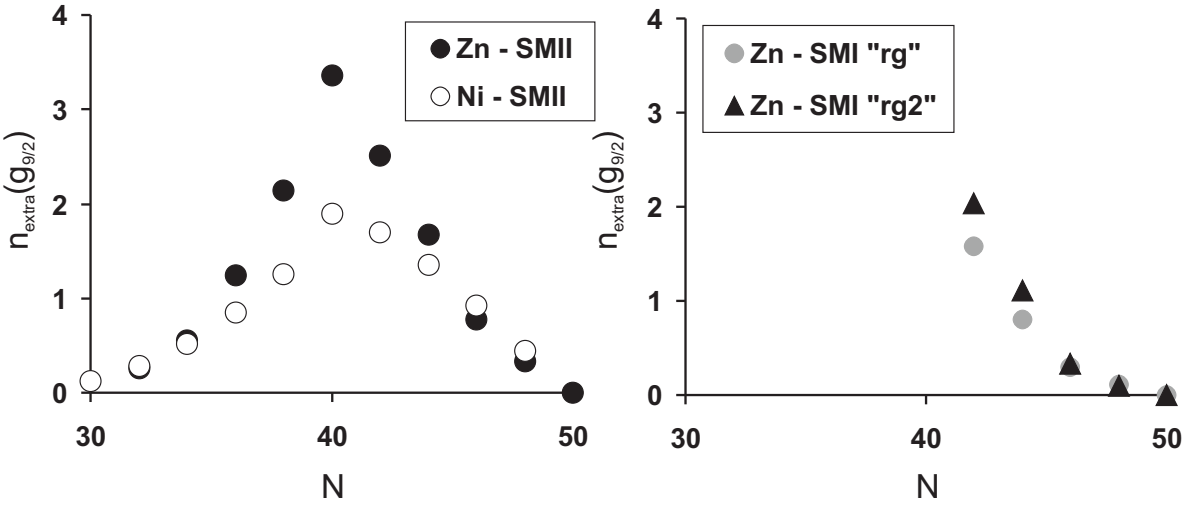

Figure 6.6: *The number of additional neutrons in the $1g_{9/2}$ orbit, compared to the normal occupancy of N-40 for Ni and Zn isotopes. Left : SMII calculations for Ni and Zn, Right : SMI calculations for Zn with "rg" and "rg2" interactions.*

6.1.4 The B(E2,$2_1^+ \rightarrow 0_1^+$) systematics

In Fig. 6.7 A/B adopted and current experimental B(E2,$2_1^+ \rightarrow 0_1^+$) values for Zn isotopes are shown together with SMI (A) and SMII (B) predictions. B(E2,$2_1^+ \rightarrow 0_1^+$) values for ^{62,64,70}Zn were adopted from lifetime measurements ([Ken02, Les05a, Les05b]), values for ^{66,68}Zn are averaged values from both lifetime measurements ([Les05a, Les05b]) and multiple coulomb excitation studies ([Koi03, Koi04]) at 4.2 MeV/u. The data points on ^{72,74}Zn were recently obtained at the GANIL facility by intermediate energy coulomb excitation (in-flight fragmentation) [Lee02, Per06]. Data points on ^{74,76,78}Zn were added by this work. The result for ^{74}Zn (0.201(16) e^2b^2) is in good agreement with the adopted value from [Per06] (0.204(15) e^2b^2).

SMI calculations

Two SMI calculations were performed with (e_π,e_ν)=(1.9e,0.9e) and are shown in Fig. 6.7 A. The dashed black line reproduces the B(E2) values for ^{68,70,72}Zn very well, but fails to reproduce the still increasing E2 strength in ^{74}Zn. The interaction used in SMI is referred to as "rg" and is based on the G-matrix interaction from [Hjo95], with a modified monopole part [Now96, Smi04, Van04a, Van04b] and is the best fit to data in the region. This interaction was successfully applied to odd Cu isotopes [Van04a, Van04b]. The dot-dashed line is a modified version of "rg", referred to as "rg2", with corrections of three monopoles and with the addition of few multipoles [Smi06]. The "rg2" interaction improves the description of the monopole shift in odd-A Cu isotopes, as shown in Fig. 6.7 G, where the single particle energies in odd Cu isotopes are shown together with "rg" (dashed black line) and "rg2" (dot-dashed black line) calculations. Higher B(E2,$2_1^+ \rightarrow 0_1^+$) values are calculated in both ^{72,74}Zn with "rg2".
An enhanced p-n interaction between $\pi 1f_{5/2}$-$\nu 1g_{9/2}$, compared to $\pi 2p_{3/2}$-$\nu 1g_{9/2}$ or-

bitals would enhance the collectivity in the nucleus. This in turn depends on the position of the $1f_{5/2}$ orbit and is determined by the attractive monopole interaction between $\pi 1f_{5/2}$-$\nu 1g_{9/2}$. The better description of this monopole interaction by "rg2", as observed in the monopole shift in Cu, might explain the calculated increase in B(E2) strength for ^{72,74}Zn.
In Fig. 6.6 (right) the number of additional neutrons in the $1g_{9/2}$ (relative to N-40 neutrons) is plotted. With "rg2", a higher (additional) occupation is calculated for ^{72,74}Zn. The additional $1g_{9/2}$ neutrons bring in an additional amount of E2 strength, as suggested in [Per06].

SMII calculations

In Fig. 6.7 B, two SMII calculations are shown. (For comparison with SMI, the SMII calculations for odd-Cu SPE are repeated in Fig. 6.7 G, indicating the adequate description of the monopole shift.) The effective charges used in SMII are (e_π,e_ν)=(1.56e,1.00e). The dashed black line, reproduces the experimental trend for A>70. It should be pointed out that in the SMII valence space a small *isovector* charge (defined as $e_{IV}=\frac{1}{2}(e_\nu\text{-}e_\pi+1)$) of 0.22 is needed. In the $^{100}_{50}$Sn region, large isovector charges were needed as well in large scale shell model calculations [Gor97,Dau00]. Remarkably, the SMII calculations do not reproduce the B(E2,$2^+_1 \rightarrow 0^+_1$) values for A≤70. Though, at A=70 the sum of the experimental $2^+_1 \rightarrow 0^+_1$ (16.5 W.u.) and $2^+_1 \rightarrow 0^+_2$ (7.5 W.u.) E2 transition strength is 24 W.u., which corresponds to the calculated value. This indicates the influence of the calculated 0^+_2 state, which is too high in energy in SMII. Therefore all E2 strength from the 2^+_1 state is contained in the $2^+_1 \rightarrow 0^+_1$ transition. A remarkable improvement is obtained in the SMII result when the input $1g_{9/2}$ single particle energy is *increased* by 400 keV (dashed black line). The experimental trend for A≤72 is improved whereas the trend for A≥74 is only slightly modified. These results indicate that the B(E2,$2^+_1 \rightarrow 0^+_1$) strength for A≥72 is dominated by $(\nu 1g^2_{9/2})_{J=2} \rightarrow (\nu 1g^2_{9/2})_{J=0}$ transitions (the 2^+_1 state is predominantly a $1g_{9/2}$ excitation, see table 6.1). The analysis of the 2^+_1 wave function in table 6.1 shows a decreased neutron pair scattering from ^{76}Zn on (<20% 2p-2h component), compared to >50% for ^{72,74}Zn. This reduces the total E2 strength in ^{76,78}Zn, compared to ^{72,74}Zn, as observed experimentally.
In Fig. 6.6 the amount of additional neutrons in the $1g_{9/2}$ is plotted, calculated with SMII (left). Similar to SMI, the additional occupation drops drastically for N≥46.

Other calculations from literature

For comparison shell model results taken from [Les05a] are plotted in Fig. 6.7 A as well. The full grey line represents calculations performed in the pf valence space outside a ^{40}Ca core with the Kuo-Brown residual interaction (LSSM-1, see [Les05b] for further details). The dashed grey line corresponds to a $pf_{5/2}$-$g_{9/2}$ model space outside a ^{56}Ni core (LSSM-2). No excitations from the $f_{7/2}$ proton orbital are taken into account in the latter. The LSSM-1 calculations, reproduce the B(E2,$2^+_1 \rightarrow 0^+_1$) and B(E2,$4^+_1 \rightarrow 2^+_1$) trends up to N<38. From N=38 on, the inclusion of the $1g_{9/2}$ orbital in the valence space becomes important (LSSM-2). Additional information on the g-factor of the 2^+_1 state indicates that neutron pair scattering across N=40 is of prime importance in order to reproduce the experimental values (see [Ken02]).
In [Per06], shell model occupancies of the $\nu 1g_{9/2}$ orbital were calculated. The authors

conclude that pairing correlations start to empty the fp orbitals in Zn isotopes earlier and to a larger extent than in Ni isotopes thereby shifting the minimum in B(E2,$2_1^+ \rightarrow 0_1^+$) to N=38, compared to N=40 in Ni. In this work a similar observation was made (see Fig. 6.6). The enhanced filling of the $\nu 1g_{9/2}$ brings a direct contribution to the B(E2) value through the $1g_{9/2}^{J=2}$ configuration. From table 6.1 it is clear that the amount of neutron pair scattering decreases drastically in ^{76,78}Zn. This might be linked to the sudden decrease in B(E2) strength in these isotopes, which is reproduced by the shell model calculations. Comparing the $1g_{9/2}$ occupation in the SMI calculations for "rg" and "rg2" interactions, it is seen that the latter enhances the pair scattering for A=72,74 compared to "rg". This increase is reflected as well in the higher B(E2) values in these isotopes, as calculated by "rg2", which is in better agreement with experiment in for ^{74}Zn.

Shell model conclusions

The above shell model calculations (SMI,SMII,LSSM-1 and LSSM-2) indicate the decreasing impact of $f_{7/2}$ proton excitations for heavier Zn isotopes (A≥68) and the increasing impact of neutron pair scattering to the $1g_{9/2}$ orbit in heavier Zn isotopes (A≥68). From a comparison of "rg" and "rg2" interactions, it was concluded that the monopole interaction between $\pi 1f_{5/2}$-$\nu 1g_{9/2}$ enhances the p-n interaction and leads to more collectivity. A sharp decrease in neutron pair scattering to the $1g_{9/2}$ from ^{76}Zn on, observed in the 2_1^+ wave function components (SMII), is similar to the sharp decrease in B(E2) strength from ^{76}Zn, so there might be a link between these observations. The higher neutron occupation in the $1g_{9/2}$ and the higher B(E2) values in ^{72,74}Zn, calculated with "rg2" show the link between high B(E2) and enhanced neutron (pair) scattering to $1g_{9/2}$. The large amount of neutron $1g_{9/2}^2$ configuration in the 2_1^+ state in ^{76,78}Zn (77-97%, compared to 5-27% in ^{74,76}Zn) might be linked to the strongly decreasing B(E2,$2_1^+ \rightarrow 0_1^+$) strength in ^{76,78}Zn, since the 2_1^+ state is then predominantly a neutron excitation.

6.1.5 The B(E2,$4_1^+ \rightarrow 2_1^+$) systematics

In Fig. 6.7 C,D and F calculated E2 transitions strengths are shown for $4_1^+ \rightarrow 2_1^+$, $2_2^+ \rightarrow 2_1^+$ and $2_2^+ \rightarrow 0_1^+$. The available experimental data are given as well. The only experimental points for A>70 are provided by this work (open circles in Fig. 6.7 C), though with large error bars due to the limited statistics[1]. The A=68 data point stems from a multiple coulomb excitation experiment [Koi03], whereas the remaining data points stem from life time measurements ([Les05a, Ken02]). The shell model calculations, both SMI and SMII, reproduce the new experimental B(E2,$4_1^+ \rightarrow 2_1^+$) transition strengths above A=70. Remarkably, SMII fails to reproduce the B(E2,$4_1^+ \rightarrow 2_1^+$) values for A<70. When the $1g_{9/2}$ orbit is lowered by 400 keV, the agreement improves, similar to the observation in the B(E2,$2_1^+ \rightarrow 0_1^+$) values. Overall, the calculated B(E2,$4_1^+ \rightarrow 2_1^+$) strength overestimates the experimental observed strength for A<70. The discrepancy for A=64 is remarkable, since the shell model predicts a considerable increase in B(E2,$4_1^+ \rightarrow 2_1^+$) strength, whereas experimentally a lower value then A=62,66 is observed. LSSM-1 and LSSM-2 calculations from [Ken02] are shown in Fig. 6.7 C as well. The same conclusion as for the B(E2,$2_1^+ \rightarrow 0_1^+$) values can be drawn (see above, this paragraph), concerning the impact of $\nu 1g_{9/2}$ excitations on the

[1]The measurement of B(E2,$4_1^+ \rightarrow 2_1^+$) values was not included in the original goal of the experiments described in this work.

E2 strength. In [Les05b] the g-factor of the 4_1^+ state could only be reproduced when a considerable amount of $\nu 1g_{9/2}^2$ configuration was introduced, indicating the dominance of $1g_{9/2}^2$ admixtures in the wave function.
The remaining B(E2,$2_2^+ \rightarrow 2_1^+$) and B(E2,$2_2^+ \rightarrow 0_1^+$) strengths will be discussed in the paragraph on collective models, since they are an indication for the applicability of the various collective models on neutron rich Zn isotopes.
In conclusion, all shell model calculations on Zn isotopes above A=68 (N=38) indicate an important contribution from $\nu 1g_{9/2}^2$ configuration in the wave function of the low lying excited 2_1^+ and 4_1^+ states. The B(E2,$2_1^+ \rightarrow 0_1^+$) strength is thus dominated by the specific E2 strength between $(\nu 1g_{9/2})_{J=0}$ and $(\nu 1g_{9/2})_{J=2}$ configurations. For the lighter Zn isotopes, excitations from $\pi f_{7/2}$ influence the low lying B(E2,$2_1^+ \rightarrow 0_1^+$) and B(E2,$4_1^+ \rightarrow 2_1^+$) strength.

6.1.6 Comparison to neighboring even-even isotopes

In Fig. 6.9 B(E2,$2_1^+ \rightarrow 0_1^+$) systematics is compared for neighboring even-even isotopes $_{28}$Ni,$_{30}$Zn,$_{32}$Ge,$_{34}$Se,N=48 and N=50 isotones. SMII calculations are indicated for $^{58-76}$Ni,$^{60-80}$Zn and $^{74-82}$Ge. SMI calculations are shown for ^{72,74,76,78,80}Zn and ^{76,78,80,82}Ge.
In Fig. 6.9 A the B(E2,$2_1^+ \rightarrow 0_1^+$) systematics of Ni isotopes is shown together with SMII calculations and two shell model calculation from literature. The first calculation (long dashed line) is taken from [Sor02] and the utilized model space consists of ($1f_{7/2}2p_{3/2}1f_{5/2}2p_{1/2}$) proton orbitals and ($2p_{3/2}1f_{5/2}1g_{9/2}$) neutron orbitals, outside a ^{48}Ca closed core. The solid grey line is taken from [Ken01], where a $1f_{7/2}2p_{3/2}1f_{5/2}2p_{1/2}$ valence space was used. In [Ken01] the full shell model calculation was performed with a limited number of proton excitations out of the $f_{7/2}$ orbital. The bell shape curve was reproduced when up to five protons were allowed to excite across Z=28 (see Fig. 6.9 A). The main difference between SMII and the two literature shell model results is the inclusion of $f_{7/2}$ proton excitations in the latter. The difference between SMII and the result from [Sor02] decreases for ^{68,70,72}Ni, hinting the dominance of $1g_{9/2}$ neutron excitations, and a decrease of the $\pi f_{7/2}$ contribution to the B(E2) above N=40. The recent experimental B(E2,$2_1^+ \rightarrow 0_1^+$) in ^{70}Ni is not reproduced by any SM calculation. The high value has been interpreted in [Per06] as a rapid polarization of the proton core induced by the filling of the neutron $1g_{9/2}$ orbit, which is in turn a reflection of the strong monopole interaction between $\pi 1f_{5/2}$-$\nu 1g_{9/2}$.
The results on radioactive ^{78,80,82}Ge isotopes shown in Fig. 6.9C are taken from a recent low energy coulomb excitation experiment in inverse kinematics at ORNL [Pad05]. A downward trend in B(E2,$2_1^+ \rightarrow 0_1^+$) values from N=42 to N=50 is observed for Ge isotopes, similar to the observed downward trend in Zn (N=44 to N=48). The same trend is observed in Se isotopes (see Fig. 6.9d) as well. The systematic trend hints a strong N=50 subshell closure.
The higher B(E2,$2_1^+ \rightarrow 0_1^+$) values compared to Zn isotopes indicate an increased collectivity in these nuclei. Several collective models have been applied successfully to lighter Ge isotopes (A<72) [Koi03, Toh01, Toh00, Kot90, And94]. For N>40 Ge isotopes, the behavior is analogue to the Zn isotopes : an identical decrease of the E(2_1^+) state in Zn and a drastic lowering of the B(E2,$2_1^+ \rightarrow 0_1^+$) strength.

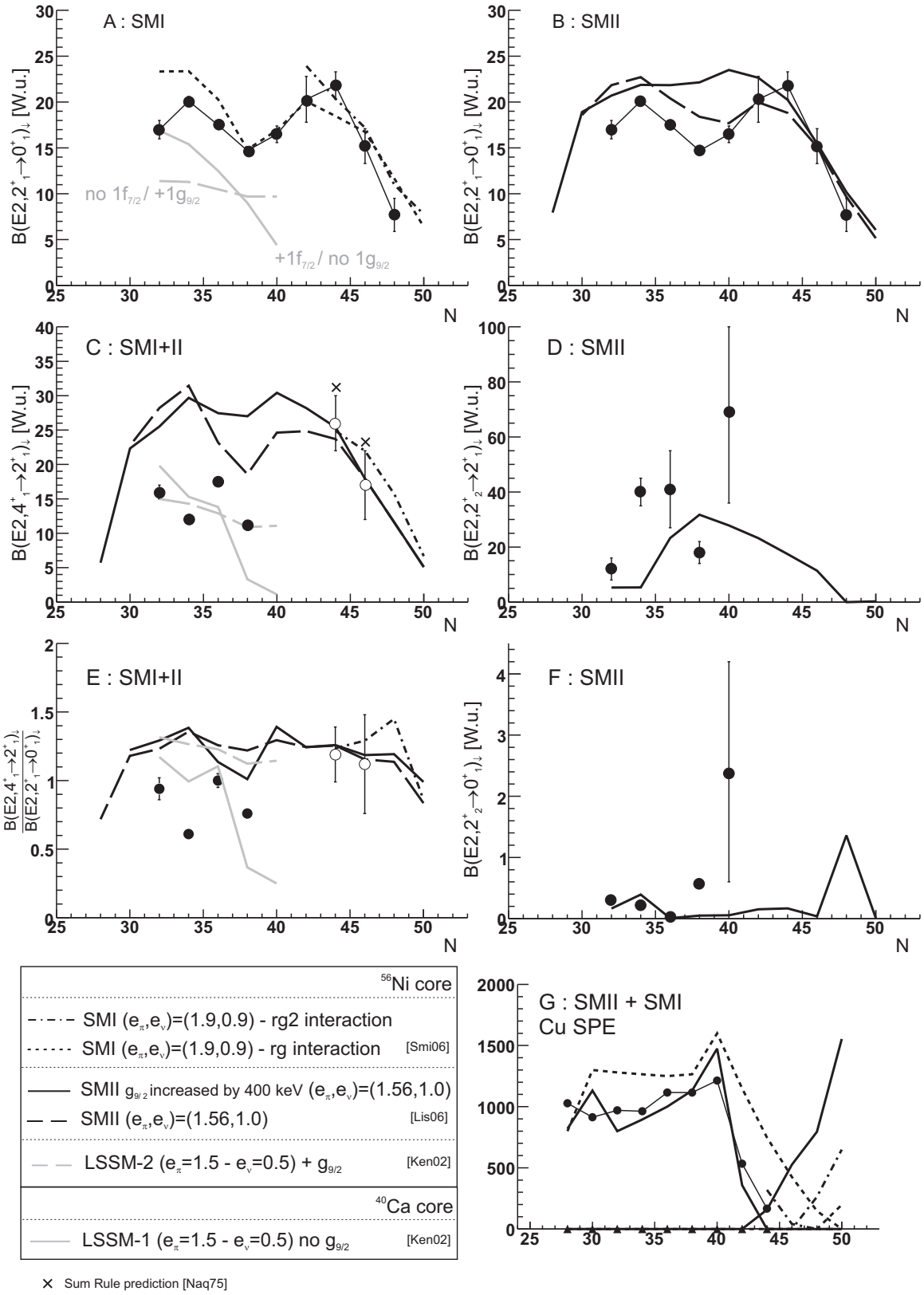

Figure 6.7: *Experimental and shell model results for Zn isotopes : (A) B(E2,$2_1^+ \rightarrow 0_1^+$) , SMI and LSSM-1/2 shell model calculations. (B) B(E2,$2_1^+ \rightarrow 0_1^+$) and SMII calculations. (C) B(E2,$4_1^+ \rightarrow 2_1^+$) . (D) B(E2,$2_2^+ \rightarrow 2_1^+$). (E) B(E2,$4_1^+ \rightarrow 2_1^+$) /B(E2,$2_1^+ \rightarrow 0_1^+$) . (F) B(E2,$2_2^+ \rightarrow 0_1^+$).*

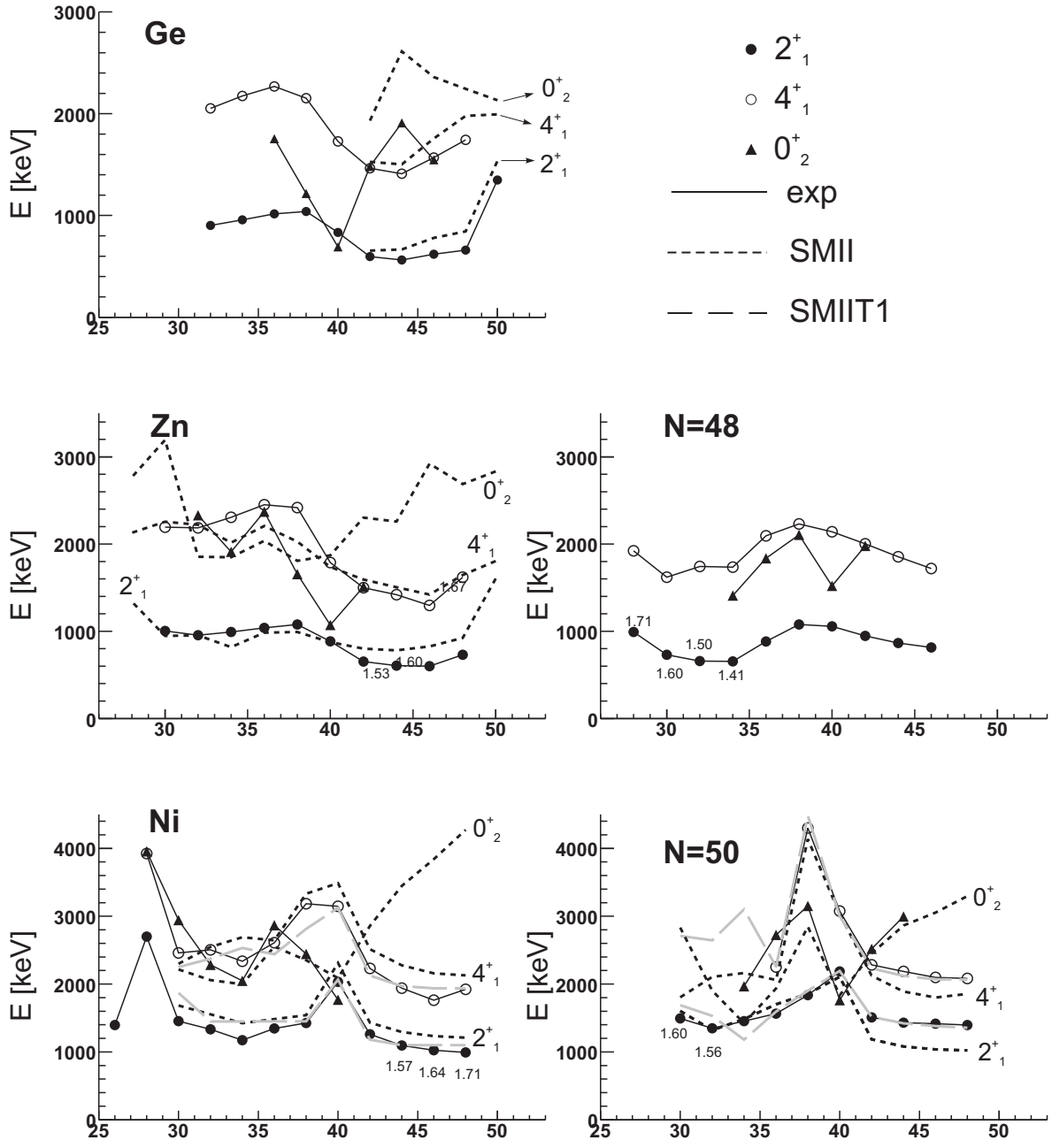

Figure 6.8: *$E(2^+_1)$,$E(4^+_1)$ and 0^+_2 levels for Ni, Zn, Ge, N=48 and N=50 isotopes compared with SMII calculations.*

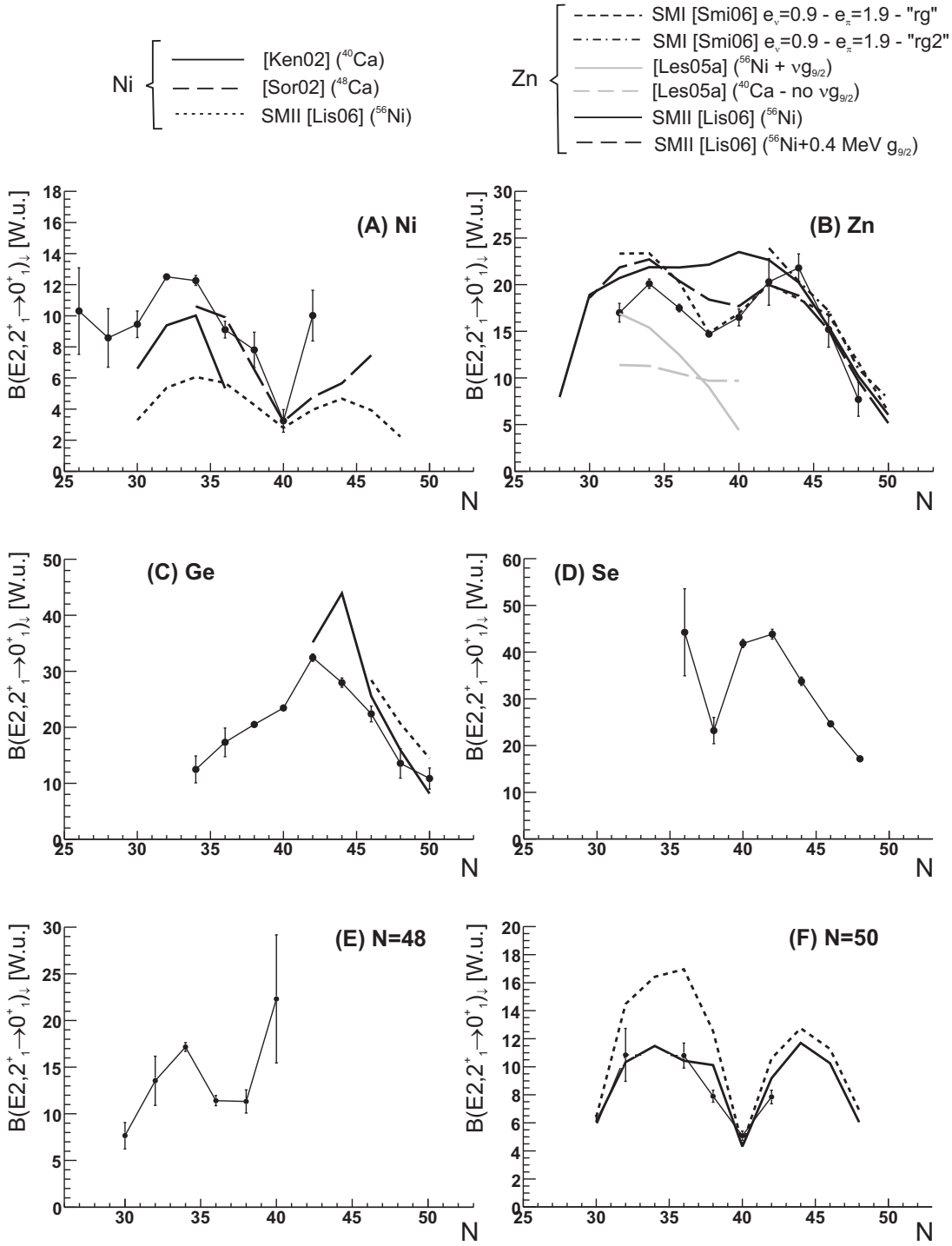

Figure 6.9: *$B(E2,2_1^+ \rightarrow 0_1^+)$ values for Ni,Zn,Ge and Se isotopes compared with SMII calculations.*

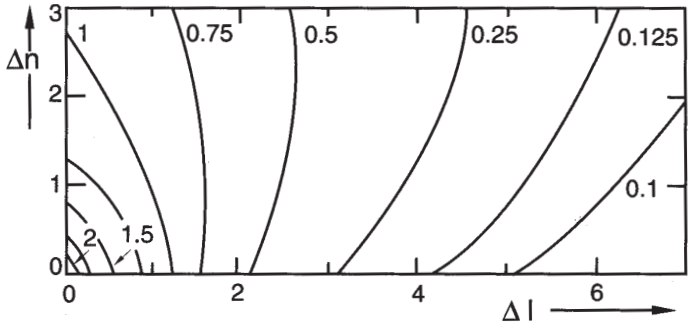

Figure 6.10: *Evolution of the radial overlap between the $1s_{1/2}$ wave function and any other (nlj)-wave function with Δn=n-1 and Δl=l [Hey95].*

6.2 Seniority versus Collectivity

In the previous paragraph it was shown that the current shell model description in the $pf_{5/2}$-$g_{9/2}$ space (SMI-II) quite accurately describes the evolutionary trend of Zn isotopes for N>40. The importance of the $1g_{9/2}$ orbit on the experimental observables was highlighted repeatedly. This dominance of the nuclear structure by a single high-j orbit will be elaborated upon in this paragraph.
Collectivity and configuration mixing in the nuclear medium is driven primarily by the residual proton-neutron interaction. In heavy Zn isotopes (A>70), the residual proton-neutron interaction is limited to the "normal parity" $2p_{3/2}$-$1f_{5/2}$ proton orbitals and the $1g_{9/2}$ neutron orbital. The increased $B(E2,2_1^+ \rightarrow 0_1^+)$ value for ^{72}Zn was interpreted as a gradual increase of collectivity. For a deformation parameter $\beta \approx 0.23$ positive parity Nilsson orbitals penetrate in negative parity region, offering the possibility to generate large B(E2) strength [Lee02]. In a recent publication it was pointed out that collectivity develops faster in nuclei where both protons and neutrons are in the first half of the shell (or both in the second half) compared to one filling below and the other above midshell [Cak06]. Applying this result to the major shell between nucleon numbers 28 and 50 (22 valence nucleons), it can be expected that collective nucleon motion will develop slowly in heavy (A≥70) Zn isotopes (2 valence protons and >12 valence neutrons). Though, from radial overlap arguments ([Cas00, Hey95] and illustrated in Fig. 6.10 for a $1s_{1/2}$ orbital with any nlj-orbital), the residual interaction is considerably larger between $(1\pi f_{5/2}, 1\nu g_{9/2})$ orbitals then between $(2\pi p_{3/2}, 1\nu g_{9/2})$ orbitals. Since the proton wave function calculated by SMII has increasingly more $1f_{5/2}$ content (due to the monopole migration) it might be expected that collective behavior might be enhanced. These contradictory results (slowly developing collectivity versus enhanced proton-neutron interaction) raises the question whether heavy Zn isotopes exhibit collective behavior. The development of collectivity will be hindered by the neutron shell closure at N=50, as indicated by the strong reduction of the $B(E2,2_1^+ \rightarrow 0_1^+)$ values in Zn, Ge and Se.

In reference [Res04] a restoration of seniority like behavior was shown to appear when the structure is dominated by a relatively high j(j≥7/2) single particle orbit. In typical collective regions the $B(E2,J \rightarrow J\text{-}2)_{J>2}$ scale with the $B(E2,2_1^+ \rightarrow 0_1^+)$ (i.e. over all collective regions $B(E2,4_1^+ \rightarrow 2_1^+) \approx 1.5 B(E2,2_1^+ \rightarrow 0_1^+)$ [Res04]). A parabolic behavior of $B(E2,2_1^+ \rightarrow 0_1^+)$ would be accompanied by similar parabolic behavior for

B(E2,$4_1^+ \rightarrow 2_1^+$) values. This is in complete contrast with the B(E2,$4_1^+ \rightarrow 2_1^+$) trend in regions where seniority (ν) is a good quantum number (i.e. where the structure is dominated by like nucleon excitations). In the latter case the seniority conserving transitions (J→J-2,J>2) are proportional to :

$$\left(\frac{2j+1-2n}{2j+1-2\nu}\right)^2 \tag{6.1}$$

whereas the seniority changing transition J=2→J=0 is proportional to

$$\frac{(n-\nu+2)(2j+3-n-\nu)}{2(2j+3-2\nu)} \tag{6.2}$$

(see [Res04, Tal63]). This behavior is plotted in Fig. 6.11 A. In [Res04], regions in the nuclear chart where seniority-like behavior could be expected to (re-)appear (assuming "normal" magic numbers) were proposed. The proposed regions include the (Z=28,30,32-N=40-50) region (see Fig. 6.11 C). The B(E2,J→J-2)$_{J>2}$ trends lack experimental input to check the seniority picture. For both Ni and Zn isotopes with N>40 the B(E2,$8_1^+ \rightarrow 6_1^+$) was found only in ^{70,76}Ni and ^{78}Zn([Maz05], [Dau00]). The fact that the B(E2,$8_1^+ \rightarrow 6_1^+$) strength in ^{72,74}Ni was not observed could be explained by SMII calculations and is linked with the a low lying ν=4 6_2^+ state, which is a faster decay channel for the 8_1^+ ($\Delta\nu$=2, see Fig. 6.11 A and [Maz05]). The new experimental data from this work sheds light on the B(E2,$4_1^+ \rightarrow 2_1^+$) trend in heavy Zn isotopes. In Fig. 6.7A and B these trends are plotted for Zn isotopes (J≤4). The new experimental data confirms the trend predicted by shell model calculations. A seniority like behavior of the B(E2,$4_1^+ \rightarrow 2_1^+$) values seems to be ruled out, at least for the B(E2,$4_1^+ \rightarrow 2_1^+$) value in this region of the nuclear chart. It can be concluded that a simple seniority picture where N=40 is a sub-shell closure is not valid in this region.
In [Del05] the seniority picture was "recovered" by assuming a sub-shell closure at N=38. The calculated seniority B(E2) parabola from that work reproduces the high B(E2) values in ^{72,74}Zn (see Fig. 6.11B). A more microscopic interpretation for the increased B(E2) strength in ^{74} is given in [Per06].

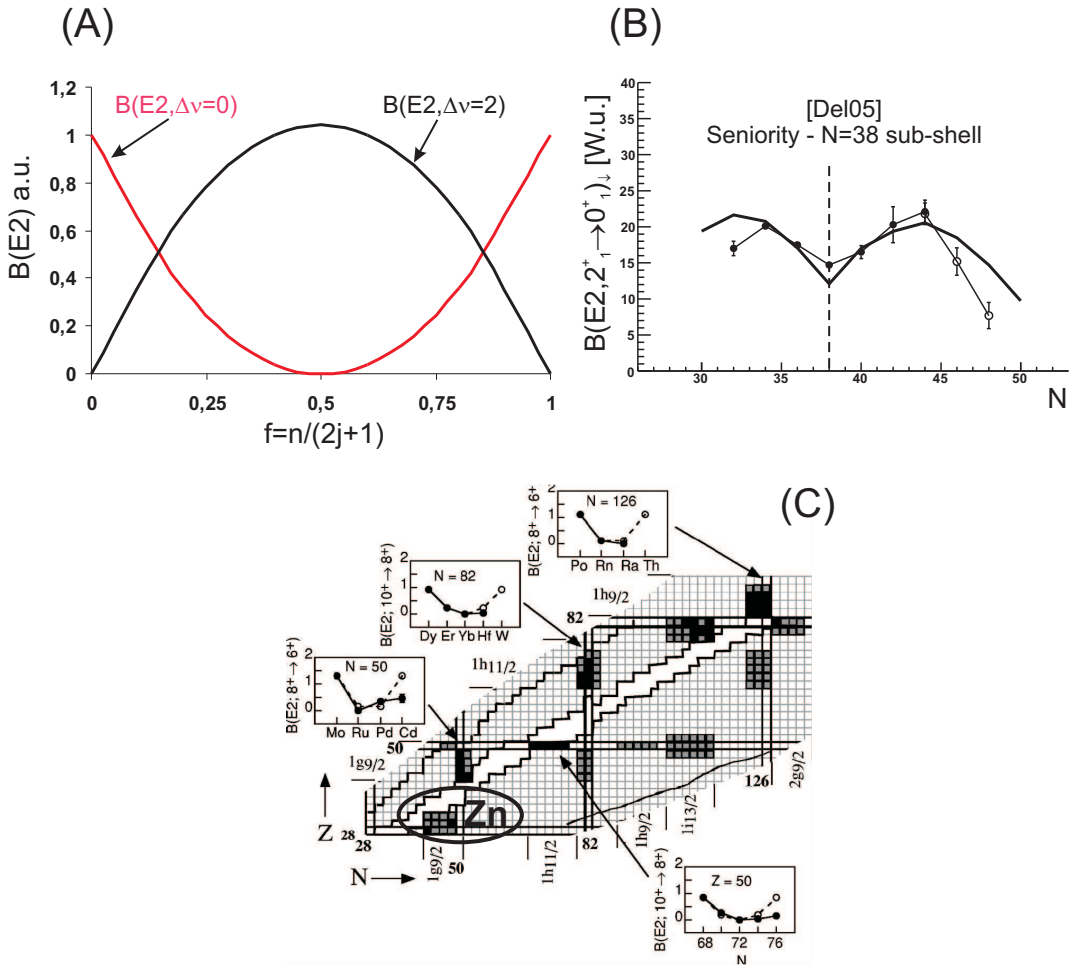

Figure 6.11: *A. Seniority behavior of $B(E2,2_1^+ \rightarrow 0_1^+)$ and $B(E2,4_1^+ \rightarrow 2_1^+)$ values. - B. Seniority calculation of the B(E2) strength in Zn isotopes, assuming a neutron shell closure at N=38. - C. Regions where seniority like behavior can be expected for $B(E2,J\rightarrow J\text{-}2)_{J>2}$ are indicated in gray. Nuclei with known $B(E2,J\rightarrow J\text{-}2)_{J>2}$ are indicated in black (fig. taken from [Res04]).*

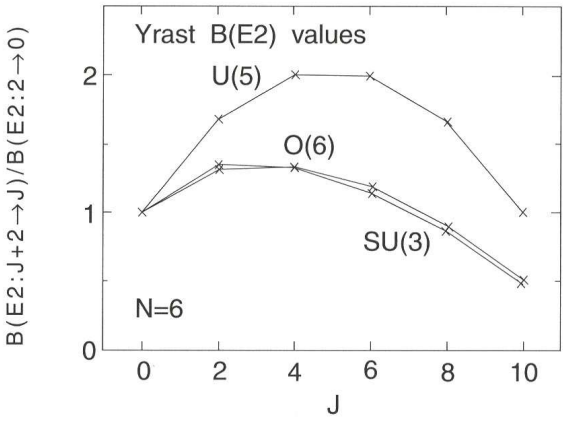

Figure 6.12: *B(E2,J→J-2)/B(E2,2→0) ratio in the Interacting Boson Model. Figure taken from [Cas00].*

6.3 Collective Models

The stable even-even Zn isotopes (A=64,66,68,70) are generally interpreted with the collective vibrational model, where the structure is characterized by a 1-phonon 2_1^+ level and a triplet of 2-phonon states (2_2^+,4_1^+,0_2^+) at approximately twice the 2_1^+ energy. Due to residual interactions between the two phonons, the degeneracy of the triplet is in general lifted. This feature is referred to as "anharmonicity". The ratio of E(2_2^+,4_1^+,0_2^+)/E(2_1^+) in vibrational nuclei ranges from 2.0 to 2.4 [Cas00]. These limits are indicated in Fig. 6.5. It is seen that all Zn isotopes exhibit similarities to a typical vibrational nucleus. Nevertheless transitions rates are found to be in conflict with the basic vibrational picture. A summary is given in the following with selected examples of more advanced collective model descriptions for the stable ^{66,68}Zn isotopes.

The B(E2,$4_1^+ \rightarrow 2_1^+$) /B(E2,$2_1^+ \rightarrow 0_1^+$) ratio : In the harmonic vibrational model, the B(E2,$4_1^+ \rightarrow 2_1^+$) /B(E2,$2_1^+ \rightarrow 0_1^+$) ratio is 2, due to the selection rule $\Delta N_{ph}=\pm 1$, where N_{ph} is the number of phonons. For the same reason the B(E2,$2_2^+ \rightarrow 0_1^+$) transitions strength should be zero. For the stable ^{62,64,66,68}Zn, accurate measurements of the B(E2,$4_1^+ \rightarrow 2_1^+$) value were performed with lifetime measurements (A=62 [Ken02], A=64,68 [Les05a], [Les05b]) and multiple coulomb excitation (A=66,68 [Koi03,Koi04]). These results are summarized in Fig. 6.7 C and compared to SMII calculations and adopted shell model calculations from literature (LSSM-1/2 [Ken02]). The latter highlights the importance of the $1g_{9/2}$ neutron orbital in the reproduction of B(E2,$4_1^+ \rightarrow 2_1^+$) transition strengths. In [Les05b] a g-factor measurement of the 4_1^+ state in ^{68}Zn indicated the dominance of the $\nu 1g_{9/2}^2$ configuration in the 4_1^+ state of ^{68}Zn. The experimental B(E2,$4_1^+ \rightarrow 2_1^+$) /B(E2,$2_1^+ \rightarrow 0_1^+$) ratios range from 0.6-1., far from the vibrational value of 2. Other collective model approaches such as *the rigid rotor model* or *the Interacting Boson Model* predict values of ≈1.43 (rigid rotor), ≈1.3-1.4 (O(6),SU(3) in IBM) and ≈1.6-1.7 (U(5) in IBM) (IBM ratio's are given in Fig. 6.12). Although the collective ground state band cannot be interpreted as a pure vibrational band (nor as a rotational band), more advanced collective models, discussed in the following, do reproduce the observed transition ratios.

For A=68 a Nilsson-Strutinsky calculation showed two distinct minima at γ=60°, one at β=0.10 and one at 0.18 [Koi04], indicating that one collective band is build on the 0_1^+ state and is not influenced by the $1g_{9/2}$ orbit (the potential minimum does not contain $1g_{9/2}$ orbitals below the Fermi surface), while the second collective band is build on the 0_2^+ state and is strongly affected by the $1g_{9/2}$ (the potential minimum

contains $1g_{9/2}$ orbitals below the Fermi surface) [Koi04]. The latter argument (the 0_2^+ being influenced by the $1g_{9/2}$) is similar to the argument of neutron pair scattering to the $1g_{9/2}$.
For A=66, a Deformed Configuration Mixing shell model calculation reproduces the B(E2,$4_1^+ \rightarrow 2_1^+$) /B(E2,$2_1^+ \rightarrow 0_1^+$) ratio of 0.96(7) [Koi03] [Aha81].
The new experimental B(E2,$4_1^+ \rightarrow 2_1^+$) /B(E2,$2_1^+ \rightarrow 0_1^+$) values for A=74,76, although with large error bars are surprisingly well predicted by both shell model calculations (SMI and SMII). Again, the typical vibrational value of 2 is experimentally not observed. The enhancement of the B(E2,$4_1^+ \rightarrow 2_1^+$) /B(E2,$2_1^+ \rightarrow 0_1^+$) might indicate more collective motion in these neutron rich Zn isotopes, which might be expected from the arguments given in par.6.2.

The B(E2,$2_2^+ \rightarrow 0_1^+$) strength : In the current experiments on A=74,76,78 Zn isotopes nothing can be deduced related to the B(E2,$2_2^+ \rightarrow 2_1^+$) and B(E2,$2_2^+ \rightarrow 0_1^+$). Experimental data on these transitions is rather scarce (even for stable Zn isotopes), but small excitation strengths have been observed, which indicates that the two phonon state is mixed with the one phonon state within the vibrational model. Indeed, in [Lig72] a wave function of the 2_2^+ state was deduced from the (e,e') form factor for this state. The wave function expanded in 1- and 2-phonon wave functions indicated a 94% 1-phonon component. In the same reference the large anharmonicities, when pairs of neutrons are added in the pf shell, are related to a less rigid or softer vibrator having a more diffuse surface than a rigid vibrator.
These selected examples of advanced collective model calculations show that stable Zn isotopes (N<40) can be interpreted with collective models. They offer an explanation for the reduced transition rate ratio's observed in these nuclei and predict deformed band structures. Again, the influence of the $1g_{9/2}$ orbit is a major influence in these interpretations. Arguments given in this and the previous paragraph indicate that heavier Zn isotopes might exhibit collective motion which is more similar to typical vibrational motion. Though, the development of collectivity should be strongly hindered by the stablizing effect of the N=50 shell closure.

6.4 The 2_1^+ Quadrupole Moment

In order to investigate the deformation of heavy Zn isotopes, more experimental data is necessary. Especially B(E2,$2_2^+ \rightarrow 2_1^+$) transitions rates and $<2_1^+ ||\mathcal{M}(\mathrm{E2})||2_1^+>$ matrix elements are crucial parameters in order to discuss possible deformation effects in the low-lying band structures.
Approximate relations exist connecting transition strengths between 2_1^+ ,2_2^+ ,0_1^+ and 0_2^+ states. These relations are based on sum rules within the vibrational model. Two of these are given by :

$$B(E2, 4_1^+ \rightarrow 2_1^+) = \frac{10}{7}(B(E2, 2_1^+ \rightarrow 0_1^+) + B(E2, 2_1^+ \rightarrow 0_2^+)) \quad (6.3)$$

$$|Q_{2_1^+}|^2 = \frac{32\pi}{35}(B(E2, 4_1^+ \rightarrow 2_1^+) - B(E2, 2_2^+ \rightarrow 2_1^+)) \quad (6.4)$$

[Naq75]. Another collective relation between the quadrupole moment $Q_{2_1^+}$ and the B(E2,$2_1^+ \rightarrow 0_1^+$) is obtained in the *rotational model* ([Naq75]) :

$$\begin{aligned} B(E2, 0_1^+ \rightarrow 2_1^+) &= \frac{5}{16\pi}|eQ_0|^2 \\ |Q^{rot}_{2_1^+}| &= 0.91\sqrt{B(E2, 0_1^+ \rightarrow 2_1^+} \end{aligned} \tag{6.5}$$

with $Q^{rot}_{2_1^+}$=$Q_0 \cdot \frac{3K^2-J(J+1)}{(J+1)(2J+3)}$ (K=0 for 2_1^+), though the rotational model does not apply to Zn nuclei, where only a limited number of valence protons and neutrons are available. The new experimental data on A=74 provides evidence for a negative quadrupole moment of the 2_1^+ state. The error bars are too big to give a definite value, though from the Fig. 5.8 limits can be given, based on the consistency between CM1 and CM2 B(E2) values within their error bar. The known experimental quadrupole moments are summarized in Fig. 6.13. The open triangles correspond to values obtained from electron scattering experiments [Sto05] and the filled triangles are quadrupole moments obtained from the fitting of matrix elements in multiple coulomb excitation experiments [Koi03, Koi04]. It is clear that there remains uncertainty on the sign of the quadrupole moment for ^{68}Zn. In neighboring isotopes, the overall trend is towards negative quadrupole moments (Ge,Se). In Fig. 6.13 the quadrupole moments resulting from the SMII calculations are plotted together with the experimental data for Ni, Zn and Ge isotopes. Some overall correspondence is found in the trends predicted by the shell model. For all Zn isotopes the SMII calculation predicts negative quadrupole moments. The non-zero $Q_{2_1^+}$ provides additional evidence for the non-vibrational character of ^{74} Zn, since the vibrational model predicts a zero quadrupole moment [Koi03]. The aforementioned relations between B(E2,$2_1^+ \rightarrow 0_1^+$) , B(E2,$4_1^+ \rightarrow 2_1^+$) and Q_{2^+}-values can be applied to the A=74,76 results, where the 2_2^+ state is not considered. The latter is a crude assumption, since within the vibrational model B(E2,$2_2^+ \rightarrow 2_1^+$)=2·B(E2,$2_1^+ \rightarrow 0_1^+$) . Though, a qualitative estimate of the collective properties will be given here. The results are summarized in table 6.2. It is seen that large quadrupole moments are obtained for the 2_1^+ state, while the B(E2,$4_1^+ \rightarrow 2_1^+$) values are close to the experimental value. In Fig. 6.7 B, the B(E2,$4_1^+ \rightarrow 2_1^+$) values obtained here are indicated by the crosses.

^{74}Zn	experimental input	shell model input	relation		model prediction experiment	model prediction shell model	experiment	shell model
B(E2,$2_1^+ \rightarrow 0_1^+$) =	21.7 W.u.	20.2 W.u.	(6.3)	B(E2,$4_1^+ \rightarrow 2_1^+$) =	31 W.u.	31 W.u.	26(4) W.u.	25 W.u.
B(E2,$2_1^+ \rightarrow 0_2^+$) =		1.15 W.u.						
B(E2,$4_1^+ \rightarrow 2_1^+$) =	26 W.u.	25 W.u.	(6.4)	$Q_{2_1^+}$ =	±0.37 b	±0.21 b	<0. b	-0.27 b
B(E2,$2_2^+ \rightarrow 2_1^+$) =		17.4 W.u.						
B(E2,$2_1^+ \rightarrow 0_1^+$) =	21.7 W.u.	20.2 W.u.	(6.5)	$Q_{2_1^+}^{rot}$ =	±0.41 b	±0.39 b	<0. b	-0.27 b

Table 6.2: *Application of collective relations between B(E2,$2_1^+ \rightarrow 0_1^+$) , B(E2,$4_1^+ \rightarrow 2_1^+$) and $Q_{2_1^+}$ to the experimental data.*

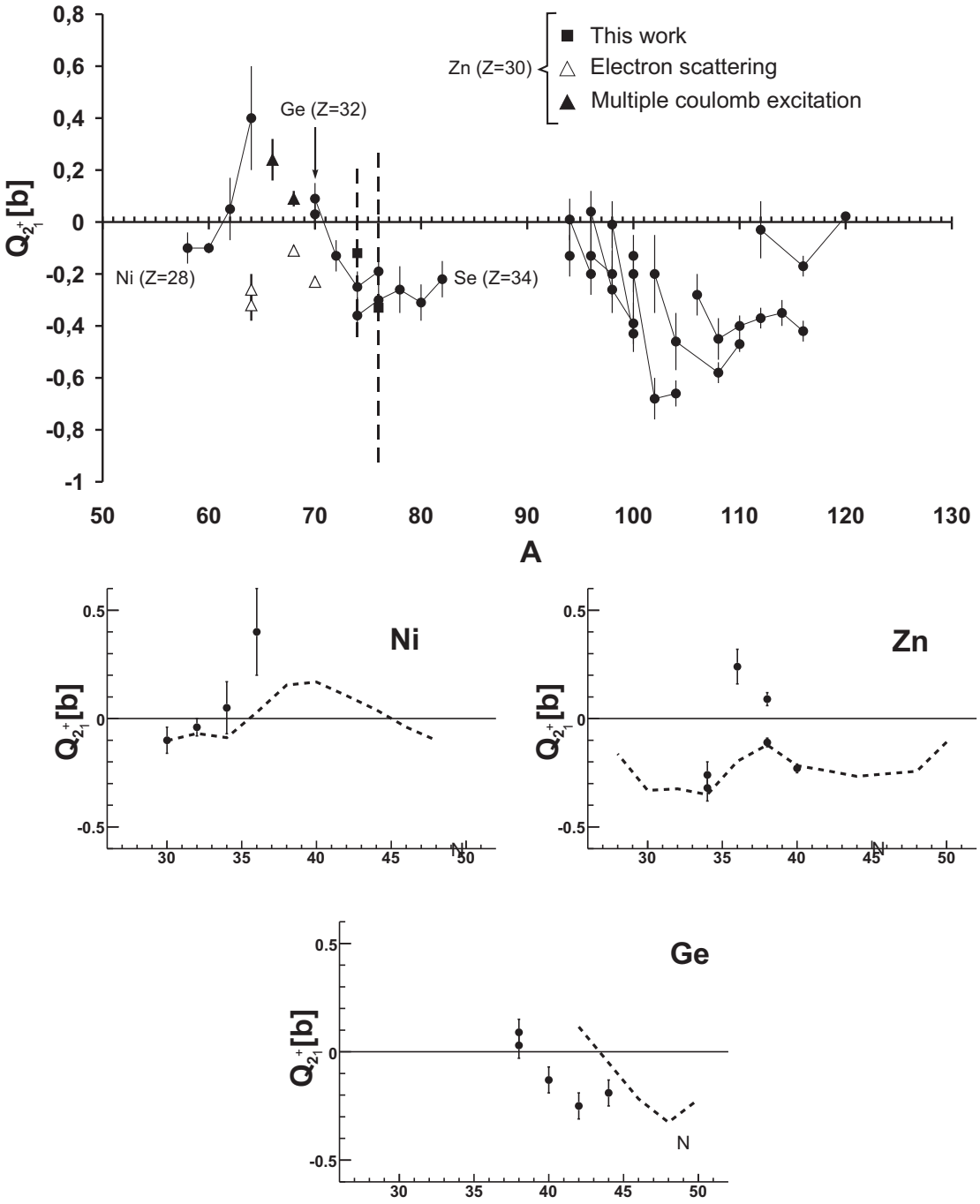

Figure 6.13: *Experimental quadrupole moments for Z≥28 and ≤50, together with estimated quadrupole moments from the current experiment. For Zn isotope, a discrepancy on the sign of the quadrupole moment exists for ^{66}Zn. Double values in the same isotopic chain are related to destructive and constructive interference terms (2_2^+ -2_1^+) in the experimental technique (coulomb excitation re-orientation). Shell model predictions (SMII) are compared to experimental data for Ni, Zn and Ge in the three bottom plots.*

6.5 The Nilsson Model

In Fig. 6.14 the Nilsson orbitals are given for N/Z=28-50. Filling neutrons in the $1g_{9/2}$ orbital, they occupy downsloping orbitals up to N=44, thus the deformed configuration becomes energetically more favorable. Experimentally for N=44 a maximum in collectivity is observed, for β_2=0.24. Whereas the last neutrons for N=46 are placed on an orbital which is rather insensitive to deformation. Experimentally, a sudden decrease in collectivity is indeed observed in ^{76}Zn. For N>46 neutrons fill upsloping orbitals and favor a more spherical configurations and the B(E2) value drops drastically. The tendency towards prolate deformation (β_2>0, $Q_{2_1^+}$<0) is consistent with the experimental tendency to a negative quadrupole moment for the 2_1^+ state.
The contribution of proton excitations in the Zn nuclei across the Z=28 shell might be hindered by the filled downsloping 1/2[321] orbital. It becomes thus energetically less favorable for protons to jump across the Z=28 shell, contrary to an empty 1/2[321] proton orbital in Ni isotopes. In the latter, protons might favor a more deformed configuration in this orbital. Proton excitations across Z=28 have been confirmed by shell model calculations in $^{N<40}$Ni isotopes [Ken01].

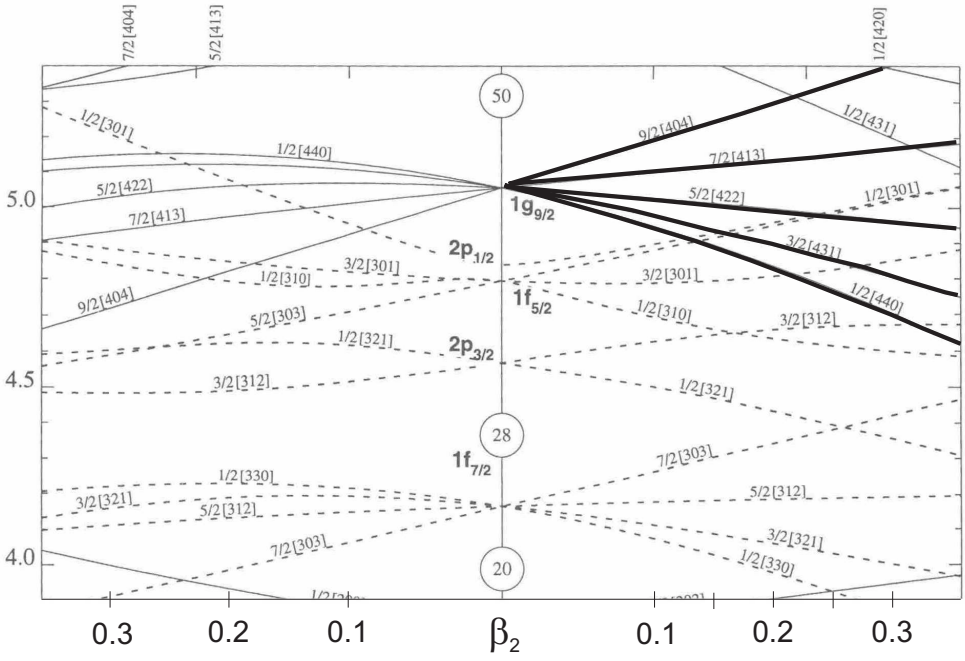

Figure 6.14: *Nilsson orbital occupation for N>40.*

6.6 The Grodzins Rule

The global systematics of the product $B(E2,0_1^+ \rightarrow 2_1^+) \cdot E(2_1^+)$ =constant, known as the Grodzins rule, makes it possible to predict the τ_γ (or, equivalently the $B(E2,2_1^+ \rightarrow 0_1^+)$) of the 2_1^+ level from the knowledge of $E(2_1^+)$. This phenomenological rule has been reviewed by Raman *et al.* [Ram01] and is given in eq. 2.10 in Chapter 3. The predicted $B(E2,2_1^+ \rightarrow 0_1^+)$ values for Ni, Zn and Ge isotopes based on the latter formula

and the known E(2_1^+) values are plotted in Fig. 6.15 (solid black line). A significant deviation is observed for neutron rich isotopes, where experimental data is available ($^{A\geq 76}$Ge,$^{A\geq 76}$Zn). The values for radioactive ^{72,74}Zn fit exactly to the Grodzins predictions. A modified Grodzins rule was proposed by Habs *et al.*, including an explicit a+b(N-$\bar{N}$) dependence (see Chapter 3, eq. 2.11) where $\bar{N}$ is the neutron number of the stable nucleus in an isobaric chain and a,b are fitted to E(2_1^+) ·B(E2,$2_1^+ \rightarrow 0_1^+$) data on nuclei between Z=50-82 and with E(4_1^+) /E(2_1^+) >2.2 [Hab02], yielding parameters a=1.26 and b=-0.077. The experimental trend downward to N=50 of the B(E2,$2_1^+ \rightarrow 0_1^+$) values is better followed by this modified Grodzins rule (small dashed line). The values for ^{62,64}Zn fit much better to this modified version as well. The predictions for Ni isotopes remain roughly the same for the lighter Ni isotopes, whereas significant different predictions are obtained for heaver Ni isotopes (A>68, including the assumed "doubly magic" ^{78}Ni). This raises the question whether this modified Grodzins Rule, which applies well for Zn and Ge isotopes, remains applicable in neutron rich Ni isotopes.

Further experimental evidence for these phenomenological predictions are definitely necessary (especially for Ni isotopes) in order to validate the modified Grodzins rule. Applying an identical fitting procedure to available experimental data on Z=28-50 isotopes with the same condition E(4_1^+) /E(2_1^+) >2.2, a new "modified Grodzins rule" was obtained with parameters a=1.076 and b=-0.039. The same trend down to N=50 is predicted, though less steep (long dashed line).

In conclusion, for neutron rich systems, far away from the line of stability, the constancy in the product of the energy of the 2_1^+ state and the B(E2,$2_1^+ \rightarrow 0_1^+$) seems to fail. Though, by including an explicit dependence on the neutron excess (N-$\bar{N}$) and fitting this dependence to nuclei where the collective model of the nucleus is established (Z=50-82), the predictions are in better agreement with recent experimental results (Zn and Ge).

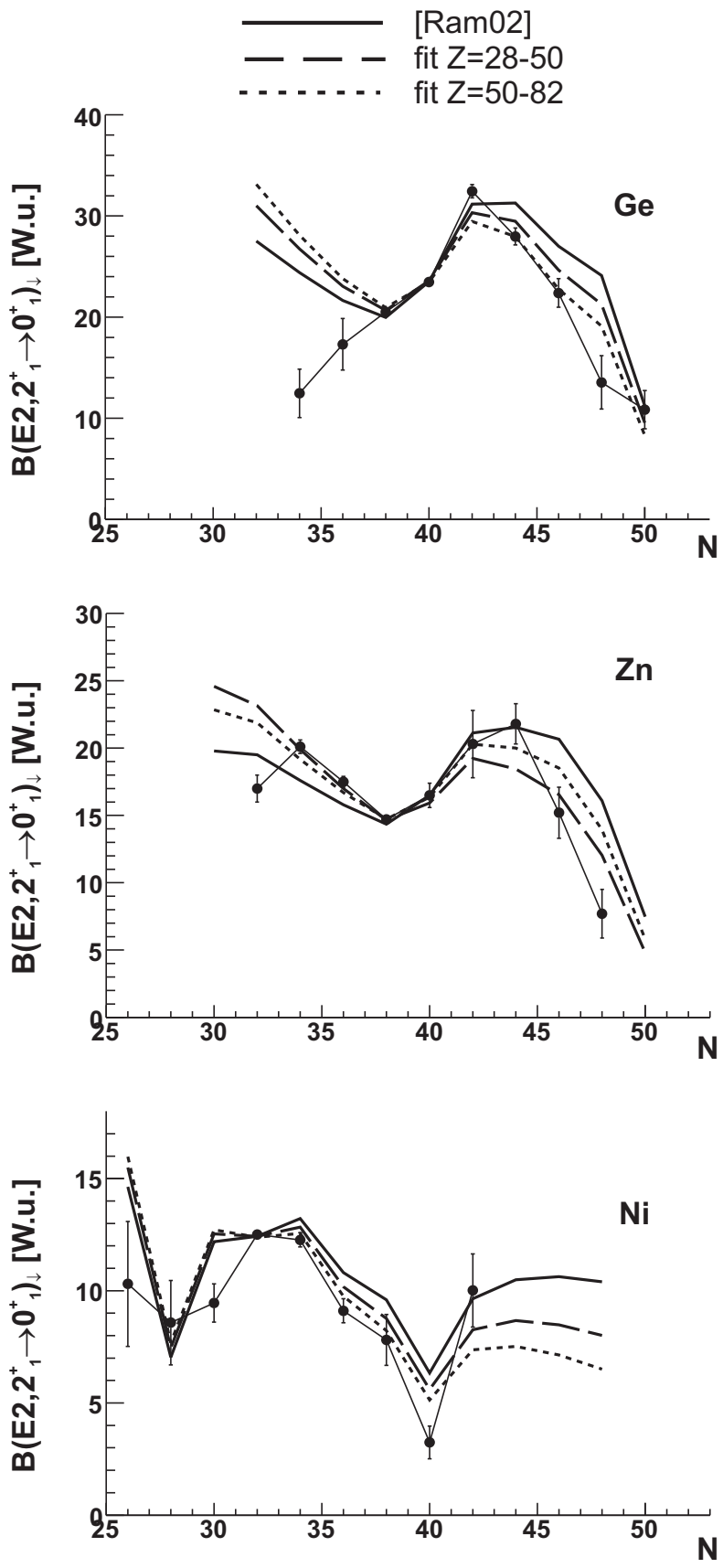

Figure 6.15: *Experimental $B(E2,2_1^+ \rightarrow 0_1^+)$ values for Ni,Zn and Ge isotopes compared to the empirical Grodzins rule and two modified versions of this rule, including an explicit N-$\bar{N}$ dependence.*

6.7 Global Systematics

In Fig. 6.16 the E(2_1^+) and B(E2,$2_1^+ \rightarrow 0_1^+$) systematics is plotted for isotopes with 28≤Z≤40. A drop in B(E2) strength and thus a decreased collectivity for N approaching 50 is observed in all these isotopes. The maximum collectivity between N=40-50 shifts from N=44 in Zn to N=42 in Ge and Se and eventually to N=40 in Kr, Sr and Zr. For Zn isotopes it has been pointed out that an increased neutron pair scattering across the N=40 neutron gap into the $1g_{9/2}$ orbital brings in an additional amount of E2 strength and this increased occupancy of $1g_{9/2}$ sets in earlier in Zn then in Ni [Per06]. The shift of the maximum B(E2) might reflect that this onset to additional $1g_{9/2}$ occupancy starts even earlier for Z>30.
Along the N=40 line, a gradual decrease of E(2_1^+) is observed, indicating the increased collectivity due to the additional protons outside the Z=28 shell and their interaction with the full neutron pf-shell. At the proton shell closure Z=28, the 2_1^+ state raises sharply in ^{68}Ni. Adding more neutrons into the $1g_{9/2}$ orbital after it has been half filled seems to decrease the collectivity for 36≤Z≤40 isotopes, as seen from the sudden increases of the E(2_1^+) and sharp decrease of B(E2) strength.
The near constancy of E(2_1^+) for 28≤Z≤34 isotopes hints a seniority like $(\nu 1g_{9/2}^2)_{J=2}$ character of the 2_1^+ state. Remarkably, at N=44, all E(2_1^+) become nearly identical for all isotopes with 28≤Z≤40.
On the N=44 line, the B(E2,$2_1^+ \rightarrow 0_1^+$) strength increases from Zn to Ge and becomes roughly identical for Se, Kr, Sr and Zr (peaking at Sr, 2 proton holes in the Z=40 shell). Assuming a predominantly $(\nu 1g_{9/2}^2)$ character for the 2_1^+ state in isotonic N=44 Zn, Ge and Se, the increase in B(E2,$2_1^+ \rightarrow 0_1^+$) might be attributed to increased proton E2 excitations in the pf shell. Since the $1f_{5/2}$ proton orbital becomes *presumably* the ground state in $^{73}_{29}Cu_{44}$, an increased monopole interaction between $\pi 1f_{5/2}$ and $\nu 1g_{9/2}$ might be expected, leading to enhanced p-n interaction (see Fig. 6.10). A completely filled $1f_{5/2}$ ground state would correspond to Z=34 (Se). The increasing B(E2,$2_1^+ \rightarrow 0_1^+$) in the series Zn, Ge and Se might thus be a reflection of the increased strong p-n interaction (which is a source for increasing collectivity) between $\pi 1f_{5/2}$ and $\nu 1g_{9/2}$ orbitals.

6.8 Summary

B(E2,$2_1^+ \rightarrow 0_1^+$) values have been measured for neutron rich N=44,46 and 48 Zn isotopes. The current result for ^{74}Zn is in agreement with the adopted value from [Per06]. The highest collectivity in the Zn isotopic chain is found to be at N=44. Adding two more neutrons reduces strongly the collectivity at N=46 and 48.
Shell model calculations reproduce the decrease in B(E2) strength but require modification of the input $1g_{9/2}$ single particle level or modification of three monopole parts and the addition of multipole parts.
B(E2,$4_1^+ \rightarrow 2_1^+$) values are measured for the first time in these neutron rich Zn isotopes and are in remarkable agreement with shell model predictions. When filling neutrons across mid-shell, between N=40 and 50 (half filled $1\nu g_{9/2}$ orbital) the collectivity decreases strongly. This is observed in other isotopes with 30≤Z≤40 as well. A strong N=50 neutron shell closure might explain this strong reduction. Shell model calculations in the $pf_{5/2}$-$g_{9/2}$ space reproduce this trend very well.
Within the Nilsson model, the decrease of the B(E2,$2_1^+ \rightarrow 0_1^+$) values is interpreted to originate from the strongly upsloping Nilsson orbitals for N>46. The hindrance of

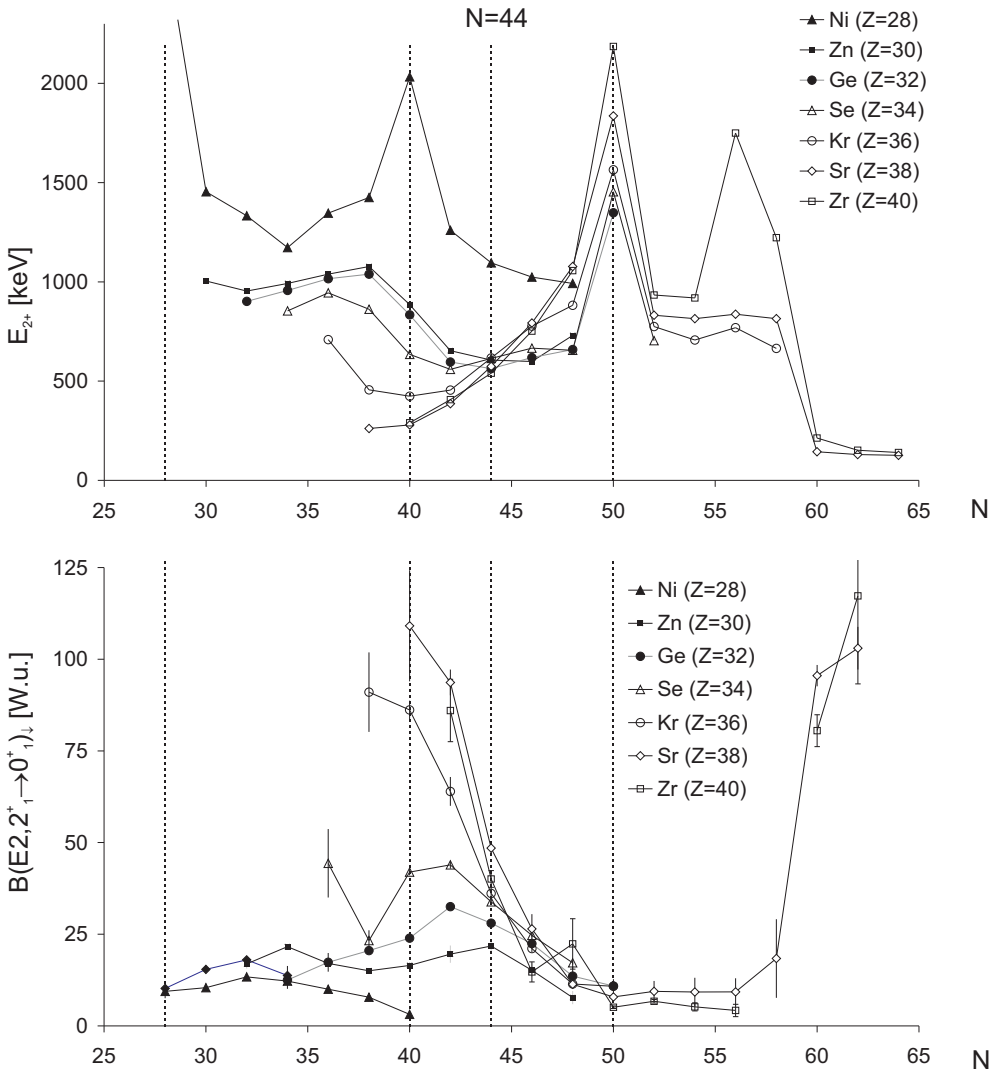

Figure 6.16: *Global B(E2,$2_1^+ \rightarrow 0_1^+$) and E(2_1^+) systematics for 28≤Z≤40 isotopes.*

proton excitations across Z=28 are qualitatively interpreted as due to a filled 1/2[321] proton orbital.
Standard global systematics for $E(2_1^+) \cdot B(E2,2_1^+ \rightarrow 0_1^+)$, governed by the phenomenological Grodzins rule, fails from N≥46 on in Zn isotopes. A similar deviation is observed in Ge isotopes. Though, incorporation of an explicit neutron dependence improves the predictions and is interpreted as the confirmation that the reduced $B(E2,2_1^+ \rightarrow 0_1^+)$ strength *is* indeed a neutron induced effect.
The 2_1^+ state in ^{78}Zn was fixed in this work and the systematics of $E(2_1^+)$ shows an increase of $E(2_1^+)$ at N=48, contrary to the observed decrease in Ni isotopes. This difference might by due to a reduced neutron pairing interaction for N/Z ratio's larger then 1.6, analogue to the observation in Te and Sn isotopes.

6.9 Outlook

Upcoming experiments on Zn isotopes up to the N=50 line will provide new insights in the structure of nuclei with N/Z>1.6. The reduced energy in ^{76}Ni should as well be reflected in the 2_1^+ energy in ^{80}Zn. Thus, the E(2_1^+) is expected to occur lower then expected from shell model calculations.
At REX-ISOLDE new experimental setups are being developed to study the level structure of neutron rich Zn isotopes by means of transfer reactions. Higher lying levels, such as the 0_1^+ and 2_2^+ state might be identified.
Coulomb excitation at higher beam energies provide much improved experimental conditions, since higher lying levels will be excited as well and the limited beam intensities form a lesser problem due to the increased excitation probability of the levels. The only drawback being the semi-classical approach which might be violated at some point. Though, specific target-beam combinations can be selected and might form a reasonable compromise.
Together with the increased beam energy at the upgraded REX-ISOLDE facility, new primary target developments have proven to be successful and dramatically improved beam purity has been achieved for Zn isotopes.
The next step in the exploration of the region around ^{78}Ni is the development of intense and pure Ni beams for Coulomb excitation and/or transfer reactions.
The development of new particle detectors for use with MINIBALL, such as the segmented Bragg detector offer the opportunity to reduce the error on the beam composition and to measure eventually quadrupole moments of the 2_1^+ states (if beam intensities are high enough).

Appendix A

GOSIA2 input file for ^{74}Zn

In the following an example input file for the A=74 experiment is given. For details, see the GOSIA2 manual ([GOS2]).
Input file for the *projectile* beam nucleus :

```
1
OP,FILE
(...)
OP,GOSI
LEVE
1,1,0,0.
2,1,2,0.606
3,1,4,1.419
0,0,0,0
ME
2,0,0,0,0
1,2,0.4,-4.,4.
2,2,0.,-2.,2.
2,3,1.,-2.,2.
0,0,0,0,0
EXPT
1,30,74
-50,120,188.3,53.8,3,1,0,0,360,0,1
CONT
(...)
OP,YIEL
0 6,1 ! energies and multipolarities
0.065,0.1,0.55,1.,1.5,2. !internal conversion coefficients
2
3.286,0.6522,2.774E-3,2.943E-4,1.819E-4,6.956E-5
24 ! number of detectors per experiment
1,1,1,1,1,1,1,1,1,1,1,1,1,1,1,1,1,1,1,1,1,1,1,1
43.5,51.6,71.0,36.7,65.9,57.9,39.0,50.4,
67.0,64.7,36.7,61.9,122.6,144.4,115.2,
112.3,129.5,140.4,120.9,108.3,137.5,108.3,136.9,124.3
21.8,60.2,35.0,143.8,146.7,114.6,207.6,
246.6,217.9,310.2,321.6,342.8,155.8,
127.2,123.2,29.2,57.3,17.8,299.8,329.1,331.4,250.6,258.6,223.1
2,1 ! normalisation transition
```

```
1 ! data sets see also op,raw
1E10,1E10 1,1 ! Normalisation of several datasets
4 ! Gamma Yields File Unit
0,0 ! Branching Ratios
0,0 ! Lifetime
0,0 ! Mixing Ratios
0,0 ! known matrix elements
OP,RAW
1
-0.71051,0.01833,-0.03984,0,0,0,0,-999.
-0.71051,0.01833,-0.03984,0,0,0,0,-999.
-0.71051,0.01833,-0.03984,0,0,0,0,-999.
-0.71051,0.01833,-0.03984,0,0,0,0,-999.
-0.71051,0.01833,-0.03984,0,0,0,0,-999.
-0.71051,0.01833,-0.03984,0,0,0,0,-999.
-0.71051,0.01833,-0.03984,0,0,0,0,-999.
-0.71051,0.01833,-0.03984,0,0,0,0,-999.
-0.71051,0.01833,-0.03984,0,0,0,0,-999.
-0.71051,0.01833,-0.03984,0,0,0,0,-999.
-0.71051,0.01833,-0.03984,0,0,0,0,-999.
-0.71051,0.01833,-0.03984,0,0,0,0,-999.
-0.71051,0.01833,-0.03984,0,0,0,0,-999.
-0.71051,0.01833,-0.03984,0,0,0,0,-999.
-0.71051,0.01833,-0.03984,0,0,0,0,-999.
-0.71051,0.01833,-0.03984,0,0,0,0,-999.
-0.71051,0.01833,-0.03984,0,0,0,0,-999.
-0.71051,0.01833,-0.03984,0,0,0,0,-999.
-0.71051,0.01833,-0.03984,0,0,0,0,-999.
-0.71051,0.01833,-0.03984,0,0,0,0,-999.
-0.71051,0.01833,-0.03984,0,0,0,0,-999.
-0.71051,0.01833,-0.03984,0,0,0,0,-999.
-0.71051,0.01833,-0.03984,0,0,0,0,-999.
-0.71051,0.01833,-0.03984,0,0,0,0,-999.
-0.71051,0.01833,-0.03984,0,0,0,0,-999.
-0.71051,0.01833,-0.03984,0,0,0,0,-999.
-0.71051,0.01833,-0.03984,0,0,0,0,-999.
-0.71051,0.01833,-0.03984,0,0,0,0,-999.
1 24
1,2,3,4,5,6,7,8,9,10,11,12,13,14,15,16,17,18,19,20,21,22,23,24
0
OP,REST
0,0
OP,INTG
11,14,170.6,214.5,29.1,83.8
165 170 175 180 185 190 195 200 205 210 215
29 32 35 40 45 50 55 60 65 70 75 80 83 85
11
160
165. 170. 175. 180. 185. 190. 195. 200. 205. 210. 215.
19.09 19.12 19.15 19.16 19.16 19.16 19.16 19.15 19.15 19.13 19.10 19.08
15,15
OP,EXIT
```

Appendix B

Coulomb Excitation of ^{74,76,78}Ga

B.1 ^{74}Ga

In Fig. B.2, the random subtracted spectrum is shown for the FULL (left) and CM1 (left) range. The bottom figures are the prompt and random coincident spectra, with a gate on the 170.9 keV transition. The same is shown in Fig. B.3 for the full A=74 laser off period. In this case, a pure ^{74}Ga beam was impinging on the ^{120}Sn target. In Fig. B.5 the level scheme of ^{74}Ga is given. The known levels were deduced from β-decay studies of ^{74}Zn [Win89]. Since the latter has a 0^+ ground state, predominantly the J=1^+ levels in ^{74}Ga are fed. There is no direct ground state feeding to ^{74}Ga. An isomeric state at 59.6 keV is present with a half life of 9.5(10) sec [Kli74]). The spin of the ground state and the isomeric state is assumed to be (3^-),(0) respectively [nndc, Win89]. This spin sequence, with ΔJ=3, is consistent with the half life of 9.5 sec [1]. The spin assignment to the 108.7 (J=1^+), 59.6 (J=(0)) and 56.6 (J=(2)) keV levels were deduced from the strong β-feeding to the 108.7 keV level and the strength of the 49. keV and 52. keV gamma rays (decay from 108.7 keV to 59.6 and 56.6 keV levels) [Kli74]. The 3.0 keV transition between 59.6 and 56.6 keV levels has the multipolarity M2 or E3, as argumented in [Kli74].
The Coulomb excitation process can be limited to E/Mλ transitions with $\lambda \leq 2$ (see Fig. 2.15). The dominating transition in the spectrum is the Doppler broadened transition at 170.9 keV. Inspection of the known level scheme of ^{74}Ga indicates a possible transition of 171.2 keV between the 56.6 and 227.8 keV levels. Tentative spin assignments are (between brackets [nndc] assignments) ground state = 3^- (3^-), 56.6 keV = 2^- (2) and 227.8 keV = $(1,2,3)^-$ ($\leq$3). In which case the 171.2 keV transition would be predominantly a fast M1 transition. Since the two levels at 56.6 and 59.6 keV are separated by merely 3.0 keV the assignment of this transition between these states relies strongly on a proper Doppler corrected peak. The resolution of the Doppler corrected transition is 4.6 keV with the mean energy at 170.94(6) keV. Excitation from the isomeric state at 59.6 keV to 227.8 keV would yield a transition line at 168.2 keV, which is excluded based on the Doppler corrected mean energy. The excitation to the 227.8 keV level might be a E2/M1 excitation : $(3^-)\rightarrow(1,2,3)(^-)$. No evidence for the 56.6 keV excitation is present since the detection limit of the MINIBALL detectors was set to $\sim$100 keV and the transition is strongly affected by the large internal conversion coefficient at this energy. The M1 assignment to the 170.9 keV de-excitation gamma is

[1] The Weisskopf single particle half-life estimate is given by $\ln(2)/(\lambda_{E3}(1+\alpha))$ where α is the internal conversion coefficient for E=59.6 keV and λ_{E3}=34$A^2E^7_{MeV}$. This estimate predicts $_{1/2}$=13.7 sec when using $\alpha\sim$100 (as in [Kli74]). The observed half life of 9.5 sec is consistent with this estimate. Other multipole estimates give values which are order of magnitude higher or lower.

supported by the fact that the transition is observed with a Doppler shift. The flight time from the target to the CD detector is of the order of 1.9-3.6 nsec and the transit time for Ga through the target is of the order of 0.3 fsec. In Fig. B.1 the half-life of a level which de-excites with a gamma ray of ΔE=200 keV is shown as a function of the B(Lλ) value (in W.u.), where L=E for electric, L=M for magnetic transitions and λ is the multipolarity. The half-life of a level is given by :

$$T_{1/2} = \frac{ln2}{\lambda_t} \tag{B.1}$$

with λ_t=(1+α)·λ_γ where α is the internal conversion coefficient. λ_γ depends on the multipolarity of the gamma transition (taken from [Ald75]) :

$$\lambda_{M1} = 1.7584 \times (\Delta E_{MeV})^3 B(M1, J_i \rightarrow J_f)_{\mu_N^2} \cdot 10^{13} sec^{-1} \tag{B.2}$$

$$\lambda_{E1} = 1.5902 \times (\Delta E_{MeV})^3 B(E1, J_i \rightarrow J_f)_{e^2fm^2} \cdot 10^{15} sec^{-1} \tag{B.3}$$

$$\lambda_{E2} = 1.2251 \times (\Delta E_{MeV})^5 B(E2, J_i \rightarrow J_f)_{e^2fm^4} \cdot 10^{9} sec^{-1}. \tag{B.4}$$

The B(Lλ) values are not known in the considered Ga isotopes, but an estimate of their order of magnitude can be performed by looking at the nearest odd-odd isotopes where B(E1),B(M1) and B(E2) values are known. In $^{74,76}_{33}As_{41,43}$, the known B(E1) values range from 10^{-7} up to 10^{-5} W.u. for transitions around 300-400 keV. B(M1) values range from 10^{-3} up to 0.5 W.u. With these values in mind, it can be seen from Fig. B.1 that, presumably, the doppler shifted de-excitation gammas will have M1 character (in the assumption that B(E1) and B(M1) values are similar in Ga as in As isotopes). The 2^- assignment to the 56.6 keV level is consistent with the M2 character of the 3.0 keV transition between 56.6 keV (2^-) and 59.6 keV (0^+) levels ([Kli74]). The latter is then consistent with an E3 character of the 59.6 keV transition (with appropriate life time of 9.5 sec). In coincidence with the 170.9 keV gamma ray a weak 236.2 keV gamma ray was observed. In the Doppler corrected (CM1) spectrum, 311(45) counts were observed in this transition with 45(7) coincident counts in the 170.9 keV transition. Assuming that the 236.2 keV and 170.9 keV transitions come in a cascade, where the 236.2 keV is the upper transition, and assuming a total efficiency of 19.3% at 170.9 keV, 60(9) coincident counts are expected in coincidence with the detected 236.2 keV. A possible cascade of three gamma rays is then given by : 236.2 keV ($J^\pi \rightarrow 3^-$) - 170.9 keV ($3^- \rightarrow 2^+$) - 56.6 keV ($2^+ \rightarrow 3^-$). The partial level scheme is given in Fig. B.5 where the new tentative spin assignments are indicated at the right. The possible direct transition of 227.8 keV from ($3^- \rightarrow 3^-$) would be of mixed E2/M1 character, though the transition is dominated by the fast M1 de-excitation channel. A new level at 464 keV is postulated. The two 1^+ levels higher then 700 keV are omitted in Fig. B.5.

From a relative comparison of the gamma yields from ^{74}Ga de-excitation and target de-excitation, the cross section for de-excitation of the 170.9 keV gamma can be given, analogue to eq. 2.40, without the relative angular distribution included. The result is summarized in tab. B.1. The error on target yields is the statistical error, without the beam contamination included. The final error on the cross section includes the error on the beam contaminations parameter "R".

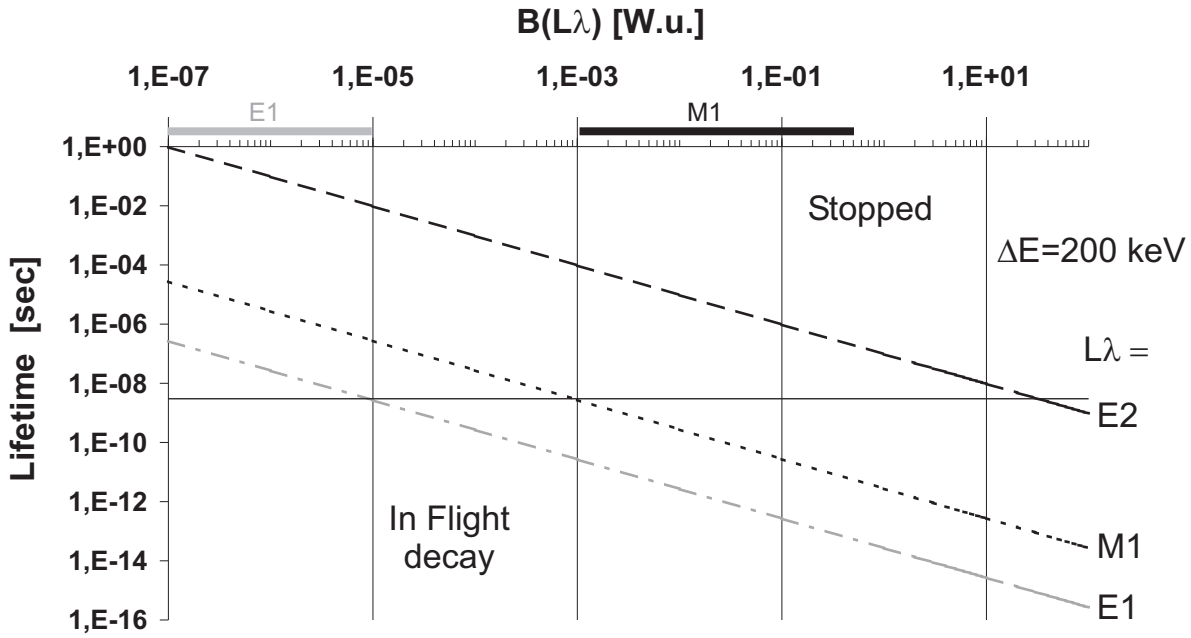

Figure B.1: *Lifetimes for Lλ=E1,E2 and M1 transitions and ΔE=200 keV as a function of the associated B(Lλ) in W.u. The full black line indicates the flight time to the particle detector. Transitions with Longer lifetimes will not be Doppler shifted. The internal conversion coefficients were* α_{M1}*=0.0111,* α_{E1}*=0.0079 and* α_{E2}*=0.0512 [nndc].*

	Ga counts	error	Sn counts	error	σ_{Sn} mb	σ_{Ga} mb	error
FULL	5600	124	2052	51	130.6	929	58
CM1	2503	83	867	33	80.0	605	44
CM2	2531	83	903	35	79.7	579	42

Table B.1: *Cross sections for the de-excitation of the 170.9 keV gamma for the three CM ranges. Limiting angles in the CM can be found in Chapter 4.*

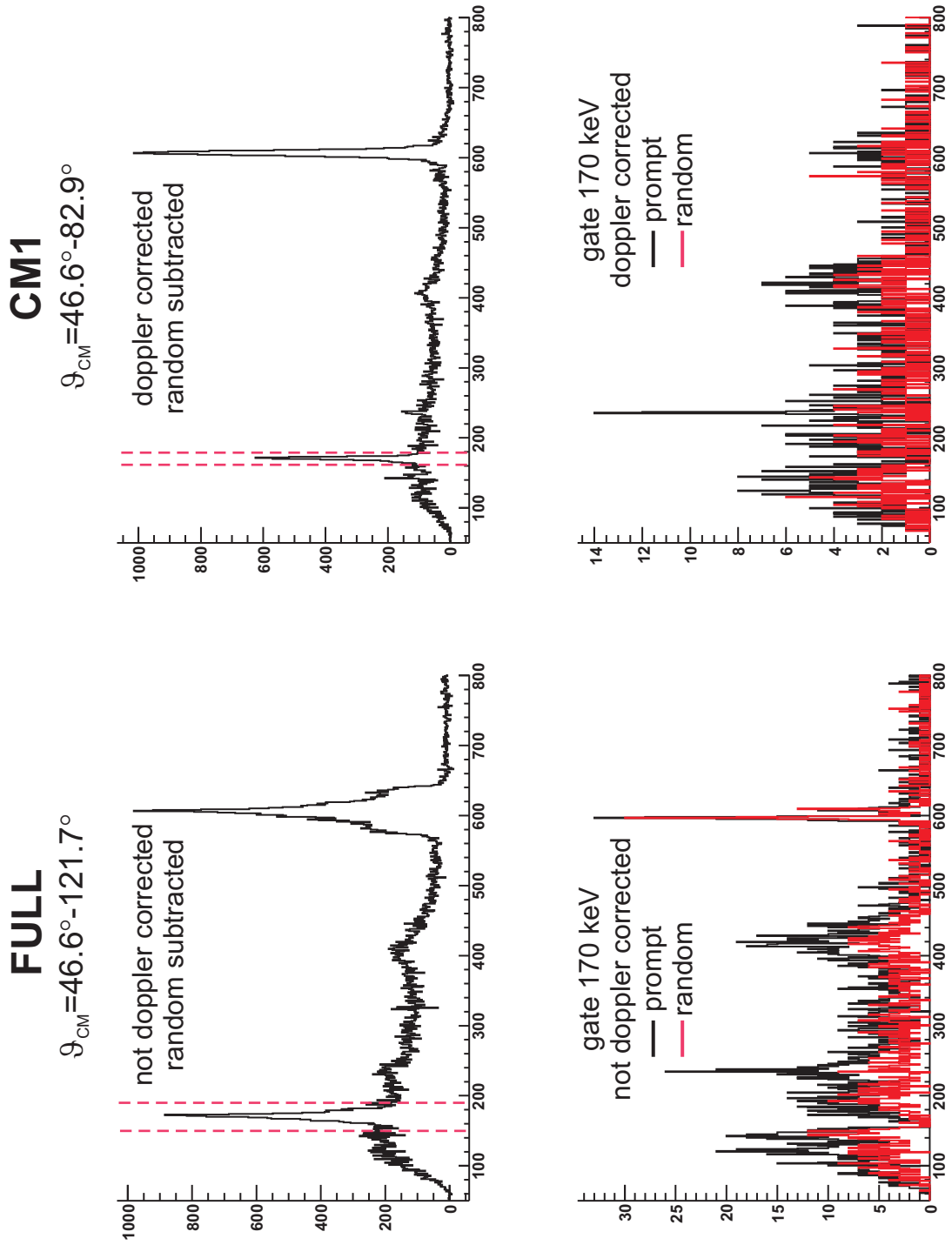

Figure B.2: *Top : random subtracted spectra over 2 CM ranges. Bottom : prompt and random spectra with a gate on the 170 keV transition. (Laser ON spectra)*

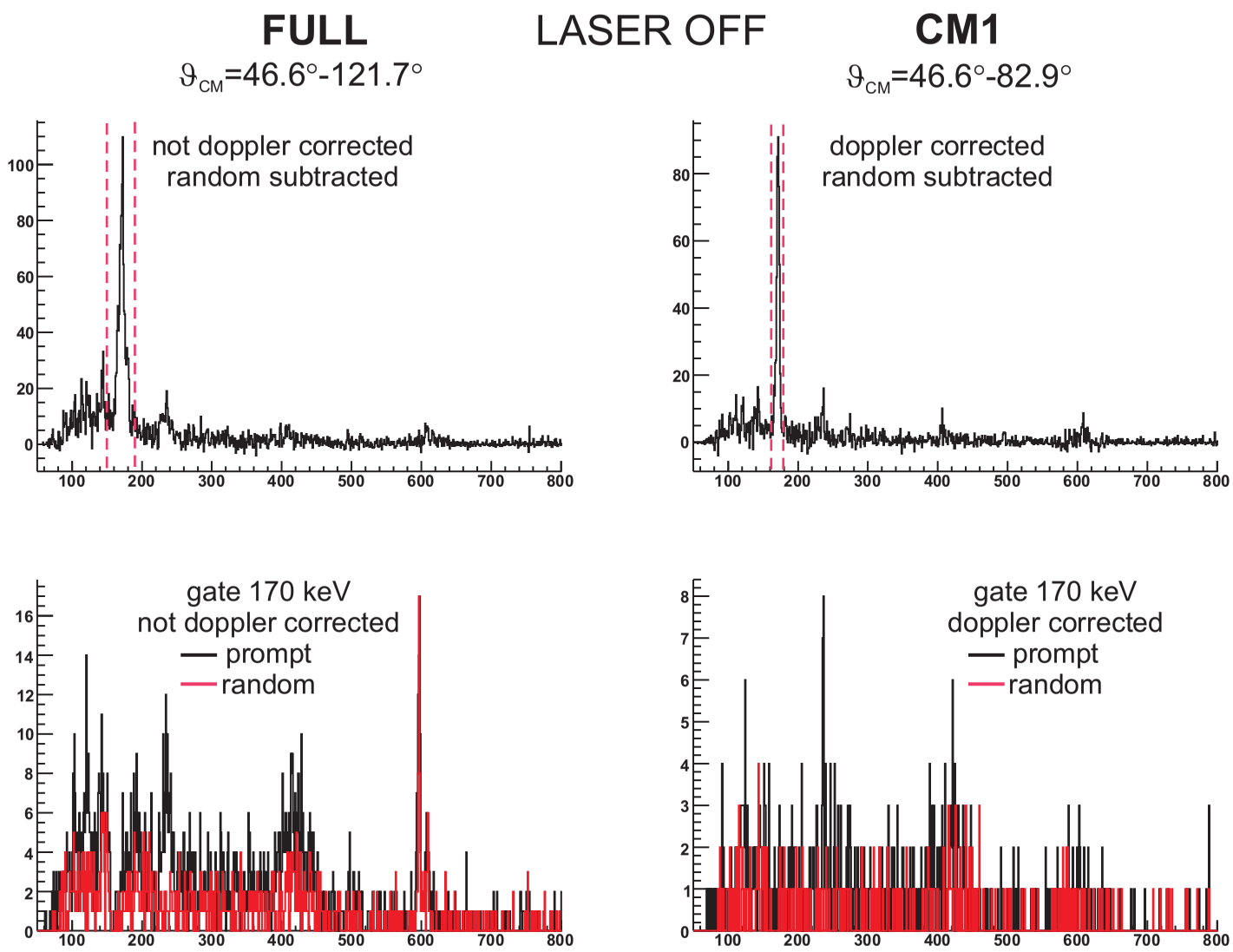

Figure B.3: *Top : random subtracted spectra over 2 CM ranges. Bottom : prompt and random spectra with a gate on the 170 keV transition. (Laser OFF spectra)*

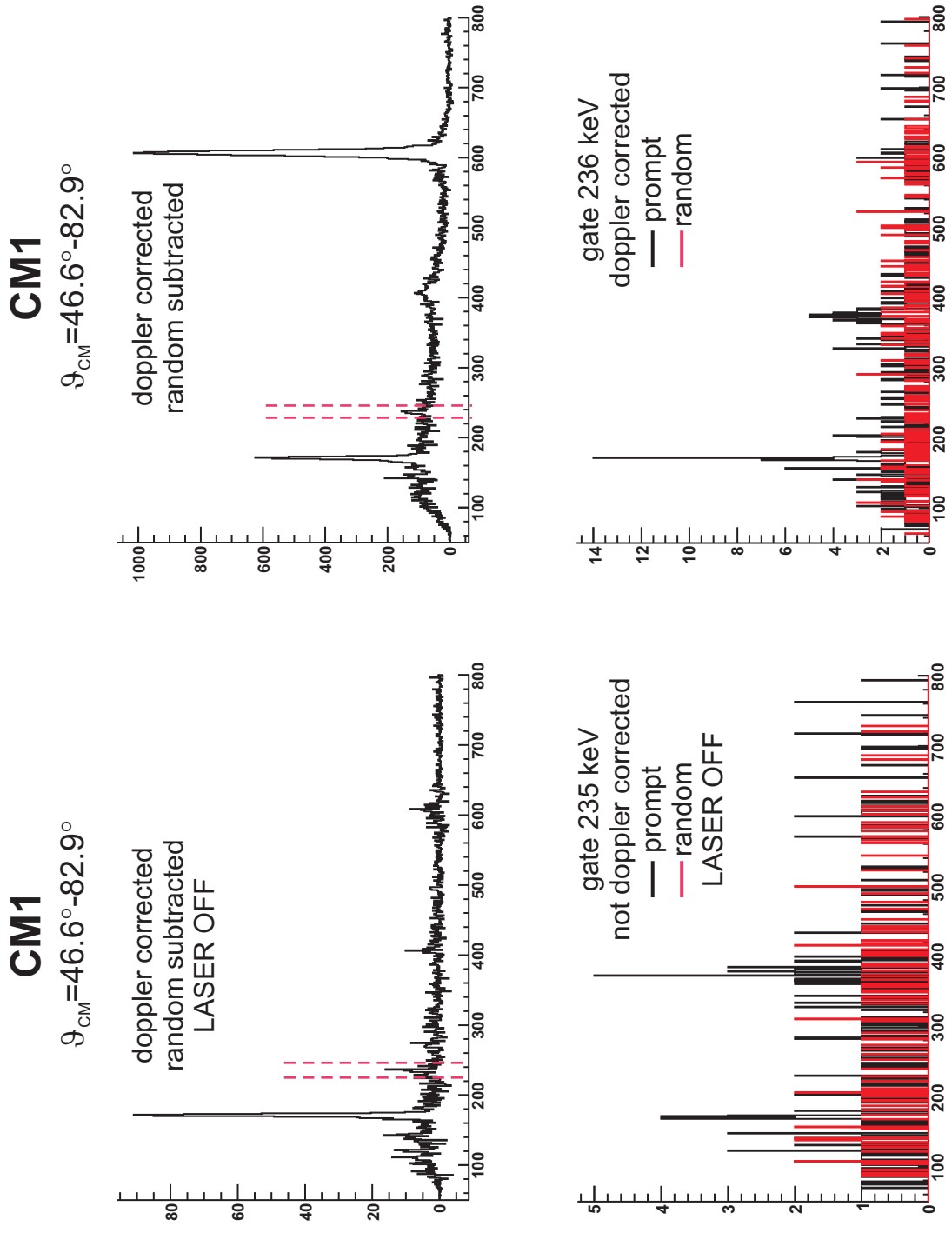

Figure B.4: *Top : random subtracted spectra over 2 CM ranges. Bottom : prompt and random spectra with a gate on the 236 keV transition. (Laser ON (right) and Laser OFF (left) spectra)*

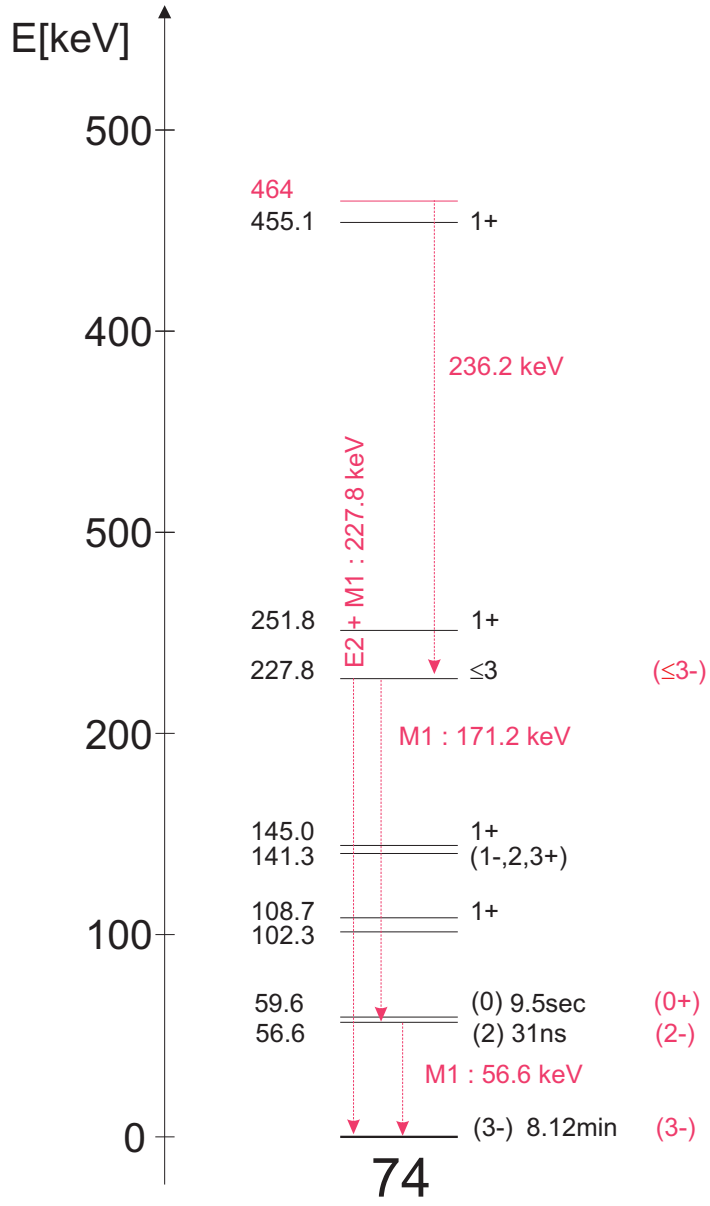

Figure B.5: *The (partial(*)) level scheme of ^{74}Ga. The observed transitions are tentatively placed in the known level scheme and new tentative spin assignments are indicated at the right in red. (*) = Two 1^+ levels higher then 700 keV are omitted.*

B.2 ^{76}Ga

In Fig. B.6,B.7 and B.8 the random subtracted spectra are shown for the FULL (left) and CM1 (right) range. The bottom figures are the prompt and random coincident spectra, with a gate on the 160 keV, 220 keV and 25 3keV transition. The same is shown in Fig. B.9,B.10 and B.11 during the full A=76 laser off period. In this case, a pure ^{76}Ga beam was impinging on the ^{120}Sn target.
Three distinct gamma transitions are observed in the spectra which can be attributed to de-excitations in ^{76}Ga : two Doppler broadened shifted transitions at 160.3(1) keV and 253.46(7) keV and a not Doppler shifted transition at 220.07(7) keV. By gating on each of these 3 transitions the the following two cascades could be distinguished (see Fig. B.6,B.7 and B.8) : (1) 253 keV + 160 keV and (2) 220 keV + 195 keV + 108 keV. In the first cascade, 1077(49) and 309(37) counts were observed in the Doppler corrected 253 keV and 160 keV transitions (respectively), where 40(6) counts in the 160 keV line were observed in coincidence with the 253 keV line and 41(6) counts in the 253 keV line in coincidence with the 160 keV line. Assuming an efficiency of 16.3% at 253 keV, 50(6) counts are expected in coincidence with the 160 keV line if the latter is the upper gamma in the cascade, which is consistent with the observed 41(6) counts. Assuming 19.7% efficiency at 160 keV, 212(10) counts would be expected in the 160 keV line in coincidence with the 253 keV line, which is far from the observed 40(6) counts. In conclusion, the cascade 253-160 keV is identified with the 160 keV gamma being the upper transition. In the second cascade, only the (delayed) prompt coincident gamma ray at 220 keV is seen in the particle coincident spectrum with 280(26) counts, whereas two coincident gamma rays are observed when gating on the 220 keV line : at 108 keV - 12(4) counts and 195 keV - 13(4) counts. Assuming efficiencies of 21.8%,18.3% at 108,195 keV (resp.), 61(6),51(5) (resp.) counts are expected in coincidence with the 220 keV gamma if the latter is the upper transition in the cascade, which is not consistent with the observation. In conclusion, the 220 keV line stems possibly from an excitation to a level at this energy, while it is fed by two other transitions which stem from the excitation of 2 higher lying levels. Since the Doppler corrected spectrum (see Fig. B.7) still shows an appreciable peak shape for these two gamma's it can be assumed that they were Doppler broadened. The second transition of 195(2) keV ends up at an energy of 220.07(7)+195(2)=415.1(2.1) keV which would fit the highest level of the first cascade.
The Doppler shift of the transition provides an indication for the multipolarity of the transitions. The flight time from target to CD ranges from 1.9 to 3.6 nsec for ^{76}Ga in the CM1 range. As discussed above for ^{74}Ga, most doppler shifted transitions around 200 keV might be of M1 character, assuming similar order of magnitude for B(E1), B(M1) and B(E2) values in Ga as in As isotopes. The partial level scheme is shown in Fig. B.12 [nndc] (levels above 1 MeV are omitted). Levels are known from β-decay studies of ^{76}Zn. The two identified gamma cascades cannot be placed in the known level scheme of ^{76}Ga. Therefore, four new levels are tentatively suggested which would fit to the observed transitions.
From a relative comparison of the gamma yields from ^{76}Ga de-excitation and target de-excitation, the cross section can be given, analogue to eq. 2.40, without the relative angular distribution included. The result is summarized in tab. B.2. The error on target yields is the statistical error, without the beam contamination included. The final error on the cross section includes the error on the beam contaminations parameter "R".

	E	Ga	error	Sn	error	σ_{Sn}	σ_{Ga}	error
	keV	counts		counts		mb	mb	
	160.3	643	57				197	28
FULL	220.1	718	43	656	28	130.7	249	31
	253.5	2459	73				908	103
	160.3	309	37				139	24
CM1	220.1	280	26	252	63	72.6	143	22
	253.5	1077	49				587	76
	160.3	305	37				107	18
FULL	220.1	399	29	347	20	80.0	158	22
	253.5	1112	48				470	58

Table B.2: *Cross sections for the de-excitation of the 160.3, 220.1 and 253.5 keV transitions for the three CM ranges. Limiting angles in the CM can be found in Chapter 4.*

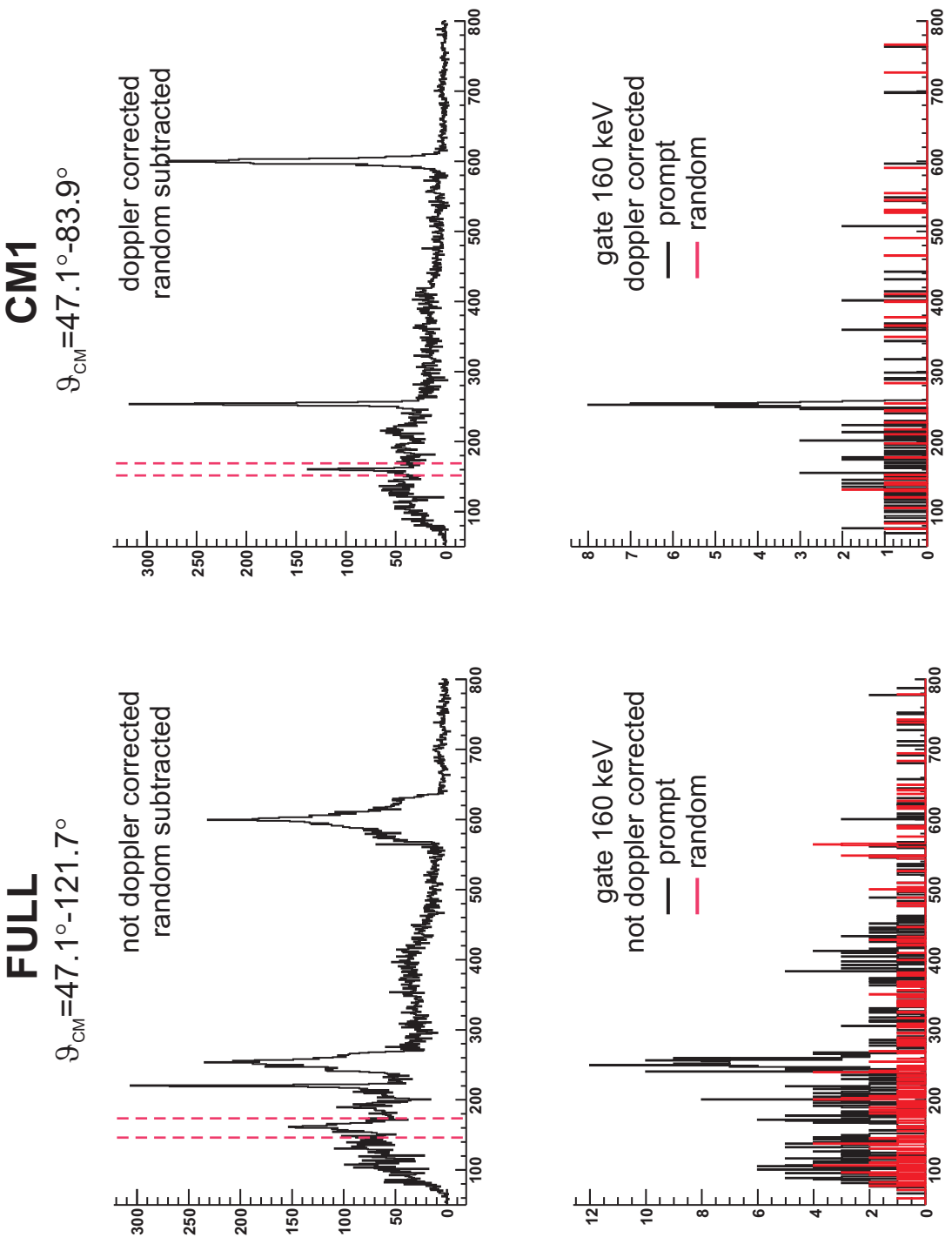

Figure B.6: *Top : random subtracted spectra over 2 CM ranges. Bottom : prompt and random spectra with a gate on the 160 keV transition. (Laser ON spectra)*

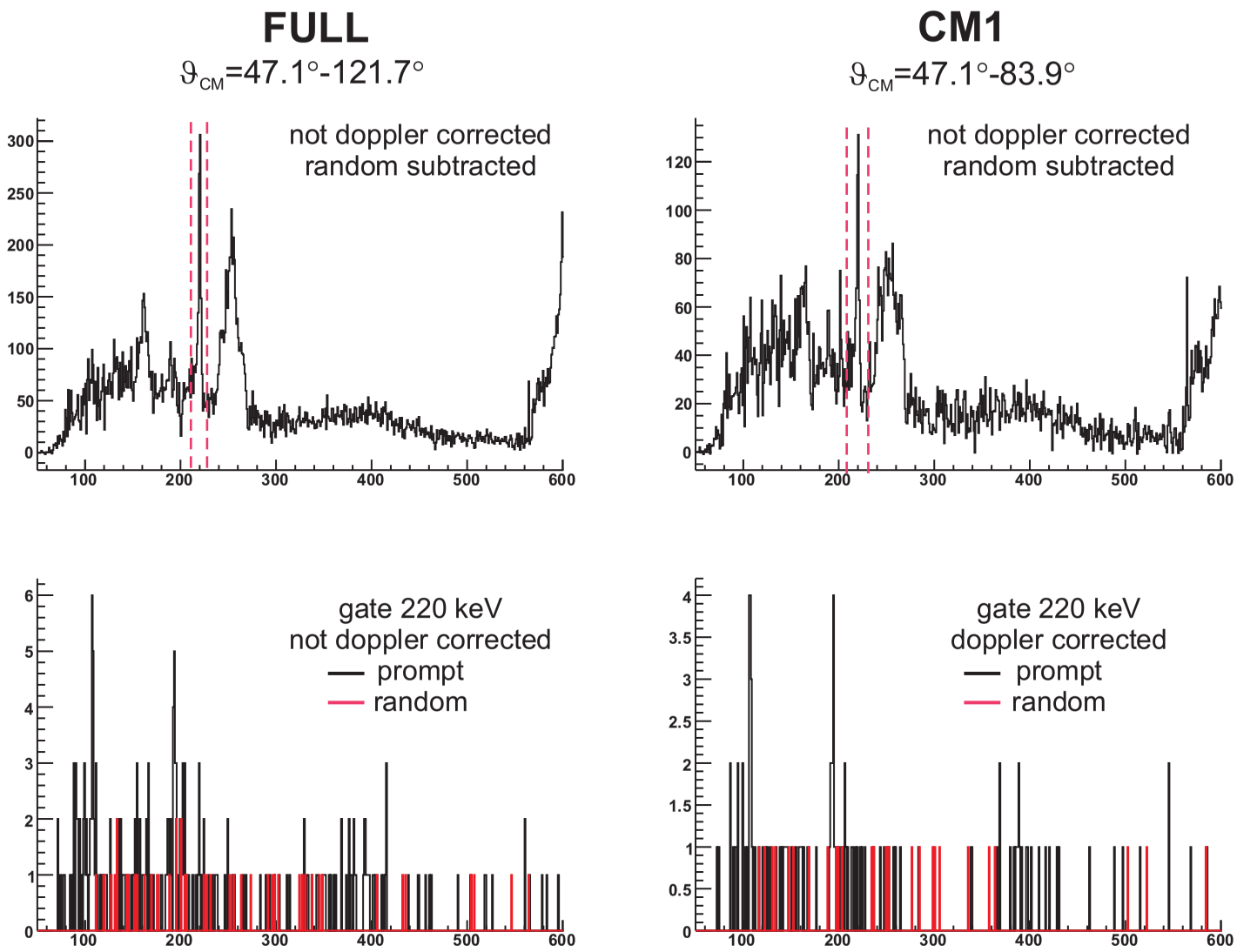

Figure B.7: *Top : random subtracted spectra over 2 CM ranges. Bottom : prompt and random spectra with a gate on the 220 keV transition. (Laser ON spectra)*

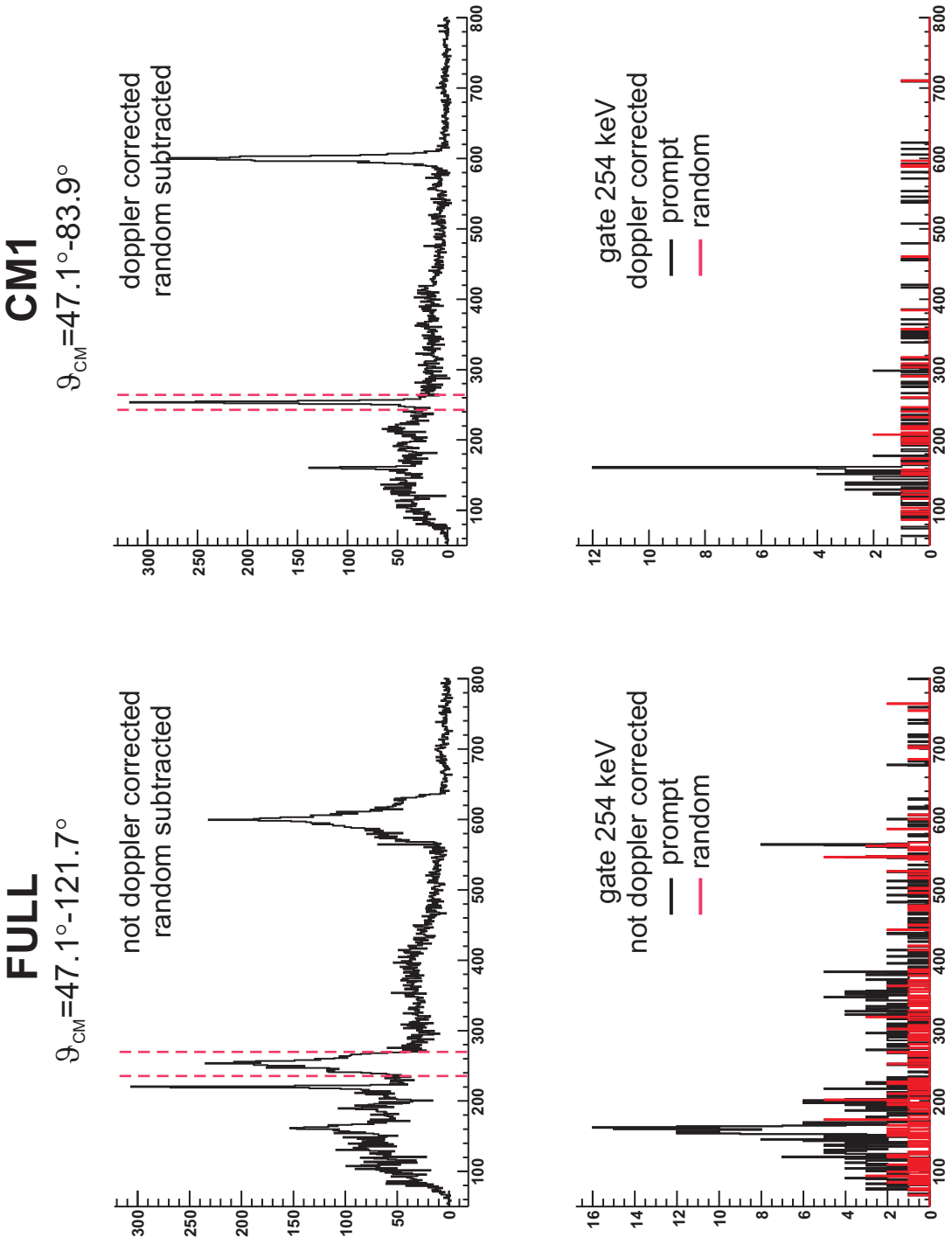

Figure B.8: *Top : random subtracted spectra over 2 CM ranges. Bottom : prompt and random spectra with a gate on the 254 keV transition. (Laser ON spectra)*

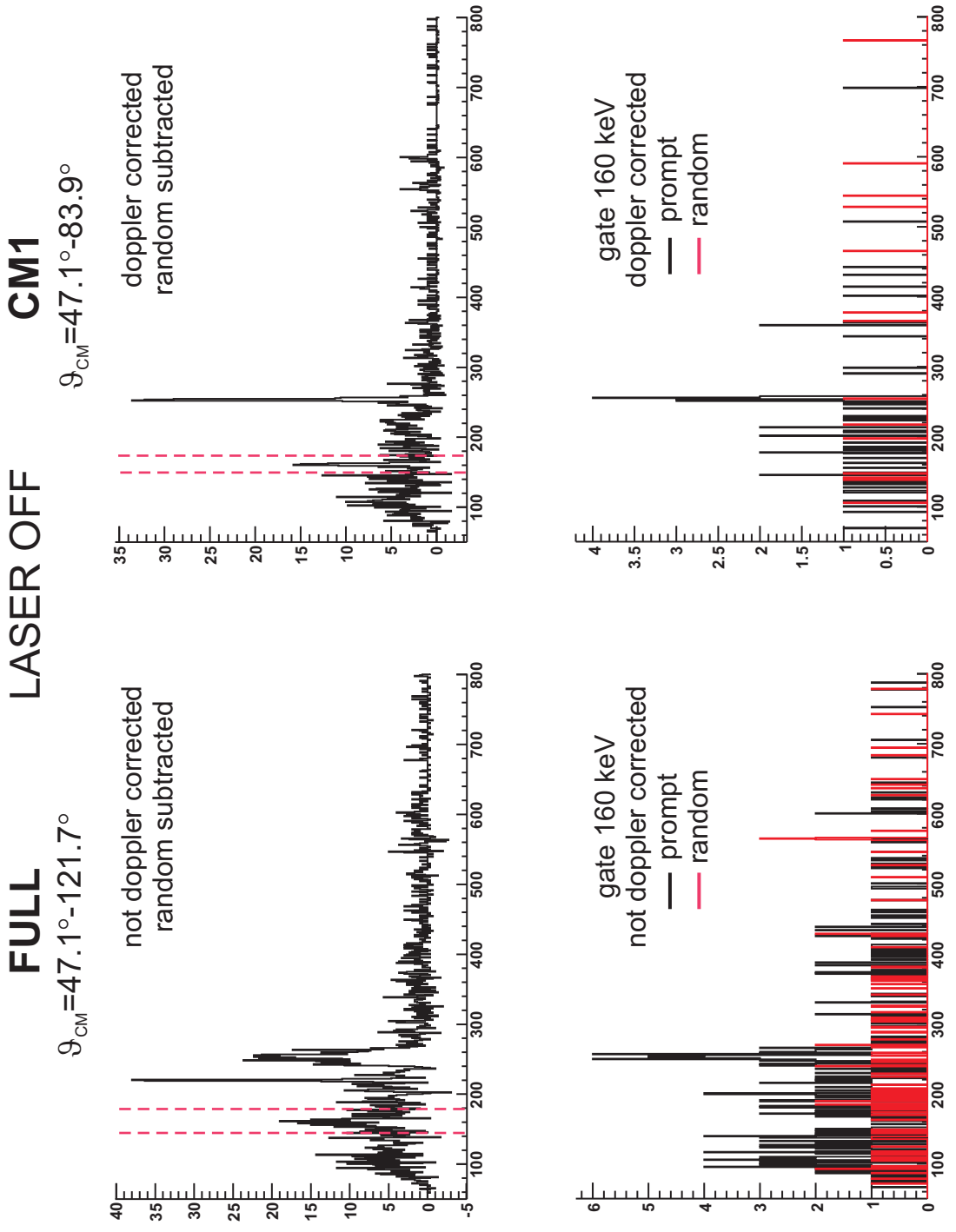

Figure B.9: *Top : random subtracted spectra over 2 CM ranges. Bottom : prompt and random spectra with a gate on the 160 keV transition. (Laser OFF spectra)*

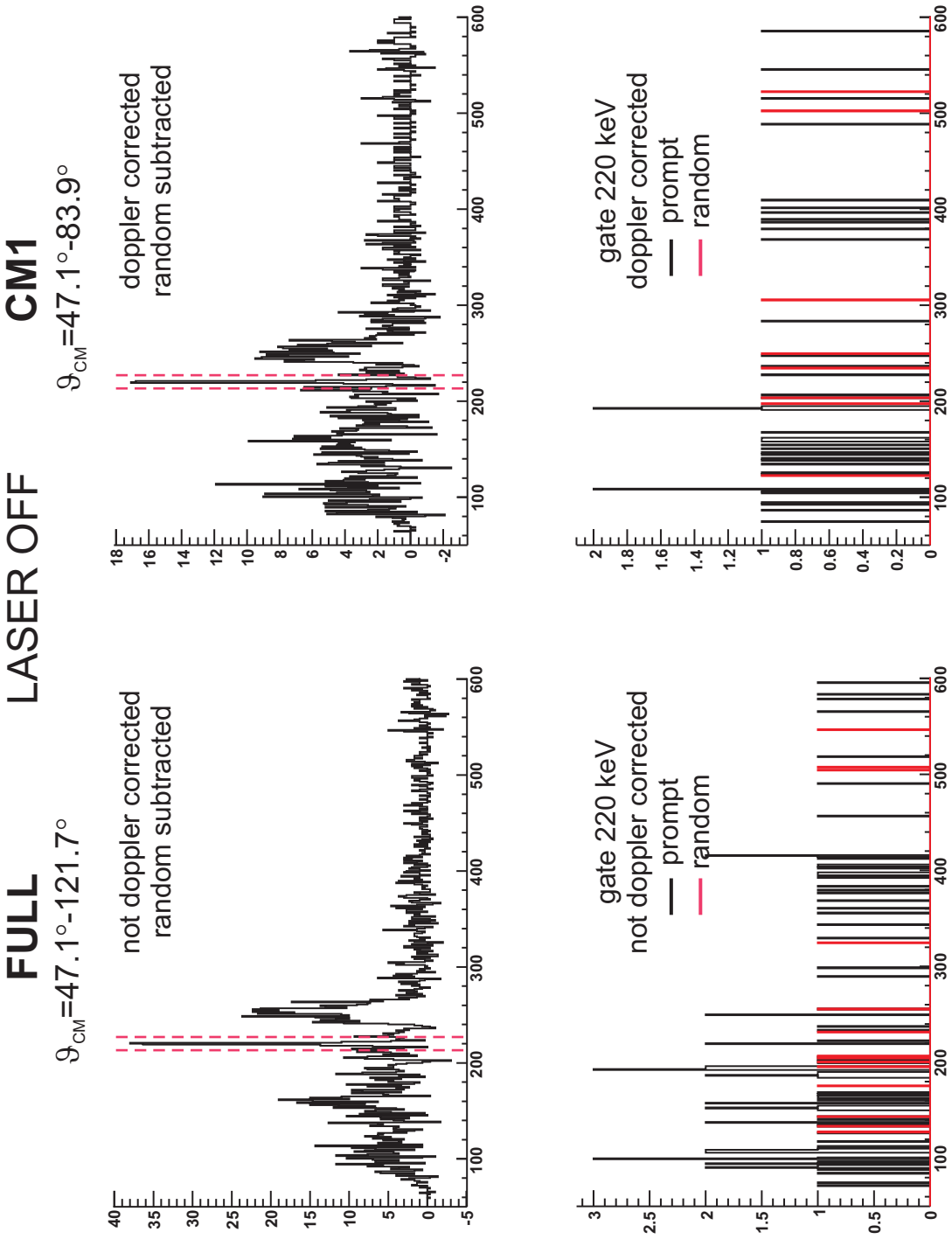

Figure B.10: *Top : random subtracted spectra over 2 CM ranges. Bottom : prompt and random spectra with a gate on the 220 keV transition. (Laser OFF spectra)*

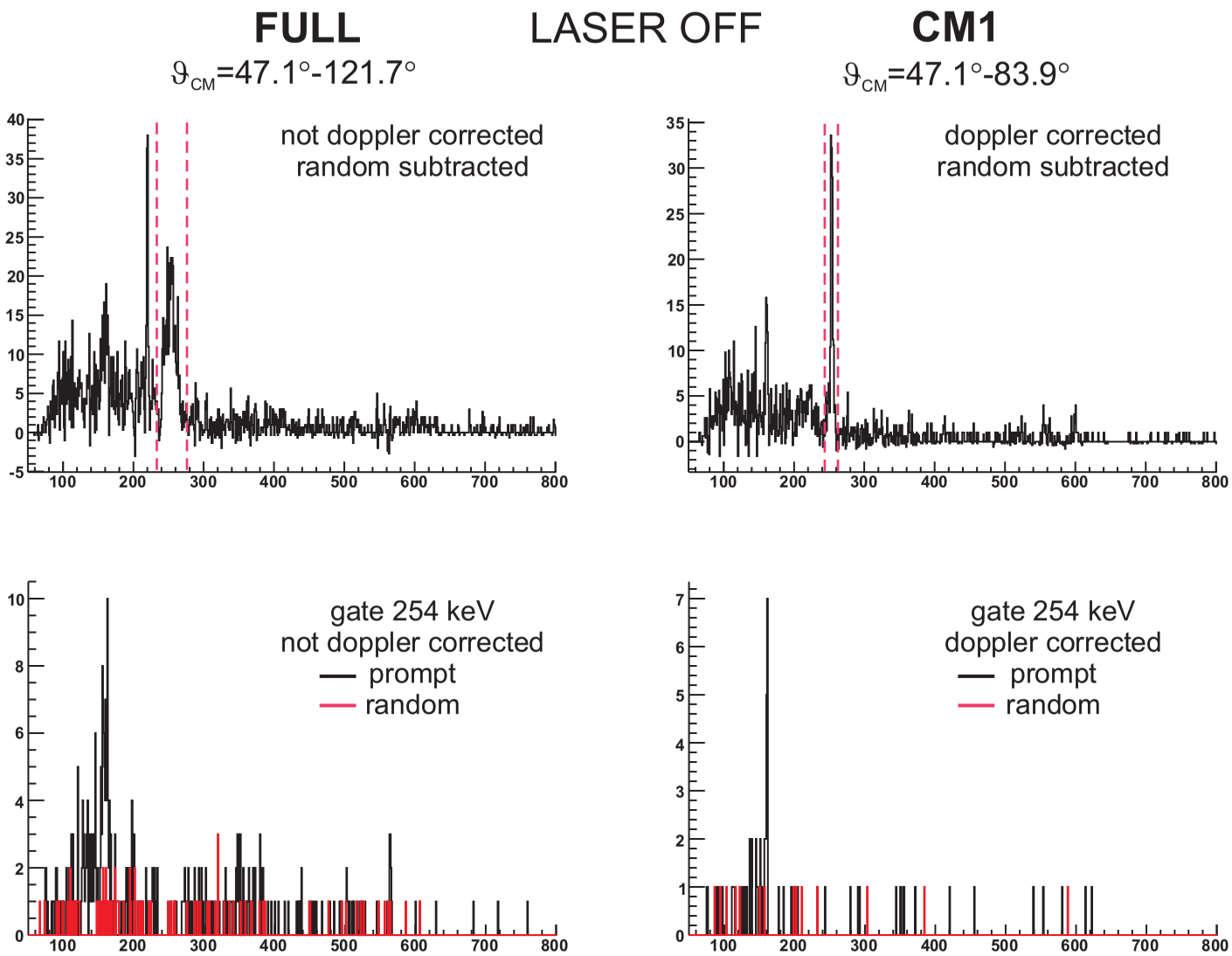

Figure B.11: *Top : random subtracted spectra over 2 CM ranges. Bottom : prompt and random spectra with a gate on the 254 keV transition. (Laser OFF spectra)*

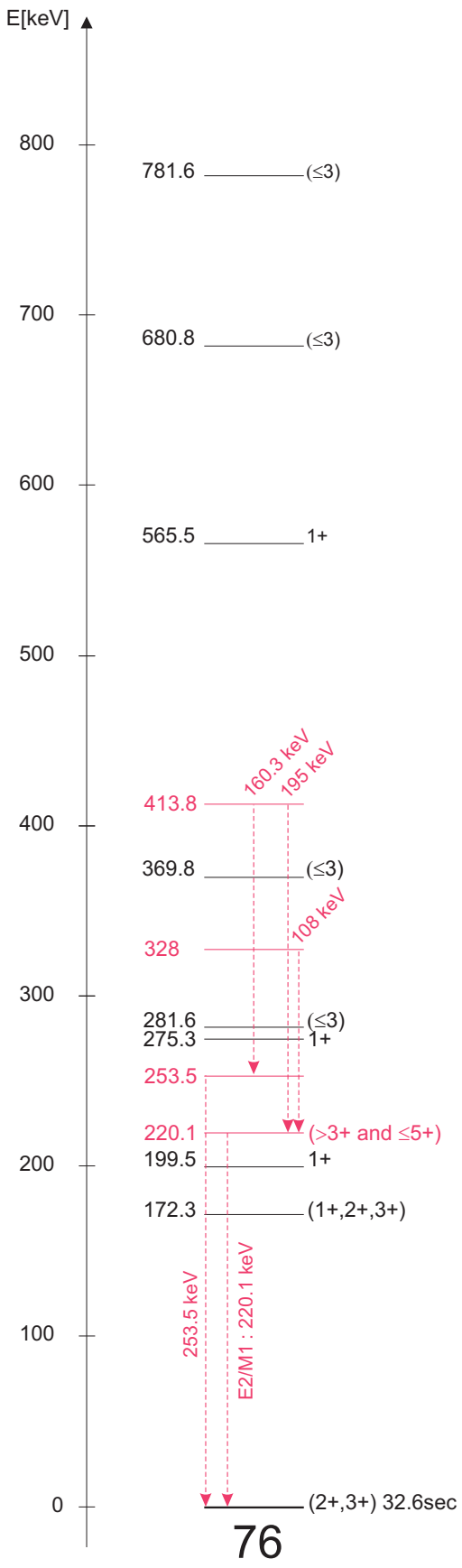

Figure B.12: *The (partial(*)) level scheme of ^{76}Ga. The observed transitions are tentatively placed in the level scheme and new tentative spin assignments and new levels are indicated in red. (*) = all levels above 1 MeV are omitted.*

B.3 ^{78}Ga

In Fig. B.13 the random subtracted spectrum is shown for the FULL (left-top) and CM1 (right-rop) range. The latter spectrum is Doppler corrected. The bottom figures are the prompt and random coincident spectra, with a gate on the 280 keV transition for both CM ranges. The same is shown in Fig. B.14 for the full A=78 laser off period. In this case, a reasonably pure ^{78}Ga beam was impinging on the ^{108}Pd target.
A Doppler broadened transition is observed at 282.9 keV. In coincidence with this gamma ray, 24(5) counts are observed in the region around 150 keV. From the poor statistics it is not clear whether these counts can be attributed to 2 or 1 transition(s). The line at 282.9 keV is possibly an M1 transition from the ground state (3+) to the known level at 281.4 keV with spin (1+,2,3+). The flight time from target to CD detector is again of ranging from 1.8-3.6 nsec. If the ground state is indeed 3^+ and the transition is M1, $J^\pi=1^+$ can be removed from the possible angular momenta.
In tab. B.3, the cross section for production of the 282.9 keV gamma ray is given. The cross section was deduced in the same way as $^{A=74,76}$Ga. The error on target yields is the statistical error, without the beam contamination included. The final error on the cross section includes the error on the beam contaminations parameter "R".

	Ga counts	error	Pd counts	error	σ_{Pd} b	σ_{Ga} mb	error
FULL	279	30	1536	44	2.13	869	197
CM1	141	17	878	33	1.51	544	127
CM2	132	22	688	30	1.12	483	127

Table B.3: *Cross sections for the de-excitation of the 282.9 keV gamma for the three CM ranges. Limiting angles in the CM can be found in Chapter 4.*

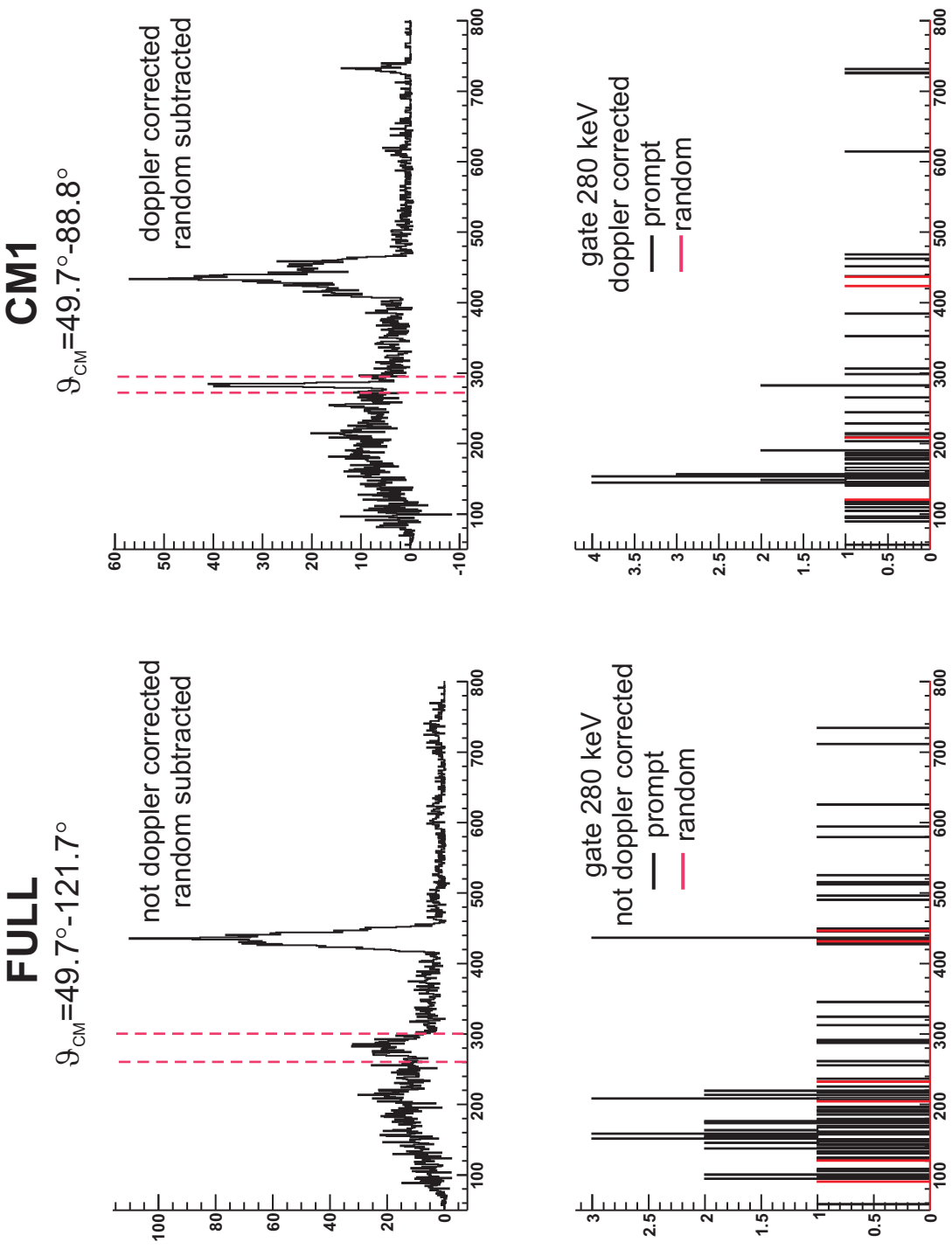

Figure B.13: *Top : random subtracted spectra over 2 CM ranges. Bottom : prompt and random spectra with a gate on the 280 keV transition. (Laser ON spectra)*

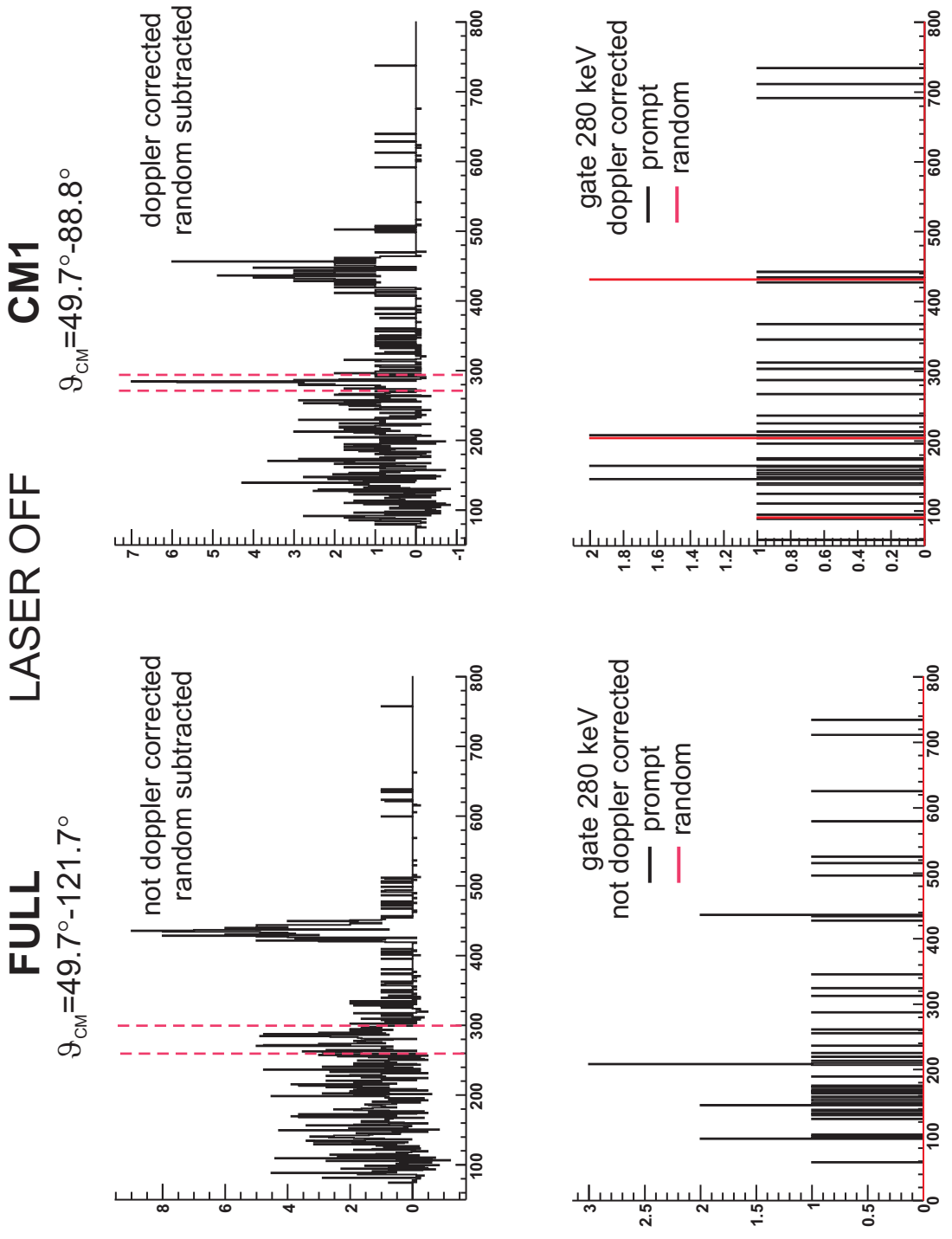

Figure B.14: *Top : random subtracted spectra over 2 CM ranges. Bottom : prompt and random spectra with a gate on the 280 keV transition. (Laser OFF spectra)*

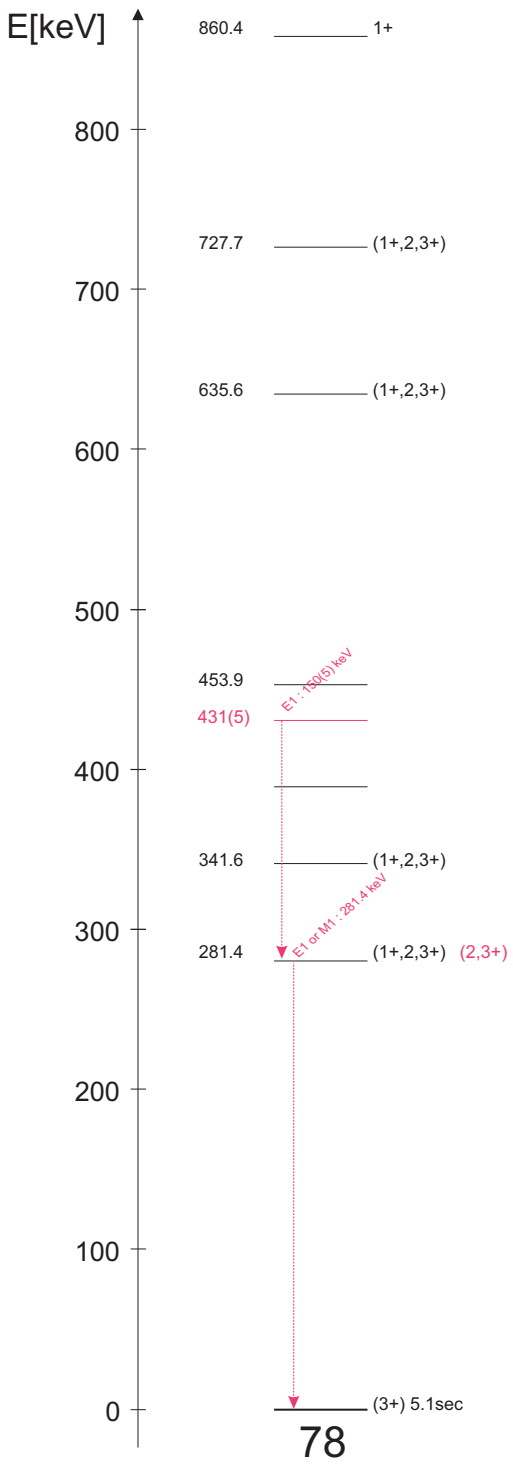

Figure B.15: *The (partial(*)) level scheme of ^{78}Ga. The observed transitions are tentatively placed in the known level scheme and new tentative spin assignments are indicated at the right in red. (*) = all levels above 900 keV are omitted.*

Appendix C

Coulomb Excitation of ^{74,76} Zn : Experiment 2003

In 2003, a first Coulomb excitation experiment was performed on ^{74,76}Zn. The experiment partly failed because of an electronics problem : the fast coincidence between particles and gamma's was not set properly so the CD detector was overwhelmed with elastically scattered particles. Switching of the "downscaling" and reducing the beam intensity resulted in a first coulex spectrum of ^{74,76}Zn. These spectra are shown in Fig. C.1.

The RIB was heavily contaminated in 2003, consisting of ^{74}Ga (∼8(2)%), ^{66}Zn (∼9(2)%) and ^{40}Ar (41(10)%), where the (%) is referring to % of the Zn beam. The number of counts in the $2_1^+ \rightarrow 0_1^+$ transition in ^{74}Zn is 289(17). Adopting the result from the 2004 experiment, the number of expected counts from the target (^{120}Sn) $2_1^+ \rightarrow 0_1^+$ transition is 8. Experimentally 20(4) counts are observed in this region. Taking into account the target excitation by all contaminants, calculated by GOSIA and the (%) of the contaminant, the resulting number of target excitation by Zn is estimated to be 7(3) counts.

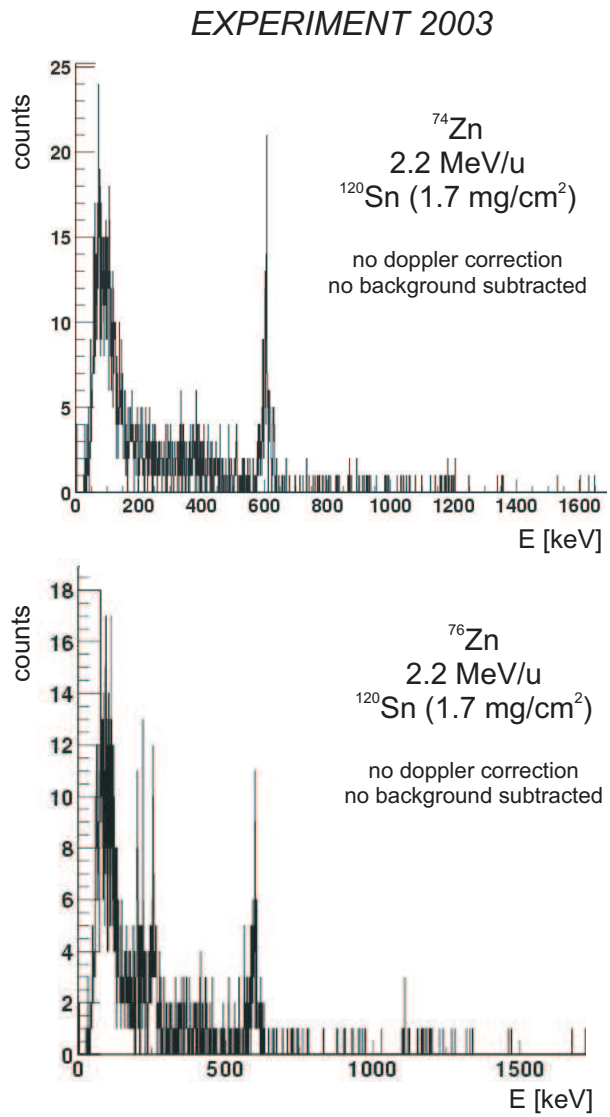

Figure C.1: *Coulex spectrum for ^{74}Zn (top) and ^{76}Zn (bottom), at 2.2 MeV/u on a 1.7 mg/cm^2 ^{120}Sn target.*

Appendix D

Timing properties

The negative values for the "prompt coincidence window" in the time difference spectrum of Fig. 5.2 are a consequence of the specific "timestamping" properties of the MINIBALL setup in 2004. The scheme in Fig. D.1 is a sketch of how the negative time difference values appear in the raw data stream. This scheme can be seen as an add-on to the logics scheme of Fig. 3.22.

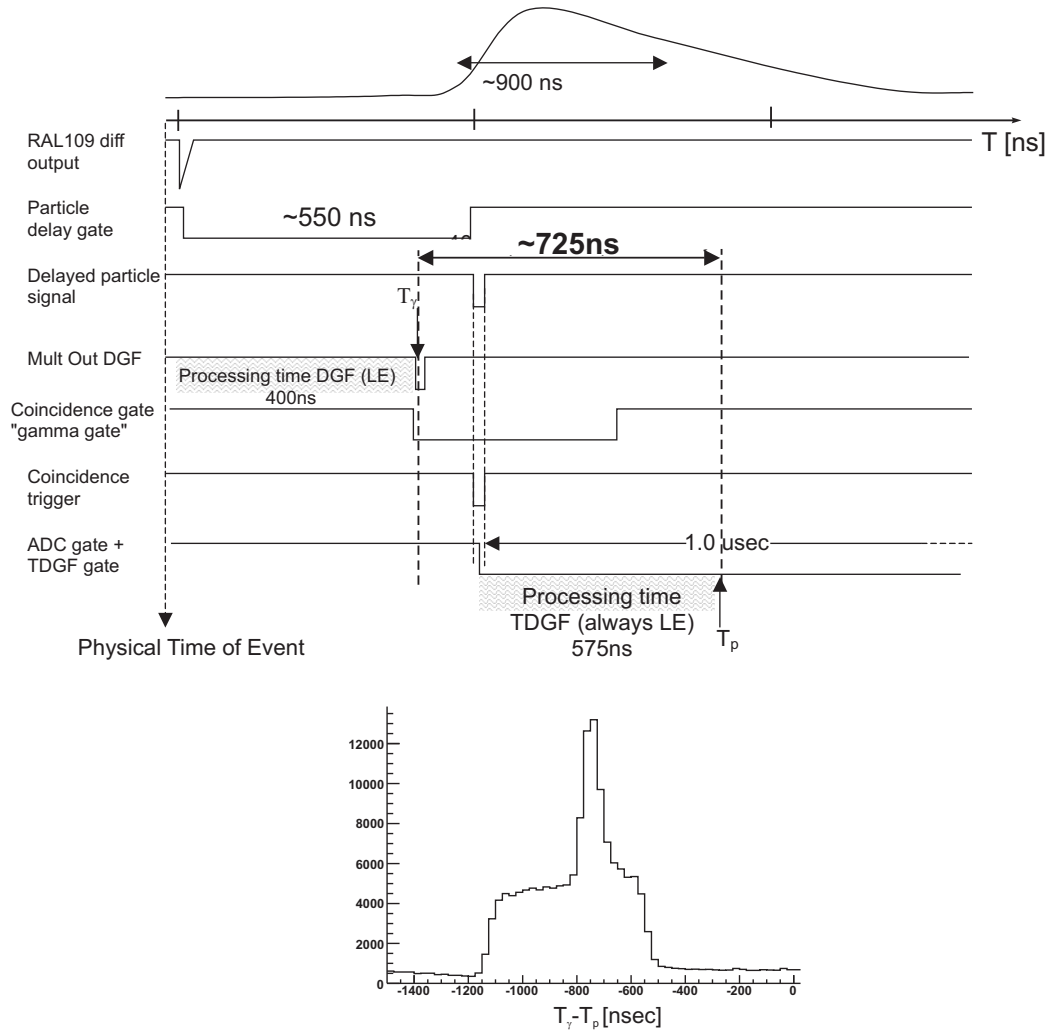

Figure D.1: *The specific timing properties of the particle and gamma branch in the MINIBALL setup (2004).*

Samenvatting

Inleiding

De wetenschappelijke kennis over de structuur van de materie heeft een vlucht genomen op het einde van de 19^e-begin 20^{ste} eeuw. In die tijd werd ontdekt dat materie is opgebouwd uit individuele *atomen*. Het atoom bestaat uit een bijzonder klein volume, de atoomkern, die omgeven is door een uitgestrekte elektronenwolk. De typische dimensie van een atoom is 10^{-10} m, terwijl de atoomkern typisch een straal heeft van enkele 10^{-15} m. De atoomstraal wordt bepaald door de elektronenwolk die zich rond de atoomkern bevind. De kleine atoomkern bestaat uit elektrisch neutrale neutronen (N=het neutrongetal) en positief geladen protonen (Z=het protongetal of het atoomgetal). Beiden dragen bijna de volledige massa van het atoom en worden nucleonen genoemd. De nucleonen worden bij elkaar gehouden in het kleine kernvolume door de *sterke interactie*. Deze laatste is een van de vier natuurkrachten (de gravitationele, electromagnetische en zwakke interactie zijn de drie overige). De vraag die in de kernfysica gesteld wordt is hoe een complex systeem van interagerende nucleonen zich binnen het kernvolume *organiseren*.

Hierbij staat de vraag centraal hoe de kracht tussen de interagerende nucleonen kan beschreven worden. Doordat de verschillende nucleonen met hun omgeving interageren kan de *vrije* nucleon-nucleon interactie niet zonder meer toegepast worden. Deze zogenaamde *in-medium* effecten worden in rekening gebracht in *residuele interacties*.

Informatie over de structuur van een atoomkern kan bekomen worden door de karakteristieke straling die een atoomkern uitzend. In het geval van radioactieve atoomkernen is deze straling op natuurlijke wijze aanwezig. Een radioactieve atoomkern is een onstabiele combinatie van een aantal protonen en neutronen. Door bv. een proton(neutron) om te zetten naar een neutron(proton) of een aantal protonen en/of neutronen uit het kernvolume te sturen zal een radioactieve kern zich naar een meer stabiele configuratie omzetten. In het geval van stabiele atoomkernen kan straling *geinduceerd* worden. Dit kan gebeuren in laboratoria, waar energetische bundels van atomen of andere deeltjes op stabiele atoomkernen worden gestuurd.

De grondtoestand van de atoomkern is een toestand van *minimale energie*. Wanneer een hoeveelheid energie wordt toegevoegd zal de atoomkern naar een geëxciteerde (of : aangeslagen) toestand gebracht worden. Deze geëxciteerde toestanden worden bepaald door de residuele interactie tussen de individuele nucleonen. Een geëxciteerde toestand wordt gekenmerkt door een spin (J) en pariteit (π). De grondtoestand van atoomkernen met een even aantal protonen en neutronen is altijd een $J^\pi=0^+$ toestand. De eerste aangeslagen toestand is in de meeste gevallen een 2^+ toestand.

De aangeslagen toestanden in een atoomkern kunnen berekend worden d.m.v. theoretische modellen. Een van de eerste kernmodellen was het *schillenmodel*, waar de atoomkern wordt voorgesteld door een *potentiaalput*. Daarin groeperen nucleonen zich in verschillende *schillen*, gescheiden door grote energieverschillen. Het succes van dit model is te danken aan de exacte voorspelling van de *magische nucleon getallen*. Een atoomkern met een *magisch* aantal nucleonen is stabieler dan een *niet-magische* kern. Het aantal nucleonen dat zich in de verschillende schillen bevindt, komt inderdaad exact overeen met deze *magische* nucleon getallen. Een *schil* binnen het schillenmodel bevat op z'n beurt een aantal *orbitalen*, die gescheiden worden door kleinere energieverschillen.
De ingrediënten voor berekeningen met het schillenmodel zijn de residuele nucleon-nucleon interactie en een computer die de vele mogelijke combinaties van nucleonen in de valentie orbitalen kan berekenen. Voor de berekeningen wordt enkel rekening gehouden met nucleonen die zich buiten een gesloten schil bevinden. Enkel deze zogenaamde *valentie*-nucleonen bepalen het excitatie spectrum van de kern. Een belangrijke beperking hierbij is dat een gesloten schil mogelijks wel bijdraagt tot het excitatiespectrum, vooral in regio's waar een exces aan neutronen of protonen aanwezig is.
Een tweede kernmodel vertrekt vanuit een geometrisch beeld van de kern. Op die manier wordt de kern beschreven als een klein sferisch volume dat door zich te vervormen in een aangeslagen toestand komt. Zo kan het kernvolume een vibratie- of rotatiebeweging uitvoeren. De energiespectra vertonen karakteristieken die typisch zijn voor zulke bewegingen. In het geval van een vibrationele kern, worden de aangeslagen toestanden van een kern beschreven door *phononen*. Een phonon heeft een angulair momentum 2. Op natuurlijke wijze vloeit daaruit voort dat de eerste aangeslagen toestand in vibrationele kernen een 2^+ toestand is.

Motivatie

In dit werk wordt nagegaan hoe zware, neutron-rijke en radioactieve Zn kernen (30 protonen en 44 tot 48 neutronen) kunnen beschreven worden met de huidige kernmodellen. De 30 protonen hebben twee protonen buiten het magische nucleon getal 28, terwijl de 44 tot 48 neutronen 6 tot 2 neutronen minder hebben dan het magische nucleon getal 50. Het neutrongetal 40 is in deze atoomkernen een intrigerend getal, aangezien het een zogenaamde sub-schillen sluiting betreft. Binnen de schil 28-50 is het laatste orbitaal dat gevuld wordt het $g_{9/2}$ orbitaal, hetwelke 10 nucleonen kan bevatten. De positie van het $g_{9/2}$ orbitaal is cruciaal voor het optreden van een aanzienlijke N/Z=40 (sub-)schillen sluiting.

Het bijzondere aan dit onderzoek is dat het hier radioactieve atoomkernen betreft die niet op natuurlijke wijze voorkomen op aarde. Daarom moeten de experimenten uitgevoerd worden aan een laboratorium waar radioactieve ionenbundels beschikbaar zijn. Een daarvan in Europa is het *ISOLDE* laboratorium in CERN.

De atoomkern wordt onderzocht aan de hand van verschillende observabelen. Zo kan het excitatie-spectrum (de verschillende energie niveaus) bekomen worden door de gamma straling op te meten tijdens het β-verval van radioactieve elementen. Een andere manier om informatie uit de kern te halen is door de kern te laten interageren met andere atoomkernen (waardoor de kernen geëxciteerd worden) en de daaropvol-

gende de-excitatie straling op te meten. In de vorige paragraaf werd reeds aangehaald dat de meeste even-even kernen een 0^+ grondtoestand en een eerste aangeslagen 2^+ toestand hebben. De waarschijnlijkheid waarmee de even-even atoomkern die overgang kan maken noemt men de B(E2)-waarde van de atoomkern. Deze B(E2) waarde bevat cruciale informatie over de *natuur* van de 2^+ toestand. B(E2) kunnen uitgedrukt worden in *Weisskopf Units* (W.u.). Een B(E2) waarde van 1 W.u. is een 1-deeltjes overgangswaarschijnlijkheid. B(E2) waarden van 50 of meer W.u. zijn typisch voor kernen waar veel nucleonen collectief verantwoordelijk zijn voor de excitatie. Lage B(E2) waarden zijn dus een indicatie dat de excitatie gebeurd door een beperkt aantal nucleonen.

In dit werk werd de B(E2) overgangswaarschijnlijkheid opgemeten tussen de 0^+ grondtoestand en de eerste aangeslagen 2^+ toestand in de even-even Zn kernen $^{74}_{30}Zn_{44}$, $^{76}_{30}Zn_{46}$ en $^{78}_{30}Zn_{48}$.
In een voorgaand doctoraatsonderzoek (Van Roosbroeck, KU Leuven, 2002) werden zware Zn kernen ($^{70-78}$Zn) onderzocht en er werd geobserveerd dat de 2^+ toestanden in deze kernen globaal een lagere energie hebben in vergelijking met de 2^+_1 energie in lichtere Zn kernen. De energie daling van een 2^+ toestand is algemeen een indicatie voor meer collectiviteit in de atoomkern. De vraag is dus hoe collectiviteit zich ontwikkeld in deze atoomkernen. De B(E2) waarde is precies de experimentele observabele die deze evolutie weergeeft. In diezelfde experimenten (Van Roosbroeck, 2002) werd geobserveerd dat een tweede 0^+ toestand zeer sterk verlaagd wordt in excitatie-energie en bereikt een minimum bij een neutrongetal van 40. Een tweede 0^+ toestand werd ook geobserveerd in $^{68}Ni_{40}$ en $^{72}Ge_{40}$, waar die zelfs de eerste aangeslagen toestand wordt van de atoomkern. In ^{68}Ni werd deze verklaard door een toegenomen verstrooiing van neutron-paren over de N=40 sub-schil.

Tot voor dit werk waren de B(E2) waarden in Zn isotopen gekend tot massa 74 (44 neutronen). De twee laatste Zn isotopen (^{72,74}Zn) zijn radioactieve isotopen, waarvan de B(E2) waarden recentelijke werden opgemeten [Lee02, Per06]. Deze gekende B(E2) waarden toonden een geleidelijke toename van collectief gedrag in de atoomkern vanaf neutrongetal 38. Dit werd geinterpreteerd als een toename van neutron-verstrooiing over de N=40 sub-schil [Per06], waardoor er meer interactie tussen valentie-protonen en neutronen ontstaat en waardoor collectiviteit toeneemt.
Deze toegenomen bezetting van het $g_{9/2}$ orbitaal werd ook geobserveerd in $^{68}_{28}Ni_{40}$ (proton schillensluiting en neutron sub-schillen sluiting). De B(E2) waarde in deze proton-magische kern is opmerkelijk laag in vergelijking met de andere proton (en neutron) magische Ni kern (^{56}Ni). De lage B(E2) waarde werd verklaard door een toegenomen verstrooiing van neutron paren over de N=40 sub-schil (die ook verantwoordelijk werden geacht voor de tweede 0^+ toestand bij lage excitatie energie) en door het uitgesproken neutron karakter van de 2^+ toestand. B(E2) waarden in Ge-isotopen (32 protonen) werden opgemeten tot de neutron schillensluiting N=50. De waarden zijn typisch 20-35 W.u., maar worden drastisch verlaagd vanaf N=44 tot aan de N=50 schillensluiting.

De experimenten beschreven in dit werk breiden de kennis van de B(E2) waarden in de Zn isotopen uit tot dicht bij de N=50 lijn (^{80}Zn). De B(E2) waarde in deze neutron-magische kern kan gebruikt worden om de effectieve proton lading te bepalen binnen de gebruikte valentieruimte of om na te gaan hoe sterk de Z=28 en N=50 schillensluitingen zijn bij deze extreme N/Z verhouding van 1.67. De nieuwe B(E2)

waarden tonen alvast de evolutie aan van de B(E2) waarden naar de N=50 lijn.

Experimentele technieken

Coulomb Excitatie

De B(E2) waarden kunnen opgemeten worden door een Coulomb excitatie te induceren in de radioactieve ^{74,76,78}Zn isotopen. In een Coulomb excitatie reactie worden twee atoomkernen met elkaar in botsing gebracht. Door de elektrische lading van beide atomenkernen worden ze door de elektromagnetische wisselwerking verstrooid tijdens de botsing. Dit verstrooiingsproces kan zowel elastisch als inelastisch gebeuren. In het geval van elastische verstrooiing spreekt men van *Rutherford* verstrooiing, waarbij de atoomkern geen inwendige energie opneemt. In het geval van inelastische verstrooing wordt de atoomkern inwendig geëxciteerd naar 1 van z'n aangeslagen toestanden. In dat geval spreekt men van Coulomb excitatie. Het inelastiche verstrooiingsproces bevat precies de structurele informatie over de atoomkern. In het geval van even-even kernen is de meest waarschijnlijke excitatie die naar het eerste aangeslagen 2^+ niveau. Het aantal kernen dat tijdens het verstrooiingsproces geëxciteerd wordt naar de 2_1^+ toestand is een maat voor de B(E2) waarde in de atoomkern.

Het Coulomb excitatie proces wordt exact beschreven door de welgekende elektromagnetische interactie ([Ald75]). De werkzame doorsnede voor het exciteren van een atoomkern, onder de invloed van het elektromagnetisch veld van de botsingspartner, kan dus precies berekend worden. De ongekende B(E2) waarde is de enige parameter in de berekening van de werkzame doorsnede.
In de beschouwde experimenten werden de Zn isotopen versneld tot een energie van ∼200 MeV en in botsing gebracht met stabiele atoomkernen in een trefschijf (^{120}Sn of ^{108}Pd). De werkzame doorsnede voor excitatie van de stabiele trefschijfkernen kan exact berekend worden aangezien de B(E2) voor deze kernen gekend is. Door een relatieve vergelijking van het aantal geëxciteerde trefschijfkernen en het aantal geëxciteerde Zn kernen kan de B(E2) waarde in Zn kernen bepaald worden.

REX-ISOLDE (CERN)

De radioactieve neutronrijke Zn isotopen werden geproduceerd aan de *radioactieve ionenbundel* faciliteit ISOLDE (CERN,Zwitserland) door middel van proton geinduceerde fissie van een Uranium trefschijf. De zware Uranium kernen bevinden zich in een Uranium-grafiet *koker* die in een *trefschijf-container* is geplaatst. De fissieproducten diffunderen uit de *trefschijf-container* naar een dunne *transmissielijn*. In dit dunne buisje (*transmissielijn*) wordt resonant laser licht gezonden. Met behulp van drie resonante laser frequenties worden selectief elektronen uit de elektronenwolk van Zn atomen naar het continuüm gebracht. Hierdoor komen de Zn atomen in een 1^+ ladingstoestand. De elektrisch geladen atomen worden vervolgens door een 60 kV potentiaal uit de trefschijf-container gehaald, waarna ze gescheiden worden naargelang hun massa. Naast de laser-geioniseerde ^{A}Zn isotopen waren er isobare (met dezelfde massa) contaminanten aanwezig die oppervlakte ionisatie ondergingen in de transmissielijn, dit door de extreme temperatuur van de transmissielijn (∼2000°C). In de beschouwde experimenten was de enige dominante contaminatie afkomstig van isobare Ga isotopen. Na de massa separatie wordt de isobare atoombundel (Zn+Ga atomen) naar een *Penning Trap* gebracht waar ze continu worden geinjecteerd en periodiek (∼25 Hz) in

pakketjes worden doorgestuurd. De pakketjes komen terecht in de *Electron Beam Ion Source* (=EBIS), waar ze met een intense elektronenbundel interageren en tot een hoge ladingstoestand worden gebracht ($\sim$20-21$^+$). Aan dezelfe repetitiefrequentie waarmee ze geinjecteerd werden in de EBIS, worden de atomen geinjecteerd in de REX-ISOLDE naversneller. Deze laatste is een lineaire versneller die de atomen versnelt tot een energie van $\sim$3.0 MeV/u (MeV per nucleon, in dit geval $\approx$200 MeV) .

An het einde van de lineaire versneller bevind zich de trefschijf waar de Coulomb excitatie van de stabiele trefschijf kernen en de radioactieve inkomende Zn kernen geinduceerd wordt. De trefschijf is omringd door acht Germanium detectoren, dewelke de gamma-stralen detecteren die wordt uitgezonden wanneer de geëxciteerde toestand vervalt naar de grondtoestand. De cluster detectoren vormen samen de MINIBALL opstelling. Iedere cluster detector bevat drie Germanium kristallen, die elk op hun beurt zes maal elektrisch gesegmenteerd zijn. Dit brengt het totaal aantal *onafhankelijke* Germanium segmenten in de MINIBALL opstelling tot 144. Deze hoge segmentatie van de Germanium detectoren heeft tot doel de richting van de uitgezonden de-excitatie gamma straal heel precies te bepalen. Aangezien de geëxciteerde atoomkern enkele pico-seconden (afhankelijk van de B(E2) waarde) na de excitatie terug vervalt naar de grondtoestand zal de uitgezonden gamma straal met een doppler verschuiving waargenomen worden, aangezien de de-exciterende kern nog steeds met hoge snelheid beweegt ($\sim$0.07c). Het inelastisch verstrooide atoom wordt gedetecteerd in een Si detector dewelke bestaat uit vier onafhankelijke kwadranten. De kwadranten zijn op hun beurt gesegmenteerd, zodat de verstrooiingshoeken van het atoom kunnen bepaald worden (zowel θ als ϕ). Door de kennis van de verstrooiingshoeken van de atoomkern en de emissierichting van de gamma straal is een Doppler correctie mogelijk van de gedetecteerde gamma energie.

Resultaten

Een moeilijkheid bij deze radioactieve ionenbundel experimenten betreft de isobare bundel contaminatie, in dit geval Ga. De ongekende B(E2) waarde van de Zn isotopen wordt bepaald aan de hand van een relatieve vergelijking met de gedetecteerde de-excitatie van de trefschijfkern. Deze laatste wordt ook geëxciteerd door de isobare Ga kernen, dus moet het aantal gedetecteerde gamma stralen afkomstig van de trefschijfkernen *genormaliseerd* worden naar het aantal de-excitaties die geinduceerd werden door Zn atomen. Daarom moet de bundelcompositie exact gekend zijn. Deze kan bepaald worden door de laser-ionisatie periodiek te blokkeren. Daardoor valt de extractie van Zn atomen uit de trefschijf-container tot nul en is er enkel extractie van Ga (er wordt aangenomen dat de Ga extractie niet beïnvloed wordt door laser ionisatie). Door gelijke tijdsintervallen te vergelijken met en zonder laser ionisatie kan de verhouding van het aantal Zn atomen tot het aantal Ga atomen bepaald worden. De informatie hiervoor kan bekomen worden door het aantal verstrooide deeltjes in de Si deeltjes detector te vergelijken, of door het verschil in gedetecteerde trefschijf de-excitaties te vergelijken tijdens periodes met en zonder laser ionisatie. Een bijkomende check van de bundel compositie werd bekomen door de bundel in een ΔE-E ionisatie kamer te sturen, waar een expliciete bepaling van het atoomgetal Z een beeld geeft van de bundel compositie. Deze meting bevestigde dat de bundel enkel uit Zn en Ga atomen bestond.

Voor deze experimenten werden uitgevoerd was de energie van de 2$^+$ toestand in

^{78}Zn onzeker. Nu, door de selectieve Coulomb excitatie van 2^+ toestanden in even-even kernen, kan deze 2^+ toestand geconfirmeerd worden en wordt de systematiek van 2^+ energieën uigebreid tot N=48.
Deze experimenten leverden B(E2,$2_1^+ \rightarrow 0_1^+$) waarden op voor de drie onderzochte Zn isotopen, maar eveneens konden B(E2,$4_1^+ \rightarrow 2_1^+$) waarden bepaald worden door geobserveerde $4_1^+ \rightarrow 2_1^+$ de-excitaties, afkomstig van dubbele excitaties : $0_1^+ \rightarrow 2_1^+ \rightarrow 4_1^+$. Deze waarden zijn de enige B(E2,$4_1^+ \rightarrow 2_1^+$) waarden boven N=40 in de Zn atomen. De B(E2,$2_1^+ \rightarrow 0_1^+$) waarde voor ^{74}Zn die in dit werk gemeten werd is in overeenstemming met de waarde die recentelijk opgemeten werd aan een ander Europees labo voor kernonderzoek (GANIL, Frankrijk) [Per06].

De B(E2) systematiek voor Zn isotopen toont dat er inderdaad meer collectiviteit optreedt vanaf N=38 (de 2_1^+ energie verlaagd en de B(E2,$2_1^+ \rightarrow 0_1^+$) verhoogd) maar die collectiviteit bereikt een maximum bij N=44, waarna de B(E2) waarden uit dit werk aantonen dat er een drastische verlaging optreedt van de B(E2,$2_1^+ \rightarrow 0_1^+$) tot N=48 (zie Fig. 5.29). Deze plotse sterke daling van de B(E2,$2_1^+ \rightarrow 0_1^+$) wanneer neutronen in het $g_{9/2}$ orbitaal worden gevuld werd eveneens waargenomen in Ge (Z=32) and Se (Z=34) isotopen.
Schillenmodel berekeningen, waar enkel valentie nucleonen buiten een ^{56}Ni kern in rekening worden gebracht zijn in goede overeenstemming met de huidige experimentele resultaten. Enkel voor de lichtere Zn kernen (proton-rijk) en bij N=44 zijn er afwijkingen. Doch, deze goede overeenstemming wordt enkel bekomen wanneer hoge *effectieve* ladingen worden toegekend aan protonen en neutronen (protonen 1.9e en neutronen 0.9e). Dit kan er op wijzen dat een gesloten ^{56}Ni kern (Z=N=28, magische nummers) niet voldoet aan de eisen van een *inerte* kern. Het optreden van proton excitaties over Z=28 werd reeds herhaardelijk gerapporteerd in de literatuur [Lis04, Ots05, Maz05, Les05a, Ken01, Per06]. De sterke daling van de B(E2,$2_1^+ \rightarrow 0_1^+$) waarde in neutron rijke Zn kernen kan er ook op wijzen dat de 2_1^+ toestand voornamelijk een neutron excitatie is binnen het $g_{9/2}$ orbitaal, wat bevestigd wordt door de schillenmodel berekeningen, waar 77% (^{76}Zn) tot 97% (^{78}Zn) van de 2_1^+ neutron golffunctie uit $g_{9/2}$ excitaties bestaat.
De B(E2,$2_1^+ \rightarrow 0_1^+$) systematiek van Zn isotopen werd berekend met twee schillenmodel berekeningen. Beiden vertrekken ze van een realistische nucleon-nucleon interactie gebaseerd op G-matrix theorie. De schillenmodel berekening door N. Smirnova ([Smi04, Smi06],label SMI) bevat een correctie van de monopool term van de residuele interactie, dewelke verantwoordelijk is voor de positie van 1-deeltjes energy niveaus. In de schillenmodel berekening door A. Lisetskiy ([Lis04,Lis06],label SMII) wordt gebruik gemaakt van een residuele interactie die gefit werd aan experimentele data in dezelfde regio van de kernkaart (Ni,Cu, N=48 en N=50 isotonen). De resultaten van beide schillenmodel berekeningen werden eerste vergeleken met de proton 1-deeltjes niveaus in neutron rijke Cu (Z=29) kernen. In deze kernen werd geobserveerd dat de excitatie energie van het $1f_{5/2}$ niveau sterk verlaagd wordt wanneer neutronen in het $1g_{9/2}$ orbitaal worden gevuld. Dit werd in [Fra01] toegeschreven aan de sterke attractieve monopool interactie tussen neutronen in de $1g_{9/2}$ en het proton in de $1f_{5/2}$. Dezelfde interactie is sterk repulsief tussen een proton in $1f_{7/2}$ en een neutron in $1g_{9/2}$ orbitals. Bij A=73 zijn het $1f_{5/2}$ en $2p_{3/2}$ niveau bijna ontaard. Dit wordt vrij goed gereproduceerd door de SMII berekeningen, terwijl SMI berekeningen deze bijna-ontaarding berekenen rond A=79. Hoewel hier dus een aanzienlijk verschil is in de beschrijving de proton 1-deeltjes niveaus, blijken de resultaten voor de B(E2,$2_1^+ \rightarrow 0_1^+$) waarden in zware Zn kernen niet sterk verschillend. Dit kan er op wijzen dat de 2_1^+ toestand

hoofdzakelijk een neutron excitatie is.

De verhouding van de 4_1^+ over de 2_1^+ energie is ongeveer 2 voor alle Zn isotopen. Deze verhouding wijst op een vibrationeel karakter voor de 2_1^+ toestand (collectief model van de atoomkern). Het vibrationele model voorspelt verder dat ook de verhouding van B(E2,$4_1^+ \rightarrow 2_1^+$) over B(E2,$2_1^+ \rightarrow 0_1^+$) 2 is. De B(E2,$4_1^+ \rightarrow 2_1^+$) waarden voor lichtere kernen voldoen niet aan deze voorwaarde, want daar zijn verhoudingen gemeten van <1. De nieuwe B(E2,$4_1^+ \rightarrow 2_1^+$) waarden voor ^{74,76}Zn tonen een verhouding van ongeveer 1.2, wat er op wijst dat hier nog steeds het vibrationele model niet van toepassing is.

Conclusies en Vooruitzichten

In dit werk werden drie Coulomb excitatie experimenten beschreven, uitgevoerd aan de *radioactieve ionenbundel*-faciliteit REX-ISOLDE te CERN, Zwitserland. Deze experimenten leverden drie B(E2,$2_1^+ \rightarrow 0_1^+$) waarden op voor de radioactieve ^{74,76,78}Zn kernen en twee B(E2,$4_1^+ \rightarrow 2_1^+$) waarden voor ^{74,76}Zn. Verder werd de energie van de 2_1^+ toestand in ^{78}Zn bevestigd. De nieuwe B(E2,$2_1^+ \rightarrow 0_1^+$) waarden werden vergeleken met twee schillenmodel berekeningen waarbij verschillende residuele interacties werden gebruikt in de valentie ruimte buiten een ^{56}Ni kern. De experimentele B(E2,$2_1^+ \rightarrow 0_1^+$) waarden worden gereproduceerd door beide berekeningen. Beide gebruiken echter hoge effectieve ladingen voor neutronen (SMI=0.9e en SMII=1.0e) en mogelijke contributies van proton excitaties over de Z=28 schil zijn niet inbegrepen. Mogelijks is dat laatste verantwoordelijk voor de noodzaak aan de hoge neutron effectieve lading.
De drastische daling van de B(E2,$2_1^+ \rightarrow 0_1^+$) waarden vanaf N=46 werd toegeschreven aan het dominante neutron karakter van de 2_1^+ toestand in deze zware Zn kernen.
De B(E2,$2_1^+ \rightarrow 0_1^+$) waarde in ^{80}Zn werd opgemeten in de zomer van 2006. Uit schillenmodel berekeningen zal moeten blijken hoeveel B(E2,$2_1^+ \rightarrow 0_1^+$) sterkte de twee protonen buiten de Z=28 schil inbrengen en hoe stabiel de N=50 schillensluiting is. Schillenmodel berekeningen waar proton excitaties over de Z=28 schil zijn inbegrepen zijn hierin cruciaal.
Coulomb excitatie studies aan dezelfde experimentele opstelling in CERN kunnen uitgebreid worden naar bv. $_{Z=28}$Ni of $_{Z=26}$Fe isotopen om de stabiliteit van de Z=28 schil te onderzoeken.
Het REX-ISOLDE project zal in de komende jaren uitgebreid worden en de radioactieve bundels zullen naversneld kunnen worden tot 3-5 MeV/u. Dit opent perspectieven om hoger aangeslagen toestanden te bevolken en Coulomb excitatie te induceren op isotopen waarvan de bundelintensiteit zeer laag is, aangezien de probabiliteit voor Coulomb excitatie toeneemt met de energie.
Met een nieuwe detectieopstelling op het einde van de lineaire versneller kunnen in de toekomst ook transfer reacties onderzocht worden. Dit opent perspectieven om de tweede 0^+ toestand rond N=40 verder te exploreren, aangezien deze toestand in Coulomb excitatie niet geobserveerd kan worden.
Met de komst van een Bragg-detector of een ionisatie kamer kan de fout of de B(E2) waarde (die vrij groot is door de onzekerheid op de bundelcompositie) gereduceerd worden. Binnen enkele jaren komt er een massa separator na de lineaire versneller, zodat het excitatiespectrum van de atoomkernen nog gedetailleerder kan onderzocht worden.

Bibliography

[Aha81] D.P. Ahalpara *et al.*, Nucl. Phys. A **371** (1981) 210.

[Ald56] K. Alder *et al.*, Rev. Mod. Phys. **28** (1956) nr 4.

[Ald75] K. Alder and A. Winther, "Electromagnetic excitation : Theory of coulomb excitation with heavy ions", North-Holland, Amsterdam-Oxford, 1975.

[Ame05] F. Ames *et al.*, Nucl. Instr. Meth. A **538** (2005) 17.

[Ame04] F. Ames *et al.*, Rev. of Sc. Instr. **75** (2004) 1607.

[And94] W. Andrejtscheff *et al.*, Phys. Lett. B **329** (1994) 1.

[Ban02] I.M. Band *et al.*, At. Data and Nucl. Data Tables **81** (2002) 1-334.

[Bee04] J.R. Beene *et al.*, Nucl. Phys. A **746** (2004) 471.

[Ber82] M. Bernas *et al.*, Phys. Lett. B **113** (1982) 280.

[Ber03] M. Bernas *et al.*, Nucl. Phys. A **725** (2003) 213.

[Boh75] A. Bohr and B.R. Mottelson, "Nuclear Structure", Benjamin, London (1975).

[Boi05] Miniball GEANT4 simulation package, URL http://www.mpi-hd.mpg.de/mbwiki/wiki/MiniballSimulation

[Bre06] N. Bree, Master Thesis, KU Leuven, 2006.

[Bro88] B. Brown and B. Wildenthal, Ann. Rev. Nucl. Part. Sci. **38** (1988) 29.

[Bru77] P.J. Brussaard and P.W.M. Glaudemans, Shell Model Applications in Nuclear Spectroscopy, North Holland Publishing, Amsterdam, 1977

[Cak06] R.B. Cakirli *et al.*, Phys. Rev. Lett. **96** (2006) 132501.

[Cas00] R.F. Casten, Nuclear Structure From a Simple Perspective, Oxford Science Publications, Oxford, 2000.

[Cau02] E. Caurier *et al.*, Eur. Phys. Jour. A **15** (2002) 145.

[Coe85] E. Coenen, PhD these, p. 15-16, KU Leuven.

[Czo] T. Czosnyka, D. Cline and C.Y. Wu, GOSIA User's Manual

[Dau00] J.M. Daugas *et al.*, Phys. Lett. B **476** (2000) 213.

[Dea04] S. Dean *et al.*, Eur. Phys. Jour. A **21** (2004) 243.

[Del05] I. Deloncle and B. Roussiere, nucl-th/0309050.

[Dew04] H. De Witte, Doctoral dissertation, "Probing the nuclear structure along the Z=82 closed shell : decay- and laser spectroscopic studies of Pb, Bi and Po nuclei",2004,KU Leuven.

[Dob94] J. Dobaczewski *et al.*, Phys. Rev. Lett. **72** (1994) 981-984.

[Duf96] M. Dufour *et al.*, Phys. Rev. C **54** (1996) 1641.

[Fed79] P. Federman and S. Pittel, Phys. Rev. C **20** (1979) 820.

[Fed00] V.N. Fedoseyev *et al.*, Hyp. Int. **127**,(2000) 409.

[Fir96] R.B. Firestone, Table of Isotopes, John Wiley & Sons Inc., 1996.

[Fla05] K. Flanagan, U. Koster, L. Weissman, private communication.

[Fra98] S. Franchoo *et al.*, Phys. Rev. Lett. **81** (1998) 3100.

[Fra01] S. Franchoo *et al.*, Phys. Rev. C **64** (2001) 054308.

[Fyn03] H.O.U. Fynbo, Nucl. Instr. Meth. B **207** (2003) 275-282.

[Gla01] T. Glasmacher, Nucl. Phys. A **693** (2001) 90.

[Gol04] V.V. Golovko *et al.*, Phys. Rev. C **70** (2004) 014312.

[Gor97] M. Gorska *et al.*, Phys. Rev. Lett. **79** (1997) 2415.

[GOS2] T. Czosnyka, GOSIA2 URL http://www.slcj.uw.edu.pl/index.php?id=81

[Gro62] L. Grodzins, Phys. Lett. **2** (1962) 88.

[Gue05] C. Guenault *et al.*, Eur. Phys. Jour. A **64** (2001) 054308.

[Gun00] C. Gund, Doctoral dissertation, "The 6-fold Segmented MINIBALL Module Simulation and Experiment",2000,MPI Heidelberg.

[Hab94] D. Habs *et al.*, Proposal to the ISOLDE committee : "Radioactive beam EXperiment at ISOLDE", CERN/ISC 94-25 (1994).

[Hab00] D. Habs *et al.*, Hyp. Int. **129** (2000) 43.

[Hab02] D. Habs *et al.*, INTC-P-156 (2002).

[Her06] A.J. Herlert, private communication (2006).

[Hey94] K. Heyde, "Basic Ideas and Concepts in Nuclear Physics", Institute of Physics Publishing, Bristol, 1994

[Hey95] K. Heyde, "The Nuclear Shell Model", Springer-Verlag, Berlin Heidelberg, 1990

[Hjo95] M. Hjorth-Jensen *et al.*, Phys. Rep. **261** (1995) 125.

[Hon04] M. Honma *et al.*, Phys. Rev. C **69** (2004) 034335.

[ISO06] ISOLDE web page, URL http://isolde.web.cern.ch/ISOLDE.

[Ken01] O. Kenn *et al.*, Phys. Rev. C **63** (2001) 064306.

[Ken02] O. Kenn *et al.*, Phys. Rev. C **65** (2002) 034308.

[Kes03] O. Kester *et al.*, Nucl. Instr. Meth. B **204** (2003) 20.

[Kli74] J. van Klinken *et al.*, Phys. Rev. C **9** (1974) 2252.

[Koi03] M. Koizumi *et al.*, Eur. Phys. Journ. A **18** (2003) 87.

[Koi04] M. Koizumi *et al.*, Nucl. Phys. A **730** (2004) 46.

[Kor05] W. Korten *et al.*, Nucl. Phys. A **752** (2005) 255.

[Kos05] U. Koster *et al.*, Conf. Proc. 3rd Int. Workshop on Nuclear Fission and Fission-Product spectroscopy (2005).

[Kos06] U. Koster, private communication

[Kot90] B. Kotlinski *et al.*, Nucl. Phys. A **519** (1990) 646.

[Kra88] K. Krane, "Introductory Nuclear Physics", Wiley, New York (2006).

[Kra94] G. Kraus *et al.*, Phys. Rev. Lett. **73** (1994) 1773.

[Kru00] R. Krucken, J. Res. Natl. Inst. of Stand. Technol. **105** (2000) 53.

[Kuo68] T.T.S. Kuo and G.E. Brown, Nucl. Phys. A **114** (1968) 235.

[Lan03] K. Langanke *et al.*, Phys. Rev. C **67** (2003) 044314.

[Lee02] S. Leenhardt *et al.*, Eur. Phys. Jour. A **14** (2002) 1.

[Les05a] J. Leske *et al.*, Phys. Rev. C **71** (2005) 034303.

[Les05b] J. Leske *et al.*, Phys. Rev. C **72** (2005) 044301.

[Let97] J. Lettry *et al.*, Nucl. Instr. Meth. B **126** (1997) 130.

[Let98] J. Lettry *et al.*, Rev. Sci. Instr. **69** (1998) 761-763.

[Lew80] D.A. Lewis *et al.*, Phys. Rev. **C22** (1980) 2178.

[Lig72] J.W. Lightbody Jr., Phys. Lett. **38B** (1972) 475.

[Lis04] A.F. Lisetskiy *et al.*, Phys. Rev. C **70** (2004) 044314.

[Lis05] A.F. Lisetskiy *et al.*, Eur. Phys. Jour. A **25** (2005) 95.

[Lis06] A.F. Lisetskiy, unpublished

[Lun06] Lund/LBNL Nuclear Data Base, URL http://nucleardata.nuclear.lu.se/nucleardata/toi/

[Lut05] R. Lutter, "MED Data Structure", URL=http://www.bl.physik.uni-muenchen.de/marabou/html/doc/MedStructure.pdf

[Lut06] R. Lutter *et al.*, URL=http://www.bl.physik.uni-muenchen.de/marabou/html/

[Mac01] R. Machleidt, Phys. Rev. C **63** (2001) 024001.

[Mac05] H. Mach *et al.*, J. Phys. G : Nucl. Part. Phys. **31** (2005) S1421-S1426.

[Mae06] A. De Maesschalck, PhD these, Universiteit Gent.

[May50] M.G. Mayer, Phys. Rev. **78** (1950) 16-23.

[Maz05] C. Mazzocchi *et al.*, Phys. Lett. B **622** (2005) 45.

[Mor04] D.J. Morrissey and B.M. Sherrill, in "The Euroschool Lectures on Physics with Exotic Beams, Vol. I", Lecture notes in physics, Springer Verlag, Berlin Heidelberg, 2004

[Naq75] I.M. Naqib, J. Phys. G : Nucl. Phys. **3** (1975) L19.

[Nav03] P. Navratil *et al.*, Phys. Rev. C (2003).

[Ney03] G. Neyens, Rep. Prog. Phys. **66** (2003).

[Nie05] O. Niedermaier, Doctoral dissertation, "Low Energy Coulomb Excitation of the Neutron-Rich Mg Isotopes ^{30}Mg and ^{32}Mg",2005,MPI Heidelberg.

[nndc] Evaluated Nuclear Structure Data File (ENSDF), URL http://www.nndc.bnl.gov/ensdf/index/jsp

[Now96] F. Nowacki, Ph.D. thesis, IRes, Strasbourg, 1996.

[Oro00] A.M. Oros-Peusquens *et al.*, Nucl. Phys. A **669** (2000) 81.

[Ost02] A.N. Ostrowski *et al.*, Nucl. Instr. Meth. A **480** (2002) 448.

[Ots05] T. Otsuka *et al.*, Phys. Rev. Lett. **95** (2005) 232502.

[Pad05] E. Padilla-Rodal *et al.*, Phys. Rev. Lett. **94** (2005) 122501.

[Per06] O. Perru *et al.*, Phys. Rev. Lett. **96** (2006) 232501.

[Pet06] P. Petkov *et al.*, Nucl. Instr. Meth. A **560** (2006) 564.

[Pov81] A. Poves *et al.*, Phys. Rep. **70** (1981) 235.

[Pov01] A. Poves *et al.*, Nucl. Phys. A **694** (2001) 157.

[Rad02] D.C. Radford *et al.*, Phys. Rev. C **88** (2002) 222501.

[Rad05a] D.C. Radford *et al.*, Nucl. Phys. A **752** (2005) 264.

[Rad05b] D.C. Radford *et al.*, Eur. Phys. Jour. A **25** (2005) 383.

[Ram01] S. Raman *et al.*, Atomic Data and Nuclear Data Table **78** (2001) 1-128.

[Res04] J.J. Ressler *et al.*, Phys. Rev. C **69** (2004) 034317.

[Rex06] Technical Report on REX-ISOLDE, 2006.

[Rin80] P. Ring and P. Schuck, "The Nuclear Many-Body Problem", Springer-Verlag, Berlin Heidelberg, 1980.

[Rik00] J. Rikovska *et al.*, Phys. Rev. Lett. **85** (2000) 1392.

[Sar01] S. Sarkar *et al.*, Phys. Rev. C **64** (2001) 014312.

[Sie05] T. Sieber, private communication.

[Smi04] N. Smirnova *et al.*, Phys. Rev. C **69** (2004) 044306.

[Smi06] N. Smirnova, private communication

[Sor02] O. Sorlin *et al.*, Phys. Rev. Lett. **88** (2002) 092501.

[Spe98] K.-H. Speidel, Phys. Rev. C **57** (1998) 2181.

[SRI] J.F. Ziegler, J.P. Biersack, SRIM2003 URL http://www.srim.org

[Sto05] N.J. Stone, Atomic Data and Nuclear Data Tables **90** (2005) 75-176.

[Sve95] L.E. Svensson *et al.*, Nucl. Phys. A **584** (1995) 547.

[Sug03] M. Sugawara *et al.*, Eur. Phys. Jour. A **16** (2003) 409.

[Tal63] A. Talmi and I. deShalit, "Nuclear Shell Theory", Academic Press, New York, 1963.

[Ter02] J. Terasaki *et al.*, Phys. Rev. C **66** (2002) 054313.

[Toh00] Y. Toh *et al.*, Eur. Phys. Jour. A **9**, 353 (2000).

[Toh01] Y. Toh *et al.*, J. Phys. G **27**, 1475 (2001).

[Ube71] H. Uberall, Electron Scattering from Complex Nuclei, Academic Press, New York, 1971.

[Van98] P. Van Duppen *et al.*, Nucl. Instr. Meth. B **134** (1998) 267.

[Van00] K. Van Esbroeck, Diploma Thesis K.U. Leuven (unpublished) (2000).

[Van04a] J. Van Roosbroeck *et al.*, Phys. Rev. C **69** (2004) 034313.

[Van04b] J. Van Roosbroeck *et al.*, Phys. Rev. Lett. **92** (2004) 112501.

[Van05] J. Van Roosbroeck *et al.*, Phys. Rev. C **70** (2005) 054307.

[Van06] P. Van Duppen, in "The Euroschool Lectures on Physics with Exotic Beams, Vol. II", Lecture notes in physics, Springer Verlag, Berlin Heidelberg, 2006.

[Vri77] H.F. de Vries *et al.*, Z. Physik A **2886** (1977) 1.

[Wal06] W.B. Walters, seminar IKS, KU Leuven.

[Wap03a] A.H. Wapstra *et al.*, Nucl. Phys. A **729** (2003) 129.

[Wap03b] A.H. Wapstra *et al.*, Nucl. Phys. A **729** (2003) 337.

[Wil80] W. Wilcke *et al.*, At. Data and Nucl. Data Tables **25** (1980) 389.

[Win89] J.A. Winger *et al.*, Phys. Rev. C **39** (1989) 1976.

[XIA] X-Ray Instrument Associates, URL=http://www.xia.com

[Xia88] X. Ji and B.H. Wildenthal, Phys. Rev. C **37** (1988) 1256.